Novel Mg-Ca-based alloys as anode materials for primary aqueous Mg-air battery

Dissertation

zur Erlangung des akademischen Grades

Doktor der Ingenieurwissenschaften

(Dr.-Ing.)

der Technischen Fakultät

der Christian-Albrechts-Universität zu Kiel

Min Deng

aus

Jiangxi, VR China

Kiel, 2020

Erster Gutachter: Prof. Dr. Mikhail Zheludkevich

Zweiter Gutachter: Prof. Dr. Fabio La Mantia

Datum der Disputation: 23.11. 2020

Erklärung

Hiermit erkläre ich, dass die beigefügte Dissertation, abgesehen von der Beratung durch die Betreuer, nach Inhalt und Form meine eigene Arbeit ist.

Die Arbeit, ganz oder zum Teil, wurde nie schon einer anderen Stelle im Rahmen eines Prüfungsverfahrens vorgelegt und ist abgesehen, von den im Anhang angegebenen Veröffentlichungen, nicht anderweitig zur Veröffentlichung vorgelegt worden.

Außerdem ist die Arbeit unter Einhaltung der Regeln guter wissenschaftlicher Praxis der Deutschen Forschungsgemeinschaft entstanden.

Mira Reng

Geesthacht, den 01.08.2020

Abstract

Primary aqueous Mg-air battery is a promising energy source due to its attractive performance, like theoretical high voltage (3.1 V) and superior energy density (6.8 kWh kg^{-1} of Mg anode). However, Mg-air system has not yet been widely accepted for commercial applications because of unsatisfactory practical battery properties, which are partly related to issues with respect to the anode material, including large anodic voltage drop and high self-discharge rate during operation. Therefore, searching for novel high-performance Mg anodes is significant regarding the further development of primary Mg-air system. High discharge activity, namely low anodic overvoltage, and suppressed self-discharge rate are highly aspired with respect to the newly developed Mg anodes.

The work presented in this thesis puts emphasis on developing new Mg-Ca based alloys as anode materials for primary Mg-air battery, more particularly the Mg-air system. Ca is adopted due to its more negative electrode potential than Mg and compatibility to the environment. Composition optimization of binary Mg-Ca anodes is proceeded in accordance to good corrosion resistance, highly negative discharge potential and enhanced utilization efficiency. The effect of varied microstructures on the corrosion and discharge performance of optimized binary Mg-Ca anode is investigated, revealing the importance of microstructure adjustment on achieving better anode properties. Additionally, the decisive factors affecting the utilization efficiency of Mg anodes are clarified according to a proposed novel approach aiming to separately determine the efficiency loss related to different forms of self-discharge. A better understanding is gained concerning alloy design for achieving high anodic efficiency, which elucidates that high fraction of secondary phases and non-uniform dissolution should be avoided for Mg alloy anodes. In this case, micro-alloying with indium (In) and germanium (Ge) are introduced as a new strategy for improving discharge properties of Mg-Ca anodes. Minor addition of In is able to activate the anodic discharge and, meanwhile, suppress the self-discharge. Thus, the adoption of micro-alloyed Mg-Ca-In anodes enables the Mg-air battery to yield superior power and energy density simultaneously. Micro-alloyed Mg-Ge and Mg-Ca-Ge alloys show similar discharge performance to the optimized Mg-Ca anode. Nevertheless, highly negative open circuit potential is obtained by micro-alloying of Ge to the optimized Mg-Ca anode, contributing to the boosted voltage of Mg-air battery with Mg-Ca-Ge anode in additive-containing electrolyte, in comparison to the system based on binary Mg-Ca anode. Summarizing, several novel Mg-Ca based alloys with excellent battery-concerned properties are proposed as good candidates for anode materials of primary aqueous Mg-air battery. All these alloys along with the rest components in this energy conversion device are completely benign to the environment. This work has a potential to contribute to facilitating wider application of the sustainable Mg-air battery and addressing the growing social demand for green energy.

Zusammenfassung

Wässrige Mg-Luft-Primärbatterien sind aufgrund ihrer attraktiven theoretischen Leistung, Betriebsspannung (3.1 V) und Energiedichte (6.8 kWh kg^{-1}) ein vielversprechender Energiespeicherkandidat. Der betrachtete Mg-Luft-Batterieansatz wurde jedoch aufgrund unbefriedigender praktischer Batterieeigenschaften, die teilweise mit Problemen in Bezug auf das Anodenmaterial zusammenhängen, noch nicht weit verbreitet für kommerzielle Anwendungen akzeptiert. Gründe hierfür sind zum Beispiel große Spannungsverluste an der Anodengrenzfläche durch Filmfomation und eine hohe Selbstentladungsrate durch Anodenkorrosion während des Betriebs. Daher ist die Suche nach neuartigen hochwertigen Mg-Anoden für die Verwendbarkeit des primären Mg-Luft-Systems von Bedeutung. Eine hohe Entladungsaktivität, erzielt durch niedrige anodische Potentialverluste und eine unterdrückte Selbstentladungsrate, werden daher in Bezug auf die neu entwickelten Mg-Anodenmaterialien in den Fokus der Entwicklungsarbeit gerückt.

Die in dieser Arbeit vorgestellten Ansätze konzentrieren sich auf die Entwicklung neuer Legierungen auf Mg-Ca-Basis als Anodenmaterialien für primäre Mg- Batterien, insbesondere das Mg-Luft-System. Ca wird aufgrund seines theoretisch negativeren Elektrodenpotentials zu Mg und seiner Verträglichkeit mit der Umwelt als sehr guter Kandidat identifiziert. Die Optimierung der Komposition von binären Mg-Ca-Anoden erfolgt hinsichtlich einer guten (Selbst-)Korrosionsbeständigkeit, einem stark negativen Entladungspotential und einer verbesserten Entladeeffizienz. Der Einfluss verschiedener Mikrostrukturen auf die Korrosions- und Entladungsleistung einer optimierten binären Mg-Ca-Anode wird untersucht. Dies zeigt, wie wichtig die Anpassung der Mikrostruktur für die Erzielung besserer Anodeneigenschaften ist. Zusätzlich werden die entscheidenden Faktoren, die die Nutzungseffizienz von Mg-Anoden beeinflussen, gemäß einem vorgeschlagenen neuen Ansatz für Anodenmaterialentwicklung geklärt. Er zielt darauf ab, den Effizienzverlust in Bezug auf verschiedene Formen der Selbstentladung separat zu bestimmen. Es wird ein besseres Verständnis hinsichtlich des Legierungsdesigns zur Erzielung einer hohen anodischen Effizienz gewonnen. Es wird gezeigt, dass ein hoher Anteil an Sekundärphasen und eine ungleichmäßige Auflösung (Entladung) für Mg-Legierungsanoden vermieden werden sollten. Zu diesem Zweck wird das Mikrolegieren mit Indium (In) und Germanium (Ge) als neue Strategie zur Verbesserung der Entladungseigenschaften von Mg-Ca-Anoden eingeführt. Eine geringfügige Zugabe von In kann die anodische Entladung aktivieren und gleichzeitig die Selbstentladung unterdrücken. Die Verwendung von mikrolegierten Mg-Ca-In-Anoden ermöglicht es der Mg-Luft-Batterie, gleichzeitig eine überlegene Leistung und Energiedichte zu erzielen (XXX). Mikrolegierte Mg-Ge- und Mg-Ca-Ge-Legierungen zeigen eine ähnliche Entladungsleistung wie die optimierte Mg-Ca-Anode. Durch Mikrolegieren mit Ge wird an der optimierten Mg-Ca-Anode ein hochnegatives Leerlaufpotential induziert. Der Ansatz führt zu erhöhten Betriebsspannungen der Mg-Luft-Batterie mit Mg-Ca-Ge-Anode in additivhaltigem Elektrolyten im

Vergleich zum System basierend auf binärer Mg-Ca-Anode. Die Arbeit stellt zusammenfassend dar, welche neuartigen Legierungen auf Mg-Ca-Basis mit hervorragenden batteriebezogenen Eigenschaften als gute Kandidaten für Anodenmaterialien einer primären wässrigen Mg-Luft-Batterie verwendet werden können. Alle diese Legierungen sowie die übrigen Komponenten dieses Batteriekonzeptes sind absolut umweltfreundlich. Hoffentlich wird diese Arbeit dazu beitragen, eine breitere Anwendung der nachhaltigen Mg-Luft-Batteriesysteme zu ermöglichen und die wachsende (gesellschaftliche) Nachfrage nach grüner Energie zu befriedigen.

Table of Contents

1 Introduction

Batteries, as electrochemical power sources, are capable of converting chemical energy (mass) into electric energy. They are widely used in a variety of equipment in different scales, ranging from electric vehicles to portable electronics and transient implantable devices. Nowadays, the research and development on batteries become a social focus due to the greatly rising demand for renewable green energy and increasing application of electrical vehicles and various electronic products in different fields. In principle, all batteries are classified into primary and secondary types. Primary batteries are designed as non-rechargeable and will be discarded after energy exhaustion. The involved reactions for power generation are not reversible. Therefore, the reactants cannot be recovered through loading electric current. By contrast, secondary batteries, which are also termed as rechargeable batteries, can be used repeatedly on the basis of recharging (cyclic). The discharge reactions for generating current are able to be reversed during a charging process so that the reactants are recovered and ready for discharging again. The capability of being used for multi-times renders secondary batteries much lower total costs of ownership than primary batteries. Hence, rechargeable batteries attract most social attention at present, overshadowing the primary system. Nevertheless, primary batteries still keep a large share of battery market, since they are being utilized in numerous applications like offshore equipment, implanted medical devices, hearing aids, toys, flashlights, etc. Besides, primary batteries possess some advantages over rechargeable system, such as long shelf-life, high energy density and instant readiness [1, 2]. These merits contribute to their significance in rescue missions, remote exploration tasks and wildfire extinguishing work, where rechargeable batteries are incompetent due to the impossibility or impracticality of recharging in these cases. Moreover, primary batteries are also important as standby power sources for school, hospital and energy storage devices for renewable energy generation system. It must be noted that heavy focuses on rechargeable batteries over primary ones do not signify that primary batteries are obsolete technologies that should be weeded out. High performance and economically feasible primary batteries are still highly demanded in modern society. Thus, much effort is required concerning the study and development of primary battery system.

Primary Mg batteries, which are normally aqueous systems, are energy storage devices that adopt metallic Mg or Mg alloys as the anode. They are considered as promising power sources, since Mg anode is low in cost, benign to the environment and possesses high safety and excellent electrochemical characteristics. Nevertheless, commercialization and application of primary Mg batteries are yet limited due to the unsatisfactory practical properties related to issues from each battery component, i.e. the anode, cathode and electrolyte (details can be found in Section 2). High performance primary Mg batteries require suitable electrolytes (including additives) combining good conductivity and low causticity to Mg anode. Besides, high-quality cathodes with excellent cathodic activity or catalytic ability, which meanwhile are inert to the electrolyte solutions, are demanded. More importantly, anode

materials should possess slow self-discharge rate while maintaining low voltage drop. Specifically, the work presented in this dissertation focuses on performance boosting of primary Mg batteries (particularly aqueous Mg-air system) from anode side via developing novel high performance and "green" Mg anode materials.

This dissertation comprises of seven separate sections. State of the art review given in Section 2 is based on a published book chapter, introducing different types of primary aqueous Mg batteries, the existing problems and some proposed approaches for battery performance improvement. Section 3 presents the motivation of this work and objectives expected to be achieved, whilst Section 4 describes all materials and experimental methods (development strategy) adopted in the concerned research. Obtained results are displayed in Section 5 in form of 4 published and 1 submitted scientific papers. A general discussion on all presented experimental results is given in Section 6. Some conclusions are drawn according to all results and are described in Section 7 accompany with some outlooks concerning the applications and future research focuses of anode materials for primary aqueous Mg-based batteries.

2 Aqueous Mg primary batteries

Literatures regarding aqueous Mg batteries are reviewed in this section based on a published chapter " Chapter 12 Aqueous Mg batteries" in the book "Magnesium batteries: Research and Applications" by The Royal Society of Chemistry [3]. In this chapter, we introduce the conventional and newly proposed types of aqueous Mg batteries based on the cathode reactants as well as their working principles. Disadvantages and existing problems of water-based systems are summarized. Moreover, approaches for the battery performance improvement and associated research progress are reviewed. Lastly, some outlooks concerning the applications like in maritime environments and future research focuses of Mg-based batteries are given. More effort regarding development of novel Mg-based anodes, advanced catalysts and electrolyte additives is recommended.

Table of content of this chapter is presented as following.

Acknowledgement

Reference

CHAPTER 12

Aqueous Mg Batteries

MIN DENG[a], DANIEL HÖCHE*[a,b], DARYA SNIHIROVA[a], LINQIAN WANG[a], BAHRAM VAGHEFINAZARI[a], SVIATLANA V. LAMAKA[a] AND MIKHAIL L. ZHELUDKEVICH[a,c]

[a]Helmholtz-Zentrum Geesthacht (HZG), MagIC – Magnesium Innovation Centre, 21502 Geesthacht, Germany; [b]Helmut-Schmidt-University - University of the Federal Armed Forces, Faculty of Mechanical Engineering, Computational Material Design, 22043 Hamburg, Germany; [c]Kiel University, Faculty of Engineering, Institute of Materials Science, 24143 Kiel, Germany
*E-mail: Daniel.Hoeche@hzg.de

12.1 Introduction

Magnesium possesses several appealing qualities for energy storage, including a relatively negative electrode potential (−2.37 V *vs.* SHE) and high volumetric capacity (3832 mA h cm^{-3}).[1–3] Moreover, Mg is relatively low in cost and environmentally benign. All of these merits enable metallic Mg to be a promising anode material for use in non-aqueous and aqueous batteries. Generally, aqueous Mg batteries are not electrochemically rechargeable due to the irreversible formation of $Mg(OH)_2$ caused by the self-discharge reaction of Mg in aqueous solution. Nevertheless, aqueous Mg-based batteries can be mechanically recharged through replacing the anode, which allows these battery systems to have numerous applications, especially in marine devices.

Over the past few decades, different types of aqueous Mg batteries have been designed with various cathode materials to fulfill the requirements of

Energy and Environment Series No. 23
Magnesium Batteries: Research and Applications
Edited by Maximilian Fichtner

Published by the Royal Society of Chemistry, www.rsc.org

different system environments. However, the wider application of aqueous Mg batteries is still limited due to issues concerning the separate parts of the battery cells, *i.e.* the anode, cathode and especially water-based electrolyte. In order to promote the application of aqueous Mg batteries, numerous methods have been adopted to boost the battery performance, including development of novel electrode materials, modification of electrolyte solutions, *etc.* In this chapter, common types of aqueous Mg batteries are summarized. The main issues, such as anode self-corrosion (related to anode impurities), which hinder the wider application of aqueous Mg batteries are discussed. Moreover, some conventional and advanced approaches for boosting the performance of aqueous Mg batteries are covered based on numerous research studies. At last, some outlooks concerning the applications and research directions of aqueous Mg batteries are presented based on the authors' knowledge and experience gained from Mg-based battery development.

12.2 Types of Aqueous Mg Batteries

Various types of aqueous Mg batteries have already been developed and utilized on different occasions, such as dry cell, reserve and mechanically rechargeable types. Here we categorize them based on the different cathode materials and reactants involved in the cathodic reactions, as shown in Figure 12.1 and Table 12.1. Additionally, battery performance boosting related to the cathode material is presented separately, since the cathode characteristics, including the cathode active material, cathode structure and catalysts, exert great influence on the properties of aqueous Mg batteries. The discharge potential of the cathodic reaction and, thus, the discharge voltage of Mg batteries, varies with different cathode active materials. Severe activation polarization and concentration polarization, which are generally related to the sluggish kinetics of the cathodic reaction and limited mass transfer of the cathodic reactants, respectively, appear alongside the discharge process

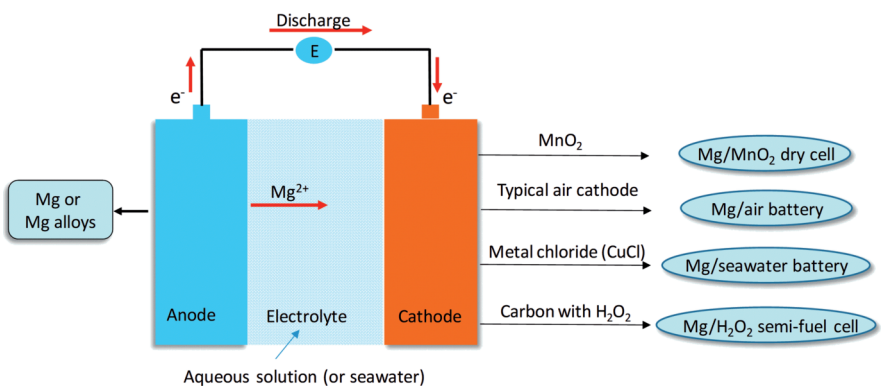

Figure 12.1 Schematic of various primary aqueous Mg-based batteries according to the cathode reactants.

Table 12.1 Characteristics of typical aqueous Mg batteries.

Battery type	Cathode reactant	Electrolyte	Theoretical voltage[a] (V)	Cathode capacity[c] (A h g^{-1})	Theoretical energy density[d] (W h kg^{-1})	Advantages	Application
Mg–MnO_2	MnO_2	Alkaline solution (*e.g.* $Mg(ClO_4)_{2\,aq}$)	2.84	0.308	759	High capacity, higher voltage than Zn–carbon, competitive cost	Military communication equipment, aircraft emergency transmitters
Mg–seawater	AgCl, CuCl, CuI, $PbCl_2$, MnO_2, *etc.*	Seawater	2.59[b]	0.187[b]	447[b]	High energy density, long unactivated shelf-time, safe	Electric torpedoes, marine devices
Mg–H_2O_2	H_2O_2 (fed into catholyte while operating)	Analyte: seawater, Catholyte: seawater, with acid (H_2SO_4)	4.15	1.577	3814	High voltage and power density, environmentally compatible	Unmanned undersea vehicles
Mg–air	O_2 (ambient air)	Neutral saline solution (*e.g.* $NaCl_{aq}$)	3.09	3.350	6800	High energy density, low cost, environmentally benign, safe	Back-up power source, remote military and telecommunication sites, undersea devices

[a]Voltage of a single cell calculated *via* standard electrode potential of each half-reaction.
[b]With AgCl active cathode material.
[c]Calculated for cathode active material only.
[d]Based on anode and cathode active materials only, excluding oxygen from the air and water in electrolyte.

and, thus, might reduce the cell voltage and cathode efficiency. Therefore, advanced cathode active materials such as active carbons with suitable catalysts are always needed to facilitate the cathodic reaction and to decrease the related activation polarization. Besides this, a suitable cathode structure is also important to solve the problems caused by the limited concentration of cathodic reactants due to species transport limitations either from the front or back side, by increasing the cathode/electrolyte interface area for example.

12.2.1 Mg–MnO_2 Dry Cell

The Mg–MnO_2 dry cell uses commercially pure Mg (cp-Mg) or Mg alloys as an anode, manganese dioxide mixed with acetylene black as a cathode and an alkaline solution (*e.g.* magnesium perchlorate with magnesium hydroxide) as electrolyte, including some chromate as an corrosion inhibitor.[4] The discharge reactions of the Mg–MnO_2 dry cell are:

$$\text{Anode: } Mg + 2OH^- \rightarrow Mg(OH)_2 + 2e \tag{12.1}$$

$$\text{Cathode: } 2MnO_2 + H_2O + 2e \rightarrow Mn_2O_3 + 2OH^- \tag{12.2}$$

$$\text{Overall: } Mg + 2MnO_2 + H_2O \rightarrow Mn_2O_3 + Mg(OH)_2 \tag{12.3}$$

When immersed in aqueous solution, Mg suffers from a parasitic reaction with water, which is termed as self-corrosion or self-discharge. The parasitic reaction is often related to local cathodic acting impurities, resulting in the formation of magnesium hydroxide, hydrogen gas and heat. Macroscopically, it can be described as:

$$Mg + H_2O \rightarrow Mg(OH)_2 + H_2\uparrow \tag{12.4}$$

The Mg–MnO_2 dry cell was developed in the early 20th century and it possesses some advantages over the primary Zn–MnO_2 battery, also commonly known as the alkaline battery. Firstly, the theoretical voltage and energy density of the Mg–MnO_2 cell are 2.8 V and 759 W h kg^{-1} (based on the anode and cathode active materials only), respectively, both higher than those of the Zn–MnO_2 system.[5] However, in practice, the voltage is decreased due to a large overvoltage of 0.7–0.9 V. Thus, the Mg–MnO_2 cell can achieve an open-circuit voltage (OCV) of only 1.9–2.0 V, still higher than that of the Zn–MnO_2 battery. Besides this, the Mg–MnO_2 dry cell has a long shelf life in an undischarged condition, even at high temperatures (>>RT), where it is twice that of the Zn system. The excellent storability is attributed to the protective film that forms on the surface of the Mg anode and the strong inhibition against secondary detrimental corrosion caused by chromate inhibitors. Therefore, the Mg–MnO_2 dry cell has been successfully used in military communication equipment and aircraft emergency transmitters.[5]

Traditional MnO_2 powders are normally used to prepare the cathode for Mg dry cells, mixed with acetylene black or carbon black. Basically, among the various crystallographic forms of MnO_2, such as α-, β-, γ- and δ-types, α-MnO_2 is a traditionally attractive material because of its specific properties for industrial applications and molecular sieves. Nevertheless, the morphologies of MnO_2 powders have an impact on their properties as a cathode material. As reported by Srither *et al.*, a cathode prepared with MnO_2 nanoparticles (average diameters of 87 and 46 nm) exhibits a higher discharge capacity (173 and 206 mA h g^{-1}, respectively) and enhanced energy density (299 and 360 W h kg^{-1}, respectively) than a cathode with micron MnO_2 powder, with a discharge capacity of 103 mA h g^{-1} at an energy density of 178 W h kg^{-1}.[6] Besides this, graphene-doped MnO_2 nanoparticles can further improve the performance of Mg–MnO_2 cells compared to a pristine MnO_2 electrode.[7] This is attributed to the higher Mg-ion storage capacity in the increased open space available in the MnO_2–graphene framework. Additionally, some organic nitro compounds have been reported to act as advanced active cathode materials for primary Mg dry cells, such as 2-β-dinitrostyrene.[8] However, as indicated by Renuka, the usage of 2-β-dinitrostyrene as a cathode decreases the voltage of the Mg primary cell in $Mg(ClO_4)_2$ solution (~0.95 V), compared to that of a traditional MnO_2 cathode (~1.5 V), even though a more stable discharge voltage can be obtained.[8]

12.2.2 Mg–Seawater Battery

The Mg–seawater battery uses cp-Mg or Mg alloys as an anode material and seawater from the ocean as an electrolyte solution. The active cathode material varies from silver chloride, cuprous chloride, lead chloride, cuprous iodide, cuprous thiocyanate to manganese dioxide.[9] The current-producing and overall reactions for this seawater battery are as follows (using a Mg/seawater/AgCl system as an example)

$$\text{Anode: } Mg \rightarrow Mg^{2+} + 2e \tag{12.5}$$

$$\text{Cathode: } AgCl + e \rightarrow Ag + Cl^{-} \tag{12.6}$$

$$\text{Overall: } Mg + 2AgCl \rightarrow 2Ag + MgCl_2 \tag{12.7}$$

The detrimental side reaction seen in eqn (12.4) between the Mg anode and water also occurs in this battery system.

The water-activated battery was developed in the 1940s to meet the need for an extremely lightweight, small sized and high-powered battery for military applications.[10] During this period, magnesium was used as the anode material in most water-activated batteries due to its attractive electrochemical properties. Normally, the water-activated battery has a long shelf life because it is constructed and stored under dry conditions

and the seawater-based electrolyte is separated from the battery system during storage. This battery, usually as a reserve type, is activated at the time of use when the electrolyte is added in by *e.g.* opening a sensor controlled valve. The huge benefit of the water-activated battery is that the electrolyte can be natural seawater from the ocean, decreasing the space and cost for battery storage and transport. The Mg–seawater battery has been successfully used in various applications with different designs and cathode materials.

A Mg/seawater/AgCl battery was first developed as a power source for electric torpedoes. Afterwards, it was adapted as a power source for marine devices, such as sonobuoys, weather balloons, air–sea rescue equipment, emergency lights, *etc.*, due to its high energy density, high power density and long shelf life in an unactivated condition.[11] Silver chloride is a well-known cathode active material for seawater batteries since it offers several advantages compared to other active materials for cathodes.[12–15] Firstly, the high reduction potential of AgCl (0.222 V) contributes towards the high discharge voltage of the Mg–seawater system.

Secondly, silver chloride can be melted, cast into ingots and rolled into sheets of up to 0.08 mm in thickness.[13] It can be used in almost any cell configuration due to its ductility and malleability. Besides this, a base current collector grid is not needed for the usage of an AgCl cathode. However, the high raw material cost hinders its commercial application in a wider range of power sources. Therefore, the request for economical alternatives to AgCl has prompted searches for substitute cathode materials. In this context, some non-silver cathodes have been proposed, such as $PbCl_2$, MnO_2 and some copper compounds, such as CuCl and CuI, despite no alternative being found to achieve discharge properties close to those of AgCl.[14,16–23] Among these non-silver cathodes, CuCl is commercially successful but shows drawbacks of low voltage, inferior energy density, low rate capability and worse resistance to storage under high humidity. CuI was found to have a superior performance and more improvements can be achieved with cathode additives such as sulphur.

The voltage increase of a CuCl electrode caused by the addition of elemental sulphur was found and explained by Amlie *et al.*[24] After sulphur addition, the electrode reaction changes from

$$CuCl + e \rightarrow Cu + Cl^- \quad (12.8)$$

to

$$CuCl_2 + e \rightarrow CuCl + Cl^- \quad (12.9)$$

where cupric chloride is generated *via* a chemical reaction between sulphur and cuprous chloride after immersion in an aqueous electrolyte:

$$2CuCl + S + e \rightarrow CuCl_2 + CuS \quad (12.10)$$

Therefore, the overall reaction can be presented as:

$$CuCl + S + e \rightarrow CuS + Cl^- \quad (12.11)$$

leading to a theoretical voltage increase of 0.506 V.

The addition of sulphur was reported to enhance the cathode voltage of other copper compounds, such as CuBr, $CuSO_4$, $Cu(HCOO)_2$, $Cu(CH_3COO)_2$ and CuC_2O_4 *via* a similar mechanism.[25] Besides, the type of sulphur allotrope used also has a great influence on the cell voltage of Mg–CuI seawater batteries, as indicated by Renuka when comparing different sulphur additives, *i.e.* cyclohexasulphur (S_6), cyclooctasulphur (S_8) and cyclododecasulphur (S_{12}).[26] Aromatic disulfide, AgCl and Ag_2S as additives for CuI cathodes have been studied, showing significant enhancement in the cell voltage of a Mg seawater system, *e.g.* from 1.08 to 1.6 V after the addition of 10 wt% S and 1.25 wt% Ag_2S into the CuI cathode.[13,27] A voltage increase upon S addition is facilitated by the presence of AgCl and Cu_2S in the CuI cathode. Interesting to know is the fact that the adoption of AgCl as an additive to CuI systems can offer a battery performance close to that supplied by an AgCl active cathode while significantly reducing the silver content.

Beyond these, Mg seawater batteries using hydrogen peroxide or dissolved oxygen in the seawater as cathode reactants have also been developed for different applications. These two types, termed as the Mg–H_2O_2 semi-fuel cell and Mg–air battery, respectively, are covered in Sections 12.2.3 and 12.2.4, respectively.

12.2.3 Mg–H_2O_2 Semi-fuel Cell

The Mg–H_2O_2 semi-fuel cell was developed by the Naval Undersea Warfare Center (NUWC) as a power source for US Navy's low rate, long endurance unmanned undersea vehicles (UUV).[28] This semi-fuel cell uses Mg as an anode and hydrogen peroxide as a cathode reactant. The cathode, serving as the reaction site for hydrogen peroxide reduction, is normally carbon paper with palladium and iridium as a catalyst and is separated from the anode by a conductive ion exchange membrane. This system uses seawater as an anolyte and a catholyte with a solution of seawater, acid and hydrogen peroxide. The cell is activated when the anolyte and catholyte are pumped into the system. In other words, with sufficient active anode material, this system has the ability to produce electrical energy as long as the catholyte is fed to the cathode, being the reason for the naming of it as a "semi-fuel cell". The half-cell reactions and overall reaction are as follows:

$$\text{Anode: } Mg \rightarrow Mg^{2+} + 2e \quad (12.12)$$

$$\text{Cathode: } H_2O_2 + 2H^+ + 2e \rightarrow 2H_2O \quad (12.13)$$

$$\text{Overall: } Mg + H_2O_2 + 2H^+ \rightarrow Mg^{2+} + 2H_2O \quad (12.14)$$

Besides reaction 12.4, secondary decomposition and precipitation reactions can occur:

$$2H_2O_2 \rightarrow H_2O + O_2 \quad (12.15)$$

$$Mg^{2+} + 2OH^- \rightarrow Mg(OH)_2 \quad (12.16)$$

$$Mg^{2+} + CO_3^{2-} \rightarrow MgCO_3 \quad (12.17)$$

The precipitation products of the reactions shown in eqn (12.16) and (12.17) decrease the voltage and energy density of the semi-fuel cell, but this issue can be solved through the addition of reacting acids such as H_2SO_4. The theoretical voltage of the acid Mg–hydrogen peroxide system is 4.14 V. Nevertheless, the practical voltage is only 1.7–1.8 V with some modification and the energy density ranges from 500–520 W h kg^{-1}.[28–30] The working conditions, including anolyte flow rate, catholyte flow rate, hydrogen peroxide concentration, current density and temperature, have a great influence on the discharge performance of this electrochemical system.[30]

In terms of Mg–H_2O_2 semi-fuel cells, the cathode material does not participate in the cathodic reaction. The cathodic reactants are fed in from the outside and then reduced in the overall battery reaction with assistance of the catalyst contained in the cathode, which is needed to accelerate the kinetics of the cathodic reaction. The combination of palladium and iridium has been widely accepted as a catalyst for the Mg–H_2O_2 system, since it shows superior performance compared to other catalysts such as silver and Pd.[28,29,31,32] A combined Pd/Ag catalyst has also been explored by electrodeposition of Pd on Ag coated nickel foam.[33] The Mg–H_2O_2 system with this Pd–Ag catalyzed porous cathode exhibits a maximum power density of 140 mW cm^{-2}, which is higher than for Ag coated Ni foam cathode (110 mW cm^{-2}) under the same operation conditions. Nevertheless, the battery performance of the Mg–H_2O_2 system is still limited by the concentration polarization of H_2O_2 when it is diluted in the flowing catholyte. Therefore, several cathode substrates have been adopted, such as nickel foams, titanium foams, carbon papers, *etc.*, and the cathode structure has been modified to decrease the H_2O_2 concentration effect.[34] Titanium foam shows the best corrosion resistance in 0.5 M H_2SO_4 solution when compared to nickel foam and silver-coated nickel foam. The adoption of a Pd/Ti cathode enhances the power density of the Mg–H_2O_2 system to 110 mW cm^{-2} compared to a Pd–Ag/Ni cathode (80 mW cm^{-2}) and enables the battery system to have good stability during 50 h of testing.[35] Moreover, carbon fibers have been applied to a carbon paper substrate to modify the cathode structure by Bessette *et al.*[36] As reported, after electrodeposition to the prepared carbon fiber cathode, well-formed Pd–Ir catalyst clusters are clearly shown, which are expected to significantly increase the surface area per volume. Hence, a superior cell voltage to current performance in the Mg–H_2O_2 system was achieved.

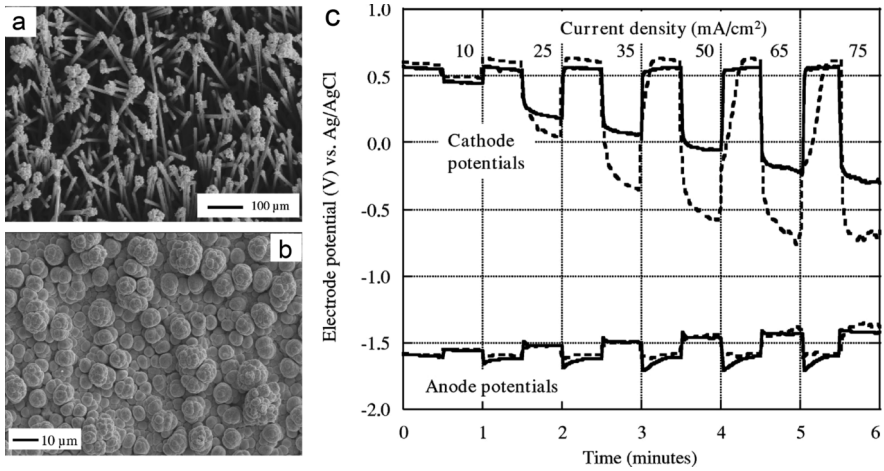

Figure 12.2 Top-view SEM images of (a) a Pd–Ir coated carbon microfiber array cathode, (b) a planar (control) Pd–Ir cathode. (c) The cathode and anode potentials of a Mg–H_2O_2 semi-fuel cell at various current densities: (—) with a carbon microfiber array-based cathode; (– – –) with a planar cathode. Reproduced from ref. 34 with permission from The Electrochemical Society, Copyright 2008.

As a further development, a method called direct charging electrostatic flocking has been used to fabricate 3D, carbon microfiber array (CMA)-based cathodes.[34] These cathodes comprise conductive carbon microfibers (11 μm in diameter, 500 μm in length) that protrude from the titanium substrate (as shown in Figure 12.2a). The CMA-based cathode with Pd–Ir catalyst enables the Mg–H_2O_2 system to have a higher voltage at a high current density (Figure 12.2c), enhanced power density (peak power density increased from 53 to 84 mW cm^{-2}) and equivalent H_2O_2 utilization, compared to planar cathodes with the same catalyst loading.

12.2.4 Mg–Air Battery (Aqueous Type)

The magnesium–air battery uses cp-Mg or a Mg alloy as an anode, an aqueous solution as an electrolyte and oxygen from the air as a cathode reactant. A typical air electrode with a catalyst is adopted as a cathode. The usage of air as a cathode reactant reduces the weight of this battery system and frees up more space for energy storage, contributing to the high energy density of the system. The reactions involved in the Mg–air cell are as follows:

$$\text{Anode: } Mg \rightarrow Mg^{2+} + 2e \tag{12.18}$$

$$\text{Cathode: } O_2 + 2H_2O + 4e \rightarrow 4OH^- \tag{12.19}$$

$$\text{Overall: } 2Mg + O_2 + 2H_2O \rightarrow 2Mg(OH)_2 \tag{12.20}$$

The theoretical voltage of the Mg–air system is 3.1 V and the energy density is 6.8 kW h kg^{-1} (based on the Mg anode only). Unavoidably, the specific voltage and energy density in practice are reduced, because of the parasitic reaction shown in eqn (12.4) again and severe overvoltage induced from different components (IR-drop, *etc.*) of the battery system. Another problem for the Mg–air system is the delayed voltage response to an increased load caused by the surface film of the discharge products, *i.e.* magnesium hydroxide. Nevertheless, the Mg–air batteries have a broad range of applications and good future prospects.

The Mg–air system was initially designed as a reserve type as the electrolyte is separated from the battery system. This battery can be stored for long time and be activated any time after adding electrolyte (water-based) into the system. Therefore, one important application of the Mg–air system is as a back-up power source for electric and solar power in schools or hospitals in case of emergencies. Besides this, the effective energy density of the Mg–air battery can be increased significantly with the addition of corrosion inhibitors to the electrolyte, contributing to its potential as a power source for remote military and telecommunication sites. Furthermore, as mentioned already in Section 12.2.2, a battery system with seawater as the electrolyte, oxygen dissolved in seawater as a cathode reactant and Mg-based material as an anode is also available. This type of battery is expected to have an energy density of 600 W h kg^{-1}, which is higher than that of other undersea power systems such as silver/zinc, Al/H_2O_2 and fuel cells.[37] Unfortunately, due to the limited solubility of oxygen in water, this system can only offer low current density and low power, therefore it is mainly used in long-term low power undersea devices, such as lighthouses, floats, undersea monitoring equipment, UUVs and sea floor borehole broadband seismic observatories.[38–40]

Also, here, the performance of Mg–air batteries is closely associated with the cathode, in which the oxygen reduction reaction (ORR) takes place. The structure of a conventional air cathode is shown in Figure 12.3, indicating four layers, *i.e.* the waterproof breathable layer, the gas diffusion layer (GDL), the catalyst layer and the current collector. The function of the waterproof layer is to prevent electrolyte leakage while enabling oxygen to penetrate from all sides. However, in some cases, this waterproof layer is not necessary as the gas diffusion layer, which is usually made from carbon materials and PTFE, can also offer the same functionality.[41–45] The catalyst layer is composed of effective catalysts to decrease the activation overpotential resulting from the sluggish kinetics of the ORR. Both the GDL and catalysts have a great influence on the performance of Mg–air batteries and much research work has been carried out to develop a superior cathode for a Mg–air system.

In fact, a series of complex electrochemical reactions are involved in the cathode oxygen reduction. In a neutral electrolyte, the related reactions can be expressed as follows, including the reaction shown in eqn (12.19):

$$O_2 + 2H_2O + 2e \rightarrow HO_2^- + OH^- \qquad (12.21)$$

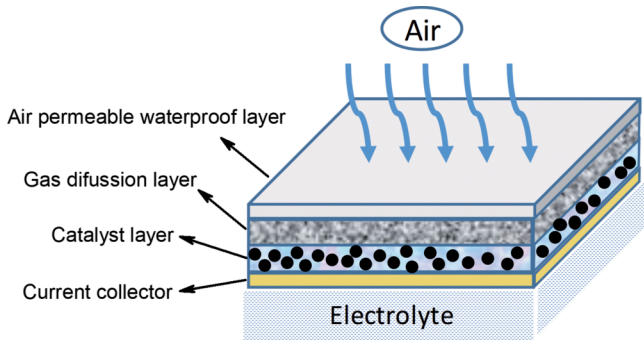

Figure 12.3 Conventional structure of a four-layer air cathode. Adapted from ref. 2 with permission from the Royal Society of Chemistry.

$$HO_2^- + H_2O + 2e \rightarrow 3OH^- \quad (12.22)$$

$$2HO_2^- \rightarrow 2OH^- + O_2 \quad (12.23)$$

Therefore, the oxygen reduction may proceed *via* a four-electron pathway (shown in eqn (12.19)) or a two-electron pathway (the reaction shown in eqn (12.21)) followed by either the reaction shown in eqn (12.22) or (12.23) on the surface of the cathode materials. The direct four-electron ORR pathway is desirable owing to its high efficiency for energy conversion, while the two-electron pathway is unfavorable because of its low efficiency and generated corrosive peroxide species.[1,2] The applied catalytic materials have a great influence on the ORR pathways and mechanisms, which, therefore, affect the battery performance in terms of a constant high power output. Hence, a promising catalyst should have good catalytic ability to favor the ORR *via* a direct four-electron pathway. Note that the ORR pathway varies not only with the catalyst category but also with its structure (surface geometry/morphology) due to its impact on oxygen transport and local surface reaction conditions. Normally most catalysts for other metal–air batteries can also operate as catalysts in Mg–air systems. Platinum shows superior ORR catalytic activity owing to the predominant four-electron pathway of the ORR, but the high price hinders its commercialization in Mg–air batteries. Therefore, the search for economical low-Pt or non-Pt catalysts draws much attention. Pt alloys doped with other transition metals, *e.g.* Fe, Ni and Co, and other modified noble metals such as Pd, Cu and Ag have been proposed as catalysts for the ORR. These catalysts show high catalytic activity and good durability. The adoption of noble metals rather than Pt reduces the cost associated with the cathode materials for Mg–air batteries. Nevertheless, more research has been devoted to explore more economically available catalysts without noble metals, such as carbon-based materials, transition metal oxides (MnO_2) and perovskite-based oxides. Various proposed catalysts for ORR and their modifications have been well summarized by Cheng *et al.* and Zhang

et al.[1,2] However, most proposed catalysts for ORR were tested and evaluated in alkaline or acidic solutions. Mg–air batteries utilize neutral solutions as the electrolyte to avoid fast self-corrosion in acidic media and high overpotential resulting from the $Mg(OH)_2$ film in alkaline solutions. Suitable catalysts working in neutral electrolytes are required for superior performance of Mg–air batteries. In the following, some novel catalysts are briefly introduced that have been evaluated recently in pH-neutral Mg–air full cells.

Zhao *et al.* proposed a Pd–Sn binary alloy as a catalyst for Mg–air batteries to reduce the cathode cost while maintaining excellent catalytic activity.[46] A cathode was prepared with 24 h heat-treated Pd–Sn as a catalyst and multi-walled carbon nanotubes (MWCNTs) as the support material. The Mg–air battery with this Pd–Sn/MWCNTs-based cathode exhibits a higher power density (more than 112.4 mW cm^{-2}) and increased durability than that with a Pd/C-based catalyst (82 mW cm^{-2}). Besides this, non-metal catalysts as low-cost alternatives have also been explored. Planar iron–polyphthalocyanine (PPcFe) catalysts for Mg–air batteries were fabricated with different PPcFe/carbon ratios and various heat treatment temperatures by Li *et al.*[45] The PPcFe/C-based cathode prepared under optimized conditions (PPcFe/C ratio 1 : 1, 400 °C) was then tested in a Mg–air full cell and compared with a pure Pt/C-based cathode. The results demonstrate that a similar discharge voltage and power density can be obtained with this PPcFe/C-based catalyst in 10 wt% NaCl solution compared with a Pt/C-based catalyst. Furthermore, based on the success of perovskite-based oxides as catalysts for the ORR in alkaline solutions, a mixed-phase mullite ($SmMn_2O_5$) has been prepared and evaluated as a catalyst for Mg–air batteries by Li *et al.*[47] The results show that the mullite-based cathode exhibits a similar catalytic activity to that of a Pt/C-based cathode in 1 M NaCl solution, while better stability is obtained. The enhanced cathode performance is attributed to the catalytic Mn sites and facilitated oxygen adsorption and diffusion by the coexistence of a CeO_2 phase. In addition to the catalysts, the support materials in the catalyst layer also exert a great influence on the cathode performance, especially for MnO_2-based cathodes because of the low electric conductivity of catalytic MnO_2. Support materials, normally based on carbon, must have good electrical conductivity and can offer sufficient reaction sites for the ORR. Modified carbon materials with nanostructures have been explored as catalyst supports for Mg–air batteries, such as graphene, carbon nanofibers (CNFs) and the aforementioned MWCNTs.[41,44,48] Both carbon black and MWCNTs show a catalytic activity for the ORR that is inferior to that of a MnO_2 catalyst. Nevertheless, the catalytic activity of MnO_2 can be significantly enhanced when combining it with carbon materials, especially MWCNTs. The Mg–air battery measurements in 10 wt% NaCl solution demonstrate that the MnO_2/MWCNT-based cathode enables the Mg–air system to have a higher voltage and enhanced power density compared with MnO_2- and MnO_2/C-based cathodes.[41] In detail, the cell voltages for MnO_2/MWCNTs-, MnO_2- and MnO_2/C-based air batteries at a current density of 20 mA cm^{-2} are 1.4, 1.13 and 1.35 V, respectively, while the peak power densities are ~70, 55 and 61 mW cm^{-2}.

Apart from the aforementioned factors, the cathode performance is also related to the porous GDL. Proper pore number and dimensions in the GDL are beneficial for lowering the overpotential resulting from oxygen diffusion limitation, and, hence, enhancing the final battery performance. Therefore, the modification of electronic conduction materials in the GDL, which are generally carbon materials, has attracted attention. Carbon fiber felts (CFF) with a three-dimensional structure and high electronic conductivity have been suggested as alternatives for traditional carbon powders in the GDL.[42,43] As reported, a Mg–air cell with a CFF-based cathode shows higher power density (maximum of about 116 mW cm^{-2}) and good stability during 1100 h of life testing at a current density of 30 mA cm^{-2} in 10 wt% NaCl solution, compared to a traditional carbon powder-based cathode using the same catalysts (maximum of around 83 mW cm^{-2}).[43]

12.2.5 Other Types

Aside from the widely researched systems mentioned above, some new aqueous Mg-based power sources with special design have been proposed recently. Liu *et al.* developed a high-specific-energy magnesium–water battery for full-depth ocean applications with water as a cathode reactant.[49] This battery system uses nickel foam with optimized Pt loading as a cathode material, serving as a location for water reduction (Volmer–Heyrovsky type). The reactions involved in this system are as follows:

$$\text{Anode: } Mg \rightarrow Mg^{2+} + 2e \tag{12.24}$$

$$\text{Cathode: } 2H_2O + 2e \rightarrow H_2 + 2OH^- \tag{12.25}$$

$$\text{Overall: } Mg + 2H_2O \rightarrow Mg(OH)_2 + H_2 \tag{12.26}$$

Instead of dissolved oxygen, the utilization of water as a cathode reactant could overcome the issue of low power density caused by low and nonuniform concentration of oxygen in ocean water. Combined with AZ91 Mg alloy as an anode, this system exhibited a high energy density of 1003 W h kg^{-1} (anode related limitation) and stable discharge for 100 days, as reported. Nevertheless, large amounts of hydrogen are produced during the battery operation and released into the sea, which, consequently, causes considerable energy loss, *e.g.* due to superfluous hydrogen at the very surface and lowered effective surface. Another battery design combining a Mg–water system with a fuel cell was proposed by Hahn *et al.* to take advantage of the produced hydrogen and to increase the energy density.[50] The illustration of this battery system is presented in Figure 12.4. In this system, the Mg–water system is submerged in a seawater electrolyte, supplying power to an outside device and, meanwhile, serves as a hydrogen generator for a fuel cell. The released hydrogen, which is produced both by cathode reaction and self-discharge of

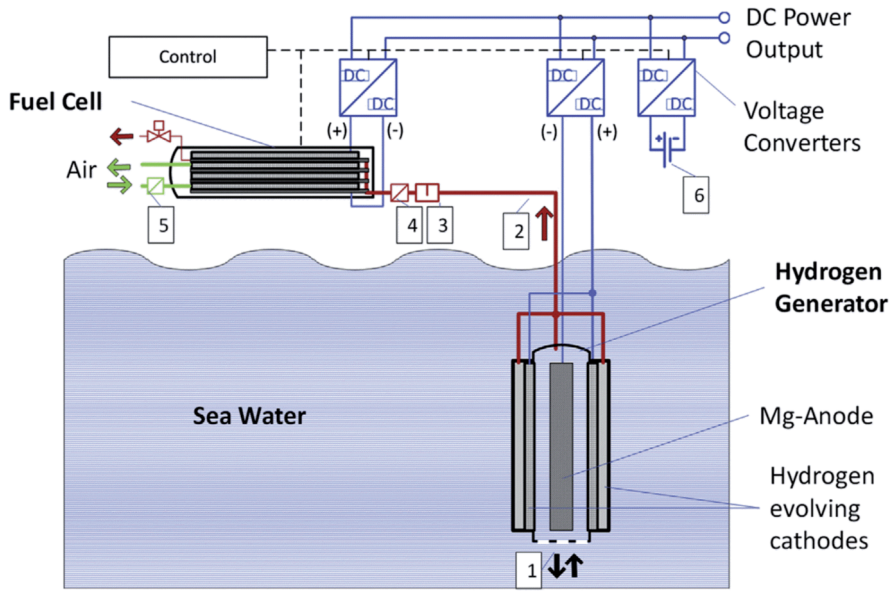

Figure 12.4 Concept of a magnesium hydrogen fuel cell power supply. (1) Bottom opening for sea water exchange and removal of reaction products, (2) hydrogen connection to fuel cell, (3) gas liquid separator, (4) hydrogen gas filter, (5) air filter, (6) secondary battery as an electrical buffer. Reproduced from R. Hahn, J. Mainert, F. Glaw and K.D. Lang, Sea water magnesium fuel cell power supply, *J. Power Sources*, **288**, 26–35., Copyright 2015, with permission from Elsevier.

the Mg anode, is collected and utilized as an anode reactant for a fuel cell above the sea level, which in parallel uses oxygen from the air as a cathode reactant. The anode and cathode reactions involved in this highly attractive fuel cell can be expressed as:

$$\text{Anode: } 2H_2 \rightarrow 4H^+ + 4e \tag{12.27}$$

$$\text{Cathode: } 2O_2 + 4H^+ + 4e \rightarrow 2H_2O \tag{12.28}$$

The overall reaction for the whole battery system can be described as:

$$2Mg + 2H_2O + O_2 \rightarrow 2Mg(OH)_2 \tag{12.29}$$

With a commercial AZ31 rolled sheet as an anode, this battery system can achieve a high energy density of more than 1200 W h kg^{-1} (again limited by the anode) when coupled with the fuel cell. Besides this, because the Mg–water system is open to the ocean, the discharge products

(magnesium hydroxide) can be continuously flushed out from the cell lowering the ohmic effects at the surface. The concentration of the electrolyte remains constant, leading to the capability of long-term stable operation of this electrochemical power system. Furthermore, Xie *et al.* reported a new battery operated by direct contact of Mg foil (anode) with foamed polyaniline (PANI, cathode).[51] No additional electrolyte is needed for this battery system. The 3D PANI cathode possesses a through-pore structure with high porosity and strong polarity, contributing to the entrapment of H_2O (humidity) from air. Thus, the involved anode and cathode reactions in this system are the oxidation of Mg and the reduction of water, separately, similar to in the Mg–water system. This proposed battery prototype could eliminate the problems caused by the electrolyte, such as self-discharge of the Mg anode, simplifying the assembling and lowering the cost.

12.3 Current Issues of Aqueous Mg Batteries

Aqueous Mg batteries have been researched and developed for a long time. They have been successfully adopted in several applications, such as the Mg–MnO_2 dry cell in military applications, the Mg–seawater system in marine devices, the Mg–H_2O_2 semi-fuel cell in UUVs and so on, as mentioned above. However, a wider commercial acceptance of the Mg-based batteries has not been realized so far owing to several disadvantages. Firstly, magnesium or magnesium alloys suffer from severe self-corrosion during discharge due to the well-known negative difference effect (NDE) that can be simply described as an increasing tendency of self-corrosion rate with enhanced polarization on Mg anodes mainly related to noble inclusions such as Fe, Cu or Ni within the anode material (typically from bad raw material quality or from inadequate anode material processing). The high self-corrosion rate decreases the utilization efficiency of Mg anodes and the specific energy of the battery system, especially at low operating current densities. Besides this, after partial discharge, the severe self-corrosion of Mg anodes also leads to a poor storage capability and, thus, reduces the service life of the entire battery system. The produced large amounts of hydrogen and the generated heat require proper battery design for gas venting and heat dissipation. Furthermore, the practical voltage is always decreased because of the large overvoltage caused either by discharge product film on the anode surface or by the sluggish kinetics of the cathodic reactions involved. The tightly adherent oxide or hydroxide film on the anode surface would also lead to voltage delay when a higher current density is required for an increasing outside electrical power consumption. Therefore, in order to promote the application of Mg-based batteries, much work has been carried out with the aim of solving these existing problems and boosting the overall performance (U–I characteristics) of aqueous Mg batteries. The main approaches and recent research progress on Mg batteries are presented in the next section.

12.4 Performance Improvement of Aqueous Mg Batteries

Some problems of Mg batteries concerning practical application can be avoided through battery design. For instance, mechanical venting of excess gas is available through a small hole in the seal washer of the Mg–MnO_2 dry cells. The storage time of most Mg-based batteries can be increased when designed as a reserve type. Anode materials can be replaced anytime and taken out of the battery system, so that battery service life can be controlled and extended. Nevertheless, in order to boost the performance of Mg-based batteries (stable U–I characteristics at high utilization efficiency), efforts are normally focused on the main components of the battery system, *i.e.* the anode, the cathode and the electrolyte. Advanced Mg anodes with more negative discharge potential (in a half-cell) and low self-corrosion rate are under development. Suitable cathode materials with catalysts are important for achieving active reaction kinetics. Besides this, battery performance can also be improved through electrolyte modification, *e.g.* the addition of proper additives, leading to electrolyte stabilization and proper electrode/electrolyte interface conditions. The main approaches and progress achieved are summarized in the following section.

12.4.1 Development of Mg Anodes

As the generator of electrons in the electrochemical power system, the Mg anode plays a key role in the battery performance. Therefore, the development of novel Mg-based anodes has attracted considerable attention. Generally, advanced Mg anodes should possess two specific properties. The first one is high utilization efficiency, which can be achieved with its low self-corrosion rate and limited "chunk effect", namely the undermining of the undissolved Mg matrix and the detachment of the secondary phases.[52–54] The second one is at a more negative discharge potential (in a half-cell measurement), which, in principle, can be obtained through negative open circuit potential and low overpotential active dissolution of Mg anodes and easier peeling or even avoidance of the discharge product film formed on the anode surface. In general, the research on Mg anodes is focused on the following three directions: improving the intrinsic properties of pure magnesium (impurity level), adding alloying elements such as Ca and adjusting the microstructure (*e.g. via* extrusion).

12.4.1.1 Improvement of Pure Magnesium

The intrinsic quality of pure Mg has a great influence on its self-corrosion and discharge properties. The corrosion rate of pure magnesium is closely linked to the content of impurities, such as Fe, Ni, Cu, *etc.*[55–58] Pure magnesium of commercial purity grade shows a high corrosion rate and low

utilization efficiency in different battery electrolytes as reported, indicating its imperfection as an anode material.[59–61] Improving the intrinsic quality of pure Mg is helpful for improving the discharge properties. High-purity Mg (99.99%) shows a better discharge voltage than some Mg alloys, *e.g.* AM50 and AZ91, as measured in a Mg–air cell under the same test conditions.[62] Besides this, instead of a conventional macroscale structure (either from cast or wrought processing), the adoption of a micro/nanoscale structure to pure Mg can also have positive effects on its discharge properties. Li *et al.* explored the discharge performance of micro/nanoscale structured Mg with various morphologies and shapes when acting as an anode material for Mg–air and Mg–MnO_2 batteries.[63,64] Mg hybrid systems consisting of micro/nano Mg spheres with different diameters can be prepared by vapor deposition processes at different temperatures (as shown in Figure 12.5). All of these prepared materials show a higher discharge voltage than commercial Mg powder when used as an anode for a Mg–MnO_2 cell due to the high electrochemical activity and reduced polarization caused by the increased surface area. Among these materials, sample C prepared at 300 °C shows the best discharge voltage (1.44 V at 25 mA g^{-1} *vs.* the 1.2 V of commercial Mg powder), which is attributed to its higher surface area caused by a mixture of micro- and nanospheres. It is worth noting that, with increasing specific surface area, the Mg anode with a micro/nanostructure unavoidably shows a fast self-corrosion rate. Therefore, a suitable electrolyte, in which the Mg anode exhibits a low self-corrosion rate, is highly desired to ensure high utilization efficiency and energy density. Another way proposed to improve the properties of Mg anode is using porous Mg thin films. Xin *et al.* prepared a series of Mg films with a thickness of 100 nm with various morphologies by magnetron sputtering at different temperatures.[65] Battery measurements indicated that a Mg–air cell with Mg films prepared at 150 °C as an anode and Pt/C as a cathode showed excellent discharge properties in 6 M KOH electrolyte, including a stable discharge voltage (0.8 to 1 V), high open circuit voltage (1.41 V) and large discharge capacity (~820 mA h g^{-1}).

12.4.1.2 Addition of Alloying Elements

Alloying is the most common method used to control the properties of Mg anodes, since numerous alloying elements can be used and they may have quite different impacts on the electrochemical properties of magnesium and the entire cell. Until now, many ternary Mg alloys have been developed as anode materials, such as Mg–Al–Zn, Mg–Al–Pb, Mg–Hg–Ga and Mg–Li–Al alloys aimed at preventing power failure by surface activation *via* the alloying element. Additionally, other alloying elements to these alloys have been explored in order to obtain a better anode performance. Figure 12.6 summarizes some commercially available and newly proposed Mg anodes from the aspects of anodic efficiency and OCP in sodium chloride solution.

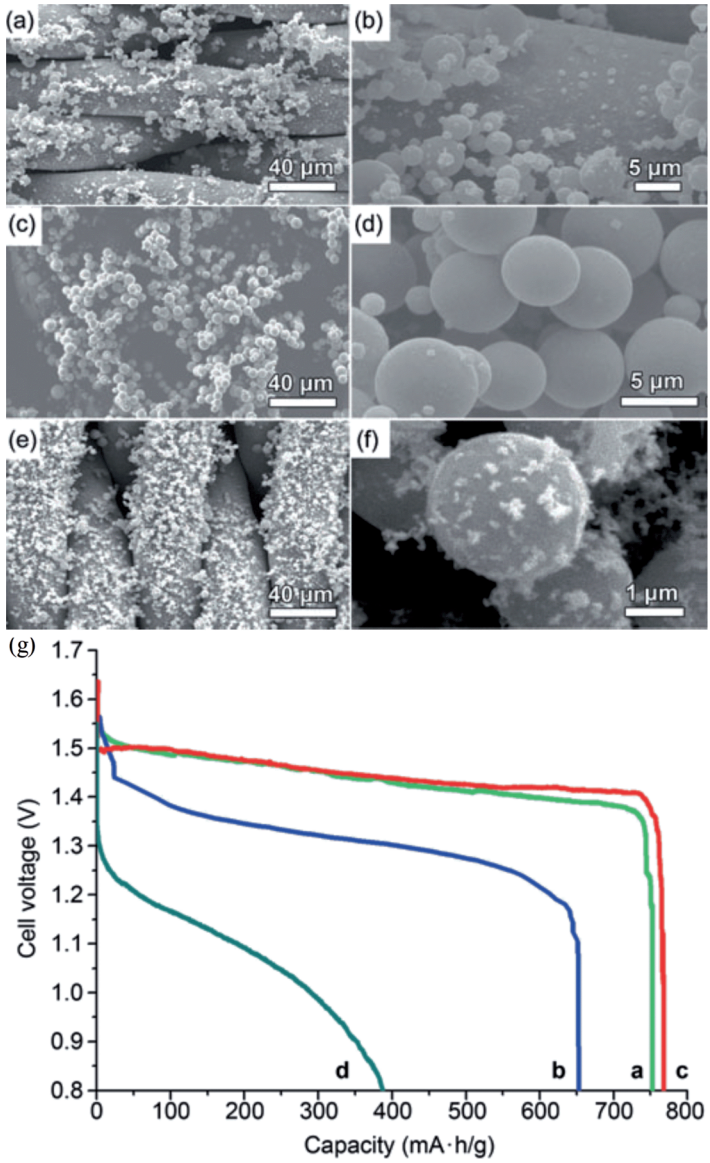

Figure 12.5 SEM images of the vapor-deposited Mg micro/nanoscale materials for different deposition temperatures: (a and b) 240 °C; (c and d) 270 °C; (e and f) 300 °C; (g) Discharge curves of different materials as anodes for a Mg–MnO_2 cell at a current density of 25 mA g^{-1} at a working temperature of 25 °C. a, b, c represents the sample vapors deposited at 240, 270 and 300 °C, respectively. Sample d is made with commercial Mg powder. The utilized electrolyte is a mixture of $Mg(NO_3)_2$ (2.6 M) and $NaNO_2$ (2.6 M). Reproduced from ref. 64 with permission from Springer Nature, Copyright 2009.

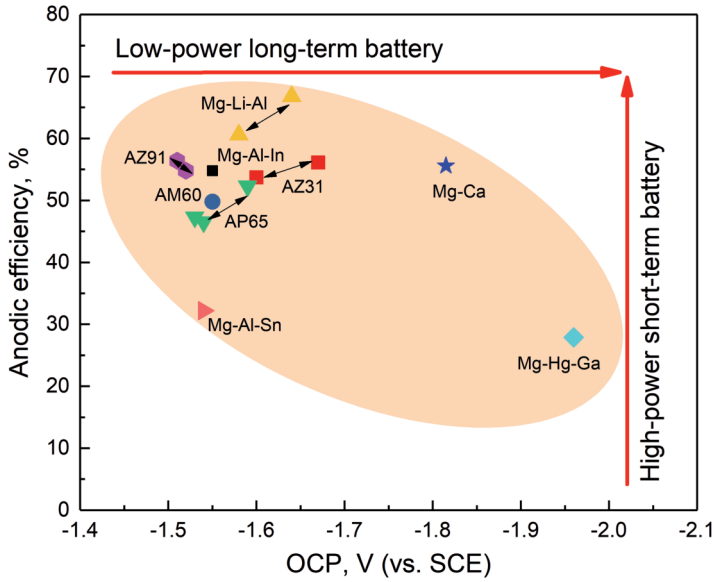

Figure 12.6 Property space for anodic efficiency *versus* the OCP of different Mg alloy anodes. All data are collected from published literatures (ref. 70–81). The anodic efficiencies of all of the anodes shown here were measured at a current density of 10 mA cm^{-2}, excluding Mg–Hg–Ga (efficiency was recorded at 20 mA cm^{-2}). All of the data were determined in 3.5 wt% NaCl solution. The OCP value is calibrated and *versus* SCE, assuming that the potential of a saturated Ag/AgCl electrode is −0.045 V *vs.* SCE electrode.

Mg–Al–Zn alloys, particularly AZ31, AZ61 and AZ91, are the most commonly used anode materials in aqueous Mg batteries, since they are commercially available and have a relatively high corrosion resistance in a Cl^- environment.[66] The good corrosion resistance is due to the reduced anodic kinetics with Al addition below solubility and suitable secondary phase morphology.[66–68] Mg–Al–Zn alloys have been used in practical Mg dry cells, Mg–air batteries, Mg–H_2O_2 semi-fuel cells and have been studied as anodes for Mg–water batteries.[4,28,49,69] They show relatively high utilization efficiency (*e.g.* 82% for AZ31 in 2 M $Mg(ClO_4)_2$ electrolyte at 40 mA cm^{-2}), excellent discharge capacity and contribute towards the high energy density of Mg-based cells.[61] However, Mg-based batteries with Mg–Al–Zn anodes normally exhibit a low cell voltage, which is due to the low open circuit voltage and more protective film caused by Al and Zn accumulation.[68] Therefore, Mg–Al–Zn alloys are mainly used in low power batteries with long service life, for example in harsh environments. Alloying with elemental indium can enhance the discharge properties of the AZ63 alloy as an anode for a Mg–CuCl battery, as reported by Li *et al.*[82] The discharge voltages of the AZ63 alloy at different current densities increase with 0.5 wt% In addition (*e.g.* from 0.45 to 0.6 V at

75 mA cm^{-2}), because the addition of In, as supposed, accelerates the dissolution of the Mg matrix (α-phase) and promotes the self-peeling of discharge products through the dissolution–reprecipitation of indium. Heat treatment was adopted to enhance the utilization efficiency and, eventually, enabled the Mg–Al–Zn–In alloy with excellent overall discharge properties.

Mg–Al–Pb alloy, especially AP65 (Mg–6%Al–5%Pb), was developed by Magnesium Elektron UK to supply a high cell voltage for high-power seawater battery applications.[5] This alloy has a more negative OCV and can supply a higher voltage than AZ alloys and pure Mg in different electrolyte solutions.[61,80,81] The high cell voltage of AP65 alloy is attributed to the promoted peeling or breakdown of discharge products caused by the synergetic effect of Al and Pb (protection and activation).[83,84] The usage of the AP65 alloy as an anode could cause severe sludge, but under some forced-flow discharge conditions the sludge problems can be controlled.[85] This alloy is used in some military applications, for example, as a power source for electric torpedoes. Except for the toxic lead, the disadvantages of Mg–Al–Pb anodes also include the high self-corrosion rate and relatively low utilization efficiency at low current densities, leading to low specific energy and shortened service life of the respective Mg-based batteries.[61,85,86] Therefore, this alloy is normally used for high-power devices with short operating time, like the mentioned electric torpedoes. Some alloying elements to the AP65 alloy, such as Zn, Mn, In, Ce/Y and La, have been studied, aimed at improving its self-corrosion and discharge properties.[80,81,87–91] The addition of 1 wt% In into the AP65 alloy can enhance its discharge potential in 3.5 wt% NaCl solution and increase its utilization efficiency at high current densities (from 82.1 to 87.7% at 180 mA cm^{-2}), but the utilization efficiency at low current density (10 mA cm^{-2}) was decreased from about 46 to 41%, due to a severe chunk effect.[80] Besides this, some work has also been carried out to optimize the composition of the Mg–Al–Pb alloy as an anode material.[83,92] Wen *et al.* suggested that, for an extruded sheet anode material, Mg-6 wt% Al-7 wt% Pb-0.5 wt% Zn alloy is the optimized composition due to its superior overall discharge properties in 3.5 wt% NaCl solution, while Wang *et al.* proposed that Mg-9 wt% Al-2.5 wt% Pb is more suitable because of the better discharge properties with low Pb content.[83,92] Recently, the AP65 alloy has been explored as an anode for Mg–air batteries. With the addition of Ce/Y alloying elements, the AP65 alloy can exhibit a higher discharge voltage and enhanced utilization efficiency than pure Mg and the AZ31 alloy, even at relatively low and moderate current densities (10 or 20 mA cm^{-2}).[81] For instance, the AP65-Ce/Y alloy shows a voltage of 1.28 V and a utilization efficiency of ~60% at 10 mA cm^{-2}, while the AZ31 alloy has a voltage of 1 V with a utilization efficiency of ~56% under the same discharge conditions.

Another Mg alloy developed for high power military applications is the Mg–Hg–Ga alloy, since it can supply a more negative discharge potential than the AP65 and AZ31 alloys.[93,94] The addition of mercury and gallium is well known to accelerate the activation of aluminum anodes.[95–97] An activation mechanism combining amalgamation, amalgam corrosion, liquid

metal embrittlement and galvanic corrosion was proposed.[96] Recently, Hg has been adopted in Mg anodes for seawater-activated batteries and a battery system with a Mg–Hg anode can supply a power density of above 150 W h kg^{-1}.[98] As reported by Feng *et al.*, a Mg-6 wt% Hg alloy exhibits extremely negative corrosion potential in 3.5 wt% NaCl solution (around −2.2 V *vs.* SCE), which, in fact, is the most negative corrosion potential reported for any Mg alloy.[66,99] While superior properties in terms of voltage and power density are achieved, Mg–Hg anodes also have drawbacks such as high self-corrosion rate, low utilization efficiency, short service life and increasing sensitivity to environmental benignity. Therefore, gallium has been used to replace mercury in Mg–Hg anodes considering the intrinsic activation effect of Ga on Al anodes. Feng *et al.* have carried out work to investigate the effect of Ga addition and content on the microstructure and respective discharge properties of Mg–Hg anodes as well as the activation mechanism.[98,99] Mg anodes could be activated by the dissolution and subsequent redeposition of Hg and Ga. Complementary, the addition of Ga accelerates the stripping of the corrosion film and the formation of Mg amalgams, which promotes the electrochemical activity. Wang *et al.* studied the effect of the Hg/Ga ratio on the phase constituents and electrochemical performance of Mg–Hg–Ga alloys, indicating that an alloy with a Hg/Ga ratio of 0.68 could be the most suitable anode material for seawater-activated batteries concerning the observed discharge properties (~1.83 V *vs.* SCE in half-cell testing) and moderate self-corrosion rate.[100]

Mg–Li alloys have also been explored as anode materials for aqueous Mg-based batteries, due to the most negative standard electrode potential of lithium (−3.05 V *vs.* SHE). However, the utilization efficiency of Mg–Li alloys as anode material is related to the Li content, since the Li has a significant effect on the self-corrosion rate of the Mg anodes. Mg–Li alloys with a relatively low Li content (<11 wt%) have a poor corrosion resistance resulting from the increased cathodic kinetics or galvanic corrosion between the α-Mg and β-Li phases when the Li content is between 5–11 wt%.[101] Despite the enhanced discharge voltage, the poor corrosion resistance of Mg–Li alloys with relatively low Li content leads to low utilization efficiency (*e.g.* ~36% for Mg-8 wt% Li-3 wt% Al-1 wt% Ce-1 wt% Y alloy at 10 mA cm^{-2}) during discharge, especially at low current densities, compared to the AZ31 alloy, as reported (~54% at 10 mA cm^{-2}).[76,102]

In contrast, with heavy Li alloying (>11 wt%) the corrosion resistance of Mg can be enhanced.[103,104] The crystal structure of the α-Mg matrix changes to bcc after Li addition of above 11 wt%, in contrast to the hcp structure of the pure primary Mg. Taking advantage of this change, the anodic dissolution kinetics of Mg are significantly restricted, which, as proposed, can be attributed to the dynamic development of a carbonate rich surface film.[103,105] As a consequence, only Mg–Li alloys with a high Li content are suitable anode materials for aqueous Mg batteries. A Mg-13 wt% Li alloy as an anode material for Mg batteries was tested by Sivashanmugam *et al.*[106] The results show that the Mg-13 wt% Li alloy has a lower self-corrosion rate than the

AZ31 alloy in various battery electrolytes, for example, 0.0059 mg cm^{-2} min^{-1} for the Mg–Li alloy *vs.* 0.1832 mg cm^{-2} min^{-1} for AZ31 in 2 M $MgCl_2$ solution. Besides this, it shows higher discharge voltages of 0.3–0.4 V at different current densities than the AZ31 alloy in a Mg/CuO full-cell setup. The alloy also possesses high anodic efficiency at relatively low current drains, for example 81% at 8.6 mA cm^{-2}. Recently, combined with other alloying elements, Mg–Li alloys with different Li content have also been proposed as anodes for either Mg–air batteries or Mg semi-full cells.[76,78,107–109] A Mg–air battery with a Mg-14 wt% Li-1 wt% Al-0.1 wt% Ce alloy as an anode shows a higher voltage at different current densities than those based on pure Mg and AZ31 alloy, *e.g.* 1.20, 1.17 and 1.13 V for Mg–Li–Al–Ce, Mg and AZ31, respectively. This alloy also exhibits enhanced anodic efficiency and discharge capacity at all of the tested current densities, supporting its possible application in Mg–air batteries. Another rare earth element, yttrium, has also been investigated as an alloying element for a Mg–Li alloy.[108] The addition of 1.2 wt% Y enhances the corrosion resistance of the Mg-8.5 wt% Li-3.2 wt% Al-1.2 wt% Ce alloy and contributes towards its boosted peak power density (from 91 to 110 mW cm^{-2}) in Mg/H_2O_2 semi-fuel cell measurements. In addition, a Mg-8 wt% Li-3 wt% Al-1 wt% Ce-1 wt% Y alloy was also evaluated as an anode material for a Mg–air battery, indicating good discharge voltage but low utilization efficiency at a relatively low current density (36% at 10 mA cm^{-2} in 3.5 wt% NaCl).[76] Nevertheless, with the addition of 1 wt% Zn, both the voltage and utilization efficiency of this alloy are enhanced, and appear to be higher than those of AZ31 and pure Mg. Zn is mainly distributed in the β-Li phase and thus weakens the galvanic corrosion between the α-Mg and β-Li phases, leading to a relative uniform dissolution of this alloy and a reduced self-corrosion rate.

Indeed, the aforementioned Mg alloys possess some attractive advantages as anode materials. However, they are all associated with specific issues, raising the need for better Mg anode materials in general. Firstly, due to the increasing social attention on environmental issues, new anode materials are needed to replace the widely used toxic Mg–Al–Pb or Mg–Hg–Ga alloys in seawater batteries. Secondly, in terms of a Mg–Li anode, the heavy Li load and need for a fourth or even fifth alloying element strongly reduces the technological tolerances leading to a significant increase in associated costs. In this case, some other low melting point elements (LMPEs), such as Ga, In and Sn, are being considered. Work has been done to explore the possibility of replacing Pb with these LMPEs in Mg–Al anodes. Mg–Al–Sn, Mg–Al–Ga and Mg–Al–In alloys have been tested either in Mg–air batteries or Mg–seawater batteries and compared with Mg–Al–Zn anodes.[71,74,82,110,111] As reported, all of these alloys show a better discharge voltage than Mg–Al–Zn anodes, attributed to the less protective oxide film on the anode surface resulting from these LMPEs. For example, the voltages of Mg-3 wt% Al-1 wt% Ga, Mg-3 wt.%Al-1 wt% Sn and Mg-3 wt.%Al-1 wt% In at 5 mA cm^{-2} are 1.18, 1.21 and 1.31 V respectively, higher than that of the Mg-3 wt.%Al-1 wt% Zn alloy (1.17 V). A dissolution–reprecipitation mechanism was proposed

to explain the activation effect of In addition on a Mg anode with the assistance of X-ray diffraction (XRD), X-ray photoelectron spectroscopy (XPS) and energy-dispersive X-ray spectroscopy (EDS). However, these alloys normally have a higher self-corrosion rate than Mg–Al–Zn alloys evaluated either by polarization curves, EIS measurements or by immersion tests. Therefore, the service life of Mg batteries is definitely shortened by adopting these Mg–Al systems alloyed with LMPEs as an anode. Recently, a novel Mg–Ca anode material with both good voltage and low self-corrosion rate was presented.[72] The consideration of Ca addition was based on its more negative electrode potential (−2.87 V *vs.* SHE) than that of magnesium and the grain refinement effect of Ca on Mg metal. The content of Ca was recommended to be lower than 0.5 wt% since the increasing Mg_2Ca secondary phases, accompanied by high Ca content, severely accelerate the self-corrosion rate of Mg–Ca alloys. As presented in Figure 12.7, a Mg–air battery with a Mg-0.1 wt% Ca as an anode has a more stable and higher discharge voltage compared to anodes

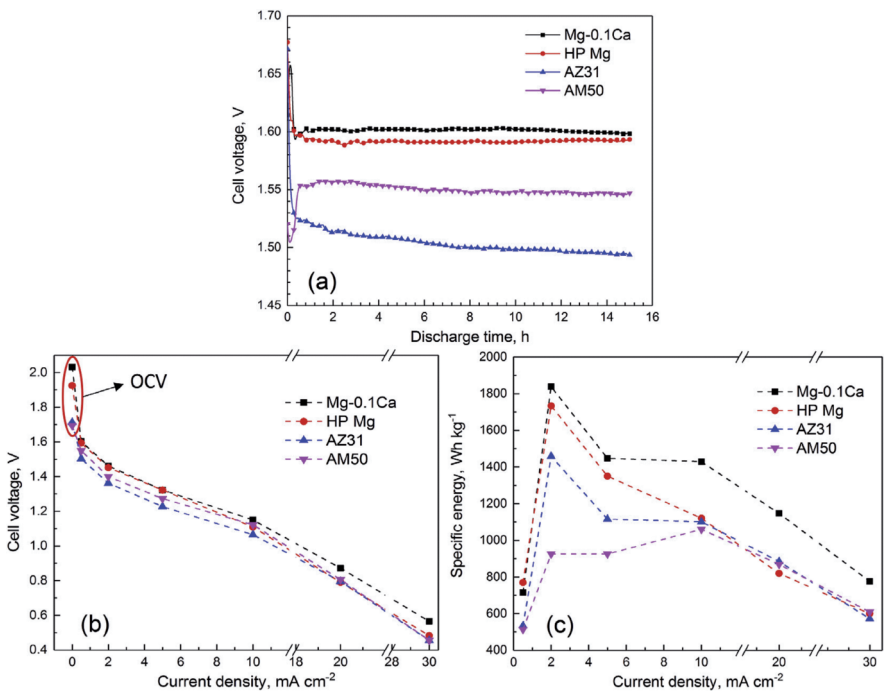

Figure 12.7 Discharge properties of Mg–air batteries with different anodes: (a) discharge curves at a current density of 0.5 mA cm^{-2}; (b) cell voltage at different current densities; (c) specific energy at different current densities. Electrolyte is 3.5 wt% NaCl solution; Cathode is a commercial air cathode with C/MnO_2 catalyst. Reproduced from M. Deng, D. Höche, S.V. Lamaka, D. Snihirova and M.L. Zheludkevich, Mg–Ca binary alloys as anodes for primary Mg–air batteries, *J. Power Sources*, **396**, 109–118., Copyright 2018, with permission from Elsevier.

based on high purity Mg, AZ31 and AM50 alloys. Besides this, a Mg-0.1 wt% Ca anode can also offer enhanced energy density, even higher than that of high purity Mg, which generally has a lower corrosion rate in a technically relevant testing solution such as 3 wt% NaCl than most Mg alloys, as already summarized in some literature reviews.[66,112]

12.4.1.3 Microstructure Tuning

Microstructure, which includes grain size, secondary phase constituent, secondary phase morphology, density of various defects and impurities, *etc.*, also has a significant effect on the self-corrosion and discharge properties of Mg anodes. Therefore, technical processing, such as deformation and subsequent heat treatment, are adopted to adjust the microstructure of Mg anodes and to obtain good overall properties. Note that sheet or rod materials of Mg anodes, which can be obtained through deformation processes, such as rolling or extrusion, are normally required in practical applications due to cell design constraints. Thus, studies concerning the effect of these processes on properties of Mg anodes are quite important as well as iterative processes for optimization. Until now, a number of studies have been carried out to reveal the influence of different processes on the microstructure, self-corrosion and discharge properties of numerous Mg anodes.[60,70,74,79,82,90,91,93,94,113–116]

Heat treatment, which can be applied to both as-cast materials and wrought materials, has a significant impact on the microstructure of Mg anodes, especially the size, quantity and distribution of the secondary phases. Consequently, the OCP of Mg anodes and the reaction kinetics of anode dissolution are affected. As demonstrated by Yan *et al.*, homogenization and aging treatment have a great effect on the self-corrosion and discharge potential of a Mg-4.8 wt% Hg-8wt% Ga alloy anode, resulting from the changing precipitation behavior of the $Mg_{21}Ga_5Hg_3$ and Mg_5Ga_2 secondary phases.[113] The self-corrosion resistance and discharge potential are improved after aging at 473 K for 96 h. This also indicates that anode pretreatment *via* heat aging under some conditions has a negative effect on the overall performance of this Mg–Hg–Ga anode. Therefore, suitable treatment parameters, including temperature and treatment duration, are urgently required. The effect of heat treatment on the discharge properties of Mg–Al–Zn anode with In addition has also been studied by Li *et al.*[82] After microstructural homogenization at 385 °C for 24 h followed by water quenching, the utilization efficiency of an AZ63-0.5 wt% In anode was enhanced (from 67 to 71% at 10 mA cm^{-2}) due to the reduced self-corrosion rate attributed to the dissolution of the secondary phases into the Mg matrix. Besides this, the discharge voltage of a Mg–CuCl seawater-activated battery was increased with this treated alloy as an anode, because of more In dissolved in the α-Mg solid solution after heat treatment, which also promotes the indium-induced dissolution–reprecipitation process.

Deformation processes such as extrusion are normally used to refine materials and to obtain a more uniform microstructure. The induced dislocations, twins, crystallographic textures, various grain orientations, incomplete recrystallization structures and subsequently, the occurrence of high surface energy could also have a remarkable influence on the discharge properties of Mg anodes. Wang *et al.* investigated the effect of hot rolling and subsequent annealing on the discharge properties of a Mg–Al–Pb anode.[114] The results show that hot rolling improves the discharge potential of the AP65 anode, attributed to the induced dislocations and twins, which accelerate the dissolution of the anode. Besides this, the utilization efficiency increased from 78.8% for the as-cast AP65 alloy to 81.5% for the as-rolled one at 180 mA cm^{-2}, because the grains are refined and the strongly cathodic Al–Mn particles are fractured by hot rolling. Subsequent annealing at 150°C for 4 h further improved the overall properties of the hot-rolled AP65 anode material. The more negative discharge potential is due to the accelerated self-peeling of the discharge products, while the increased utilization efficiency can be attributed to the decreased density of dislocations and twins (might be related to a lowered chunk effect). Generally, appropriate heat treatment processes following deformation processes are quite necessary to obtain the desired microstructure. Additionally, the different grain orientations induced by rolling could also have an effect on both the corrosion and discharge performance of Mg anodes, as indicated in the recent publication by Wang *et al.*[117] Extrusion is another widely used process to obtain a specific anode shape and uniform microstructure. In the recent research of Xiong *et al.*, a Mg-6 wt% Al-1 wt% Sn alloy anode for Mg–air batteries was extruded to achieve superior discharge properties.[74] Similarly, both discharge voltage and utilization efficiency are enhanced due to accelerated discharge activity and more uniform anode dissolution. At a discharge current density of 10 mA cm^{-2}, the utilization efficiency increases from 32.2 to 45.2% after extrusion, while the discharge potential in half-cell tests becomes more negative, from −1.605 to −1.670 V (*vs.* SCE).

12.4.2 Electrolyte Modification

The electrolyte is another determining factor for the performance of aqueous Mg-based electrochemical power sources. Firstly, the utilization efficiency of anode materials is closely related to the adopted electrolytes, since the different self-corrosion rates of Mg anodes can be detected in various solutions.[56,61] Secondly, the formation of discharge product films on the anode surface, which has a great influence on the discharge potential of Mg anodes as mentioned, is related to the electrolyte solution. Meanwhile, solution conductivity also varies with different electrolytes. High solution conductivity, which means low solution resistance, is needed to decrease the voltage loss caused by ohmic drop (IR-drop). Therefore, electrolyte modification, even in a water environment, is quite

important to gain superior battery performance. Most research concerning electrolytes for Mg-based batteries follows two directions, namely the modification of background electrolytes and the utilization of additives. Note that electrolyte modification may not be feasible for Mg–seawater batteries since the battery system is open and the electrolyte is natural seawater from the ocean.

The induced changes on Mg battery performance by the adjusted characteristics of the background electrolytes, including the soluble salt type, species concentrations, pH, *etc.*, have been deeply investigated over the last few decades.[61,63,86,118–121] Zhao *et al.* tested Mg battery performance in NaCl solutions with different concentrations.[121] Upon increasing the NaCl concentration from 3.5 to 6.5 wt%, the discharge current at a specific voltage increases while the battery life time decreases. This could be attributed to the decreased overpotential resulting from increased solution conductivity and facilitated Mg anode dissolution. Instead of an aggressive NaCl solution, other less-aggressive solutions without Cl^- have been proposed as electrolytes for Mg-based batteries, such as $Mg(ClO)_4$, $MgBr_2$, $Mg(NO_3)_2$, *etc.* The utilization efficiencies of various Mg anodes at different current densities have been demonstrated to be higher in $Mg(ClO_4)_2$ and $MgBr_2$ solutions than in $MgCl_2$ solution, owning to the reduced self-corrosion rate.[61] Besides this, Winther-Jensen *et al.* studied several chloride salts, *i.e.* $MgCl_2$, LiCl, $CaCl_2$ and NaCl, as electrolytes and anode/electrolyte interface modulators for Mg batteries under saturated conditions at pH 11.[118] The results show that, in $MgCl_2$ and LiCl saturated solutions, Mg batteries maintain a cell voltage of above 1.4 V for more than 150 h at 20 μA cm^{-2}, which cannot be achieved in saturated $CaCl_2$ and NaCl solutions. Moreover, a mixture of $MgCl_2$ and LiCl saturated solutions can further enhance the cell voltage and stability. This phenomenon is important for enhancing Mg battery performance, even if the reasons are not yet well explained.

In addition to the modification of the background solution, utilization of electrolyte additives is also an important approach for the previously introduced boosting of Mg battery performance and has already drawn much attention. Most of the prior research on electrolyte additives was focused on corrosion inhibitors. The aim was to improve the anode utilization efficiency through inhibiting the self-corrosion of Mg anodes. Meanwhile, the discharge potential of Mg anodes is also affected as a result of the varied kinetics of anode dissolution. Commonly used inhibitors for aqueous Mg-based batteries include nitrites and chromate compounds.[4,63,64,119,122] However, they are not environmentally friendly. Therefore, more effective and environmentally benign inhibitors for Mg batteries are required. Several new additives for aqueous Mg-based batteries have been evaluated, such as gallium oxide, decyl glucoside, water soluble graphene, sodium phosphate and sodium dodecyl benzenesulfonate.[102,123–125] As reported, decyl glucoside as the electrolyte additive

can improve both the cell voltage and the utilization efficiency of Mg–air battery systems.[123] The utilization efficiency of a pure Mg anode at 5 mA cm^{-2} increases from to 86.2% after the addition of 2.5 mM decyl glucoside into the electrolyte, while the voltage increases to 1.36 from 1.15 V in bare electrolyte. The significantly enhanced utilization efficiency can be attributed to the reduced self-corrosion rate resulting from the adsorption of decyl glucoside on the anode surface. The increased cell voltage is due to the enhanced open circuit voltage, which indicates the cathodic inhibition effect of decyl glucoside on local acting cathodes within the anode material. Recently, Lamaka *et al.* reported work representing results of the systematic screening of magnesium corrosion inhibitors.[126] In this work, the inhibition effect of 151 individual compounds on various Mg alloys and three grades of pure Mg was evaluated through hydrogen evolution tests in 0.5 wt% NaCl solution. The results indicate a number of new inhibitors that show higher inhibition efficiency on Mg corrosion than chromate. This work shines some light on the selection of effective electrolyte additives for aqueous Mg-based batteries. Nevertheless, more work is still needed to find suitable additives for fully assembled Mg-based batteries taking into consideration both utilization efficiency and cell voltage.

Recently, Höche *et al.* proposed a new concept to simultaneously improve the anode efficiency and discharge voltage *via* the addition of Mg^{2+} and Fe^{3+} complexing agents.[59] This idea was based on their prior research on iron complexing agents as effective corrosion inhibitors for magnesium.[55,126,127] As proposed, iron re-deposition on Mg surface accelerates the self-corrosion of impurities containing Mg.[55] Therefore, as illustrated in Figure 12.8a, preventing the re-plating of iron with strong iron complexing agents becomes a feasible method by which to suppress the self-corrosion of magnesium.[126,127] The principle for battery performance boosting based on this mechanism is presented in Figure 12.8b. Electrolyte additives as strong Fe^{3+} and moderate Mg^{2+} complexing agents were added into the battery system. The self-corrosion of Mg anodes is expected to be suppressed by preventing Fe-re-deposition and impurity activation, while the cell voltage is supposed to be enhanced through inhibiting the formation of a $Mg(OH)_2$ film and activation of the surface *via* Mg complexing. An excellent organic additive, namely salicylate, was found in this work. With the addition of 0.05 M salicylate, the utilization efficiency of a cp-Mg (220 ppm Fe) in 0.5 wt% NaCl solution was enhanced from 13.5 to 27.2%, while the discharge potential became more negative, from −1.47 V (*vs.* Ag/AgCl) to −1.61 V (*vs.* Ag/AgCl). Note that the anode material used in this work was cp-Mg that shows a high self-corrosion rate and inferior discharge performance in electrolyte solutions. Nevertheless, it indicates a new direction for choosing novel electrolyte additives for aqueous Mg-based batteries. Thus, research on complexing agents as electrolyte additives for superior Mg alloy anodes deserves more attention.

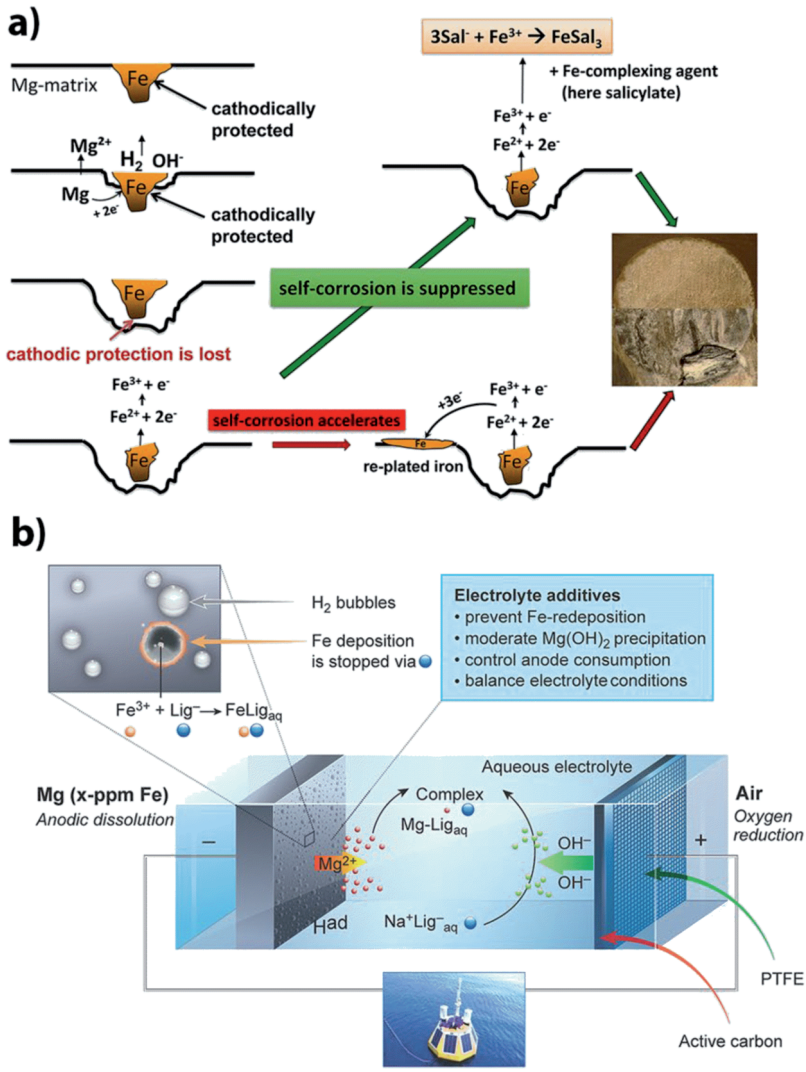

Figure 12.8 (a) Iron re-deposition mechanism on Mg corrosion and the working principles of additives (here salicylate, Sal) as a corrosion inhibitor *via* preventing Fe-re-plating. (b) Working principles of complexing agents as additives for the performance boosting of Mg-based batteries. Main aspects of the additive effect are indicated and emphasize the scope of the discovery. Reproduced from ref. 59, https://doi.org/10.1038/s41598-018-25789-8, under the terms of the CC BY 4.0 licence, http://creativecommons.org/licenses/by/4.0/.

12.5 Outlook

In this chapter aqueous Mg-based batteries were introduced with respect to battery types, involved reactions, hindrances to practical applications and also research progress. For sure, Mg-based batteries with superior theoretical battery

performance are promising future power sources, which fulfill the social requirements in terms of economic feasibility and clean energy. The various battery types supported by different cathode reactants enable Mg-based electrochemical systems to be used for applications in different fields, such as marine devices, military equipment, backup power, *etc.* Nevertheless, the practical applications and commercialization are still hindered because of the imperfect battery performance, such as low/unstable cell voltage and insufficient specific energy density. Therefore, in order to widen the application of aqueous Mg-based batteries, more work should be done on improving all of the different components of the battery system, *i.e.* the anode, cathode, electrolyte and the cell design itself.

Novel Mg anodes with a low self-corrosion rate and more negative discharge potential are required. Mg alloys with non-toxic alloying elements should be developed to replace the usage of high-quality but environmentally harmful alloys, such as Mg–Hg–Ga and Mg–Al–Pb. Meanwhile, except for good electrochemical performance, Mg anodes with simplified composition, such as binary or at most ternary alloys, are needed to reduce the cost associated with the anode preparation. The focus needs to be shifted from Mg–Al- and Mg–Li-based alloys to other novel Mg alloys, such as the Mg–Ca system.

The cathode, including the cathode structure, cathode reactants and catalysts, also plays a key role in the performance of aqueous Mg-based systems. Firstly, the cathode structure needs to be optimized, supporting enough mechanical strength and reducing battery inner resistance. Secondly, effective and low-cost cathode reactants are important, especially for Mg–seawater systems. Non-silver alternatives with a discharge performance close to that of AgCl are still required. Besides this, concerning cathodes for Mg–air and Mg–H_2O_2 systems, highly effective catalysts need to be discovered, considering not only high catalytic activity but also low cost. Modified MnO_2 and perovskite-based oxides deserve more attention as catalysts for Mg–air systems. In addition, the importance of substrate materials for cathode catalysts should also be noted. Adoption of a porous nanostructure is a feasible approach, since the significantly increased surface area can reduce polarization induced by mass transfer and gas diffusion processes.

Electrolyte modification, especially if they are water based, as an effective way of boosting battery performance, draws increasing attention nowadays. Non-aggressive solutions can be used as electrolytes to ensure relatively high anode efficiency, but the effect of these solutions on cell voltage and power density should be considered thoroughly. Electrolyte additives provide another possible and very easy to handle alternative. Except for corrosion inhibitors, other new additives that can simultaneously enhance the anode efficiency and cell voltage need to be developed, such as the newly proposed dual acting complexing agents.

Acknowledgement

Min Deng and Linqian Wang are grateful for the award of fellowships and funding from the China Scholarship Council No. 201606370031 and No. 201706370183.

References

1. F. Cheng and J. Chen, *Chem. Soc. Rev.*, 2012, **41**, 2172.
2. T. Zhang, Z. Tao and J. Chen, *Mater. Horiz.*, 2014, **1**, 196.
3. M. A. Rahman, X. Wang and C. Wen, *J. Electrochem. Soc.*, 2013, **160**, A1759.
4. R. C. Kirk and A. B. Fry, *J. Electrochem. Soc.*, 1948, **94**, 277.
5. D. Linden and T. B. Reddy, *Handbook of Batteries*, McGraw-Hill, New York, 2002.
6. S. R. Srither, M. Selvam, S. Arunmetha, R. Yuvakkumar, K. Saminathan and V. Rajendran, *Sci. Adv. Mater.*, 2013, **5**, 1372.
7. K. Narthana, R. Naveen, K. Saminathan, P. Siva, M. Selvam and P. Saha, *Int. J. Res. Adv. Eng.*, 2016, **2**, 1.
8. R. Renuka, *J. Power Sources*, 2000, **87**, 4.
9. N. G. Wang, R. C. Wang, C. Q. Peng, C. W. Hu, Y. Feng and B. Peng, *Trans. Nonferrous Met. Soc. China*, 2014, **24**, 2427.
10. J. B. Mullen and P. L. Howard, *Trans. Electrochem. Soc.*, 1946, **90**, 529.
11. R. Balasubramanian, A. Veluchamy, N. Venkatakrishnan and R. Gangadharan, *J. Power Sources*, 1995, **56**, 197.
12. J. B. Mullen and P. L. Howard, *J. Electrochem. Soc.*, 1946, **90**, 529.
13. R. Renuka, *J. Appl. Electrochem.*, 1997, **27**, 1394.
14. F. Sammoura, K. B. Lee and L. Lin, *Sens. Actuators, A*, 2004, **111**, 79.
15. K. V. Rao, *Def. Sci. J.*, 2001, **51**, 161.
16. J. R. Coleman, *J. Appl. Electrochem.*, 1971, **1**, 65.
17. L. J. Burant, *US Pat.*, 4,021,597, 1977.
18. I. C. Blake, *US Pat.*, 2,491,640, 1949.
19. J. B. Ockerman, *US Pat.*, 3,433,678, 1967.
20. L. E. Pucher, *J. Electrochem. Soc.*, 1952, **99**, 203C.
21. J. M. Dines, *US Pat.*, 2,716,671, 1955.
22. W. K. McCarter, J. F. Flood and J. T. Fischer, *US Pat.*, 5,395,707, 1995.
23. M. Hiroi, *J. Appl. Electrochem.*, 1985, **15**, 201.
24. R. F. Amlie, H. N. Honer and P. Ruetschi, *J. Electrochem. Soc.*, 1965, **112**, 1073.
25. M. Hiroi, *J. Appl. Electrochem.*, 1985, **16**, 431.
26. R. Renuka, *Mater. Chem. Phys.*, 1999, **59**, 42.
27. R. Renuka, *J. Appl. Electrochem.*, 1999, **29**, 271.
28. M. G. Medeiros, R. R. Bessette, C. M. Deschenes, C. J. Patrissi, L. G. Carreiro, S. P. Tucker and D. W. Atwater, *J. Power Sources*, 2004, **136**, 226.
29. M. G. Medeiros and E. G. Dow, *J. Power Sources*, 1999, **80**, 78.
30. M. G. Medeiros, R. R. Bessette, C. M. Deschenes and D. W. Atwater, *J. Power Sources*, 2001, **96**, 236.
31. M. G. Medeiros, E. G. Dow and R. R. bessette, *US Pat.*, 6,465,124B1, 2002.
32. M. G. Medeiros, E. G. Dow, R. R. Bessette and J. M. Cichon, *US Pat.*, 6,740,220 B1, 2004.
33. W. Yang, S. Yang, W. Sun, G. Sun and Q. Xin, *Electrochim. Acta*, 2006, **52**, 9.

34. C. J. Patrissi, R. R. Bessette, Y. K. Kin and C. R. Schumacher, *J. Electrochem. Soc.*, 2008, **155**, B558.
35. C. Shu, E. Wang, L. Jiang, Q. Tang and G. Sun, *J. Power Sources*, 2012, **208**, 159.
36. R. R. Bessette, M. G. Medeiros, C. J. Patrissi, C. M. Deschenes and C. N. LaFratta, *J. Power Sources*, 2001, **96**, 240.
37. Ø. Hasvold and N. Størkersen, *J. Power Sources*, 2001, **96**, 252.
38. W. S. D. Wilcock and P. C. Kauffman, *J. Power Sources*, 1997, **66**, 71.
39. Ø. Hasvold, T. Lian, E. Haakaas, N. Størkersen, O. Perelman and S. Cordier, *J. Power Sources*, 2004, **136**, 232.
40. M. Shinohara, E. Araki, M. Mochizuki, T. Kanazawa and K. Suyehiro, *J. Power Sources*, 2009, **187**, 253.
41. P. Yue, Z. Li, S. Wang and Y. Wang, *Int. J. Hydrogen Energy*, 2015, **40**, 6809.
42. Y. Xue, H. Miao, S. Sun, Q. Wang, S. Li and Z. Liu, *J. Power Sources*, 2015, **297**, 202.
43. C. Shu, E. Wang, L. Jiang and G. Sun, *Int. J. Hydrogen Energy*, 2013, **38**, 5885.
44. M. Jiang, H. He, C. Huang, B. Liu, W.-J. Yi and Z.-S. Chao, *Electrochim. Acta*, 2016, **219**, 492.
45. Z. Li, J. Yang, G. Xu and S. Wang, *J. Power Sources*, 2013, **242**, 157.
46. C. Zhao, Y. Jin, W. Du, C. Ji and X. Du, *J. Electroanal. Chem.*, 2018, **826**, 217.
47. Y. Li, X. Zhang, H.-B. Li, H. D. Yoo, X. Chi, Q. An, J. Liu, M. Yu, W. Wang and Y. Yao, *Nano Energy*, 2016, **27**, 8.
48. W. Yang, S. Yang, J. Guo, G. Sun and Q. Xin, *Carbon*, 2007, **45**, 397.
49. Q. Liu, Z. Yan, E. Wang, S. Wang and G. Sun, *Int. J. Hydrogen Energy*, 2017, **42**, 23045.
50. R. Hahn, J. Mainert, F. Glaw and K. D. Lang, *J. Power Sources*, 2015, **288**, 26.
51. P. Xie, M. Z. Rong and M. Q. Zhang, *Angew. Chem., Int. Ed.*, 2016, **55**, 1805.
52. G. A. Marsh and E. Schaschl, *J. Electrochem. Soc.*, 1960, **107**, 960.
53. M. Andrei, F. d. Gabriele, P. L. Bonora and D. Scantlebury, *Mater. Corros.*, 2003, **54**, 5.
54. M. E. Straumanis and B. K. Bhatia, *J. Electrochem. Soc.*, 1963, **110**, 357.
55. D. Hoche, C. Blawert, S. V. Lamaka, N. Scharnagl, C. Mendis and M. L. Zheludkevich, *Phys. Chem. Chem. Phys.*, 2016, **18**, 1279.
56. G. L. Song and A. Atrens, *Adv. Eng. Mater.*, 1999, **1**, 11.
57. J. D. Hanawalt, C. E. Nelson and J. A. Peloubet, *Trans. AIME*, 1942, **147**, 273.
58. R. E. Mcnulty and J. D. Hanawalt, *J. Electrochem. Soc.*, 1942, **81**, 423.
59. D. Höche, S. V. Lamaka, B. Vaghefinazari, T. Braun, R. P. Petrauskas, M. Fichtner and M. L. Zheludkevich, *Sci. Rep.*, 2018, **8**, 7578.
60. B. Campillo, C. Rodriguez, J. Genesca, J. Juarez-Islas, O. Flores and L. Martinez, *J. Mater. Eng. Perform.*, 1997, **6**, 449.

61. R. Udhayan, N. Muniyandi and P. B. Mathur, *Br. Corros. J.*, 1992, **27**, 68.
62. Y. D. Milusheva, R. I. Boukoureshtlieva, S. M. Hristov and A. R. Kaisheva, *Bulg. Chem. Commun.*, 2011, **43**, 42.
63. W. Li, C. Li, C. Zhou, H. Ma and J. Chen, *Angew. Chem.*, 2006, **118**, 6155.
64. C. Li, F. Cheng, W. Ji, Z. Tao and J. Chen, *Nano Res.*, 2009, **2**, 713.
65. G. Xin, X. Wang, C. Wang, J. Zheng and X. Li, *Dalton Trans.*, 2013, **42**, 16693.
66. K. Gusieva, C. H. J. Davies, J. R. Scully and N. Birbilis, *Int. Mater. Rev.*, 2014, **60**, 169.
67. M.-C. Zhao, M. Liu, G. Song and A. Atrens, *Corros. Sci.*, 2008, **50**, 1939.
68. A. Pardo, M. C. Merino, A. E. Coy, F. Viejo, R. Arrabal and S. Feliú, *Electrochim. Acta*, 2008, **53**, 7890.
69. R. P. Hamlen, E. C. Jerabek, J. C. Ruzzo and E. G. Siwek, *J. Electrochem. Soc.*, 1969, **116**, 1588.
70. M. Yuasa, X. Huang, K. Suzuki, M. Mabuchi and Y. Chino, *Mater. Trans.*, 2014, **55**, 1202.
71. X. Li, H. Lu, S. Yuan, J. Bai, J. Wang, Y. Cao and Q. Hong, *J. Electrochem. Soc.*, 2017, **164**, A3131.
72. M. Deng, D. Höche, S. V. Lamaka, D. Snihirova and M. L. Zheludkevich, *J. Power Sources*, 2018, **396**, 109.
73. M. Yuasa, X. Huang, K. Suzuki, M. Mabuchi and Y. Chino, *J. Power Sources*, 2015, **297**, 449.
74. H. Xiong, K. Yu, X. Yin, Y. Dai, Y. Yan and H. Zhu, *J. Alloys Compd.*, 2017, **708**, 652.
75. J. L. Wu, R. C. Wang, Y. Feng and C. Q. Peng, *J. Alloys Compd.*, 2018, **765**, 736.
76. N. Wang, R. Wang, Y. Feng, W. Xiong, J. Zhang and M. Deng, *Corros. Sci.*, 2016, **112**, 13.
77. X. Liu, S. Liu and J. Xue, *J. Power Sources*, 2018, **396**, 667.
78. Y. Ma, N. Li, D. Li, M. Zhang and X. Huang, *J. Power Sources*, 2011, **196**, 2346.
79. N. Wang, R. Wang, C. Peng and Y. Feng, *Corros. Sci.*, 2014, **81**, 85.
80. N. Wang, R. Wang, C. Peng, B. Peng, Y. Feng and C. Hu, *Electrochim. Acta*, 2014, **149**, 193.
81. Y. Feng, W. Xiong, J. Zhang, R. Wang and N. Wang, *J. Mater. Chem. A*, 2016, **4**, 8658.
82. J. Li, B. Zhang, Q. Wei, N. Wang and B. Hou, *Electrochim. Acta*, 2017, **238**, 156.
83. L. Q. Wang, R. C. Wang, Y. Feng, M. Deng and N. G. Wang, *J. Electrochem. Soc.*, 2017, **164**, A438.
84. N.-g. Wang, R.-c. Wang, C.-q. Peng, Y. Feng and X.-y. Zhang, *Trans. Nonferrous Met. Soc. China*, 2010, **20**, 1403.
85. J. F. King and S. L. Bradshaw, *US Pat.*, 4,332,864, 1982.
86. R. Udhayan and D. P. Bahtt, *J. Power Sources*, 1996, **63**, 103.
87. N.-g. Wang, R.-c. Wang, C.-q. Peng, Y. Feng and X.-y. Zhang, *Trans. Nonferrous Met. Soc. China*, 2010, **20**, 1936.

88. B. Chen, R.-c. Wang, C.-q. Peng, Y. Feng and N.-g. Wang, *Trans. Nonferrous Met. Soc. China*, 2014, **24**, 423.
89. H.-x. Jin, R.-c. Wang, C.-q. Peng, K. Shi and Y. Feng, *J. Cent. South Univ.*, 2012, **19**, 2086.
90. Y. Shi, C. Peng, Y. Feng, R. Wang and N. Wang, *Mater. Des.*, 2017, **124**, 24.
91. Y. Shi, C. Peng, Y. Feng, R. Wang and N. Wang, *J. Alloys Compd.*, 2017, **721**, 392.
92. L. Wen, K. Yu, H. Xiong, Y. Dai, S. Yang, X. Qiao, F. Teng and S. Fan, *Electrochim. Acta*, 2016, **194**, 40.
93. K. Yu, X. Tan, Y. Hu, F. Chen and S. Li, *Corros. Sci.*, 2011, **53**, 2035.
94. J. Zhao, K. Yu, Y. Hu, S. Li, X. Tan, F. Chen and Z. Yu, *Electrochim. Acta*, 2011, **56**, 8224.
95. A. H. Al-Saffar, V. Ashworth, W. A. Grant and R. P. Procter, *Corros. Sci.*, 1978, **18**, 687.
96. J. B. Bessone, *Corros. Sci.*, 2006, **48**, 4243.
97. D. O. Flamini, S. B. Saidman and J. B. Bessone, *Corros. Sci.*, 2006, **48**, 1413.
98. Y. Feng, R. Wang, K. Yu, C. Peng, J. Zhang and C. Zhang, *J. Alloys Compd.*, 2009, **473**, 215.
99. Y. Feng, R.-c. Wang, K. Yu, C.-Q. Peng and W.-x. Li, *Trans. Nonferrous Met. Soc. China*, 2007, **17**, 1363.
100. L. Wang, P. Li and L. He, *IOP Conf. Ser.: Mater. Sci. Eng.*, 2017, **229**, 012008.
101. Y. Song, D. Shan, R. Chen and E.-H. Han, *Corros. Sci.*, 2009, **51**, 1087.
102. D. Cao, L. Wu, Y. Sun, G. Wang and Y. Lv, *J. Power Sources*, 2008, **177**, 624.
103. W. Xu, N. Birbilis, G. Sha, Y. Wang, J. E. Daniels, Y. Xiao and M. Ferry, *Nat. Mater.*, 2015, **14**, 1229.
104. M. Sahoo, *J. Mater. Sci.*, 1982, **17**, 3564.
105. L. Hou, M. Raveggi, X. B. Chen, W. Xu, K. J. Laws, Y. Wei, M. Ferry and N. Birbilis, *J. Electrochem. Soc.*, 2016, **163**, C324.
106. A. Sivashanmugam, T. P. Kumar, N. G. Renganathan and S. Gopukumar, *J. Appl. Electrochem.*, 2004, **34**, 1135.
107. Y.-Z. Lv, Y.-Z. Jin, Z.-B. Wang, M. Liu, Y.-F. Li, L. Wang and D.-X. Cao, *Ionics*, 2014, **21**, 429.
108. Y. Lv, Y. Xu and D. Cao, *J. Power Sources*, 2011, **196**, 8809.
109. D. Cao, L. Wu, G. Wang and Y. Lv, *J. Power Sources*, 2008, **183**, 799.
110. S. Yuan, H. Lu, Z. Sun, L. Fan, X. Zhu and W. Zhang, *J. Electrochem. Soc.*, 2016, **163**, A1181.
111. T. Zheng, Y. Hu, Y. Zhang, S. Yang and F. Pan, *Mater. Des.*, 2018, **137**, 245.
112. F. Cao, Z. Shi, G.-L. Song, M. Liu and A. Atrens, *Corros. Sci.*, 2013, **76**, 60.
113. F. Yan, W. Ri-chu, P. Chao-qun, Q. Ke, W. Nai-guang, Z. Chun and Z. Jia-pei, *Corros. Sci.*, 2010, **52**, 3474.
114. N. Wang, R. Wang, C. Peng, Y. Feng and B. Chen, *Corros. Sci.*, 2012, **64**, 17.
115. Y. Feng, R.-c. Wang and C.-q. Peng, *Intermetallics*, 2013, **33**, 120.

116. G. Huang, Y. Zhao, Y. Wang, H. Zhang and F. Pan, *Mater. Lett.*, 2013, **113**, 46.
117. N. Wang, Y. Mu, W. Xiong, J. Zhang, Q. Li and Z. Shi, *Corros. Sci.*, 2018, **144**, 107.
118. B. Winther-Jensen, M. Gaadingwe, D. R. Macfarlane and M. Forsyth, *Electrochim. Acta*, 2008, **53**, 5881.
119. S. Sathyanarayana and N. Munichandraiah, *J. Appl. Electrochem.*, 1981, **11**, 33.
120. J. L. Robinson and P. F. King, *J. Electrochem. Soc.*, 1961, **108**, 36.
121. H. Y. Zhao, P. Bian and D. Y. Ju, *J. Environ. Sci.*, 2009, **21**, S88.
122. R. Renuka and S. Ramamurthy, *J. Power Sources*, 2000, **87**, 144.
123. M. A. Deyab, *J. Power Sources*, 2016, **325**, 98.
124. M. M. Dinesh, K. Saminathan, M. Selvam, S. R. Srither and V. Rajendran, *J. Power Sources*, 2015, **276**, 32.
125. Y. Li, J. Ma, G. Wang, F. Ren, Y. Zhu and Y. Song, *J. Electrochem. Soc.*, 2018, **165**, A1713.
126. S. V. Lamaka, B. Vaghefinazari, D. Mei, R. P. Petrauskas, D. Höche and M. L. Zheludkevich, *Corros. Sci.*, 2017, **128**, 224.
127. S. V. Lamaka, D. Höche, R. P. Petrauskas, C. Blawert and M. L. Zheludkevich, *Electrochem. Commun.*, 2016, **62**, 5.

3 Motivation and objectives (Anode material design targets)

Searching for high-performance and "green" Mg alloy anode materials has been the subject of intense research in the past decades. However, the practical properties of Mg anodes are still far from the theoretical pinnacles, leading to unsatisfactory battery performance. For instance, the practical voltage of Mg-air cell is normally below 1.6 V, significantly lower than the theoretical value (3.1 V). The practical capacity and energy density are also far below the theoretical values (Fig. 3-1) resulted from the low anode utilization efficiency, which is normally below 50% at relatively small current densities like 1 mA cm^{-2} [4]. Issues related to the anode materials include the parasitic self-discharge reaction and the large voltage drop caused by oxide/hydroxide layer on anode surface (Fig. 3-1). Generally, most proposed Mg alloy anodes are based on Mg-Al system [5-16] because Al is the most commonly used alloying element for corrosion resistance improvement of Mg. The enhanced corrosion property by Al alloying is believed to be associated with the formation of a protective film on alloy surface attributed to Al enrichment [17, 18]. However, it should be realized that the protective film on Mg surface is destined to result in large voltage drop during discharge [19] and, consequently, issue in a reduced battery voltage. As mentioned in the literature review section, addition of Pb and Hg are possibly able to improve the anode discharge activity via promoting peeling of discharge products, but the usage of elements with a certain toxicity should be contained. Therefore, novel Al-diluted Pb/Hg-free Mg anodes with good discharge properties are highly demanded.

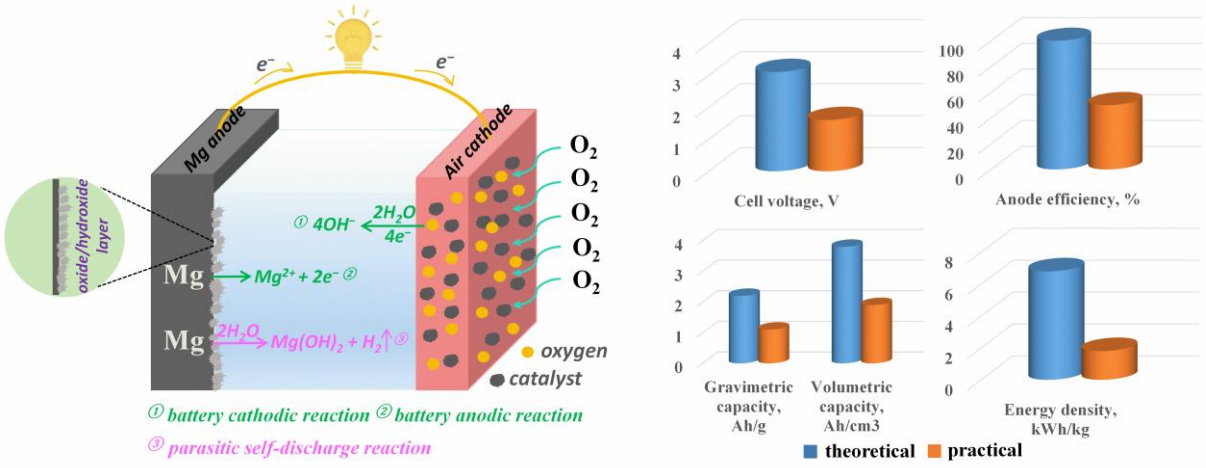

Fig. 3-1 Schematic of Mg-air battery system and theoretical properties in comparison to practical properties. Capacity and energy density are calculated based on anode only.

Calcium (Ca) possesses a good potential to be a promising alloying element for Mg anodes attributed to its proper intrinsic characteristics, like more negative theoretical electrode potential (− 2.87 V vs. SHE) than Mg and nontoxicity to the environment. Besides, as reported [20-22], Ca and related oxides show the capability of reducing the grain size of Mg and, meanwhile, Mg-Ca alloys exhibit good deformability. Ca has been investigated as an alloying element for some Mg-Al based ternary alloy

anodes, e.g. AM60 [23] and AZ91 [12], indicating a positive effect on enhancing the discharge properties. Nonetheless, research regarding the discharge properties, such as utilization efficiency and operating potential, of binary Mg-Ca alloys is vacant, which becomes the major motivation of this work. Besides, microstructure adjustment and adding other alloying elements are possibly capable of enhancing the concerned properties of Mg-Ca anodes, but the element category needs to be carefully selected and examined. Indium (In) alloying has been successfully adopted in primary Al batteries for anodic activation [24, 25]. The In-induced Al anode activation is proposed to be related to film disruption by In re-deposition on anode surface. Likewise, the effect of In addition on performance of some Mg anodes (mostly Mg-Al-based) has been investigated [14, 16, 26-28]. As reported, a Mg-air cell showed increased voltage of 1.22 V at 10 mA cm^{-2} with Mg-9 wt.%Al-1 wt.%In anode comparing to 1.16 V based on Mg-9 wt.%Al [26]. Of late, Gore et al. [29] found that the dissolution rate of a high purity Mg at OCP was increased after addition of 1 mM $InCl_3$ into 0.1 M NaCl solution, whilst the self-corrosion under anodic polarization was inhibited. Although the inhibition mechanism of In remains unclear, the authors proposed that $InCl_3$ as a electrolyte additive could be effective to boost the performance of Mg primary batteries. All these published works imply In could be a promising alloying element for optimized Mg-Ca anode. Besides, it has been demonstrated recently that germanium (Ge) as a trace alloying element was able to reduce the kinetics of cathodic HER reaction, resulting in more negative OCP and reduced corrosion rate [30-33]. The findings provide a possibility of developing novel corrosion resistant Mg anode materials with satisfying operating voltage via alloying with Ge and combination with other elements. Thus, Ge is also one potential option of alloying elements for the optimized Mg-Ca anode.

Noticeably, the utilization efficiency during discharge is a vital property for Mg anodes with great relevance to the specific capacity, energy density and service life of Mg-based batteries. It is well known that the severe self-corrosion of Mg under anodic polarization related to the negative difference effect (NDE) [34-37] results in the decreased utilization efficiency of Mg anodes. Commonly, however, only corrosion properties of Mg at open circuit potential (OCP) are reported in most papers focusing on Mg anode development [5, 7, 12, 13, 23, 38-42]. Interestingly, the corrosion behavior of Mg at OCP may differ significantly from the real-time self-corrosion under polarization [43, 44]. Besides, it should be noted that the self-corrosion of Mg includes two different processes, namely the electrochemical dissolution of Mg substrate and the detachment of undissolved metallic pieces, which is known as “chunk effect” (CE) [45-47]. The correlation between corrosion at OCP, self-corrosion under polarization and CE to utilization efficiency needs to be clarified but, unfortunately, is still blank before this study. The work described in this dissertation is also motived by the shortage of relevant research regrading clarifying the individual effect of different factors on the utilization efficiency of Mg anodes.

Flowchart presented in Fig. 3-2 indicates the anode materials selection and design strategy. With this work, the following specific objectives are anticipated to be accomplished:

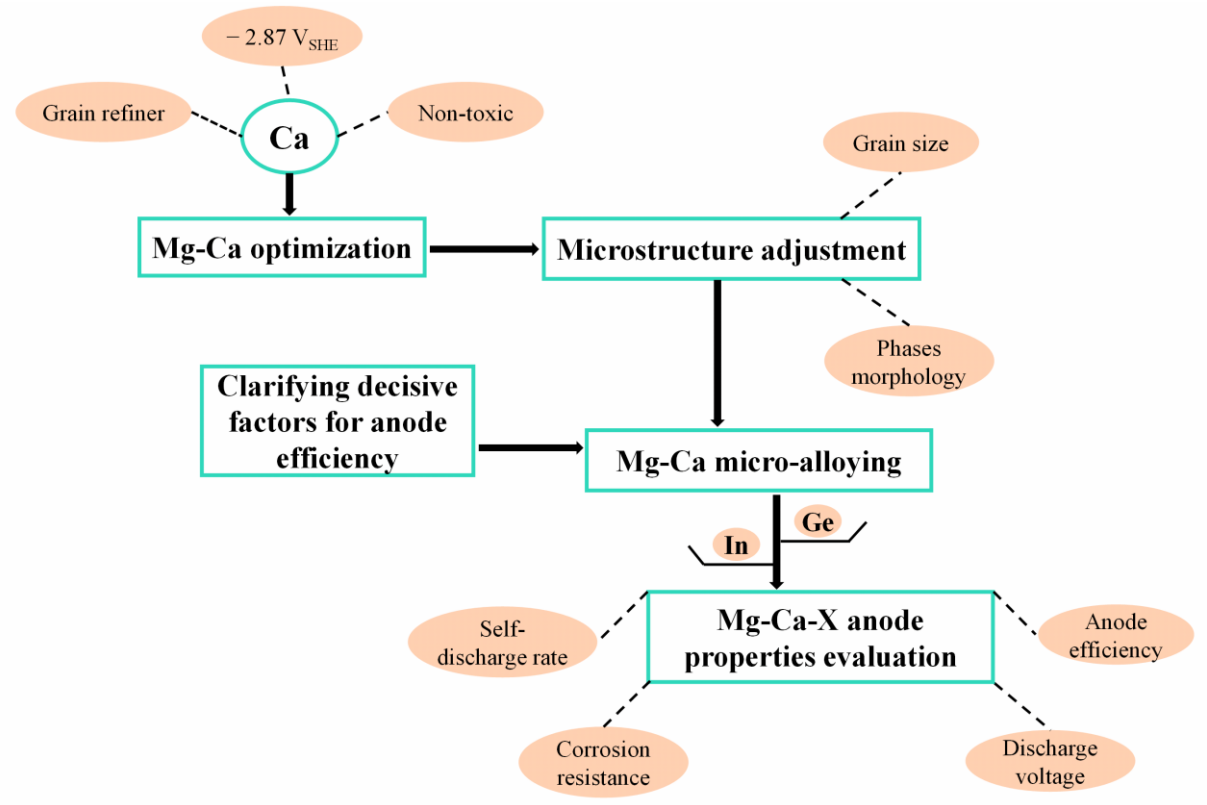

Fig. 3-2 Flowchart indicating the anode materials selection and alloying strategy.

1) Evaluating as-cast binary Mg-Ca alloys as anode materials for primary aqueous Mg-based batteries and optimizing the alloy composition in terms of good corrosion resistance and discharge performance.

2) Adjusting the microstructure (e.g. grain size, secondary phase morphology) of optimized binary Mg-Ca anodes by different solidification routes and then investigating the effect of varied microstructure on the corrosion and discharge properties, including utilization efficiency, discharge potential, specific energy density, etc.

3) To study the influence of several alloying elements (preselected indium and germanium) on the concerned properties of binary Mg-Ca anodes with the purpose of enhancing the anode quality (utilization efficiency, discharge voltage) via proper alloying categories and contents.

4) Clarifying the individual mechanistic effect of different factors, i.e. corrosion at OCP, self-corrosion under polarization and CE, on anode utilization efficiency in attempt to provide more information for designing Mg alloy anodes for battery system with high energy density and long service life.

5) To gain a deeper understanding on the discharge behavior of Mg anodes in various aqueous solutions, especially the correlation between alloy category and microstructure to the self-corrosion and discharge performance.

4 Methodology (Anode preparation and characterization strategy)

4.1 Materials preparation

In this work, all studied Mg alloys were prepared by conventional gravity casting in the cast-shop of Magnesium Innovation Centre (MagIC) at Helmholtz-Zentrum Geesthacht (HZG). Raw materials used were pure Mg ingot (99.96%, weight percent hereafter), pure Ca chips (99.9%), pure In bars (99.95%) and pure Ge bulks (99.99%). Firstly, pure Mg was melted in a boron nitride coated steel crucible placed in a furnace at 760 °C with protection of Ar and SF_6 mixed gas. Alloying elements were then added into the Mg melt, holding for 30 min followed by a manual stirring process of 5 min to achieve good composition homogeneity. Afterwards, the melt was poured into steel moulds preheated to 300 °C for solidification. Two moulds with different dimensions were used for conducting different cooling routes, i.e. air-cooling and water-cooling, to achieve varied solidification rates. The mould for air-cooling is cylindrical with inner diameter of 18 mm, while the mould for water-cooling is cylindrical with inner diameter of 60 mm. Pure Mg was also recast with the same casting process for comparison with the prepared alloys. The actual chemical composition of all prepared materials were analyzed by spark optical emission spectrometry (SOES, Ametek-Spectro), atomic absorption spectroscopy (AAS, Agilent) and X-ray micro fluorescence (μXRF, Bruker). The chemical composition of all prepared and studied materials in this work were presented in Table 4-1 as well as the cooling routes.

4.2 Microstructure characterization

In order to obtain a high-quality surface required for the microstructure observation, specimens were embedded in resin and then carefully ground and polished. The grinding process was conducted on silicon carbide (SiC) emery papers from 320 grit successively up to 4000 grit. After grinding, specimens were polished on a water free oxide polishing suspension (OPS) containing SiO_2 to remove scratches. Afterwards, specimens were rinsed with ethanol and dried by hot wind, ready for observation under a scanning electron microscope (SEM, TESCAN VEGA3) and an atomic force microscope (AFM, Nanowizard, JPK Instruments AG) combined with scanning Kelvin probe force microscope (SKPFM). Besides, the polished samples were etched in an acetic-picric acid solution before characterization with optical microscope (OM, Leica DM2500 M, Leica Microsystems).

4.2.1 Optical microscope (OM)

OM was adopted to observe the structure of grain boundaries as well as the shape of grains. Besides, optical images obtained by OM were used to quantify the average grain size of studied materials via the average grain intercept (AGI) method. Six images corresponding to various areas on the sample surface

Table 4-1 Chemical composition of all prepared and studied materials in this work (wt.%).

	Ca	Ge	In	Fe	Cu	Ni	Si	Al	Mn	Cooling route
Mg-1	<0.001	-	-	0.0043	0.0005	<0.0002	0.0041	0.0054	0.018	Air-cooling
Mg-0.1Ca-1	0.094	-	-	0.0014	0.0015	0.0007	0.011	<0.01	0.032	Air-cooling
Mg-0.5Ca-1	0.46	-	-	0.0013	0.0012	0.0009	0.020	<0.01	0.034	Air-cooling
Mg-1Ca	1.09	-	-	0.0021	0.0011	0.0007	0.023	0.016	0.031	Air-cooling
Mg-2Ca	2.25	-	-	0.0028	0.0018	0.0006	0.023	0.033	0.037	Air-cooling
Mg-4Ca	3.75	-	-	0.0038	0.0019	0.0006	0.024	0.034	0.038	Air-cooling
Mg-0.5Ca-2	0.50	-	-	0.0015	0.0016	0.0009	0.011	<0.01	0.033	Air-cooling
Mg-0.5Ca-3	0.50	-	-	0.0015	0.0016	0.0009	0.011	<0.01	0.033	Water-cooling
Mg-0.1Ca-2	0.07	-	-	0.0018	0.0012	0.0011	0.0036	<0.01	0.017	Water-cooling
Mg-0.1Ca-0.2In	0.09	-	0.25	0.0016	0.0009	0.0008	0.0052	<0.01	0.014	Water-cooling
Mg-0.2Ca-0.4In	0.19	-	0.37	0.0043	0.0009	0.0008	0.0052	<0.01	0.015	Water-cooling
Mg-2	0.0019	-	-	0.0015	0.0003	0.0002	0.0086	<0.01	0.018	Water-cooling
Mg-0.1Ge	-	0.09	-	0.0019	0.0012	0.0012	0.0048	<0.01	0.018	Water-cooling
Mg-0.1Ca-0.1Ge	0.11	0.11	-	0.0018	0.0010	0.0010	0.0060	<0.01	0.015	Water-cooling

were utilized. Fig. 4-1 shows a typical image obtained by OM corresponding to the as-cast Mg-0.5 wt.% Ca alloy prepared by air-cooling.

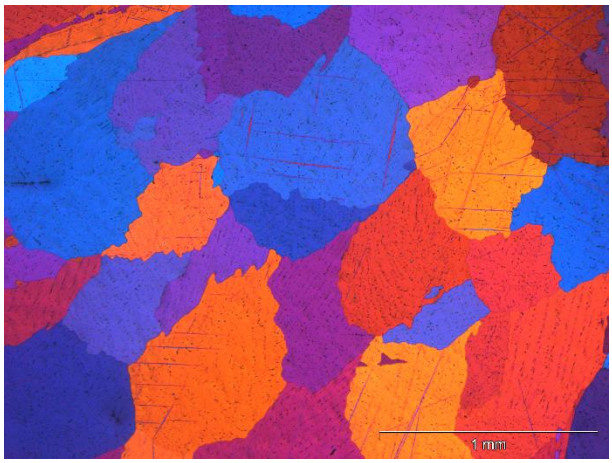

Fig. 4-1 Typical image of as-cast air-cooled Mg-0.5 wt.% Ca alloy obtained by OM.

4.2.2 Scanning electron microscope (SEM)

The size, shape and distribution of impurity particles and intermetallic particles (IMPs) in metals were distinguished with SEM via the backscattered-electron (BSE) detector. A SEM image for the as-cast Mg-0.2 wt.% Ca-0.4 wt.% In alloy via water cooling is indicated in Fig. 4-2. The chemical composition of varied particles and Mg matrix were analyzed with energy dispersive X-ray spectroscopy (EDS) equipped to the SEM. Besides, elemental mappings corresponding to specific regions were carried out under BSE model at 15 kV to demonstrate the distribution of concerned elements.

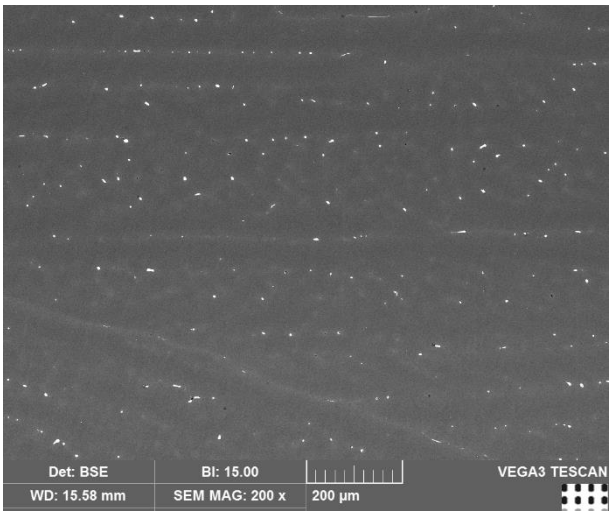

Fig. 4-2 SEM (BSE) image of as-cast water-cooled Mg-0.2 wt.% Ca-0.4 wt.% In alloy.

4.2.3 Scanning Kelvin probe force microscope (SKPFM)

Galvanic couples, formed due to the electrochemical potential difference between Mg matrix and IMPs, are driving forces for the corrosion reaction of Mg alloys. Therefore, to understand the influence of

alloying elements on corrosion properties of Mg, it is of significance to determine the potential difference between newly found IMPs and the Mg matrix. In this case, AFM combined with SKPFM was utilized to measure the Volta potential difference between IMPs and the matrix in newly produced Mg-Ca-In and Mg-Ca-Ge alloys because of the absence of concerned information. The adopted silicon probe supplied by Innovative Solutions Bulgaria Ltd. (Bulgaria) is coated with a Cr/Pt conductive coating and possesses a resonance frequency of 75 kHz and a force constant of 3 N m^{-1}. The probe was set above the sample surface with a height of 100 nm. The scanning was conducted on an area of 30 × 30 µm with a resolution of 512 × 512 pixels immediately after sample polishing via the aforementioned processes. Subsequently, JPKSPM Data Processing was used to perform the data analysis.

4.3 Electrochemical measurements

Potentiodynamic polarization (PDP) curves and electrochemical impedance spectroscopy (EIS) were measured with a Gamry interface 1000 potentiostat to evaluate the electrochemical properties and corrosion resistance of all studied Mg anodes. Samples for all electrochemical measurements were ground with SiC papers up to 1200 grit. The working surface was round with 1 cm^2 surface area. All measurements were performed in a classic three-electrode system with a Pt counter electrode, a Ag/AgCl reference electrode saturated with KCl and the Mg working electrode. The adopted solution was unbuffered 3.5 wt.% NaCl aqueous solution prepared with deionized water and 99.9 wt.% NaCl compound (Fisher Chemical).

4.3.1 Potentiodynamic polarization (PDP)

OCP measurement was performed before each polarization test to monitor the changing surface condition of each specimen. Normally after one hour the OCP value is relatively stable, elucidating the specimen retains a quasi-steady state. After that, polarization curves were measured with direct scan from –250 mV upwards to +400 mV vs. OCP at a scanning rate of 0.5 mV s^{-1}. Besides, anodic and cathodic polarization curves were also measured separately in order to deeply investigate the kinetics of anodic and cathodic reactions with respect to different Mg materials. Anodic polarization curves were obtained by scanning from –5 mV to +400 mV vs. OCP at 1 mV s^{-1}, while cathodic polarization curves were obtained by scanning from +5 mV to –400 mV vs. OCP at the same scan rate.

4.3.2 Electrochemical impedance spectroscopy (EIS)

EIS measurements were carried out to monitor the variation of corrosion resistance of Mg and Mg alloys amid a long-term immersion period in the solution. Before each EIS measurement, relatively stable OCP should be achieved to avoid severe sample polarization caused by impressed voltage. The adopted frequency range was 100 kHz to 0.01 Hz, and the sinusoidal AC voltage was 10 mV rms. Zview program was used to fit the EIS data with a specific equivalent circuit. Fig. 4-3 depicts representative EIS results, obtained from the as-cast air-cooled Mg-0.5 wt.% Ca alloy after immersion in 3.5 wt.%

NaCl solution for different times. The commonly used equivalent circuit (EC) for fitting is also shown [48, 49]. R_s in the EC represents the solution resistance. The capacitive loop appears in the high frequency range is attributed to the surface film, described with film resistance (R_f) and film capacitance (CPE_f). The second capacitive loop within the middle frequency range is ascribed to electric double layer, represented by charge transfer resistance (R_{ct}) and electric double layer capacitance (CPE_{dl}). Occasionally, some data points without a well-defined shape appear within the low frequency range, like in the EIS result for the Mg-0.5 wt.% Ca alloy obtained after immersion of 1 h in 3.5 wt.% NaCl solution (shown in Fig. 4-3). These misaligned points can be originated from the non-stationarity during acquisition of impedance spectra [50]. Therefore, they are not included in the EC and are discarded during the fitting process. The sum of R_f and R_{ct}, which is defined as R_{sum}, is utilized to evaluate the corrosion resistance of studied Mg alloys.

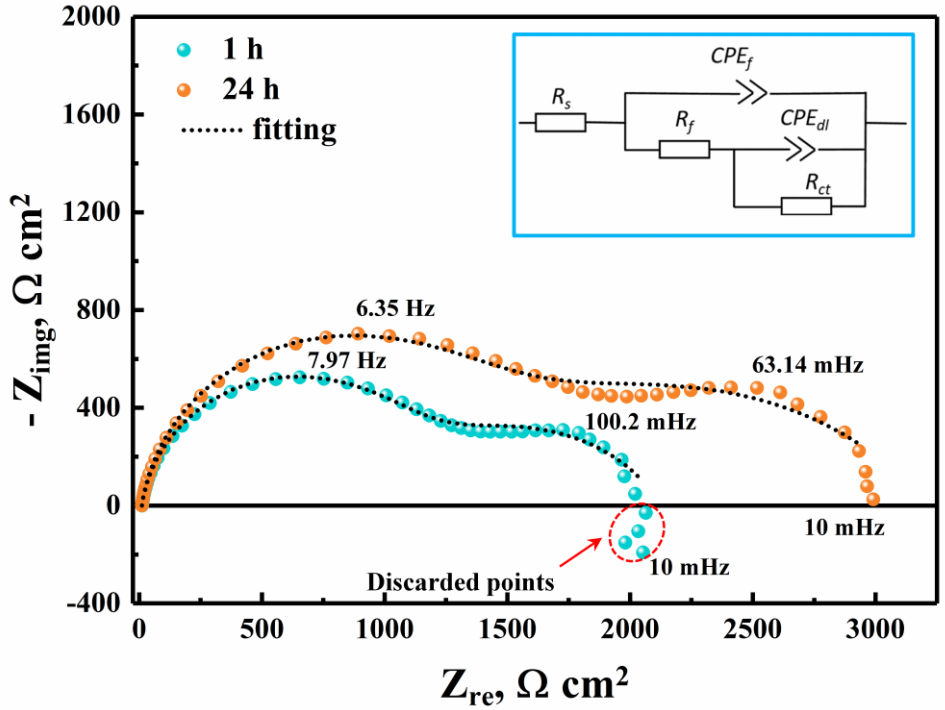

Fig. 4-3 Nyquist plots of EIS results for as-cast Mg-0.5 wt.% Ca alloy after immersion in 3.5 wt.% NaCl solution for different times. A proposed equivalent circuit for fitting is also presented.

4.4 Hydrogen evolution (HE) tests

In NaCl solution, the main reactions involved during Mg corrosion, no matter at OCP condition or under polarization, can be described as following:

$$\text{Anodic:} \quad Mg = Mg^{2+} + 2e^- \tag{4-1}$$

$$\text{Cathodic:} \quad 2H_2O + 2e^- = H_2\uparrow + 2OH^- \tag{4-2}$$

$$O_2 + H_2O + 4e^- = 4OH^- \tag{4-3}$$

$$\text{Overall:} \quad Mg + 2H_2O = Mg(OH)_2 + H_2\uparrow \tag{4-4}$$

$$2Mg + O_2 + H_2O = 2Mg(OH)_2 \tag{4-5}$$

Water reduction is the main cathodic reaction during Mg corrosion, generating abundant H_2 gas. Besides, the reduction of dissolved oxygen in water takes place as secondary cathodic reaction along Mg dissolution [51], but in many cases the contribution of ORR is not high. Accordingly, the produced hydrogen gas is able to act as an index for the corrosion rate of Mg metals. Actually, the collection of generated H_2 during corrosion with specific experimental set-ups has become a widely used approach for studying Mg corrosion. Impressing a particular potential or current with a potentiostat is vital for investigating the corrosion behavior of Mg under polarization or, in another term, during discharge, which, however, is not necessary for the corrosion evaluation at OCP. Thus, the set-ups for collecting the hydrogen gas are partly different regarding the two situations. More details are given at the following sections.

4.4.1 At OCP condition

A classic set-up for hydrogen collection at OCP is indicated in Fig. 4-4a. An Mg specimen was hung in an upturned funnel with fishing line and a plastic screw inserted into the specimen. A burette was set on top of the funnel and then all the items were placed in a beaker with 300 ml 3.5 wt.% NaCl solution. The burette was filled with solution to a specific scale at the beginning. Hydrogen gas produced by corrosion process went into the burette due to the low solubility of H_2 in the solution (0.015 ml H_2 (STP)/ml H_2O [52]) and, consequently, decreased the liquid level because of the pressure difference between the burette inner and external. In such a case, the declined volume of solution in the burette equaled to the H_2 volume. Generally, HE testing possesses high accuracy regarding assessing the corrosion rate of Mg with relatively low corrosion resistance [53-55]. However, in the case of Mg with high corrosion resistance or short time corrosion determination, HE method is not suitable considering the insufficient generated gas, which is not able to compensate the experimental error caused by some inevitable factors, like H_2 dissolution in the solution, corrosion via oxygen reduction, the changing environmental temperature and pressure.

In order to determine the corrosion rate of highly corrosion-resistant Mg and its alloys, quantifying the mass loss caused by corrosion during the whole immersion period is a better method, although only the average corrosion rate within this period can be obtained. Besides, mass loss measurements are normally conducted along with HE tests as verification for the experimental accuracy. The mass of samples was measured prior to exposure in the solution. After corrosion testing, samples were immersed into a diluted chromic acid aqueous solution (200 g l^{-1}) to remove the corrosion products. Samples were took out after no bubbles were generated, and then cleaned by ultrasonics in ethanol. Accordingly, the mass loss due to corrosion can be known after measuring the mass of sample without corrosion products. Assuming the experiments were carried out at 25 °C and 1 atm pressure, the molar volume of H_2 is 24.45 l mol^{-1}, while the molar mass of Mg is 24.31 g mol^{-1}. Therefore, the volume of produced H_2 gas (V_H, ml) can be converted into mass loss of Mg (W_H, mg) via the following equation:

$$W_H = 0.994V_H \tag{4-6}$$

Thus, corrosion rates related to HE tests (P_H) and mass loss measurements (P_W) were calculated according to HE rate (ΔV) and mass loss rate (ΔW) respectively via the following formulas [56, 57]:

$$P_W\,(\text{mm y}^{-1}) = 2.1\Delta W\,(\text{mg cm}^{-2}\,\text{d}^{-1}) \quad (4\text{-}7)$$

$$P_H\,(\text{mm y}^{-1}) = 2.088\Delta V\,(\text{ml cm}^{-2}\,\text{d}^{-1}) \quad (4\text{-}8)$$

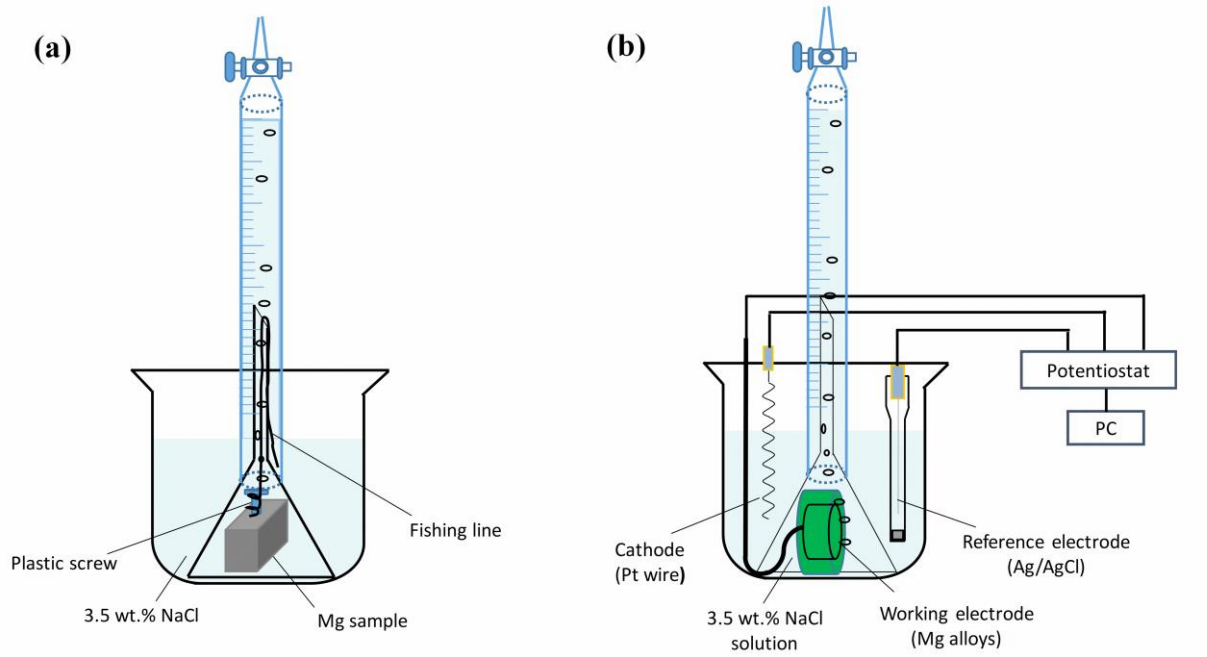

Fig. 4-4 Experimental set-ups for hydrogen collection (a) at OCP condition and (b) under polarization.

4.4.2 During discharge

Fig. 4-4b presents the experimental set-up for HE testing during discharge with applied current densities. The specimen was embedded in resin and connected with copper wire from backside for conducting. The aforementioned three-electrode system was applied. The sample was connected with a potentiostat for current loading. Evolved hydrogen gas volume was recorded within the whole discharge test and, thus, the real-time HE rate can be obtained. The self-discharge rate of Mg anodes during the discharge process was then calculated via Faraday's law of electrolysis.

$$m = \frac{QM}{Fz} = \frac{ItM}{Fz} \quad (4\text{-}9)$$

Thus

$$I = \frac{mFz}{tM} \quad (4\text{-}10)$$

Where m (g) is the mass of consumed Mg, M (g mol^{-1}) is the molar mass of Mg metal, I (A) is constant current, t (s) is time, F (96485 C mol^{-1}) is the Faraday constant and z is the number of electrons transferred per ion. The current generated by Mg consumption can be calculated accordingly. Similarly, the current density associated with the self-discharge of Mg anodes (I_{self}, mA cm^{-2}), can be determined by the real-time HE rate (V_{RH}, ml cm^{-2} h^{-1}) via the following:

$$I_{self} = \frac{mFz}{tM} = \frac{0.994V_{RH}Fz}{3600M} = 2.22V_{RH} \quad (4\text{-}11)$$

4.5 Half-cell discharge testing

The discharge tests in half-cell were performed under constant current densities. The aforementioned three-electrode system was used. The working electrode was a Mg anode sample with 1 cm^2 working surface area. Relatively low current densities, normally below 10 mA cm^{-2}, were adopted. The lowest applied current density was 1 mA cm^{-2}. Occasionally, EIS measurements were conducted immediately after discharge tests to evaluate the activity of the anodes, which is largely dependent on the surface products film. After discharge measurements, the anodic utilization efficiency and capacity were calculated based on the mass loss of samples determined after removing discharge products with chromic acid aqueous solution. The utilized equations are indicated as follow [23, 58]:

$$\text{Utilization efficiency (\%)} = \frac{W_{theo}}{\Delta W} \times 100\% \quad (4\text{-}12)$$

$$\text{Specific capacity (Ah } g^{-1}) = \frac{I \times t}{\Delta W} \quad (4\text{-}13)$$

Where I (A) is the discharge current, t (h) is discharge time, ΔW (g) is the practical mass loss of samples during discharge process and W_{theo} (g) is the theoretical mass loss due to faradaic process. ΔW was determined by measuring the mass of samples before discharge and after removal of discharge products. The theoretical mass W_{theo} was calculated via the following equation [58, 59]:

$$W_{theo} = \frac{I \times t}{F \times \sum(\frac{x_i \times n_i}{m_i})} \quad (4\text{-}14)$$

Where F represents the Faraday constant (26.8 Ah mol^{-1}), x_i, n_i, m_i represent the mass fraction, number of exchanged electrons and atomic weight, respectively, of each element in the materials.

4.6 Surface qualitative analysis

X-ray photoelectron spectroscopic (XPS) measurements were carried out to investigate the Mg anode surface after discharge via a Kratos Axis Ultra DLD instrument (Kratos Analytical, Manchester UK) equipped with a monochromatic Al Kα anode working at 15 kV (225 W). Survey spectra and region spectra were recorded with a pass energy of 160 eV and 20 eV, respectively. The investigated area of the sample was selected as 700×300 µm. In order to analyze the inside of the surface film, Ar etching was applied for 30 min by a rate of 10 nm min^{-1} related to Ta_2O_5. The acceleration voltage and extraction current for the Ar etching were 3.8 kV and 160 mA separately. The XPS data were validated and evaluated using CASA-XPS software (version 2.3.18). The C 1s signal was used for spectra calibration and adjusted to 284.5 eV. Background subtraction (U2 Tougaard) was carried out for calculation and deconvolution of the region spectra. To distinguish the concerned elements from different possible chemical states, binding energy corresponding to each peak was compared with the standard in NIST XPS Database (https://srdata.nist.gov/xps/selEnergyType.aspx).

4.7 Surface and cross-sectional morphology

Specimens after discharge testing were observed under SEM, with the secondary electron (SE) detector, to characterize the surface topography of discharge products film. Definitely, because of the poor conductivity of discharge products, which were mainly $Mg(OH)_2$, the samples were subjected to sputter coating with Au under 20 mA for 60 s prior to the SEM observation. Besides, the surface morphologies corresponding to samples after discharge and removal of discharge products were also checked, surely without sputter coating due to good conductivity of Mg substrate. 3D reconstruction of the sample surface without products was conducted via SEM combined with Alicona Mex program for images processing. Depth profiles were obtained to examine the surface roughness and homogeneity for evaluating the dissolution behavior of Mg anodes. Additionally, cross-sectional morphologies of specimens after discharge were checked. Samples after discharge were embedded in resin with the intersecting surface exposing outside. The embedded samples were then ground and polished with the same process mentioned above. Sputter coating was proceeded to the polished samples before observation in SEM, due to the poor conductivity of resin, to acquire high quality images.

4.8 Mg-air battery testing

To evaluate the potential of all prepared Mg alloys as anode materials for primary Mg batteries, discharge tests were carried out in a lab-made Mg-air full cell. The configuration for battery discharge measurements under constant current densities is presented in Fig. 4-5a. The sample was embedded in resin exposing a working surface of 15×15 mm, and connected with copper wire from backside. The electrolyte was normally blank 3.5 wt.% NaCl solution, occasionally with electrolyte additives if it was indicated. The adopted cathode was a commercially air cathode with C/MnO_2 as catalysts. The surface of the cathode exposed to the electrolyte was circular with 2.5 cm^2 area. A porous resin block was compressed onto the cathode and fixed with a screw for air (oxygen) supplying. Cell voltage was recorded within the whole discharge period under different current densities. Thereafter, mass loss during discharge testing was determined after removing discharge products with the diluted chromic acid. Consequently, specific energy density related to the anode materials can be calculated via the following formula:

$$\text{Specific energy density (W h g}^{-1}) = \frac{\int_0^t U \times I \times \Delta t}{\Delta W} \quad (4\text{-}15)$$

Where U is the simultaneously recorded discharge voltage (V), I is the impressed current (A), t is the total time for discharge (h) and ΔW (g) is the mass loss of anode during discharge tests.

Long-term battery failure tests were also performed with a different configuration indicated in Fig. 4-5b. The only difference between the two configurations was the geometry of the specimens. A strip corresponding to each Mg anodes was used. The dimension of the immersed part for each specimen was the same 30×5×2.5 mm. The batteries with varied anode materials were operated under a constant

load until reaching a cut-off voltage, which was set as 0.5 V. The battery voltage was recorded simultaneously. After that, battery service life and average voltage can be obtained from the voltage-time curves. Further, anodic utilization efficiency and specific energy density were calculated via the same equations mentioned above, as the mass loss of anodes were known.

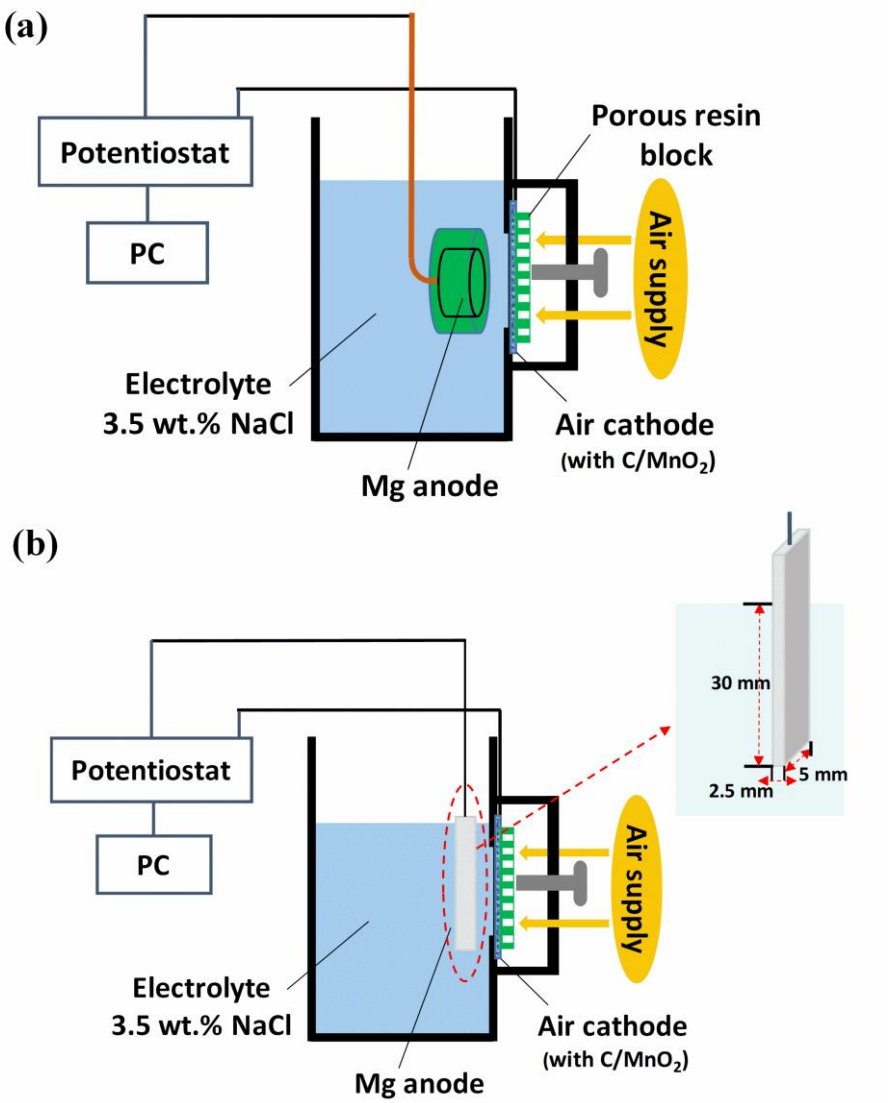

Fig. 4-5 Configurations of a lab-made Mg-air battery: (a) for discharge measurements; (b) for battery failure tests.

4.9 Reference anode materials

In order to verify the advances of the newly developed Mg alloy anodes in this work, several commercially used Mg anode materials were also included in the battery testing for purpose of comparison, including a high-purity Mg (HP Mg), a commercial AZ31 alloy and a commercial AM50 alloy (all as-cast). The chemical composition of the three materials is indicated in Table 4-2. Low impurity contents are shown, especially concerning the main detrimental impurities for Mg corrosion, i.e. Fe, Ni and Cu [34, 60, 61]. Note that the HP Mg used in this work has been studied previously by

Lamaka et al. [61], indicating a low corrosion rate in NaCl solution due to low Fe content in impurity-enriched precipitates.

Table 4-2 Chemical composition of commercially Mg anodes for comparison (wt.%).

Materials	Ca	Fe	Al	Mn	Cu	Ni	Si	Zn	Mg
HP Mg	<0.0001	0.0050	0.0030	0.0008	<0.0001	<0.0002	<0.0001	0.0035	99.98
AM50	0.0011	0.0002	4.85	0.430	0.0017	0.0005	0.0637	0.0418	94.61
AZ31	0.0011	0.0011	2.97	0.358	0.0019	0.0007	0.0309	0.732	95.90

5 Results (Published and submitted)

The work described in this thesis aims at developing novel anode materials for primary aqueous Mg-based batteries as well as revealing the decisive factors affecting anode performance. The obtained results are presented in form of 4 published papers in scientific journals and 1 submitted manuscript. The evaluation of binary Mg-Ca alloys as anode materials for Mg-air battery was carried out in ***paper 1***, proposing that Mg-Ca alloys with Ca contents lower than 0.5wt.% are better candidates in comparison to some commercial Mg anodes like AZ31, AM50 and HP Mg. Then, the effect of microstructure, particularly secondary phase morphology, on corrosion and discharge properties of binary Mg-Ca anode was investigated in ***paper 2***. Meanwhile, the intermittent discharge performance of binary Mg-Ca anodes was assessed. ***Paper 3*** studied the contribution of different self-corrosion mechanisms to utilization efficiency loss of Mg anodes, providing a guide for developing novel Mg alloy anodes. It was indicated that a large fraction of secondary phases in Mg anodes should be avoid to reduce the efficiency loss related to chunk effect. According to ***paper 3***, micro-alloying with other elements should be desirable to improve the performance of binary Mg-Ca anode. Thus, the effect of elaborately selected elements, i.e. In and Ge, was studied in ***paper 4*** and ***paper 5*** respectively following the strategy of micro-alloying, showing considerable enhancement of concerned anode properties. Mg-0.1wt.%Ca-0.2wt.%In and Mg-0.1wt.%Ca-0.1wt.%Ge were recommended as high-performance anode materials for next generation primary Mg batteries. Roadmap for the anode development process based on these papers are presented in Fig. 5-1. Specifically, the motivation and main results related to each study are separately summarized preceding each publication.

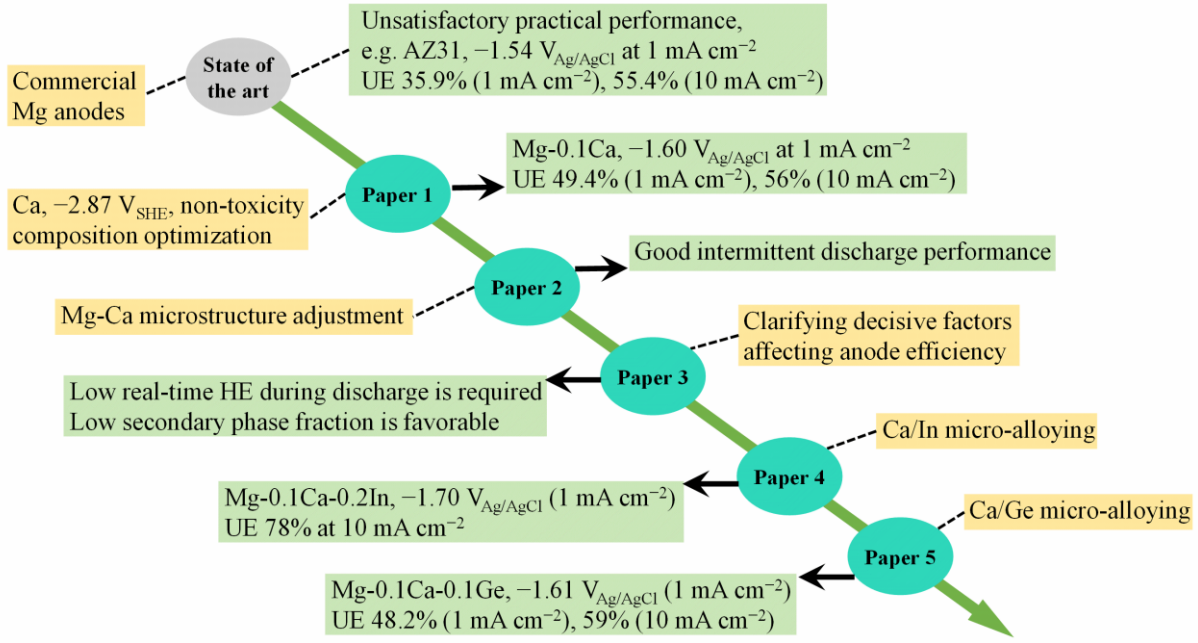

Fig. 5-1 Roadmap for the anode development process presented in this thesis. UE represents utilization efficiency, while HE means hydrogen evolution. All mentioned data value were determined in 3.5 wt.% NaCl solution.

5.1 Mg-Ca binary alloys as anodes for primary Mg-air batteries

Paper 1: Mg-Ca binary alloys as anodes for primary Mg-air batteries (published in Journal of Power Sources)

The aim of this work was to evaluate the possibility of binary Mg-Ca alloys as anode materials for primary Mg batteries (Mg-air system in this case). Five Mg-Ca alloys with varied Ca contents were prepared via casting followed by air-cooling. The microstructure, corrosion resistance and discharge properties of all Mg-Ca alloys were determined with different methods. Accordingly, composition optimization was proceeded in terms of high corrosion resistance and improved discharge properties, e.g. highly negative discharge potential and enhanced utilization efficiency. The optimized Mg-Ca alloy, i.e. Mg-0.1 wt.% Ca, was then evaluated in a Mg-air full cell and compared with some commercially Mg anode materials. Obtained results indicated that the battery based on the Mg-0.1 wt.% Ca anode exhibited higher cell voltage and specific energy density than those based on high purity Mg, AZ31 and AM50 anodes. Hence, the micro-alloyed binary Mg-Ca (0.1~0.5 wt.%) is a good candidate for the anode material of primary aqueous Mg batteries.

Journal of Power Sources 396 (2018) 109–118

Contents lists available at ScienceDirect

Journal of Power Sources

journal homepage: www.elsevier.com/locate/jpowsour

Mg-Ca binary alloys as anodes for primary Mg-air batteries

Min Deng[a,*], Daniel Höche[a,b], Sviatlana V. Lamaka[a], Darya Snihirova[a], Mikhail L. Zheludkevich[a,c]

[a] MagIC—Magnesium Innovation Centre, Helmholtz-Zentrum Geesthacht (HZG), 21502, Geesthacht, Germany
[b] Computational Material Design, Faculty of Mechanical Engineering, Helmut-Schmidt-University University of the Federal Armed Forces, 22043, Hamburg, Germany
[c] Institute of Materials Science, Faculty of Engineering, Kiel University, 24143, Kiel, Germany

HIGHLIGHTS

- Effect of Ca on self-corrosion and discharge properties of Mg was studied.
- Composition of Mg-Ca alloy as anode for primary Mg-air battery was optimized.
- Mg-air battery with Mg-0.1 wt.%Ca as anode shows superior discharge properties.

ARTICLE INFO

Keywords:
Magnesium-calcium alloy
Magnesium-air battery
Self-corrosion
Discharge properties

ABSTRACT

In this research, Mg-Ca binary alloys are evaluated as anode material candidates for primary Mg-air batteries. The effect of Ca content on self-corrosion and discharge performance of Mg anode is investigated through microstructure characterization, electrochemical measurements and half-cell discharge tests. Then the composition of Mg-Ca alloys is optimized in terms of reduced self-corrosion and improved discharge performance. The basic characteristics of Mg-air batteries with optimized Mg-Ca alloy as anode are tested and compared to those based on high purity Mg and defined commercial Mg alloys. The results show that Mg-0.1 wt. % Ca alloy has the best self-corrosion behavior and discharge performance among all prepared Mg-Ca alloys. The Mg-air battery with Mg-0.1 wt. % Ca alloy as anode offers higher cell voltage and specific energy than those based on high purity Mg, AM50 and AZ31 alloys.

1. Introduction

Metal-air batteries exhibit high specific energy density because they utilize oxygen from atmosphere as oxidant, reducing the weight of battery system [1]. Besides, the consumption of electrode materials in metal-air batteries does not cause CO_2 emissions into the environment. Hence, metal-air batteries are becoming promising power source for electric devices and vehicles. Some metals such as lithium, zinc, magnesium and aluminum are possible anode materials for metal-air batteries and have been researched by many scholars in recent decades [2–5]. Among these metals, Mg attracts much attention because it has second-most negative electrode potential (i.e., −2.37 V (vs. SHE)), high theoretical specific capacity (i.e., 2.2 A h g^{-1}), high specific energy density (i.e., 6.8 kW h kg^{-1}) and relatively low cost. In principle, Mg-air batteries can be designed as primary batteries as well as rechargeable batteries. However, rechargeable Mg-air batteries are still far from being practical because of low energy conversion efficiency and low high-rate stability attributed to the absence of suitable electrolytes and efficient catalysts at air cathodes [6,7]. In contrast, aqueous primary Mg-air battery systems can be easily assembled and reused through replacing exhausted Mg anodes. The aqueous electrolytes can be simple saline solutions that are easy to get and environmentally benign. Unfortunately, despite these advantages, the practical application of Mg-air batteries is still limited due to some technical issues [4]. Firstly, the operating voltage of Mg-air batteries is much lower than the theoretical value because of the voltage drop caused by the corrosion products on anode/electrolyte interface and sluggish kinetics of electrode reaction. Secondly, Mg suffers severe self-corrosion during discharge in aqueous electrolyte, reducing the utilization efficiency and specific energy density of anodes. This unexpected parasitic reaction leads to huge efficiency loss of Mg-air battery systems.

To solve these issues and promote the application of Mg-air batteries, developing novel Mg alloys as anode materials is a feasible method. Up to now, some Mg alloys such as Mg-Al-Zn [8,9], Mg-Al-Mn [10], Mg-Al-Pb [11,12], and Mg-Li [13] series alloys have been developed for Mg-air batteries, and the effect of some other alloying elements, e.g., In, Ce, Y, Sn and Ga, has been researched [11,14,15]. It has been reported that Mg-6 wt.% Al-5 wt.% Pb alloy shows higher

* Corresponding author. Helmholtz- Zentrum Geesthacht, Max-Planck-Str. 1, 21502, Geesthacht, Germany.
E-mail address: Min.Deng@hzg.de (M. Deng).

https://doi.org/10.1016/j.jpowsour.2018.05.090
Received 15 March 2018; Received in revised form 15 May 2018; Accepted 29 May 2018
Available online 14 June 2018
0378-7753/

discharge voltage and power density than pure Mg(99.99 wt.%) in home-made Mg-air battery test [11]. Besides, the addition of In can improve the discharge voltage of Mg-6 wt.% Al-5 wt.% Pb alloy and increase its utilization efficiency at high current densities. However, the toxic element Pb can be very harmful to the environment. According to the report of Ma et al. [13], Mg-14Li-1Al-0.1Ce alloy might be a good candidate for anodes of Mg-air batteries because of its higher operating voltage and specific capacity than pure Mg and AZ31 alloy. Nonetheless, the safety issue during the preparation of Mg-Li alloys cannot be ignored. Recently, Mg-Al-Sn alloys that are more environmentally benign attracted attention of scientists [16,17]. Xiong et al. [17] reported that Mg-6 wt.% Al-1wt.% Sn alloys after annealing at 200 °C can exhibit similar discharge voltage and power density to Mg-Al-Pb alloy. The limiting factor of this alloy is the low utilization efficiency, which is below 50% at 10 mA cm^{-2} even after extrusion and heat treatment. Therefore, novel Mg anodes with both high discharge voltage and utilization efficiency still need to be developed.

Calcium is a fully environmentally friendly element, and it has more negative standard electrode potential than magnesium, i.e. −2.87 V (vs. SHE). Hence, it is reasonable that the addition of Ca into Mg can improve the discharge voltage of Mg anodes. It has been reported that the addition of Ca can shift the open circuit potential of Mg-Mn alloy to more negative value [18]. Yuasa et al. [19] studied the effect of Ca on the discharge performance of AM60 alloy as anode for Mg-air battery. The results show that the Ca addition can increase the specific capacity and anodic efficiency of AM60 alloy because of more uniform corrosion. Besides, owning to Ca addition, the operating time before failure of anode sheet with thickness of 1 mm increases from 11 to 14 h to more than 16 h, due to the thin and cracked discharge product layer, which allows the electrolyte to penetrate easily. Recently, research on Mg-Ca binary alloys is mainly focusing on its application as biomaterials [20–27]. As reported, Ca addition with appropriate quantity can improve the corrosion resistance of magnesium, but the measurement were mostly carried out in simulated body fluid (SBF) [24,28].

Mg-Ca alloys might be promising candidate for anodes of primary Mg-air batteries, but there is still no systemic research on their discharge and self-corrosion properties in aqueous electrolyte for air batteries. The aim of this work is to explore the possibility of Mg-Ca binary alloys as anodes for primary Mg-air batteries. Five Mg-Ca alloys with different compositions are prepared, and their discharge and self-corrosion properties in sodium chloride solution are evaluated. At last, Mg-Ca binary alloy with optimum composition is selected and its discharge properties as anodes for lab-made Mg-air battery are compared to pure Mg and some commercial alloys.

2. Materials and methods

2.1. Materials preparation

Mg-xCa (x = 0.1, 0.5, 1, 2, 4 wt.%) binary alloys were prepared via casting using pure Mg (99.96 wt. %) and pure Ca (99.0 wt. %). For comparison, pure Mg ingots were also prepared via the same casting procedures and named as recast-Mg. The original materials were melted in a steel crucible at 760 °C with protection of Ar and SF_6 gas. Afterwards, the molten metals were poured into cylindrical steel molds with diameter of 18 mm and cooled in air. The steel molds were preheated at 300 °C before casting. The chemical compositions of as-cast pure Mg and Mg-Ca binary alloys were analyzed though optical emission spectrometry (spark OES) and atomic absorption spectroscopy (AAS). The results are presented in Table 1, indicating low concentrations of Fe, Ni and Cu, which are detrimental to the corrosion resistance of Mg [29–31].

2.2. Microstructure analysis

Optical microscopy (OM) and scanning electron microscopy (SEM) were used to study the microstructure of Mg-Ca alloys. Before observation, Mg-Ca alloy samples were ground with emery papers up to 4000 grit, and then polished with oxide polishing suspension (OPS) to remove most scratches. OM images of Mg-Ca alloys were taken after etching in acetic-picric acid solution. The grain size of recast Mg and Mg-Ca alloys were measured using linear intercept method. For each material, six images of different fields of view were analyzed to measure the average grain size.

2.3. Electrochemical measurements

Potentiodynamic polarization curves were obtained by a Gamry interface 1000 potentiostat in 3.5 wt. % NaCl solution. Typical three electrodes system was used with Pt plate as a counter electrode, saturated Ag/AgCl electrode as reference and samples as working electrode. Samples were ground with emery papers up to 1200 grit and then put into an electrochemical cell. Before testing, the samples were immersed into the solution for 30 min to get stable open circuit potential (OCP). The potentiodynamic polarization tests were proceeded within a potential range from - 400 mV to 400 mV (vs. OCP) at a scanning rate of 0.5 mV s^{-1}. Corrosion current density was calculated through extrapolating the cathodic polarization curve to corrosion potential. The region for linear fitting is between - 200 mV and - 100 mV (vs. corrosion potential). Besides, electrochemical impedance spectroscopy (EIS) measurements were also performed using the same electrochemical equipment. The frequency ranged from 100 kHz to 0.01 Hz and the sinusoidal excitation voltage applied to the cells was 10 mV rms. In order to obtain stable surface state, before measurement the samples were immersed in the electrolyte for 1 h. All the electrochemical tests for every material were repeated at least three times to ensure reproducibility.

2.4. Half-cell discharge tests

Discharge curves at constant current density in half-cell arrangement were tested in 3.5 wt. % NaCl solution. The discharge potential was referred to saturated Ag/AgCl electrode. The surface area for discharge testing was 1 cm^2, and the applied current densities were 0.5 mA cm^{-2}, 2 mA cm^{-2}, 5 mA cm^{-2} and 10 mA cm^{-2}. After discharge, the surface morphology of these materials was characterized by SEM. Utilization efficiencies and specific capacity of recast Mg and as-cast Mg-Ca alloys were calculated after removing corrosion products from the surface with 200 g L^{-1} chromic acid aqueous solution. The equations used for utilization efficiency and specific capacity calculation are listed as follow [19,32]:

$$Utilization\ Efficency\,(\%) = \frac{W_{theo}}{\Delta W} \times 100\% \quad (1)$$

$$Specific\ capacity\ (mAh\ g^{-1}) = \frac{I \times t}{\Delta W} \times 1000 \quad (2)$$

Where I is the discharge current (A), t is discharge time (h), ΔW (g) is the weight loss of samples during discharge process and W_{theo} (g) is the theoretical weight loss due to faradaic process. Weight loss ΔW was measured by weighing the mass of samples before and after discharge. The theoretical weight W_{theo} can be calculated through the following equation [32,33]:

$$W_{theo} = \frac{I \times t}{F \times \sum\left(\frac{x_i \times n_i}{m_i}\right)} \quad (3)$$

Where F represents the Faraday constant (26.8 A h mol^{-1}), x_i, n_i, m_i represent the mass fraction, number of exchanged electrons and atomic weight, respectively, of each element in the materials.

Table 1
Chemical compositions of recast-Mg and Mg-Ca binary alloys (wt. %).

Materials	Ca	Fe	Al	Mn	Cu	Ni	Si	Zn	Mg
recast Mg	< 0.001	0.0043	0.0054	0.0184	0.0005	< 0.0002	0.0041	0.0028	Bal.
Mg-0.1Ca	0.094	0.0014	< 0.01	0.032	0.0015	0.0007	0.011	0.0034	Bal.
Mg-0.5Ca	0.46	0.0013	< 0.01	0.034	0.0012	0.0009	0.020	0.0033	Bal.
Mg-1Ca	1.09	0.0021	0.016	0.031	0.0011	0.0007	0.023	0.0038	Bal.
Mg-2Ca	2.25	0.0028	0.033	0.037	0.0018	0.0006	0.023	0.0032	Bal.
Mg-4Ca	3.75	0.0038	0.034	0.038	0.0019	0.0006	0.024	0.0034	Bal.

Table 2
Chemical compositions of materials for comparison (wt. %).

Materials	Ca	Fe	Al	Mn	Cu	Ni	Si	Zn	Mg
HP Mg	< 0.0001	0.0050	0.0030	0.0008	< 0.0001	< 0.0002	< 0.0001	0.0035	99.98
AM50	0.0011	0.0002	4.85	0.430	0.0017	0.0005	0.0637	0.0418	94.61
AZ31	0.0011	0.0011	2.97	0.358	0.0019	0.0007	0.0309	0.732	95.90

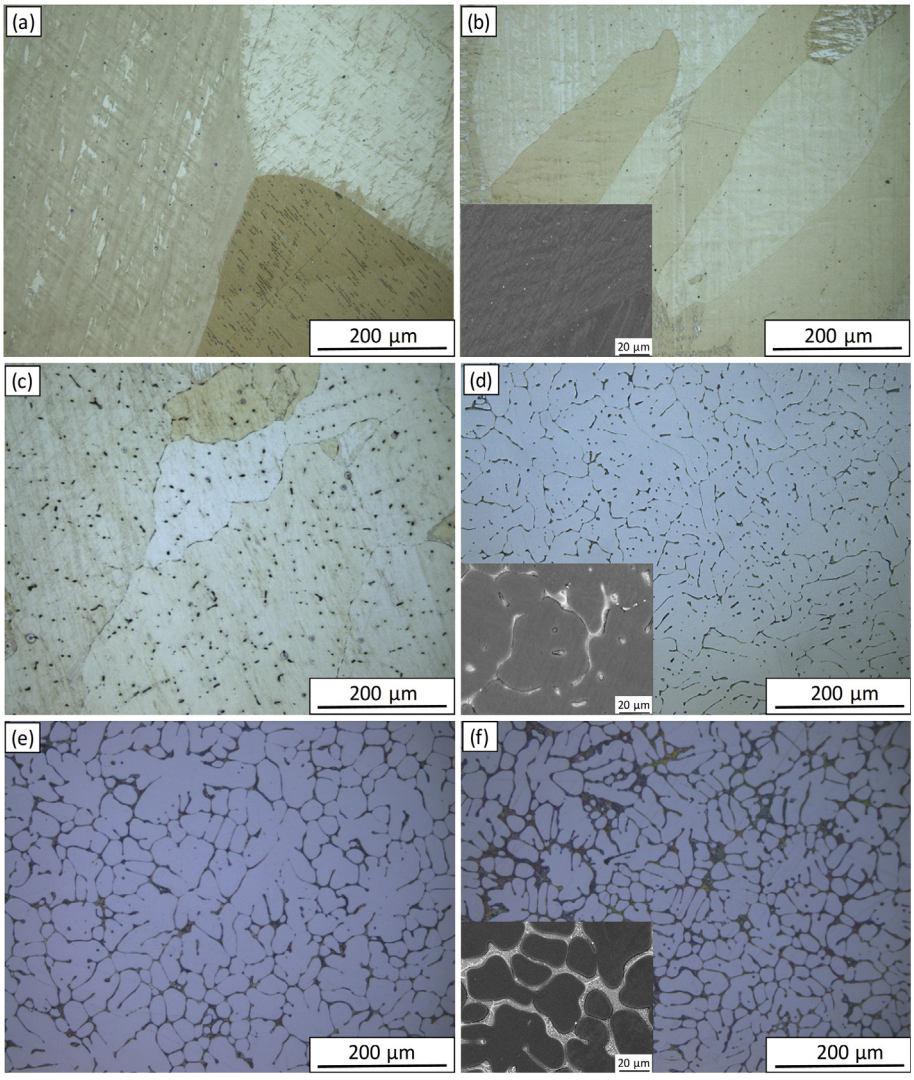

Fig. 1. Optical micrographs of: (a) recast Mg; (b) Mg-0.1Ca; (c) Mg-0.5Ca; (d) Mg-1Ca; (e) Mg-2Ca; (f) Mg-4Ca. The insets in (b) (d) and (f) are corresponding SEM images.

2.5. Magnesium-air battery tests

The discharge properties of magnesium-air battery were measured in a lab-made full cell. The optimized Mg-Ca alloy as anode was tested and compared to high purity Mg (HP Mg), commercial AM50 and AZ31 magnesium alloy. The chemical compositions of HP Mg, AM50 and AZ31 alloys used in this research are listed in Table 2. The electrolyte in Mg-air battery test was 3.5 wt. % NaCl solution. The cathode was

Table 3
Average grain size of recast Mg and as-cast Mg-Ca alloys.

Materials	recast Mg	Mg-0.1Ca	Mg-0.5Ca	Mg-1Ca	Mg-2Ca	Mg-4Ca
Grain size (μm)	919 ± 450	497 ± 226	245 ± 46	181 ± 37	166 ± 32	142 ± 25

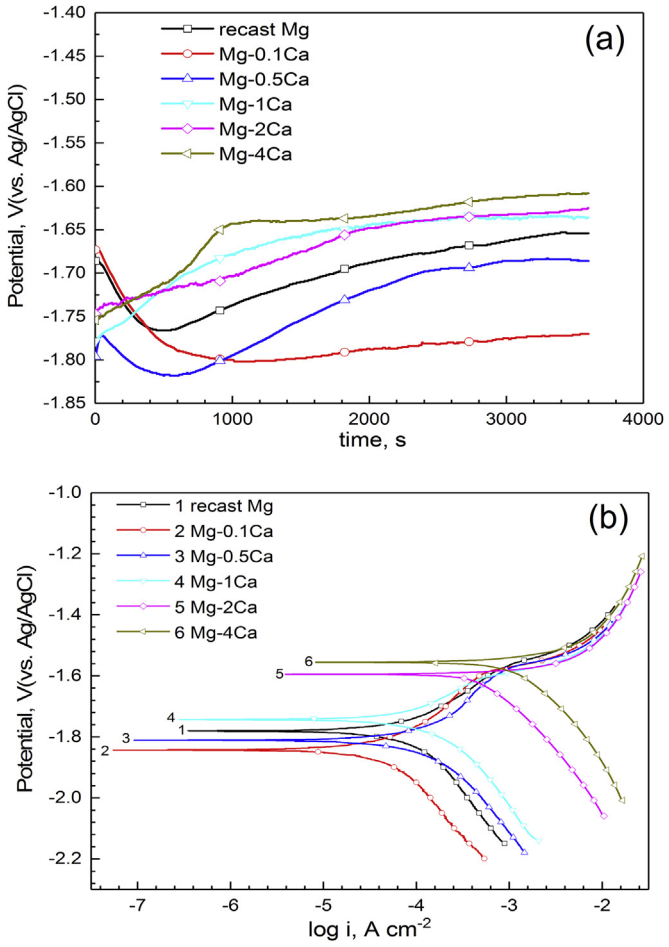

Fig. 2. OCP (a) and polarization curves (b) of recast Mg and Mg-Ca alloys in 3.5 wt. % NaCl solution.

Table 4
Electrochemical parameters of recast Mg and Mg-Ca alloys.

Material	E_{OC} (V vs. Ag/AgCl)	E_{corr} (V vs. Ag/AgCl)	I_{corr} (μA cm^{-2})
Pure Mg	−1.65	−1.78	84.1 ± 15.1
Mg-0.1Ca	−1.77	−1.84	63.0 ± 19.3
Mg-0.5Ca	−1.69	−1.81	132.5 ± 11.6
Mg-1Ca	−1.64	−1.74	152.9 ± 0.6
Mg-2Ca	−1.63	−1.60	427.6 ± 45.1
Mg-4Ca	−1.61	−1.56	1062.8 ± 70.8

commercial air cathode with carbon/MnO_2 as catalysts and Nickel mesh as the current collector. The surface areas of anodes exposed to the electrolyte are all approximately 2.5 cm^2. The discharge voltage of the cell was measured at different current densities. The average voltage during a whole discharge test was calculated and set as the cell voltage of Mg-air battery. After discharge, the specific energy based on magnesium anode was calculated through the following equation [34]:

$$\textit{Specific energy}\ (Wh\ kg^{-1}) = \frac{\int_0^t U \times I \times \Delta t}{\Delta W} \quad (4)$$

Where U is the discharge voltage (V), I is the discharge current (A), t is the discharge time (h) and ΔW (kg) is the weight loss of anode during the discharge.

3. Results and discussion

3.1. Microstructure of Mg-Ca alloys

Fig. 1 shows the optical images of recast Mg and as-cast Mg-Ca alloys with different Ca content. It can be seen that Ca addition causes grain refinement to magnesium, and further grain refinement can be observed with increasing Ca content. The calculated average grain sizes according to OM images are presented in Table 3, indicating that the grain size decreases with increasing Ca content. Besides, distinct dendrites appears in the microstructure of Mg-Ca alloys with high Ca content (≥2 wt. %). The formation of dendrites is due to the significant constitutional undercooling in regions near to the solid/liquid interface caused by high Ca content [23]. The constitutional undercooling is also the major driving force for nucleation, so that many nucleation sites will be activated and more crystal nucleuses will form in the constitutionally undercooled zone [35]. Therefore, the grain size is likely to be smaller. In addition, because of the low solubility of Ca in Mg, numerous Ca atoms accumulate in the regions adjacent to the solid/liquid interface, thus restricting the growth of grain due to the slow diffusion of Ca atoms [23,24,35]. The phase composition of as-cast Mg-Ca binary alloys has been reported in many papers [22–24], indicating a typical composition consisting of α-Mg solid solution and Mg_2Ca intermetallic as shown in the Mg-Ca phase diagram [36]. The insets in Fig. 1(b, d and f) shows the SEM images of as-cast Mg-Ca alloys. Mg-0.1Ca alloy exhibits the microstructure with only some small particles distributing in the grain interior. In contrast, for Mg-Ca alloys with high Ca content, eutectic structure composed of α-Mg and Mg_2Ca exists not only along grain boundaries but also in the interdendritic regions. Obviously, the rising Ca content also causes a significant increase of Mg_2Ca phase amount as indicated by the inserted SEM images and in other papers [21,23,24].

3.2. Open circuit potential of Mg-Ca alloys

Fig. 2a presents the open circuit potential of recast Mg and as-cast Mg-Ca alloys in 3.5 wt. % NaCl solution. After immersion in solution, the open circuit potential of recast Mg and Mg-Ca alloys all suffer a rapid change before reaching a stable value. The immersion time for reaching the stable state varies with the Ca content. The average value of measured OCP in last 100 s during the whole 1-h OCP test is set as E_{oc} and shown in Table 4. It can be found that the addition of Ca in Mg can shift the E_{oc} toward negative direction. However, the E_{oc} would increase with the rising content of Ca. Mg-0.1Ca alloy exhibits most negative open circuit potential during the last 100 s measurement, i.e., - 1.770 V vs. Ag/AgCl. Theoretically, calcium has more negative standard electrode potential than magnesium, so the dissolution of active Ca into Mg matrix might cause a decrease of electrode potential of pure magnesium, as shown in this work. However, the E_{oc} Mg-Ca alloys become less negative with increasing Ca content, which is probably due to the different reaction rates of cathodic hydrogen evolution. Potentiodynamic polarization curves of recast Mg and Mg-Ca alloys are presented in Fig. 2b. The cathodic branch of polarization curve is driven with hydrogen evolution reaction. Obviously, the addition of calcium element shows significant effect on the cathodic process. With the increasing content of Ca, cathodic polarization curve keeps moving to position

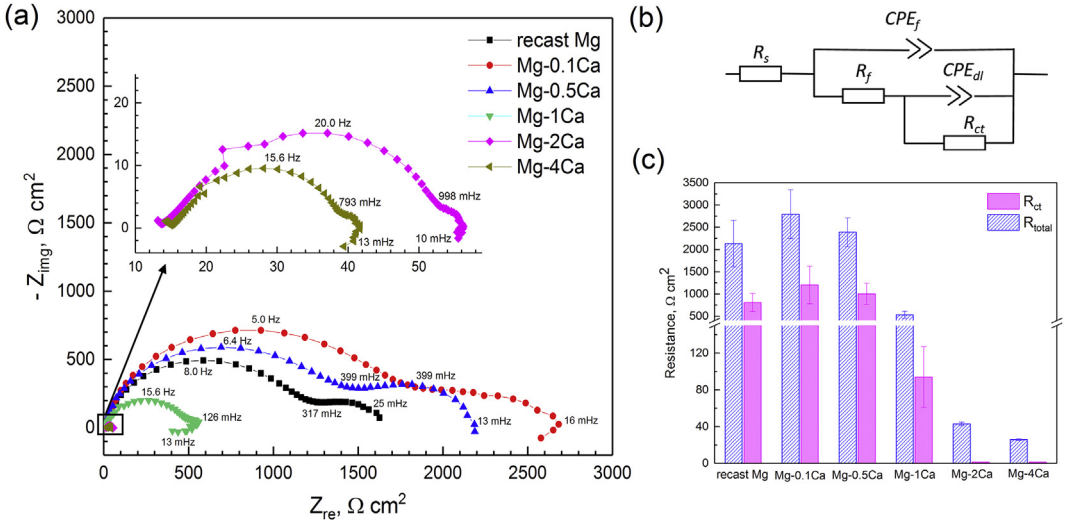

Fig. 3. EIS results of recast Mg and as-cast Mg-Ca alloys at OCP in 3.5 wt. % NaCl solution: (a) Nyquist plots; (b) Equivalent circuit; (c) Charge transfer resistance and total resistance after fitting.

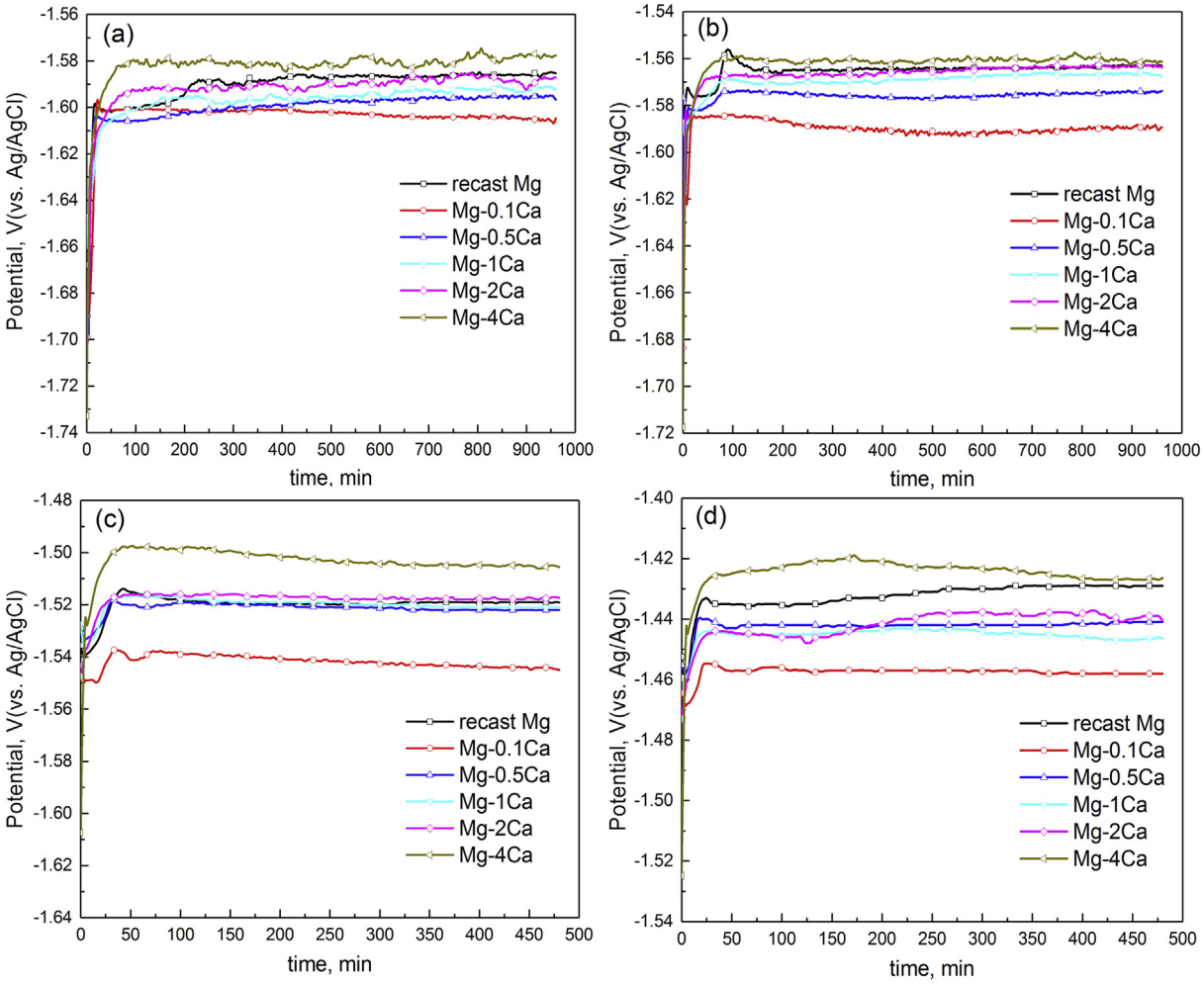

Fig. 4. Discharge curves of recast Mg and Mg-Ca alloys in 3.5 wt. % NaCl solution at current density:(a) 0.5 mA cm^{-2}; (b) 2 mA cm^{-2}; (c) 5 mA cm^{-2}; (d) 10 mA cm^{-2}.

with higher current. The cathodic current density of Mg-0.1Ca alloy at −2.0 V (vs. Ag/AgCl) is 141.9 μA cm^{-2}, while that of Mg-1Ca alloy is 877.6 μA cm^{-2}. This indicates that the kinetic of cathodic reaction tends to be faster with higher Ca content in magnesium. The dissolution of calcium into magnesium matrix and the slow cathodic reaction rate lead to the most negative open circuit potential of Mg-0.1Ca alloy among all researched materials in this work.

Table 5
Discharge properties of recast Mg and as-cast Mg-Ca alloys.

	Current (mA cm^{-2})	recast Mg	Mg-0.1Ca	Mg-0.5Ca	Mg-1Ca	Mg-2Ca	Mg-4Ca
Discharge potential (V vs. Ag/AgCl)	0.5	−1.590	−1.604	−1.600	−1.597	−1.592	−1.582
	2	−1.565	−1.590	−1.576	−1.569	−1.566	−1.562
	5	−1.520	−1.542	−1.521	−1.520	−1.518	−1.503
	10	−1.432	−1.458	−1.442	−1.445	−1.440	−1.425
Utilization efficiency (%)	0.5	30.9 ± 1.6	39.7 ± 1.0	38.5 ± 0.2	25.6 ± 0.4	21.1 ± 1.0	14.2 ± 0.8
	2	42.5 ± 4.7	55.5 ± 0.8	50.3 ± 4.0	46.9 ± 1.2	26.5 ± 0.2	16.9 ± 2.3
	5	45.8 ± 0.1	58.2 ± 2.1	53.3 ± 2.0	49.2 ± 1.3	39.5 ± 0.6	30.4 ± 1.8
	10	49.6 ± 0.7	55.6 ± 1.1	54.3 ± 1.6	50.0 ± 1.3	42.9 ± 0.1	32.6 ± 1.3
Specific capacity (mAh g^{-1})	0.5	660 ± 35	886 ± 22	857 ± 5	576 ± 9	467 ± 22	311 ± 17
	2	948 ± 106	1238 ± 17	1156 ± 93	1042 ± 27	587 ± 5	371 ± 50
	5	1022 ± 3	1299 ± 47	1188 ± 44	1093 ± 30	876 ± 13	669 ± 40
	10	1107 ± 16	1241 ± 25	1245 ± 49	1109 ± 28	950 ± 3	716 ± 28

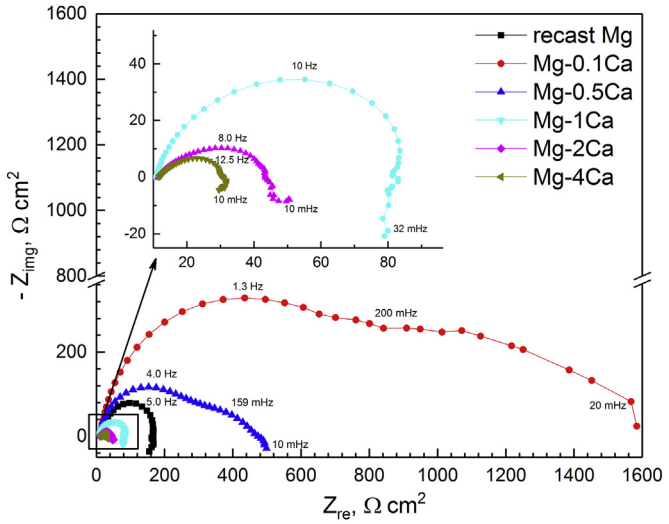

Fig. 5. Nyquist plots of recast Mg and Mg-Ca alloys after discharge in 3.5 wt. % NaCl solution at 2 mA cm^{-2} for 2 h.

3.3. Self-corrosion performance of Mg-Ca alloys

Self-corrosion in electrolytes during discharge is the most important factor that decreases the utilization efficiency of magnesium batteries. Therefore, it is necessary to investigate the self-corrosion performance of magnesium anodes. Values of corrosion current density, I_{corr}, extracted from polarization curves of as-cast pure Mg and Mg-Ca alloys are summarized in Table 4. The corrosion current density tends to become higher with increasing Ca content, which indicates that the self-corrosion rate of Mg-Ca alloy in NaCl solution would increase with increasing Ca content. The self-corrosion behavior of as-cast pure Mg and Mg-Ca alloys were also investigated with EIS measurements at open circuit potential. The EIS results are shown in Fig. 3. The Nyquist plots (Fig. 3a) of recast Mg, Mg-0.1Ca and Mg-0.5Ca alloy show two large capacitive loops within the whole frequency range. The high frequency capacitive loop results from the oxide film present on the surface of alloy and the one at middle frequencies is responsible for charge transfer process. On the other hand, for Mg-Ca alloys with higher Ca content (≥1 wt. %), the middle capacitive loop diminishes, indicating a very low polarization resistance. Instead, an inductive loop at low frequency, which might be related to the non-stationality during the measurements [37], appears in EIS spectrum of Mg-1Ca, Mg-2Ca and Mg-4Ca alloys. The equivalent circuit for all materials is presented in Fig. 3b. Film resistance (R_f) and film capacitance (CPE_f) are used to present the first capacitive loop in the equivalent circuit, while R_s represents solution resistance. The middle frequency time constant is described by charge transfer resistance (R_{ct}) and electric double layer capacitance (CPE_{dl}). Besides, the incomplete inductive loop in EIS spectrum of Mg-1Ca, Mg-2Ca and Mg-4Ca alloys is not presented in the equivalent circuit since it can be originated from the non-stationarity during acquisition of impedance spectra.

Fig. 3c shows the charge transfer resistance, R_{ct}, and total resistance, R_{total}, of recast Mg and as-cast Mg-Ca alloys after fitting EIS results with Zview software. Obviously, both R_{ct} and R_{total} increase after the addition of Ca with low concentration, but will decrease with rising content of Ca. It indicates that the addition of low content of Ca can improve the corrosion resistance of Mg in NaCl solution. However, for Mg-Ca alloys, the corrosion resistance will weaken with increasing Ca content. This is consistent with the results getting from polarization curves. Mg-Ca alloy with Ca addition of 0.1% exhibits best corrosion resistance in 3.5 wt. % NaCl solution among all researched materials in this work. The corrosion behavior of Mg-Ca alloys has been widely studied in the past decade, suggesting that the effect of Ca on the corrosion of magnesium relates to two aspects: the grain refinement of Ca addition in Mg and the precipitation of active Mg_2Ca phase [21–23]. On one hand, it has been claimed that solid film on grain boundaries is likely to be more stable compared to the bulk surface [38,39], while grain boundaries can also act as corrosion barriers [40,41]. Therefore, in many cases, grain refinement can be beneficial for improving the corrosion resistance of magnesium. This is one of the reasons Mg-0.1 and Mg-0.5Ca alloys have higher corrosion resistance than recast pure Mg. Besides, it is noteworthy that Fe concentration in Mg-0.1Ca and Mg-0.5Ca alloys is lower than in recast Mg, which also contribute to their different corrosion performance, even though the Fe concentrations are all below Fe tolerance limit in as-cast Mg. On the other hand, Mg_2Ca phase has been studied and claimed to be more electrochemically active than α-Mg [21,22,42], leading to galvanic corrosion between Mg_2Ca phase and α-Mg matrix. The increasing Ca content introduces more Mg_2Ca phase into Mg-Ca alloys, which means more micro anode-cathode sites are formed. Hence, the increasing Ca content accelerates the galvanic corrosion in Mg-Ca alloys and consecutively decreases the corrosion resistance. For Mg-Ca alloys with high Ca content, the positive effect on corrosion resistance caused by grain refinement is probably exceeded by the negative effect caused by increasing Mg_2Ca amounts, so they exhibits low corrosion resistance in sodium chloride solution.

3.4. Discharge properties of Mg-Ca alloys

Discharge curves of recast Mg and Mg-Ca alloys at different current density are measured in 3.5 wt. % NaCl solution in a half-cell. Materials that exhibit more negative discharge potential during half-cell test can possibly supply higher voltage when serve as anodes in fully assembled batteries. Discharge results of recast Mg and Mg-Ca alloys are presented in Fig. 4. The average discharge potential during complete discharge tests are calculated and listed in Table 5. All the materials can maintain relatively stable discharge potential during the whole discharge tests at different current density. However, the value of discharge potential varies with the increasing Ca content. From Fig. 4 and Table 5, we can

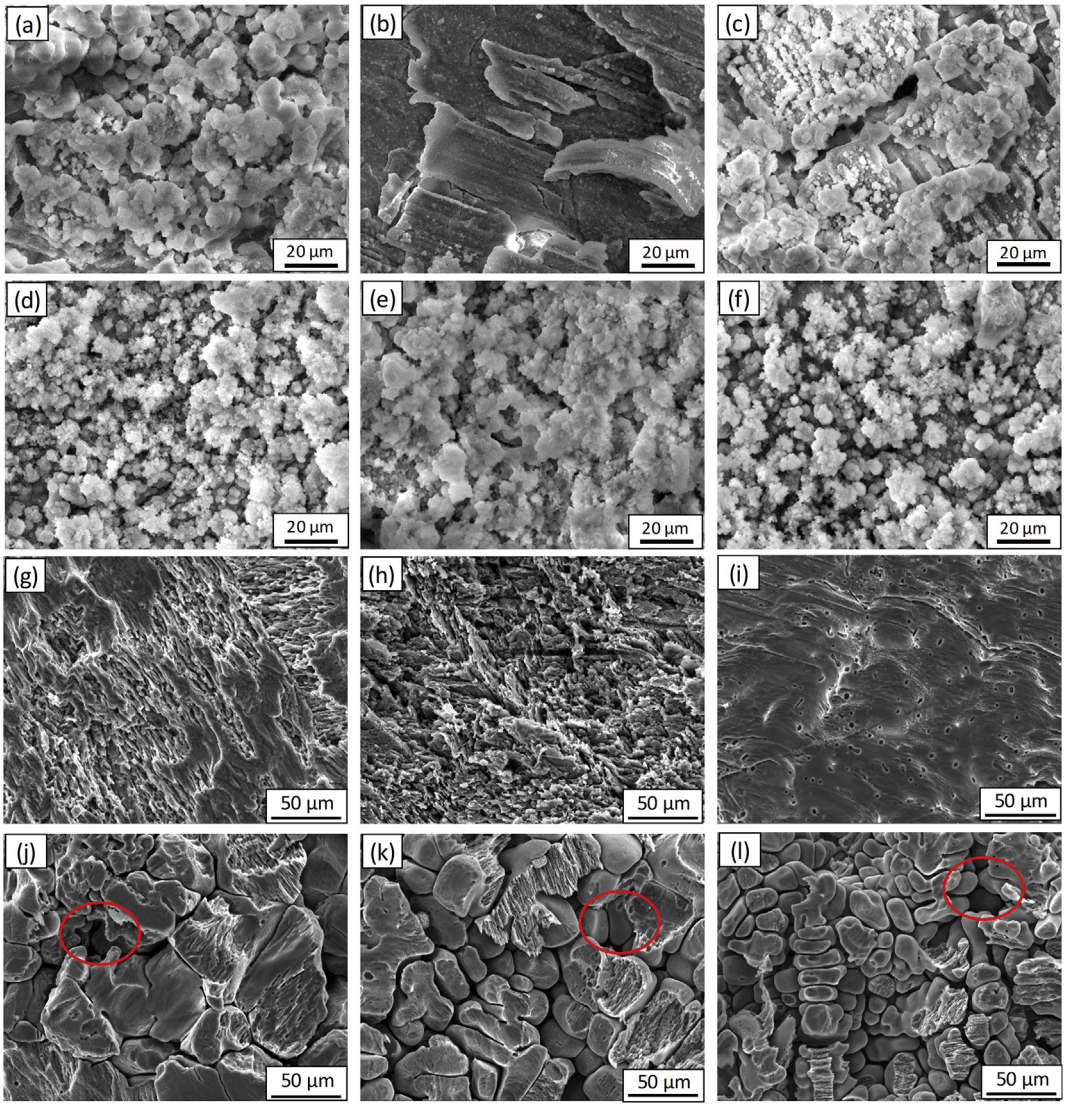

Fig. 6. Surface morphologies of (a) recast Mg, (b) Mg-0.1Ca, (c) Mg-0.5Ca, (d) Mg-1Ca, (e) Mg-2Ca, (f) Mg-4Ca after discharge in 3.5 wt. % NaCl solution at 2 mA cm^{-2} for 2 h, and surface morphologies after discharge at 0.5 mA cm^{-2} for 16 h and removing all discharge products: (g) recast Mg, (h) Mg-0.1Ca, (i) Mg-0.5Ca, (j) Mg-1Ca, (k) Mg-2Ca, (l) Mg-4Ca.

see that most Mg-Ca alloys have more negative discharge potential than recast Mg, even though the discharge potential becomes less negative with increasing Ca content. Mg-0.1Ca alloy shows most negative discharge potential at all current densities, such as −1.604 V (vs. Ag/AgCl) at 0.5 mA cm^{-2} compared with −1.590 V for recast Mg.

The potential of anodes during discharge can be expressed as

$$E_{anode} = E_0 - \eta_{ct} - \eta_{diff} - iR \quad (5)$$

where E_O is the open circuit potential, η_{ct} is the charge transfer overpotential, η_{diff} is the diffusion overpotential caused by discharge products film, i is the current on load and R is the electrolyte resistance between the reference electrode and polarized anode [43,44]. In this work, all the materials are tested with the same cell arrangement, which means the same electrolyte resistance, so that the potential loss caused by iR drop can be considered as the same. In principle, E_O indicates the most negative value of potential one anode can present. However, during discharge, potential loss caused by η_{ct}, η_{diff} and iR drop always exists and increases with the rising current density on load [45]. From the OCP measurement results presented in Fig. 2a, we can know that the OCP difference between Mg-0.1Ca alloy and other Mg-Ca alloys ranges from 80 mV to 160 mV. However, the difference of discharge potential at different current densities is just 4 mV–40 mV, which is much smaller than the OCP difference. This phenomenon indicates the overpotential during discharge caused by η_{ct} and η_{diff} varies with the Ca content in Mg-Ca alloys. It is not easy to calculate or measure the η_{ct} and η_{diff} separately because of the complicated physical structure of the electrodes and the unstable surface conditions. Nevertheless, EIS has been considered as a good method to investigate the η_{ct} and η_{diff} during cell operating [44,46]. Fig. 5 presents the EIS results of recast Mg and Mg-Ca alloys after discharge at 2 mA cm^{-2} for 2 h. The Nyquist plots of Mg-0.1Ca and Mg-0.5Ca alloys after discharge both show a large capacitive loop in high frequency, indicating a protective film in the surface. This film will inhibit the mass diffusion process, leading to large diffusion overpotential. By contrast, for recast Mg and Mg-Ca alloys with high Ca content, the loop in high frequency shrinks sharply with increasing Ca content, indicating a film with less protection. Therefore, for recast Mg and Mg-Ca alloys, the mass diffusion through the discharge products film can be easy, so that the diffusion overpotential is most likely to be low. This statement can be proven by surface morphologies of recast Mg and Mg-Ca alloys after discharge at 2 mA cm^{-2} for 2 h, as presented in Fig. 6a–f. The surface of Mg-0.1Ca (Fig. 6b) and Mg-0.5Ca (Fig. 6c) are covered by dense discharge products, which prevents the penetration of solution and reactants. For Mg-

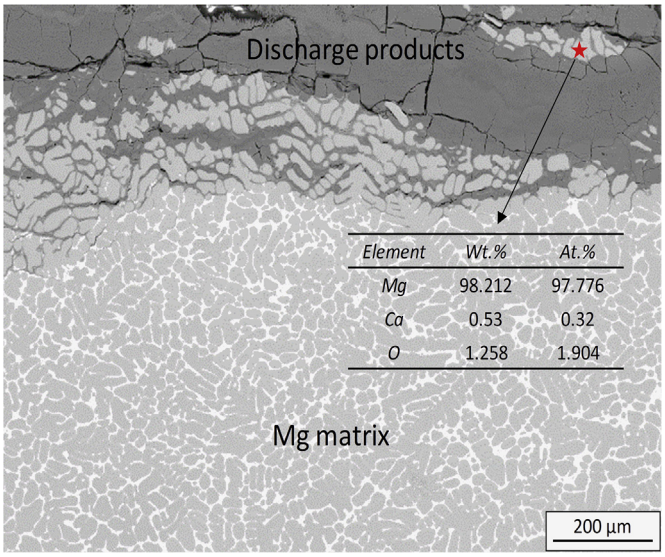

Fig. 7. SEM image of Mg-4Ca alloy after discharge in 3.5 wt. % NaCl solution at 10 mA cm^{-2} for 8 h (cross section).

Ca alloys with high Ca content, the discharge products covering the electrode surface are much more loose and porous. The solution and reactants can penetrate through the film easily, leading to low diffusion overpotential. Besides, from the Nyquist plots, we can see that the diameter of capacitive loop in middle frequency diminishes or even disappears with increasing Ca content, which means the charge transfer resistance will decrease with the increase of Ca content. Therefore, Mg-Ca alloys with higher Ca content can exhibit higher electrochemical activity during discharge than Mg-0.1Ca and Mg-0.5Ca alloys. In other words, the charge transfer overpotential will decrease with rising Ca content in Mg-Ca alloys. Mg-0.1Ca alloy suffers large charge transfer overpotential and diffusion overpotential during discharge, but it has much more negative OCP than other materials, so that it can still present most negative discharge potential with current densities on load.

Table 5 also presents the utilization efficiency and specific capacity of recast Mg and as-cast Mg-Ca alloys. Be similar to the self-corrosion resistance, the utilization efficiency and specific capacity can be improved by the addition of Ca, but decrease with increasing Ca content in Mg-Ca alloys. Mg-0.1Ca alloy shows the highest utilization efficiency and capacity at all current densities, such as 58.2% and 1299 mAh g^{-1} at current density of 5 mA cm^{-2}, respectively, comparing to 30.6% and 669 mAh g^{-1} of Mg-4Ca alloy. The utilization efficiency and specific capacity of magnesium anodes are affected not only by the self-corrosion during discharge but also by the "chunk effect" induced by the detachment of some metallic particles or pieces during discharge process [11,19,47]. On one hand, during discharge, self-corrosion leads to mass loss of anodes and this part of mass loss cannot be utilized to supply energy for applied loads, reducing the utilization efficiency and capacity of anodes. Therefore, the best self-corrosion resistance of Mg-0.1Ca alloy is one of the reason that it exhibits highest utilization efficiency and specific capacity among all the materials. On the other hand, during discharge, some metallic particles or pieces may drop off from the surface because other metallic parts surrounding these metallic pieces have dissolved. These detached metallic parts also cannot take part in the discharge process, thus reducing the utilization efficiency and capacity of anodes. Fig. 6g–l also shows the surface morphologies of recast Mg and Mg-Ca alloys after discharge at 0.5 mA cm^{-2} for 16 h and removing discharge products with chromic acid solution. Be similar to recast Mg, the surface morphology of Mg-0.1Ca alloy after discharge indicates uniform dissolution of anode surface during discharge, so the "chunk effect" on utilization efficiency

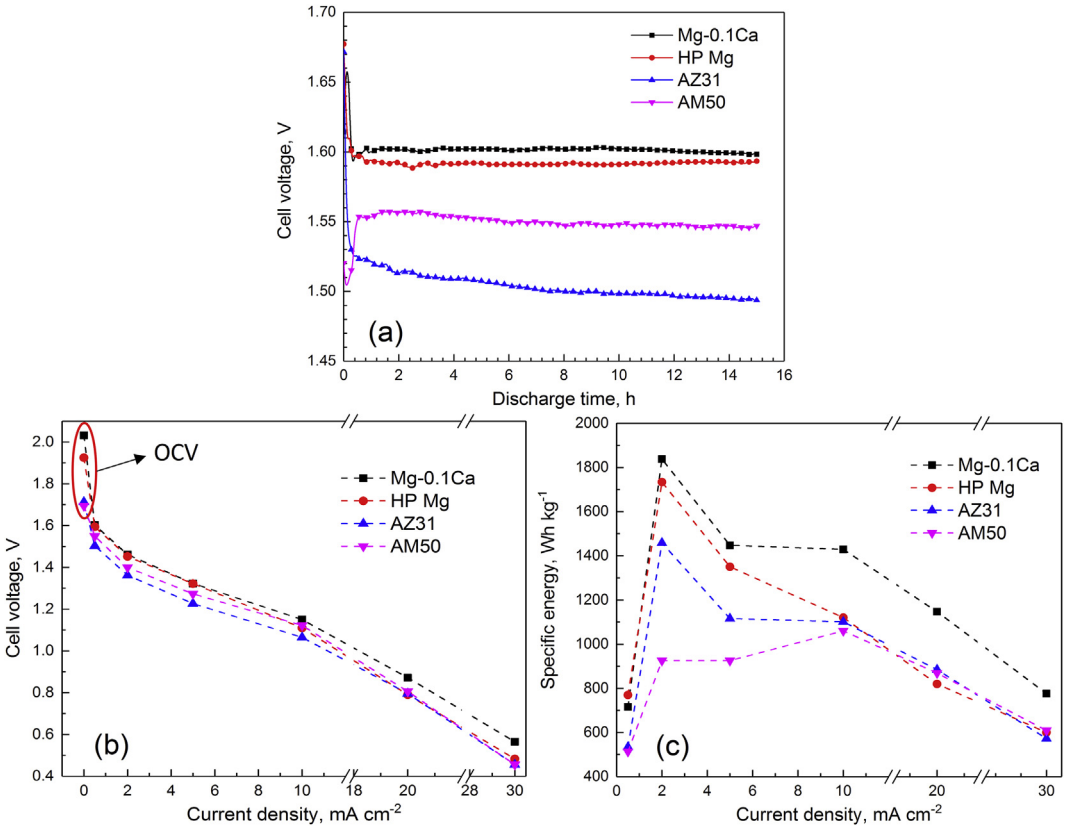

Fig. 8. Discharge properties of Mg-air batteries with different anodes: (a) discharge curves at current density of 0.5 mA cm^{-2}; (b) cell voltage at different current densities; (c) specific energy at different current densities. Electrolyte is 3.5 wt. % NaCl solution; Cathode is commercial air cathode with C/MnO_2 catalyst.

is limited. It is remarkable that many pits distribute uniformly on the surface of Mg-0.5Ca alloy after discharge (Fig. 6i). These pits are left by the preferential dissolution of Mg_2Ca phase that distributes evenly in grain interior. For Mg-Ca alloys with high Ca content, the surface morphologies after discharge are different and special, as shown in Fig. 6j–l. Some matrix phase has been partially dissolved, while some matrix phase is still complete. The continuously Mg_2Ca eutectic enclosing interdendritic regions (as shown in the inserted SEM images in Fig. 1d, f) has been preferentially dissolved, leaving some narrow cracks around these matrix phase. The dissolution of eutectic continues deeply and, unavoidably, promotes the undercutting of matrix phase, leading to the detachment of some undissolved grains. This is consistent with the corrosion mechanism of Mg-Ca alloys proposed by Jeong et al. [23]. Therefore, for Mg-Ca alloys with high Ca content, the "chunk effect" is severe, reducing the utilization efficiency of anodes. The detachment of undissolved grains leaves some holes on the surface of Mg-Ca alloys, as marked in Fig. 6j–l. In addition, the detachment of undissolved grains can also be observed clearly by SEM images of Mg-4Ca alloys after discharge at 10 mA cm^{-2} for 8 h, as shown in Fig. 7. The marked region in discharge products is confirmed to be Mg matrix pieces by the inserted EDX results. These undissolved metallic pieces have been detached from Mg anodes surface and would be dissolved independently. In conclusion, Mg-Ca alloys with low Ca content (0.1 wt. % and 0.5 wt. %) have high utilization efficiency and specific capacity because of the high self-corrosion resistance and limited impact of "chunk effect". Mg-Ca alloys with high Ca content show low self-corrosion resistance and severe "chunk effect", so that their utilization efficiencies and capacity are much lower.

3.5. Magnesium-air battery properties

In half-cell measurements, Mg-0.1Ca alloy shows best discharge potential and utilization efficiency among all Mg-Ca alloys. Therefore, we select Mg-0.1Ca alloy as the optimized Mg-Ca alloy and test its discharge properties as anode in full-assembled Mg-air battery. High purity Mg, AZ31 and AM50 alloys are also tested in the same Mg-air battery configuration for comparison. Fig. 8a shows the discharge curves of Mg-air batteries with different anodes at 0.5 mA cm^{-2}. At the initial stage of nearly half an hour, the voltage of Mg-air battery with Mg-0.1Ca anode decreases sharply, due to the accumulation of discharge products on the anode surface. Afterwards, the voltage keeps stable during the whole discharge process of more than 15 h. Fig. 8 also presents the discharge properties of Mg-air batteries with different Mg alloy anodes at different current densities, including cell voltage (Fig. 8b) and specific energy (Fig. 8c). Mg-air battery with Mg-0.1Ca alloy as anode exhibits higher cell voltage at all current densities than Mg-air batteries with other alloys as anode. The open circuit voltage (OCV) of Mg-air battery with Mg-0.1Ca anode can reach 2.032 V, which is higher than HP Mg (1.925 V) and also higher than that of Mg-Al-Pb anode (1.8 V) as tested by Wang et al. (3.5 wt. % NaCl as electrolyte, MnO_2 as cathode catalyst) [11]. At current density of 0.5 mA cm^{-2}, the cell voltage of Mg-air battery with Mg-0.1Ca as anode can reach 1.6 V. Besides, from Fig. 8c we can also see that Mg-0.1Ca alloy can supply higher specific energy than HP Mg and other magnesium alloys when serves as anode for Mg-air battery, especially at high current densities. The peak specific energy of Mg-0.1Ca alloy in Mg-air battery can be above 1800 Wh kg^{-1}. At current density of 10 mA cm^{-2}, its specific energy is 1429 Wh kg^{-1}, higher than that of Al anode after equal channel angular pressing (1096 Wh kg^{-1}) in Al-air system with 2 M NaCl as electrolyte as reported [48]. Accordingly, Mg-0.1Ca alloy can be a promising candidate for anode of Mg-air batteries. Besides, it is notewothy that the cell voltage and specific energy of HP Mg in Mg-air battery can be much higher than AZ31 and AM50 alloys and close to those of Mg-0.1Ca alloy. Interestingly, this situation just happens when discharging at low current densities. With increasing discharge current density, Mg-air battery with HP Mg as anode can just offer cell voltage and specific energy which are approximate to those of Mg-batteries with AZ31 and AM50 anodes, and much lower than that based on Mg-0.1Ca alloy. The reason for this phenomenon is still not clear and need to be studied further in the future.

4. Conclusions

In this work, the effect of Ca content on self-corrosion and discharge performance of magnesium is investigated. The chemical composition of Mg-Ca alloys is optimized for best half-cell discharge performance. Afterwards, the basic characteristics of Mg-air battery with optimized Mg-Ca alloy as anode are measured and compared to those based on high purity Mg (50 ppm Fe), AM50 and AZ31 alloys. As a result, the following conclusions can be drawn:

(1) The addition of Ca improves the discharge performance of magnesium, due to the high electrochemical activity of Ca and the induced grain refinement. However, with the increasing Ca content, discharge potential of Mg-Ca alloys becomes less negative and the utilization efficiency tends to be lower because of the increasing amount of Mg_2Ca phase. Mg-0.1Ca alloy shows best discharge potential, highest utilization efficiency and capacity among all prepared alloys.
(2) Mg-air battery with Mg-0.1Ca alloy as anode shows higher cell voltage and specific energy than those based on high purity Mg, AM50 and AZ31 alloys. The open circuit voltage of Mg-air battery based on Mg-0.1Ca alloy is up to 2.0 V and the cell voltage reaches 1.6 V at current density of 0.5 mA cm^{-2}. The peak specific energy of Mg-0.1Ca anode appears at current density from 2 to 10 mA cm^{-2} and reaches above 1800 Wh kg^{-1}.
(3) Mg-Ca alloys with appropriate low Ca content (e.g., 0.1 wt. %) are the promising candidates as anode material of Mg-air batteries.

Acknowledgements

The authors are grateful for the technical support of Eng. Ulrich Burmester and Eng. Volker Heitmann during the course of this work. M. Deng acknowledges the award of fellowship and funding from China Scholarship Council (201606370031). Additionally, Dr. D. Snihirova would like to acknowledge Humboldt foundation for Postdoctoral grant.

References

[1] Md Rahman, X. Wang, C. Wen, J. Electrochem. Soc. 160 (2013) A1759–A1771.
[2] A. Kraytsberg, Y. Ein-Eli, J. Power Sources 196 (2011) 886–893.
[3] Y. Li, H. Dai, Chem. Soc. Rev. 43 (2014) 5257–5275.
[4] T. Zhang, Z. Tao, J. Chen, Mater. Horiz. 1 (2014) 196–206.
[5] D.R. Egan, C. Ponce de León, R.J.K. Wood, R.L. Jones, K.R. Stokes, F.C. Walsh, J. Power Sources 236 (2013) 293–310.
[6] C.-S. Li, Y. Sun, F. Gebert, S.-L. Chou, Adv. Energy Mater. 7 (2017) 1700869.
[7] R. Mohtadi, F. Mizuno, Beilstein J. Nanotechnol. 5 (2014) 1291–1311.
[8] M. Yuasa, X. Huang, K. Suzuki, M. Mabuchi, Y. Chino, Mater. Trans. 55 (2014) 1202–1207.
[9] G. Huang, Y. Zhao, Y. Wang, H. Zhang, F. Pan, Mater. Lett. 113 (2013) 46–49.
[10] Y.D. Milusheva, R.I. Boukoureshtlieva, S.M. Hristov, A.R. Kaisheva, Bulg. Chem. Commun. 43 (2011) 42–47.
[11] N. Wang, R. Wang, C. Peng, B. Peng, Y. Feng, C. Hu, Electrochim. Acta 149 (2014) 193–205.
[12] L.Q. Wang, R.C. Wang, Y. Feng, M. Deng, N.G. Wang, J. Electrochem. Soc. 164 (2017) A438–A446.
[13] Y. Ma, N. Li, D. Li, M. Zhang, X. Huang, J. Power Sources 196 (2011) 2346–2350.
[14] Y. Lv, Y. Xu, D. Cao, J. Power Sources 196 (2011) 8809–8814.
[15] S. Yuan, H. Lu, Z. Sun, L. Fan, X. Zhu, W. Zhang, J. Electrochem. Soc. 163 (2016) A1181–A1187.
[16] T. Zheng, Y. Hu, Y. Zhang, S. Yang, F. Pan, Mater. Des. 137 (2018) 245–255.
[17] H. Xiong, K. Yu, X. Yin, Y. Dai, Y. Yan, H. Zhu, J. Alloy. Comp. 708 (2017) 652–661.
[18] J.G. Kim, Y.W. Kim, Mater. Corros. 52 (2001) 137–139.
[19] M. Yuasa, X. Huang, K. Suzuki, M. Mabuchi, Y. Chino, J. Power Sources 297 (2015) 449–456.
[20] C.L. Liu, Y.J. Wang, R.C. Zeng, X.M. Zhang, W.J. Huang, P.K. Chu, Corrosion Sci. 52 (2010) 3341–3347.

[21] N.T. Kirkland, N. Birbilis, J. Walker, T. Woodfield, G.J. Dias, M.P. Staiger, J. Biomed. Mater. Res. B Appl. Biomater. 95 (2010) 91–100.
[22] J.W. Seong, W.J. Kim, Acta Biomater. 11 (2015) 531–542.
[23] Y.S. Jeong, W.J. Kim, Corrosion Sci. 82 (2014) 392–403.
[24] S.E. Harandi, M. Mirshahi, S. Koleini, M.H. Idris, H. Jafari, M.R.A. Kadir, Mater. Res. 16 (2013) 11–18.
[25] R.-C. Zeng, W.-C. Qi, H.-Z. Cui, F. Zhang, S.-Q. Li, E.-H. Han, Corrosion Sci. 96 (2015) 23–31.
[26] J. Song, Z. Wang, Y. Huang, A. Srinivasan, F. Beckmann, K.U. Kainer, N. Hort, Metall. Mater. Trans. 46 (2015) 6003–6017.
[27] M. Mohedano, B.J.C. Luthringer, B. Mingo, F. Feyerabend, R. Arrabal, P.J. Sanchez-Egido, C. Blawert, R. Willumeit-Römer, M.L. Zheludkevich, E. Matykina, Surf. Coating. Technol. 315 (2017) 454–467.
[28] Y. Wan, G. Xiong, H. Luo, F. He, Y. Huang, X. Zhou, Mater. Des. 29 (2008) 2034–2037.
[29] D. Hoche, C. Blawert, S.V. Lamaka, N. Scharnagl, C. Mendis, M.L. Zheludkevich, Phys. Chem. Chem. Phys. 18 (2016) 1279–1291.
[30] D. Mercier, J. Swiatowska, S. Zanna, A. Seyeux, P. Marcus, J. Electrochem. Soc. 165 (2018) C42–C49.
[31] S.V. Lamaka, B. Vaghefinazari, D. Mei, R.P. Petrauskas, D. Höche, M.L. Zheludkevich, Corrosion Sci. 128 (2017) 224–240.
[32] M.C. Lin, C.Y. Tsai, J.Y. Uan, Corrosion Sci. 51 (2009) 2463–2472.
[33] Y.Y. Chen, T. Duval, U.D. Hung, J.W. Yeh, H.C. Shih, Corrosion Sci. 47 (2005) 2257–2279.
[34] L. Fan, H. Lu, J. Power Sources 284 (2015) 409–415.
[35] Y.C. Lee, A.K. Dahle, D.H. Stajohn, Metall. Mater. Trans. 31A (2000) 2895–2906.
[36] M. Mezbahul-Islam, A.O. Mostafa, M. Medraj, J. Mater. 2014 (2014) 1–33.
[37] V. Shkirskiy, A.D. King, O. Gharbi, P. Volovitch, J.R. Scully, K. Ogle, N. Birbilis, ChemPhysChem 16 (2015) 536–539.
[38] K.D. Ralston, N. Birbilis, C.H.J. Davies, Scripta Mater. 63 (2010) 1201–1204.
[39] H.S. Kim, G.H. Kim, H. Kim, W.J. Kim, Corrosion Sci. 74 (2013) 139–148.
[40] N.N. Aung, W. Zhou, Corrosion Sci. 52 (2010) 589–594.
[41] T. Zhang, Z. Ji, S. Wu, Mater. Des. 32 (2011) 2742–2748.
[42] A.D. Südholz, N.T. Kirkland, R.G. Buchheit, N. Birbilis, Electrochem. Solid State Lett. 14 (2011) C5–C7.
[43] David Linden, T.B. Reddy, Handbook of Batteries, McGraw-Hill, New York, 2002.
[44] S. Nakamura, H. Nishikawa, T. Aoki, Y. Ogami, J. Power Sources 186 (2009) 278–285.
[45] C. Daniel, J. Besenhard, Handbook of Battery Materials, Wiley-VCH, Weinheim, 2012.
[46] X. Yan, M. Hou, L. Sun, D. Liang, Q. Shen, H. Xu, P. Ming, B. Yi, Int. J. Hydrogen Energy 32 (2007) 4358–4364.
[47] N. Wang, R. Wang, C. Peng, Y. Feng, Corrosion Sci. 81 (2014) 85–95.
[48] L. Fan, H. Lu, J. Leng, Electrochim. Acta 165 (2015) 22–28.

5.2 Revealing the impact of second phase morphology on discharge properties of binary Mg-Ca anodes for primary Mg-air batteries

Paper 2: Revealing the impact of second phase morphology on discharge properties of binary Mg-Ca anodes for primary Mg-air batteries (published in Corrosion Science)

The motivation of this work was to investigate the effect of varied microstructures, specifically secondary phase morphologies, on corrosion and discharge properties of binary Mg-Ca anodes. Mg-0.5 wt.% Ca alloy, with a Ca content within the optimized composition range, was adopted as the studied material to ensure a relatively high fraction of second phase. Two alloys with different microstructures were prepared via casting followed by air-cooling and water-cooling respectively. The air-cooled alloy showed fine Mg_2Ca phase and impurity particles dispersing uniformly, while the water-cooled alloy exhibited relatively continuous Mg_2Ca phase distributed along the grain boundaries. Water-cooling enabled the alloy a lower corrosion rate due to uniform corrosion behavior and less impurity particles. Besides, Mg-air battery testing indicated the water-cooled anode had higher utilization efficiency and yielded boosted specific energy density than the air-cooled one. The different secondary phase morphologies affected the propagation of discharge cracks and the formation of chunks, leading to varied efficiency loss caused by chunk effect. Discharge cracks in the air-cooled anode tended to be larger and then connected with each other to promote the formation of undissolved chunks. By contrast, discharge cracks in the water-cooled anode exhibited a tendency of penetrating along grain boundaries because of the preferential dissolution of Mg_2Ca phase, leading to uniform discharge and, thus, less efficiency loss by chunk effect.

Corrosion Science 153 (2019) 225–235

Contents lists available at ScienceDirect

Corrosion Science

journal homepage: www.elsevier.com/locate/corsci

Revealing the impact of second phase morphology on discharge properties of binary Mg-Ca anodes for primary Mg-air batteries

Min Deng[a,*], Daniel Höche[a,b], Sviatlana V. Lamaka[a], Linqian Wang[a], Mikhail L. Zheludkevich[a,c]

[a] MagIC – Magnesium Innovation Centre, Helmholtz-Zentrum Geesthacht (HZG), 21502 Geesthacht, Germany
[b] Computational Material Design, Faculty of Mechanical Engineering, Helmut-Schmidt-University University of the Federal Armed Forces, 22043 Hamburg, Germany
[c] Institute of Materials Science, Faculty of Engineering, Kiel University, 24143 Kiel, Germany

ARTICLE INFO

Keywords:
Mg-air battery
Phase morphology
Self-corrosion
Intermittent discharge

ABSTRACT

Mg-0.5 (wt.%)Ca alloys with different microstructures are prepared through casting followed by different cooling rates. The impact of microstructure, especially second phase morphology, on self-corrosion and discharge performance of Mg-0.5Ca alloys is investigated. The water-cooled Mg-0.5Ca alloy shows a lower self-corrosion rate than the air-cooled one and enables the Mg-air cell to possess increased utilization efficiency and enhanced energy density. Intermittent discharge tests are performed to study the battery performance after no-discharge intervals. All results indicate that the water-cooled Mg-0.5Ca cast alloy could be a promising anode material for aqueous Mg-air batteries with long-term storage and under intermittent discharge.

1. Introduction

Aqueous primary Mg-air batteries have attracted attention for some time due to their high theoretical energy density (6.8 kW h kg^{-1} based on anode), discharge voltage (3.1 V), volumetric capacity of metallic Mg (3832 mA h cm^{-3}, vs. 2061 mA h cm^{-3} for Li) and relatively low cost [1–3]. Despite these advantageous characteristics, the spread of this technology is rather limited because of a number of critical obstacles related to the self-corrosion and discharge kinetics of metallic Mg-based anodes. A number of research works have been dedicated to overcoming the limitations of Mg-air batteries for practical applications, such as poor self-corrosion resistance and surface blockage of the anode. Performance boost for the primary Mg-air system can be achieved by developing novel Mg anodes [4–7] as well as tailoring electrolyte compositions [8–13]. During the past decades, several types of Mg alloys have been proposed for use in Mg-air systems, i.e., Mg-Al-Zn [14,15], Mg-Al-Pb [16], Mg-Al-Sn [17–19] and Mg-Li [20–22]. Nevertheless, the practical voltage and specific capacity of such systems are still much lower than the theoretical values. In addition, the Pb commonly used in Mg-Al-Pb alloys is harmful to the environment despite its positive impact on the discharge voltage of Mg-air batteries. Furthermore, in terms of Mg-Li anodes, quaternary or even quintenary alloys doped with several alloying elements, like Zn, Y, Ce or Al, are necessary to ensure both a high voltage and low self-corrosion rate. The large amount of alloying elements that have a higher density than Mg would decrease the gravimetric capacity of the Mg anodes and substantially reduce the technical tolerances, leading to a large increase in associated costs. In this context, novel binary Mg-Ca anodes with a minor amount of Ca (less than 0.5 wt.%) were proposed in our previous work [23], in which battery performance as a function of different anodes was compared. The results demonstrate the application potential of Mg-Ca anodes due to their superior discharge performance compared to that of high-purity Mg and some commercial magnesium alloys.

It is well known that the microstructure, including the grain size, second phase morphology and distribution, has a great effect on the corrosion resistance and electrochemical performance of Mg alloys. Therefore, microstructure tuning through various processing methods, e.g., heat treatment and plastic deformation, has become the most popular approach to improve the discharge properties of Mg anodes [15,24–27]. As demonstrated by Huang et al. [14], an as-rolled AZ31 anode shows a higher discharge activity and voltage than the as-cast material when acting as the anode for a Mg-air battery. Regarding Mg-Ca alloys, the impact of microstructure on corrosion resistance has been widely investigated, but most studies were performed on Mg-Ca alloys with high Ca contents (≥1 wt.%) and in biomedical solutions [28–31]. Jeong et al. [31] studied the effect of microstructural refinement on the corrosion resistance of Mg-Ca alloys by indirect extrusion. No improvement in the corrosion resistance for a Mg-0.4 wt.% Ca alloy in Hank's solution was found in this research, and they attributed this to

* Corresponding author at: Helmholtz-Zentrum Geesthacht, Max-Planck-Str. 1, 21502 Geesthacht, Germany.
E-mail address: Min.Deng@hzg.de (M. Deng).

https://doi.org/10.1016/j.corsci.2019.03.050
Received 9 January 2019; Received in revised form 29 March 2019; Accepted 31 March 2019
Available online 03 April 2019
0010-938X/

the competition between grain refinement and increased dislocation and twin densities.

Nevertheless, the influence of second phase morphology and distribution in Mg-Ca alloys with a low Ca content is still unclear. To the best of our knowledge, no research has revealed the effect of the microstructure on the discharge properties of Mg-Ca anodes for primary Mg-air systems. Therefore, the aim of this work is to investigate the effect of the microstructure, especially the second phase morphology and distribution, on the self-corrosion rate of binary Mg-Ca alloys as well as their capability as an anode material. In addition, the application prospect of Mg-Ca alloys is also studied when serving as anodes for aqueous Mg-air batteries with long storage times under intermittent discharge. The Mg-0.5 wt.%Ca alloy was chosen as the research object in this work to ensure a relatively high content of the second phase because the effect of the second phase morphology is the emphasis here. This composition is still in the range of the optimized alloy composition of binary Mg-Ca anode, i.e., Mg-(0.1˜ 0.5) wt.%Ca, as concluded in our previous work [23], which indicated only a slight difference between the discharge properties of Mg-0.1Ca and Mg-0.5Ca alloy anodes.

2. Experimental procedures

2.1. Materials preparation

Mg-0.5Ca alloys with nominal composition of Mg-0.5 wt.% Ca were prepared through conventional casting with a pure Mg ingot (99.96 wt. %) and pure Ca chips (99.0 wt. %). The raw materials were placed in a steel crucible protected by Ar and SF_6 mixed gas and then heated to 760 °C. Before casting, the melting metal was stirred for 5 min to ensure composition homogeneity. Afterwards, to obtain Mg-0.5Ca alloys with identical compositions but different microstructures, the melt was cast into two moulds with different cooling methods, i.e., in air and in water. The mould for air cooling was cylindrical with a diameter of 18 mm and a thickness of 10 mm, while the mould for water cooling was cylindrical with a diameter of 60 mm and a thickness of 6 mm. The bottom and top portions for each prepared ingot with a length of 20 mm were discarded due to the possible accumulation of impurities and oxide. Specimens for all experiments were extracted from the rest of the ingots after removing the surface oxide. The chemical composition of the prepared materials is presented in Table 1. Ca was detected with atomic absorption spectroscopy, while other elements were measured by optical emission spectrometry. The content of impurities, which have a substantial influence on Mg corrosion [13,32,33], were low and below their tolerance limitations. The two alloys that were air cooled and water cooled are referred to as AC and WC alloys, respectively.

2.2. Microstructure observation

The corresponding microstructures of the prepared alloys were characterized via optical microscopy (OM) and scanning electron microscopy (SEM). To obtain samples with a high quality, all the specimens embedded in epoxy were ground with 4000 grit silicon carbide paper followed by a polishing process with the assistance of a water-free SiO_2 oxide polishing suspension (OPS). All the specimens after polishing were immersed in ethanol and cleaned by ultrasonication. Afterwards, an acetic-picric acid solution was used for sample etching before optical microscopy analysis. The grain sizes were determined through the average grain intercept (AGI) method. In the case of both alloys, five pictures were collected with OM and then utilized to calculate the average grain size. Additionally, element analysis for second phase particles was carried out with energy dispersive X-ray spectrometry (EDX).

Table 1
Chemical composition of Mg-0.5Ca alloy (wt.%).

Material	Ca	Fe	Ni	Cu	Si	Mn	Al	Mg
Mg-0.5Ca	0.50	0.0015	0.0009	0.0016	0.011	0.033	< 0.01	Bal.

2.3. Immersion tests

The corrosion rates of the Mg-0.5Ca alloys were evaluated at a free corrosion potential and room temperature using the hydrogen collection method after immersion in a 3.5 wt.% NaCl solution. The experimental configuration used here is similar to that commonly used for studying Mg corrosion [17,34]. An inverted burette with a funnel covering the corroding sample was used to collect the evolved hydrogen during the immersion period. Each sample with a surface area of nearly 8 cm^2 was suspended and completely exposed in the solution through a fishing line and a plastic screw with a diameter of 2.5 mm. Crevice corrosion was avoided with this specimen configuration that was proposed by Shi et al. [35]. Before the hydrogen evolution test, each sample was ground with SiC sandpapers up to 1200 grit. The weight loss of each specimen after the immersion test was measured after removing the corrosion products in a diluted chromic acid solution (200 g L^{-1}). In addition, the surface morphology of each alloy after immersion for a short time was also recorded with SEM to study the origination and propagation of the corrosion. Before exposure to the solution, each sample was polished to remove most scratches. Samples after the hydrogen evolution measurement were also observed with SEM after removing the corrosion products.

2.4. Electrochemical impedance spectroscopy (EIS)

EIS measurements after discharge were performed with a potentiostat (Gamry, USA) to compare the discharge activity of the Mg-0.5Ca alloys. A typical three-electrode system was applied with the specimen serving as the working electrode. The reference and counter electrodes were saturated Ag/AgCl and Pt plates, respectively. After the specimens were ground with 1200 grit sandpaper, they were exposed to the solution with a working surface area of 1 cm^2. The samples were scanned from a high frequency (100 kHz) to a low frequency (0.01 Hz), and the sinusoidal excitation voltage was 10 mV rms. Three separate samples of each Mg-0.5Ca alloy were used for EIS measurement to ensure reproducibility.

2.5. Mg-air battery tests

A full cell constructed in the laboratory was used to compare the discharge properties of the magnesium-air system using the Mg-0.5Ca alloys as the anode. A conventional air cathode comprising a gas diffusion layer, a C/MnO_2 catalyst layer and a nickel mesh current collector layer was utilized. A 3.5 wt.% NaCl solution was adopted as the electrolyte. The working surface area of the anode for all discharge tests was approximately 2.5 cm^2. Discharge curves at different current densities, i.e., 2 mA cm^{-2} and 10 mA cm^{-2}, were recorded using a Gamry interface 1000 potentiostat. After discharge, the corrosion products on the anode surface were removed in a 200 g L^{-1} chromic acid solution. Afterwards, the specific energy density (based on the anode only) as well as the anode utilization efficiency were calculated. The following equations were used [36,37]:

$$\text{Utilization efficiency (\%)} = \frac{W_{theo}}{\Delta W} \times 100\% \quad (1)$$

$$\text{Specific energy density (Wh kg}^{-1}) = \frac{\int_0^t U \times I \times \Delta t}{\Delta W} \quad (2)$$

where U (V) represents the instantaneous cell voltage corresponding to discharge time t (h), I (A) is the applied current, ΔW (kg) represents the specific anode mass loss during each measurement, and W_{theo} (kg) is the theoretically consumed anode mass attributed to the faradaic

process. The value of ΔW was obtained via the measured weight of the specimens before the discharge test and after removal of the discharge products. The theoretical weight loss W_{theo} was obtained via the equation [38,39]:

$$W_{theo}\ (\mathrm{kg}) = \frac{I \times t}{F \times \sum (\frac{x_i \times n_i}{m_i})} \times \frac{1}{1000} \quad (3)$$

where F is the Faraday constant (26.8 Ah mol^{-1}) ; and m_i (g mol^{-1}), n_i and x_i are the atomic mass, number of exchanged electrons and mass fraction relevant to Mg and each alloying element, respectively.

Surface morphologies and corresponding corrosion sections of samples after discharge were recorded with SEM as well. In addition, an intermittent discharge test was also carried out for Mg-air batteries with both Mg-0.5Ca anodes at 2 mA cm^{-2}. In each cycle, the discharge process lasted for 10 h followed by a no-discharge period of 5 h. Five cycles were tested to evaluate the stability of Mg-Ca relevant batteries during long-term usage.

3. Results

3.1. Microstructure

Two different microstructures were obtained by the different cooling methods, as indicated by Fig. 1. The optical images (see Fig. 1(a, d)) show that water cooling slightly decreases (by ca. 16%) the grain size of this alloy compared to air cooling. The calculated grain size is 577 ± 180 μm for the AC alloy and 438 ± 53 μm for the WC alloy (average of three samples from different locations). Furthermore, the morphology and distribution of the second phase, which is generally an α-Mg/Mg_2Ca eutectic aggregate [23,40,41], also varied with different cooling methods, as demonstrated by the scanning electron microscopy images (see Fig. 1(b, c, e, f)). It is noteworthy that for both materials, the second phase morphology corresponding to the ingot horizontal plane and vertical plane are identical. For the AC material, a large number of fine second phase particles is distributed uniformly in the matrix. In contrast, for the WC material, except for a few second phase particles in the grain interior, most of the second phase is relatively continuous and is distributed along grain boundaries as dendrites. Nevertheless, the grain boundaries are not fully populated by the second phase because of its insufficient amount due to the relatively low Ca content. In other words, grains in the Mg-0.5Ca WC alloy are not completely surrounded by continuous second phases. Specimens from the centre and edge of the WC alloy ingot also exhibit the same second phase morphology, indicating good ingot homogeneity. The only difference is the slightly larger grain size of the specimen from the edge (485 ± 122 μm) compared to that from the ingot centre (381 ± 65 μm). In addition, except for the α-Mg/Mg_2Ca eutectic phase, some small impurity-rich particles with compositions of Mg-Ca-Si or Mg-Ca-Si-Fe are also found in both materials. This is consistent with the description on the microstructure of the Mg-0.8 wt.% Ca alloy by Mohedano et al. [41] and Mg-0.54 wt.% Ca alloy by Zeng et al. [42]. As shown in Fig. 1(g), the EDX results of points A and C, as marked in the SEM images, also prove the existence of Mg-Ca-Si particles. Mg-Ca-Si-Fe particles are not noted here because of their low quantity due to the low Fe content in both alloys. Particles B and D with larger sizes are regular α-Mg/Mg_2Ca eutectic phases, as shown by the EDX results.

3.2. Hydrogen evolution

Fig. 2 presents the hydrogen evolution results of the Mg-0.5Ca alloys obtained with different cooling methods. Two samples of both materials were tested in parallel under the same experimental conditions to ensure the reproducibility of the results. At the initial stage of immersion (nearly three hours), the WC alloy suffers a higher hydrogen

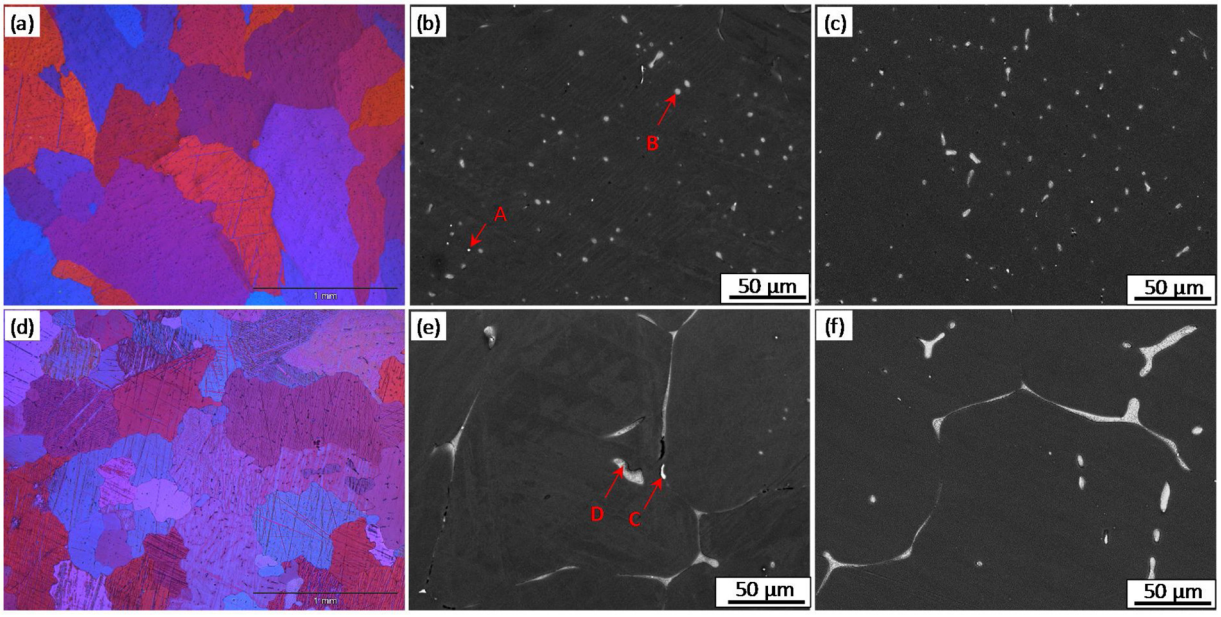

(g)

	Mg (wt.%)	Ca (wt.%)	Si (wt.%)
A	82.1	9.4	8.5
B	91.3	8.5	0.2
C	56.3	23.7	20.0
D	92.0	7.8	0.2

Fig. 1. Optical and SEM images of Mg-0.5Ca alloys: (a, b, c) AC; (d, e, f) WC. (b, e) SEM images of ingot horizontal plane; (c, f) SEM images of ingot vertical plane. Table g is the EDX results for particles marked A, B, C and D.

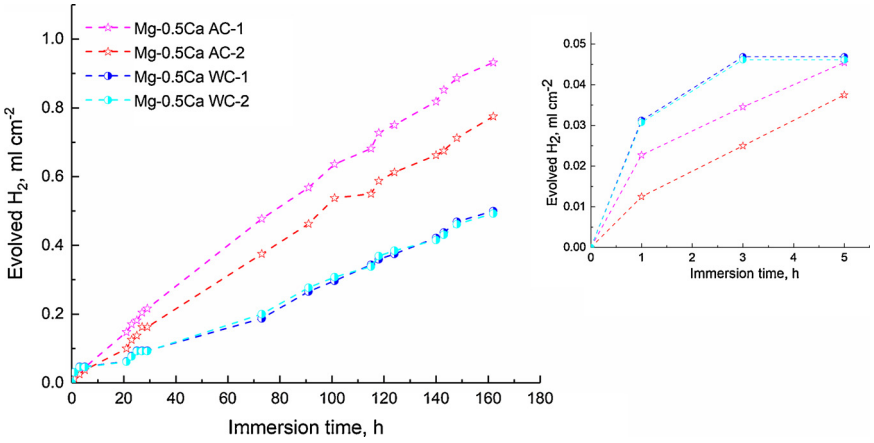

Fig. 2. Hydrogen evolution of Mg-0.5Ca alloys in 3.5 wt.% NaCl solution (unbuffered, pH 5.6).

evolution rate, indicating a faster corrosion rate than the AC alloy. Thereafter, the hydrogen evolution rate of the WC alloy slows down and is surpassed by that of the AC alloy. During the later immersion period, both materials show relatively stable hydrogen evolution rates. Concerning the whole 7-day immersion test, the WC alloy evolved less hydrogen than the AC alloy, showing that the former had a lower average corrosion rate than the latter in the 3.5 wt.% NaCl solution. With the hydrogen evolution rate, the self-corrosion rate of these two materials can be deduced according to the equation P_H (mm y^{-1}) = 2.088 V_H (ml cm^{-2} d^{-1}) [43]. The average corrosion rate obtained from hydrogen evolution data is 0.15 mm y^{-1} for the WC Mg-0.5Ca alloy and 0.26 mm y^{-1} for the AC material. It should be noted that the corrosion rate could be underestimated with the hydrogen evolution method, especially for Mg alloys with a high corrosion resistance [44,45]. In this case, corrosion rates of these alloys were also determined according to results of weight loss measurement via the conversion P_W (mm y^{-1}) = 2.1 ΔW (mg cm^{-2} d^{-1}) [43]. The measured corrosion rate is 0.20 mm y^{-1} for the WC alloy and 0.31 mm y^{-1} for the AC alloy, both are lower than the corrosion rate of most Mg alloys in similar solutions, as summarized by Cao and co-workers [46]. A low corrosion rate of the anodes during the no-discharge period is crucial for the aqueous primary Mg-air system to increase its service life. Therefore, the remarkably low overall corrosion rate enables Mg-0.5Ca alloys to be potential anode materials for primary Mg-air batteries in terms of long-term storage.

3.3. Mg-air battery properties

The cell voltage and specific energy density of the battery based on different Mg-0.5Ca anodes were tested and are presented in Fig. 3. A drastic difference is not found between the cell voltages of the electrochemical system with these two anode materials, except that the battery with AC anode shows gradually increasing voltage, while the voltage for that with WC material is relatively stable. Nevertheless, apparent differences can be found regarding the utilization efficiency as well as the specific energy density based on the anode materials during the discharge process (see Fig. 3b). The WC anode shows higher utilization efficiency than the AC anode at both current densities. Compared to that of the ordinary air cooling, the water cooling increases the utilization efficiency of the Mg-0.5Ca anode from 37.1%–44.5% at a low current density of 2 mA cm^{-2}. At a higher current density, i.e., 10 mA cm^{-2}, the increase in the utilization efficiency is less pronounced, approximately 5.7%. In the case of specific energy density, the variation is similar. The battery system based on the WC anode supplies a higher energy density than that based on the AC material, especially at lower current density.

The intermittent discharge behaviour of the batteries operating with the AC and WC alloy anodes at 2 mA cm^{-2} are presented in Fig. 4. Similar to the results presented in Fig. 3a, the cell voltage based on the AC anode increases gradually during every discharge period. However, its average voltage is found to decrease with increasing number of discharge cycles. For instance, the average voltage in the first discharge cycle is 1.506 V, while in the fifth discharge cycle it is 1.485 V. Such change is not as obvious for the intermittent discharge of the battery based on the WC anode. The average voltage is 1.499 V for the first discharge cycle, while it is 1.490 V for the fifth cycle. In other words, this battery system can maintain a stable voltage even after several closed/opened circuit cycles, which is important for the practical application of battery systems concerning sporadic switch-on and switch-off operation. In addition, the OCV of the battery with the AC anode is higher than that based on the WC anode in all intervals between the discharge processes.

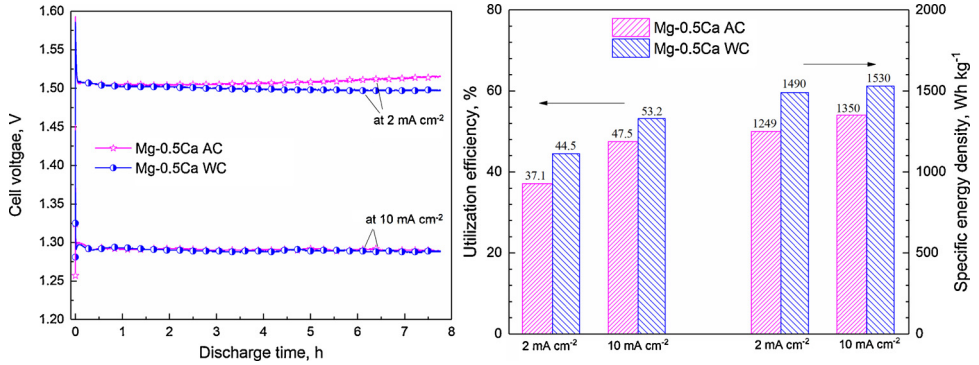

Fig. 3. Mg-air battery performance corresponding to Mg-0.5Ca anodes: (a) cell voltage; (b) utilization efficiency and energy density. 3.5 wt.% NaCl solution is adopted as the electrolyte, while C/MnO_2 acts as catalyst in the air cathode.

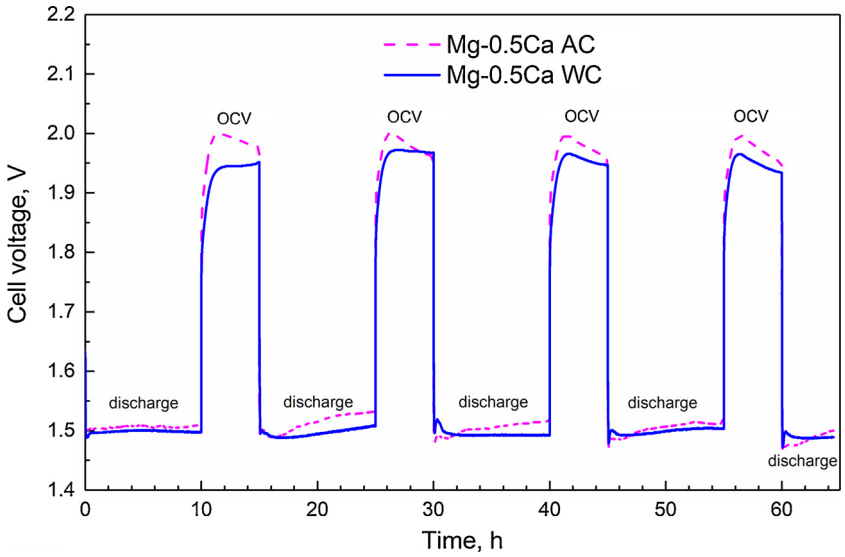

Fig. 4. Intermittent discharge curves of lab-made Mg-air cells adopting Mg-0.5Ca anodes with applied 2 mA cm^{-2} current density. 3.5 wt.% NaCl solution is adopted as the electrolyte, while C/MnO_2 acts as catalyst in the air cathode.

4. Discussion

4.1. Effect of microstructure on corrosion behaviour

It is well known that a faster solidification rate leads to finer grains due to the increased nucleation rate and decreased time for grain growth [47–49]. Therefore, the Mg-0.5Ca sample prepared with water cooling shows a smaller grain size than that prepared through air cooling. In addition, the solidification rate can also significantly affect the second phase morphology. For the alloy prepared with air cooling, the α-Mg solid solution is saturated with Ca atoms at a high temperature. During the slow solidification process, the Ca distributed uniformly in the Mg matrix and precipitated as Mg_2Ca particles due to the low solid solubility of calcium in a magnesium matrix at low temperature. By contrast, when prepared with water cooling, the faster cooling rate caused a greater segregation of the solute atoms [50] (Ca atoms in this study) and that led to the precipitation of Ca as a coarse α-Mg/Mg_2Ca eutectic structure.

The surface morphology after immersion for different times was recorded and is presented in Fig. 5 to demonstrate the dissolution process of the Mg-0.5Ca alloys. To observe the dissolution process at the very initial stage, diluted NaCl solution with a concentration of 0.5 wt.% was utilized. The surface morphologies after exposure in 0.5 wt.% NaCl solution for 5 min and 30 min are demonstrated in Fig. 5(a–d). It can be seen that the corrosion of both materials begins at some preferential points, in which impurity particles exist, as proven by the inserted EDX maps. This is reasonable because these impurity-rich particles have a large potential difference with the Mg matrix [41] and become the driving force for galvanic corrosion. Thereafter, the Mg_2Ca phases undergo corrosion due to their higher negative potential than the Mg matrix [30,51,52], which renders the Mg_2Ca to be the anode that preferentially undergoes corrosion in the micro-galvanic cell coupled with Mg matrix. After exposure to a 3.5 wt.% NaCl solution for 24 h, both Mg-0.5Ca alloys show surfaces covered with thin but compact oxide films with few micro-cracks, in addition to some coarse corrosion products in the sites that experienced galvanic corrosion (see Fig. 5e and f)). As reported, Ca-containing Mg alloys typically exhibit a protective calcium carbonate film on the surface after immersion [53]. Furthermore, the surface morphologies of both alloys after immersion for 7 days and removal of the corrosion products are also shown in Fig. 5g and h. Scratches left by the mechanical grinding are still apparent on the surface of both alloys even after 7 days of immersion, which is further evidence of the low self-corrosion rates of these two Mg-0.5Ca alloys prepared via different cooling routes. However, the AC alloy experienced localized corrosion to some extent, leaving a number of cavities and one corrosion strip on the surface, as shown in Fig. 5g. In contrast, the corrosion is more general and uniform on the WC alloy. The Mg_2Ca phases are still visible in the dendrites along the grain boundaries (see the inserted enlargement in Fig. 5h).

In conclusion, both the hydrogen evolution and surface morphologies indicate that the corrosion rates of Mg-0.5Ca alloys decrease after immersion for several hours due to the protective oxide/hydroxide film that formed on the alloy surface. The Mg-0.5Ca alloy processed with water cooling has a slower average corrosion rate than the AC alloy after a long immersion time, even though it reverses at the initial stage of several hours. Grain size is not the crucial factor for the different corrosion rates of the Mg-0.5Ca alloys because the grain refinement caused by water cooling is slight. Instead, the morphology and distribution of the second phases act as key factors for the various corrosion behaviours of the Mg-0.5Ca binary alloys. Concerning the initial exposure period in solution, the WC alloy shows a higher dissolution rate due to the presence of the continuous active Mg_2Ca phases along grain boundaries. Compared to the fine Mg_2Ca particles distributed uniformly in the AC alloy, the large second phases in the WC alloy expose a larger surface area of the anodic phases to the solution, leading to a faster overall hydrogen evolution rate. With increasing immersion time, the formation of a protective film suppresses the corrosion rates of both the WC and AC Mg-0.5Ca alloys. However, the corrosion rate of the AC material becomes higher than that of the WC material. This can be attributed to the propagation of pitting or localized corrosion caused by more impurity-rich particles and smaller Mg_2Ca particles in the AC alloy. As stated by Seong and Kim [54], there is a greater probability of isolated corrosion pits left by the dissolution of small Mg_2Ca particles that connect to form large and deep pits.

4.2. Effect of microstructure on utilization efficiency and energy density

The experimental results shown in the previous section indicate that both the utilization efficiency and energy density of the WC Mg-0.5Ca alloy are higher than those of the AC alloy at different current densities. Generally, the energy density of the Mg-air battery relates to the utilization efficiency of the electrodes as well as the cell voltage. In the case of this research, the battery voltage corresponding to the AC and WC alloy anodes has no significant difference, so the energy density

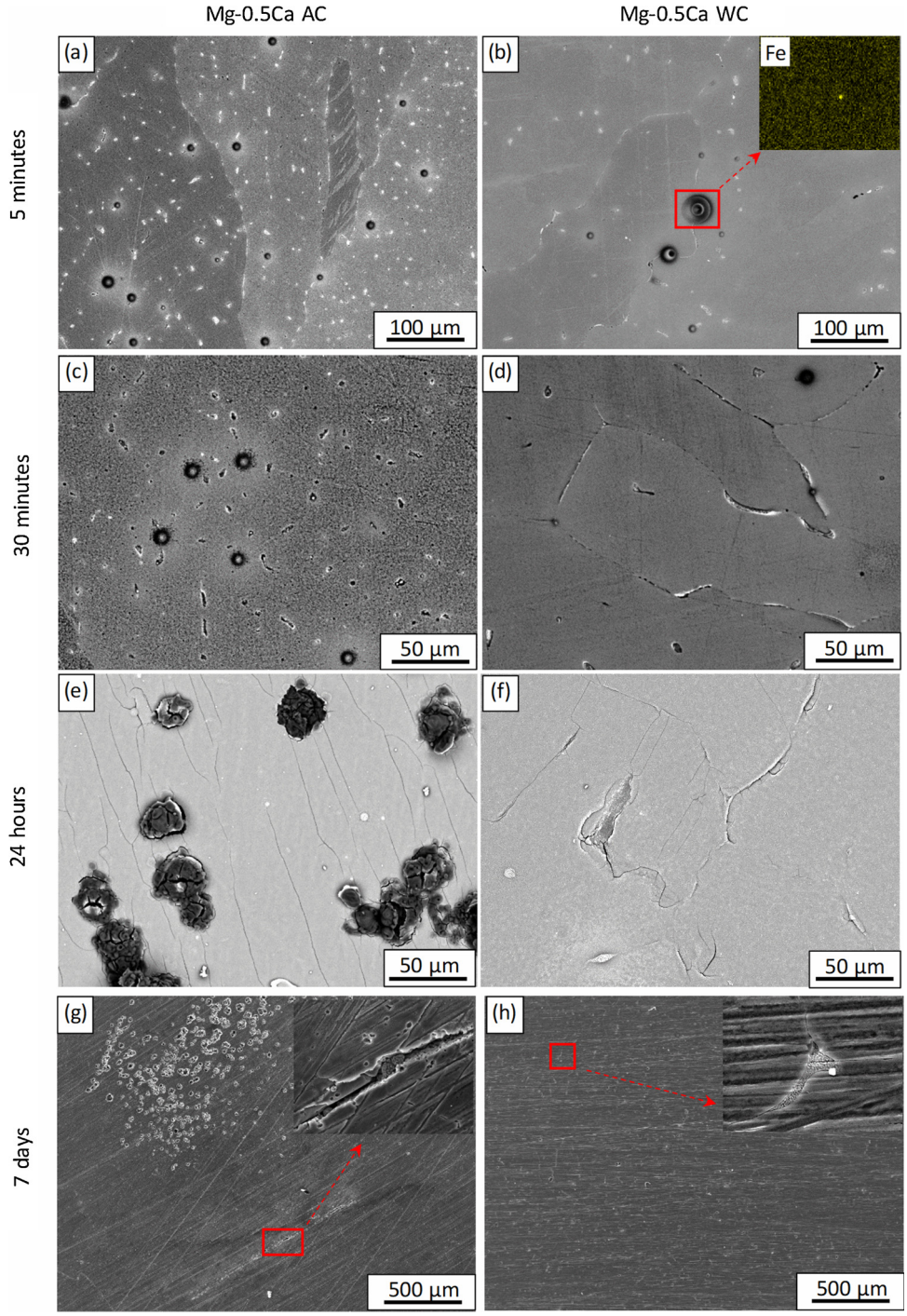

Fig. 5. Surface morphology of Mg-0.5Ca alloys after immersion for different time in: (a–d) 0.5 wt.% NaCl solution; (e–h) 3.5 wt.% NaCl solution. The surfaces after 7-days immersion are recorded after removing corrosion products. The inserted image in (b) is the EDX mapping for Fe, while in (g, h) it is corresponding enlargement of marked area.

depends only on the utilization efficiency of the anodes. According to Eq. (1), the utilization efficiency is inversely proportional to the actual weight loss of the anode during discharge. Actually, the weight loss during discharge consists of three parts, namely, the weight loss caused by impressed discharge current, the weight loss by self-corrosion of the Mg anodes and the weight loss due to the detachment of undissolved grains (known as the “chunk effect”) [16,23,55,56]. The chunk effect is also a kind of self-corrosion process occurring via different mechanisms. Therefore, the lower corrosion rate of the WC alloy measured in 3.5 wt. % NaCl solution at OCP could partly contribute to its higher utilization efficiency than that of the AC anode. To explore the contribution of the chunk effect, the surface morphologies of these two materials after discharge are shown in Fig. 6. It is remarkable that the surface of the AC anode after discharge and removal of the discharge products is rugged (see Fig. 6a), while the surface of the WC anode is more even in spite of some relatively small cavities (see Fig. 6b). From the cross-section presented in Fig. 6c, some undissolved grains can be found in the discharge product layer of the AC anode. These undissolved grains can detach from the anode surface into the solution along with the falling down of discharge products. In this way, they do not participate in the discharge process of Mg anodes and therefore decrease the utilization efficiency. In contrast, few undissolved grains can be found for the WC

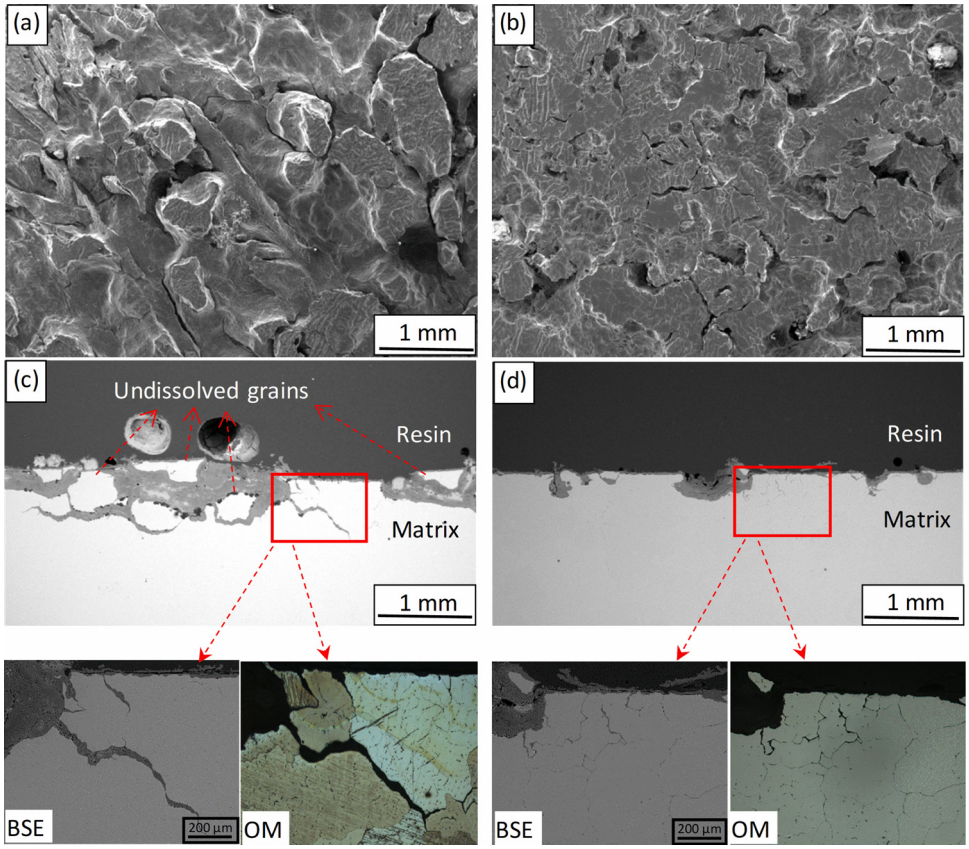

Fig. 6. Surface morphologies and cross sections of Mg-0.5Ca alloys (a, c) AC, (b, d) WC after discharge in 3.5 wt.% NaCl solution at 2 mA cm^{-2} for 16 h: (a, b) surface after removing discharge products; (c, d) cross-section with discharge products. Corresponding SEM and OM images of marked areas are also presented.

material (see Fig. 6d), indicating a slight impact of the chunk effect. In addition, for both anodes, there are some discharge cracks penetrating down into the anode substrate, as shown by the enlarged BSE images of the marked areas. These cracks or discharge channels are most likely along the grain boundaries, as demonstrated by the presented corresponding optical images. The discharge channels in the AC anode appear broad and shallow, while in the WC anode, the channels appear narrow and deep into the matrix.

To investigate the formation process of these two different discharge morphologies, the surfaces and corresponding cross-sections after discharge at 2 mA cm^{-2} for different times, i.e., 30 min, 2 h and 6 h, are presented in Fig. 7. For both Mg-0.5Ca alloys, discharge cracks appear after discharge for 30 min (see Fig. 7(a, b)). After that, these cracks show extraordinarily different propagation behaviours. In terms of the AC alloy, these cracks become large and deep with increasing discharge time (Fig. 7c). Gradually, these growing cracks connect with each other (Fig. 7e), and some matrix grains start to detach from the anode surface because of the connection of the large cracks (see cross-sections in Figs. 6 and 7). In the case of the WC anode, no large discharge cracks are found in Fig. 7(d, f). Instead, most of these discharge cracks prefer to penetrate deeply into the anode matrix along the grain boundaries (see Fig. 6d). Therefore, the surface after discharge is more even. The utilization efficiencies of these two anodes after discharge for different times are also calculated and presented in Fig. 8. A discussion of the difference between the calculated utilization efficiency after a 0.5-hour discharge is not meaningful since an experimental error may exist due to the small amount of weight loss after a short discharge. The changing utilization efficiency after long-term discharge deserves more discussion to evaluate the discharge behaviour of these two anode materials. The WC anode shows increased utilization efficiency from a 2-hour discharge to a 6-hour discharge, which could be attributed to the increased surface area after the discharge process. In principle, an increased surface area leads to a decreased applied current density, i.e., a weakened polarization. It is well known that Mg and Mg alloys under polarization suffer from fast self-corrosion because of the negative difference effect (NDE) [33,57,58]. The self-corrosion rate is related to the extent of polarization or anodic current density. A positive correlation relationship is expected. Therefore, to some extent, self-corrosion of the WC anode might decrease with prolonged discharge time due to the reduced current density caused by the increased surface area. After that, the WC anode can maintain a relatively stable utilization efficiency with increasing discharge time, owing to the balance between the slightly increased surface area and the weak chunk effect. By contrast, the utilization efficiency of the AC anode is similar to that of the WC anode after discharge for 2 h but becomes much lower after a long discharge period. This is most likely due to the emergence of a severe chunk effect after long-term discharge, as shown in Figs. 6 and 7. The positive effect of an increased surface area on the utilization efficiency is counteracted.

Based on the aforementioned discussion, a schematic illustration is proposed to describe the propagation of discharge cracks originating in the Mg-0.5Ca anodes, as shown in Fig. 9. Regarding the AC anode, crack propagation can be described as follows. (1) After application of the loading current, dissolution preferentially occurs along the grain boundaries because of the existence of active Mg_2Ca particles as well as the possibility of grain boundaries functioning as local anodes with respect to the Mg matrix [54,59,60]. Therefore, some discharge cracks originate underneath the anode surface. (2) Thereafter, because of the discontinuity of the Mg_2Ca particles, the extension of discharge cracks slows, and the dissolution develops towards the interior area of the Mg matrix, leading to shallow but spacious cracks. (3) With increasing discharge time, these large cracks connect with each other, resulting in separated grains in the centre of the cracks. These undissolved grains then detach from the anode surface and do not participate in the

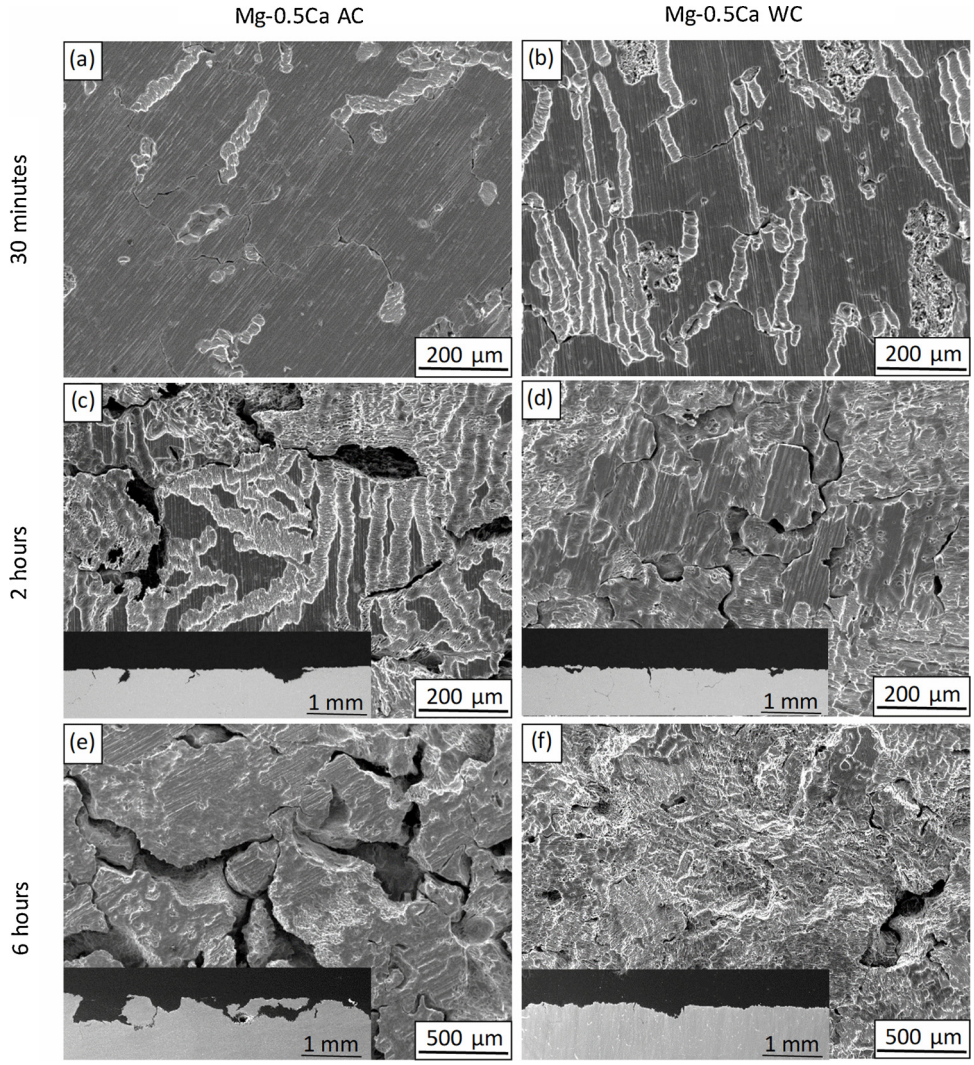

Fig. 7. Surface morphologies of Mg-0.5Ca alloys after discharge in 3.5 wt.% NaCl solution at 2 mA cm^{-2} for different time and removing discharge products. The inserted images are correspongding cross sections, in which the dark area is resin and the gray area is Mg substrate.

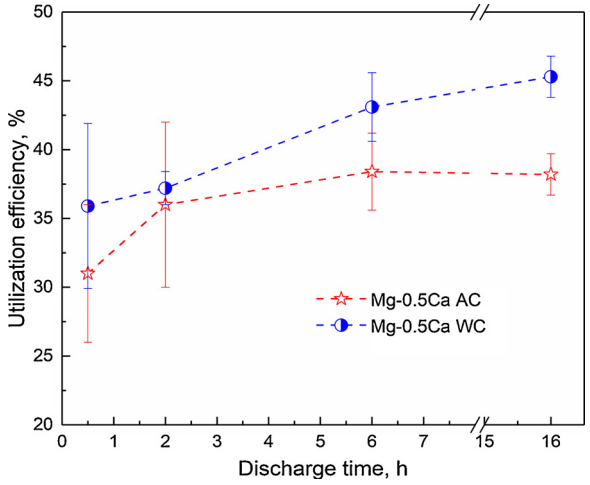

Fig. 8. Utilization efficiency of Mg-0.5Ca anodes relevant to differet discharge time in 3.5 wt.% NaCl solution at current density of 2 mA cm^{-2}.

discharge process. In the case of the WC anode, discharge cracks originate for the same reason. However, because the active Mg_2Ca phases are distributed relatively continuously along the grain boundaries, the cracks continue growing along the grain boundaries due to the preferential dissolution of the anodic second phases. In this case, the discharge cracks in the WC anode prefer to penetrate deep into the bulk anode instead of becoming spacious towards the interior area of the grains. It is worth noting that, in fact, grains in the WC Mg-0.5Ca anode are not completely surrounded by the α-Mg/Mg_2Ca eutectic (see Fig. 1(e, f)) because of the low content of Ca (volume fraction of second phase is not high enough). Therefore, most cracks that surround grains are not completely connected with each other. In other words, during discharge, most grains are not fully surrounded by cracks in every dimension because of the partially continuous second phases. These single grains can still keep contact with the bulk anode in some positions, contributing to the immobility of grains in the top layer. Consequently, the dissolution of the WC anode is uniform with little detachment of the grains. It was reported previously that in Mg-Ca anodes with a high Ca content, grains would detach from the anode matrix because of the preferential dissolution of Mg_2Ca phases fully surrounding these grains [23]. Note that these two propagation processes merely predominate in Mg-0.5C anodes prepared via air cooling and water cooling, respectively, which means they also happen in the other anode material to some extent.

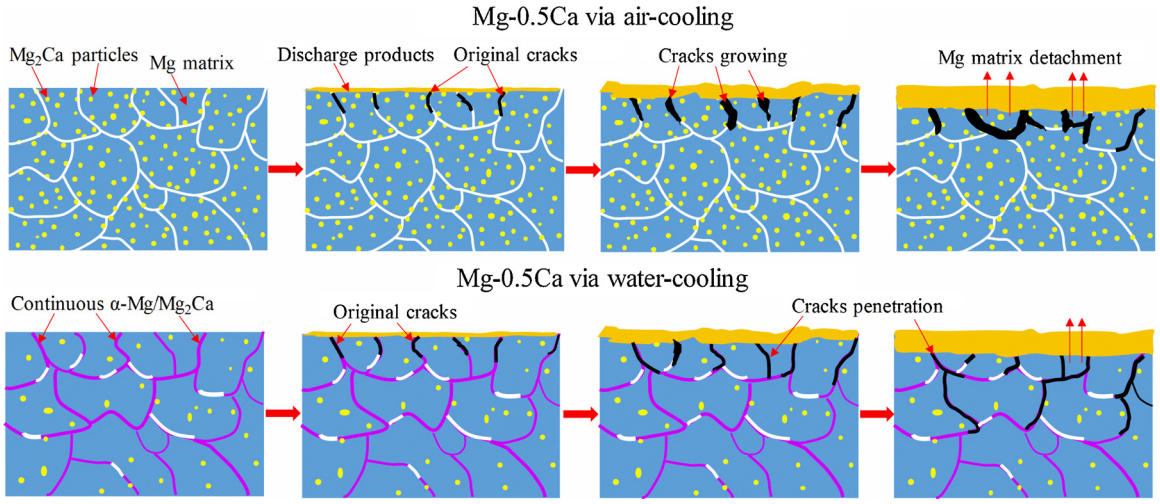

Fig. 9. Schematic illustration of the propagation process of discharge cracks in Mg-0.5Ca anodes.

4.3. Effect of microstructure on discharge voltage

The intermittent discharge curves show that the Mg-air cell utilizing the AC alloy as the anode has an enhanced OCV than that based on the WC anode, but their discharge voltages have no apparent difference. This result could be attributed to the different discharge activities of these two anodes that can be determined by EIS spectra measured after discharge. Fig. 10 shows EIS Nyquist plots of both anodes after discharge at 2 mA cm^{-2} for 1 h. The WC anode shows a lower resistance than the AC anode, indicating a higher dissolution activity (or lower overpotential) during discharge. Therefore, the battery system with the WC anode shows a similar cell voltage to that based on the AC anode. It is well known that a current or polarization applied to Mg anodes could cause a rupture of the oxide film on the metal surface [61,62]. Hence, with a low protection of the oxide film, the WC Mg-0.5Ca anode could exhibit higher dissolution activity owing to the relatively continuous α-Mg/Mg_2Ca phases. In addition, the unstable discharge voltage of the cell incorporating the AC alloy anode may be ascribed to the increasing surface area caused by the large discharge cracks.

5. Conclusions

In this work, Mg-0.5Ca alloys with various microstructures are prepared through different cooling routes. Afterwards, the effect of microstructure on the corrosion performance of Mg-0.5 wt.%Ca binary alloys is studied through immersion tests combined with surface morphology analysis. Moreover, the discharge properties of primary Mg-air batteries using Mg-0.5Ca alloy anodes are measured to study the influence of the microstructure. The following conclusions are obtained from this work:

(1) The Mg-0.5Ca air-cooled alloy shows fine Mg_2Ca particles dispersing uniformly in Mg matrix and grain boundaries. After water-cooling, the grain size of Mg-0.5Ca alloy decreases slightly, and the second phases are distributed relatively continuously along the grain boundaries. In addition, more impurity-rich particles are found in the air-cooled alloy.
(2) Both Mg-0.5Ca alloys show remarkably low overall corrosion rates, enabling them to be attractive anode materials for aqueous Mg-air batteries with long-term storage. The corrosion rate of the water-cooled alloy is lower than that of the air-cooled material, because of the greater general corrosion behaviour. The localized corrosion of the air-cooled alloy is due to a large number of fine Mg_2Ca particles and more impurity-rich particles.
(3) During discharge, the water-cooled Mg-0.5Ca anode has a higher utilization efficiency and specific energy density than the air-cooled anode, attributed to the lower corrosion rate and low amount of detached undissolved grains. Discharge cracks in the air-cooled anode tend to become larger and then promote the emergence of the chunk effect. By contrast, discharge cracks in the water-cooled anode tend to penetrate along grain boundaries, leading to uniform discharge.
(4) Mg-air batteries fabricated with these two Mg-0.5Ca anodes show similar cell voltages as a result of the higher OCV of the air-cooled anode and higher discharge activity of the water-cooled one. The water-cooled alloy could be a better anode material for Mg-air batteries under intermittent discharge due to the stable discharge voltage.

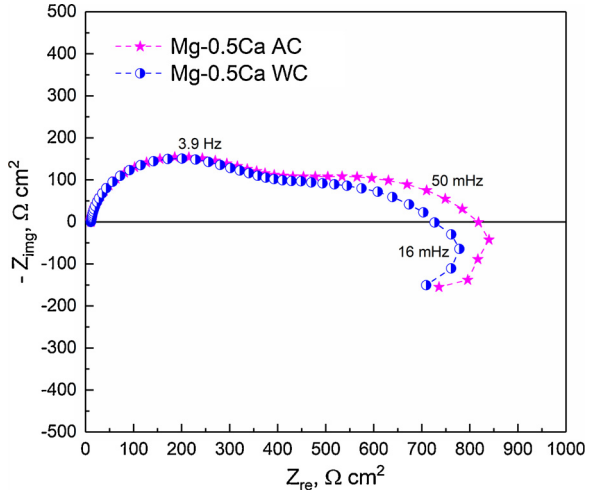

Fig. 10. Nyquist plots of the EIS spectra of Mg-0.5Ca anode after discharge at current density of 2 mA cm^{-2} for one hour in 3.5 wt.% NaCl solution.

Data availability

The raw/processed data required to reproduce these findings cannot be shared at this time as the data also forms part of an ongoing study.

Acknowledgements

The authors are grateful for the technical support from Eng. Ulrich Burmester and Eng. Volker Heitmann during the course of this work. Dr. Darya Snihirova and Bahram Vaghefinazari are sincerely

acknowledged for the suggestion on experimental setup and discussion on experimental results. Additionally, Min Deng and Linqian Wang are thankful to China Scholarship Council for the award of fellowship and funding No. 201606370031and No.201706370183.

References

[1] F. Cheng, J. Chen, Metal-air batteries: from oxygen reduction electrochemistry to cathode catalysts, Chem. Soc. Rev. 41 (2012) 2172–2192, https://doi.org/10.1039/c1cs15228a.

[2] T. Zhang, Z. Tao, J. Chen, Magnesium–air batteries: from principle to application, Mater. Horiz. 1 (2014) 196–206, https://doi.org/10.1039/c3mh00059a.

[3] M.A. Rahman, X. Wang, C. Wen, High energy density metal-air batteries: a review, J. Electrochem. Soc. 160 (2013) A1759–A1769, https://doi.org/10.1149/2.062310jes.

[4] R.P. Hamlen, E.C. Jerabek, J.C. Ruzzo, E.G. Siwek, Anodes for refuelable magnesium-air batteries, J. Electrochem. Soc. 116 (1969) 1588–1592, https://doi.org/10.1149/1.2411622.

[5] Y.D. Milusheva, R.I. Boukoureshtlieva, S.M. Hristov, A.R. Kaisheva, Environmentally-clean Mg-air electrochemical power sources, Bulgarian Chem. Commun. 43 (2011) 42–47.

[6] C. Li, F. Cheng, W. Ji, Z. Tao, J. Chen, Magnesium microspheres and nanospheres: Morphology-controlled synthesis and application in Mg/MnO2 batteries, Nano Res. 2 (2009) 713–721, https://doi.org/10.1007/s12274-009-9075-y.

[7] M. Curioni, The behaviour of magnesium during free corrosion and potentiodynamic polarization investigated by real-time hydrogen measurement and optical imaging, Electrochim. Acta 120 (2014) 284–292, https://doi.org/10.1016/j.electacta.2013.12.109.

[8] D. Hoche, S.V. Lamaka, B. Vaghefinazari, T. Braun, R.P. Petrauskas, M. Fichtner, M.L. Zheludkevich, Performance boost for primary magnesium cells using iron complexing agents as electrolyte additives, Sci. Rep. 8 (2018) 7578, https://doi.org/10.1038/s41598-018-25789-8.

[9] Y. Li, J. Ma, G. Wang, F. Ren, Y. Zhu, Investigation of sodium phosphate and sodium dodecylbenzenesulfunate as electrolyte additives for AZ91 magnesium-air battery, J. Electrochem. Soc. 165 (2018) A1713–A1717, https://doi.org/10.1149/2.0581809jes.

[10] M.A. Deyab, Decyl glucoside as a corrosion inhibitor for magnesium–air battery, J. Power Sources 325 (2016) 98–103, https://doi.org/10.1016/j.jpowsour.2016.06.006.

[11] M. Mayilvel Dinesh, K. Saminathan, M. Selvam, S.R. Srither, V. Rajendran, K.V.I.S. Kaler, Water soluble graphene as electrolyte additive in magnesium-air battery system, J. Power Sources 276 (2015) 32–38, https://doi.org/10.1016/j.jpowsour.2014.11.079.

[12] Y. Zhao, G. Huang, C. Zhang, C. Peng, F. pan, Effect of phosphate and vanadate as electrolyte additives on the performance of Mg-air batteries, Mater. Chem. Phys. 218 (2018) 256–261, https://doi.org/10.1016/j.matchemphys.2018.07.037.

[13] S.V. Lamaka, B. Vaghefinazari, D. Mei, R.P. Petrauskas, D. Höche, M.L. Zheludkevich, Comprehensive screening of Mg corrosion inhibitors, Corros. Sci. 128 (2017) 224–240, https://doi.org/10.1016/j.corsci.2017.07.011.

[14] G. Huang, Y. Zhao, Y. Wang, H. Zhang, F. Pan, Performance of Mg–air battery based on AZ31 alloy sheet with twins, Mater. Lett. 113 (2013) 46–49, https://doi.org/10.1016/j.matlet.2013.09.041.

[15] M. Yuasa, X. Huang, K. Suzuki, M. Mabuchi, y. Chino, Effects of microstructure on discharge behavior of AZ91 alloy as anode for Mg-air battery, Mater. Trans. 55 (2014) 1202–1207, https://doi.org/10.2320/matertrans.MC201403.

[16] Y. Feng, W. Xiong, J. Zhang, R. Wang, N. Wang, Electrochemical discharge performance of the Mg–Al–Pb–Ce–Y alloy as the anode for Mg–air batteries, J. Mater. Chem. A 4 (2016) 8658–8668, https://doi.org/10.1039/c6ta02574a.

[17] T. Zheng, Y. Hu, Y. Zhang, S. Yang, F. Pan, Composition optimization and electrochemical properties of Mg-Al-Sn-Mn alloy anode for Mg-air batteries, Mater. Des. 137 (2018) 245–255, https://doi.org/10.1016/j.matdes.2017.10.031.

[18] H. Xiong, K. Yu, X. Yin, Y. Dai, Y. Yan, H. Zhu, Effects of microstructure on the electrochemical discharge behavior of Mg-6wt%Al-1wt%Sn alloy as anode for Mg-air primary battery, J. Alloys Compd. 708 (2017) 652–661, https://doi.org/10.1016/j.jallcom.2016.12.172.

[19] S. Yuan, H. Lu, Z. Sun, L. Fan, X. Zhu, Wei Zhang, Electrochemical performance of Mg-3Al modified with Ga, In and Sn as anodes for Mg-air battery, J. Electrochem. Soc. 163 (2016) A1181–A11187, https://doi.org/10.1149/2.0371607jes.

[20] N. Wang, R. Wang, Y. Feng, W. Xiong, J. Zhang, M. Deng, Discharge and corrosion behaviour of Mg-Li-Al-Ce-Y-Zn alloy as the anode for Mg-air battery, Corros. Sci. 112 (2016) 13–24, https://doi.org/10.1016/j.corsci.2016.07.002.

[21] Y. Ma, N. Li, D. Li, M. Zhang, X. Huang, Performance of Mg–14Li–1Al–0.1Ce as anode for Mg-air battery, J. Power Sources 196 (2011) 2346–2350, https://doi.org/10.1016/j.jpowsour.2010.07.097.

[22] X. Liu, S. Liu, J. Xue, Dishcarge performance of the magnesium anodes with different phase constitutions for Mg-air batteries, J. Power Sources 396 (2018) 667–674, https://doi.org/10.1016/j.jpowsour.2018.06.085.

[23] M. Deng, D. Hoeche, S.V. Lamaka, D. Snihirova, M. Zheludkevich, Mg-Ca binary alloys as anodes for primary Mg-air batteries, J. Power Sources 396 (2018) 109–118, https://doi.org/10.1016/j.jpowsour.2018.05.090.

[24] N. Wang, R. Wang, C. Peng, Y. Feng, Enhancement of the discharge performance of AP65 magnesium alloy anodes by hot extrusion, Corros. Sci. 81 (2014) 85–95, https://doi.org/10.1016/j.corsci.2013.12.005.

[25] N. Wang, R. Wang, C. Peng, Y. Feng, B. Chen, Effect of hot rolling and subsequent annealing on electrochemical discharge behavior of AP65 magnesium alloy as anode for seawater activated battery, Corros. Sci. 64 (2012) 17–27, https://doi.org/10.1016/j.corsci.2012.06.024.

[26] L. Wang, R. Wang, Y. Feng, M. Deng, N. Wang, Effect of heat treatment on electrochemical properties of Mg–9 wt.%Al–2.5 wt.%Pb alloy in sodium chloride solution, JOM 69 (2017) 2467–2470, https://doi.org/10.1007/s11837-017-2276-z.

[27] B. Campillo, C. Rodriguez, J. Genesca, O. Flores, L. Martinez, Effect of heat treatment on the efficiency of Mg anodes, J. Mater. Eng. Perform. 6 (1997) 449–453, https://doi.org/10.1007/s11665-997-0115-z.

[28] M.H. Idris, H. Jafari, S.E. Harandi, M. Mirshahi, S. Koleyni, Characteristics of As-cast and forged biodegradable Mg-Ca binary alloy immersed in kokubo simulated body fluid, Adv. Mater. Res. 445 (2012) 301–306, https://doi.org/10.4028/www.scientific.net/AMR.445.301.

[29] S. Koleini, M.H. Idris, H. Jafari, Influence of hot rolling parameters on microstructure and biodegradability of Mg–1Ca alloy in simulated body fluid, Mater. Des. 33 (2012) 20–25, https://doi.org/10.1016/j.matdes.2011.06.063.

[30] J.W. Seong, W.J. Kim, Development of biodegradable Mg-Ca alloy sheets with enhanced strength and corrosion properties through the refinement and uniform dispersion of the Mg(2)Ca phase by high-ratio differential speed rolling, Acta Biomater. 11 (2015) 531–542, https://doi.org/10.1016/j.actbio.2014.09.029.

[31] Y.S. Jeong, W.J. Kim, Enhancement of mechanical properties and corrosion resistance of Mg–Ca alloys through microstructural refinement by indirect extrusion, Corros. Sci. 82 (2014) 392–403, https://doi.org/10.1016/j.corsci.2014.01.041.

[32] D. Hoche, C. Blawert, S.V. Lamaka, N. Scharnagl, C. Mendis, M.L. Zheludkevich, The effect of iron re-deposition on the corrosion of impurity-containing magnesium, Phys. Chem. Chem. Phys. 18 (2016) 1279–1291, https://doi.org/10.1039/c5cp05577f.

[33] G.L. Song, A. Atrens, Corrosion mechanisms of magnesium alloys, Adv. Eng. Mater. 1 (1999) 11–33, https://doi.org/10.1002/(SICI)1527-2648(199909)1:1<11::AID-ADEM11>3.0.CO;2-N.

[34] G.L. Song, A. Atrens, D. StJohn, An hydrogen evolution method for the estimation of the corrosion rate of magnesium alloys, Magnesium Technol. (2001) 255–262, https://doi.org/10.1002/9781118805497.ch44.

[35] Z. Shi, A. Atrens, An innovative specimen configuration for the study of Mg corrosion, Corros. Sci. 53 (2011) 226–246, https://doi.org/10.1016/j.corsci.2010.09.016.

[36] M. Yuasa, X. Huang, K. Suzuki, M. Mabuchi, Y. Chino, Discharge properties of Mg–Al–Mn–Ca and Mg–Al–Mn alloys as anode materials for primary magnesium–air batteries, J. Power Sources 297 (2015) 449–456, https://doi.org/10.1016/j.jpowsour.2015.08.042.

[37] L. Fan, H. Lu, The effect of grain size on aluminum anodes for Al–air batteries in alkaline electrolytes, J. Power Sources 284 (2015) 409–415, https://doi.org/10.1016/j.jpowsour.2015.03.063.

[38] M.C. Lin, C.Y. Tsai, J.Y. Uan, Electrochemical behaviour and corrosion performance of Mg–Li–Al–Zn anodes with high Al composition, Corros. Sci. 51 (2009) 2463–2472, https://doi.org/10.1016/j.corsci.2009.06.036.

[39] Y.Y. Chen, T. Duval, U.D. Hung, J.W. Yeh, H.C. Shih, Microstructure and electrochemical properties of high entropy alloys—a comparison with type-304 stainless steel, Corros. Sci. 47 (2005) 2257–2279, https://doi.org/10.1016/j.corsci.2004.11.008.

[40] Z. Li, X. Gu, S. Lou, Y. Zheng, The development of binary Mg-Ca alloys for use as biodegradable materials within bone, Biomaterials 29 (2008) 1329–1344, https://doi.org/10.1016/j.biomaterials.2007.12.021.

[41] M. Mohedano, B.J.C. Luthringer, B. Mingo, F. Feyerabend, R. Arrabal, P.J. Sanchez-Egido, C. Blawert, R. Willumeit-Römer, M.L. Zheludkevich, E. Matykina, Bioactive plasma electrolytic oxidation coatings on Mg-Ca alloy to control degradation behaviour, Surf. Coat. Technol. 315 (2017) 454–467, https://doi.org/10.1016/j.surfcoat.2017.02.050.

[42] R.-C. Zeng, W.-C. Qi, H.-Z. Cui, F. Zhang, S.-Q. Li, E.-H. Han, In vitro corrosion of as-extruded Mg–Ca alloys—The influence of Ca concentration, Corros. Sci. 96 (2015) 23–31, https://doi.org/10.1016/j.corsci.2015.03.018.

[43] Z. Qiao, Z. Shi, N. Hort, N.I. Zainal Abidin, A. Atrens, Corrosion behaviour of a nominally high purity Mg ingot produced by permanent mould direct chill casting, Corros. Sci. 61 (2012) 185–207, https://doi.org/10.1016/j.corsci.2012.04.030.

[44] N.T. Kirkland, N. Birbilis, M.P. Staiger, Assessing the corrosion of biodegradable magnesium implants: a critical review of current methodologies and their limitations, Acta Biomater. 8 (2012) 925–936, https://doi.org/10.1016/j.actbio.2011.11.014.

[45] A. Atrens, G.-L. Song, F. Cao, Z. Shi, P.K. Bowen, Advances in Mg corrosion and research suggestions, J. Magnes. Alloy 1 (2013) 177–200, https://doi.org/10.1016/j.jma.2013.09.003.

[46] F. Cao, Z. Shi, G.-L. Song, M. Liu, A. Atrens, Corrosion behaviour in salt spray and in 3.5% NaCl solution saturated with Mg(OH)2 of as-cast and solution heat-treated binary Mg–X alloys: X = Mn, Sn, Ca, Zn, Al, Zr, Si, Sr, Corros. Sci. 76 (2013) 60–97, https://doi.org/10.1016/j.corsci.2013.06.030.

[47] Y.L. Liu, S.B. Kang, Solidification and segregation of AI-Mg alloys and influence of alloy composition and cooling rate, Mater. Sci. Technol. 13 (1997) 331–336, https://doi.org/10.1179/mst.1997.13.4.331.

[48] G.Y. Yuan, Z.L. Liu, Q.D. Wang, W.J. Ding, Microstructure refinement of Mg–Al–Zn–Si alloys, Mater. Lett. 56 (2002) 53–58, https://doi.org/10.1016/S0167-577X(02)00417-2.

[49] A. Singh, Y. Osawa, H. Somekawa, T. Mukai, Effect of solidification cooling rate on microstructure and mechanical properties of an extruded Mg-Zn-Y alloy, Metals 8 (2018) 337, https://doi.org/10.3390/met8050337.

[50] G. Song, A. Atrens, M. Dargusch, Influence of microstructure on the corrosion of diecast AZ91D, Corros. Sci. 41 (1998) 249–273, https://doi.org/10.1016/S0010-

938X(98)00121-8.
[51] A.D. Südholz, N.T. Kirkland, R.G. Bucheheit, N. Birbilis, Electrochemical properties of intermetallic phases and common impurity elements in Mg alloys, Electrochem. Solid-State Lett. 14 (2011) C5–C7, https://doi.org/10.1149/1.3523229.
[52] N.T. Kirkland, N. Birbilis, J. Walker, T. Woodfield, G.J. Dias, M.P. Staiger, In-vitro dissolution of magnesium-calcium binary alloys: clarifying the unique role of calcium additions in bioresorbable magnesium implant alloys, J. Biomed. Mater. Res. B Appl. Biomater. 95 (2010) 91–100, https://doi.org/10.1002/jbm.b.31687.
[53] M. Mandal, A.P. Moon, G. Deo, C.L. Mendis, K. Mondal, Corrosion behavior of Mg–2.4Zn alloy micro-alloyed with Ag and Ca, Corros. Sci. 78 (2014) 172–182, https://doi.org/10.1016/j.corsci.2013.09.012.
[54] J.W. Seong, W.J. Kim, Mg-Ca binary alloy sheets with Ca contents of ≤1 wt.% with high corrosion resistance and high toughness, Corros. Sci. 98 (2015) 372–381, https://doi.org/10.1016/j.corsci.2015.05.068.
[55] M. Andrei, Dd. Gabriele, P.L. Bonora, D. Scantlebury, Corrosion behaviour of magnesium sacrificial in tap water, Mater. Corros. 54 (2003) 5–11, https://doi.org/10.1002/maco.200390010.
[56] G.A. Marsh, E. Schaschl, The difference effect and the chunk effect, J. Electrochem. Soc. 107 (1960) 960–965, https://doi.org/10.1149/1.2427579.
[57] G. Song, A. Atrens, D. Stjohn, J. Nairn, Y. Li, The electrochemical corrosion of pure magnesium in 1 N NaCl, Corros. Sci. 39 (1997) 855–875, https://doi.org/10.1016/S0010-938X(96)00172-2.
[58] R. Glicksman, The performance of zinc, magnesium and aluminum primary cell anodes. A review, J. Electrochem. Soc. 106 (1959) 457–464, https://doi.org/10.1149/1.2427380.
[59] N. Birbilis, K.D. Ralston, S. Virtanen, H.L. Fraser, C.H.J. Davies, Grain character influences on corrosion of ECPAed pure magnesium, Corros. Eng. Sci. Technol. 45 (2010) 224–230, https://doi.org/10.1179/147842209X12559428167805.
[60] D. Song, A. Ma, J. Jiang, P. Lin, D. Yang, J. Fan, Corrosion behavior of equal-channel-angular-pressed pure magnesium in NaCl aqueous solution, Corros. Sci. 52 (2010) 481–490, https://doi.org/10.1016/j.corsci.2009.10.004.
[61] N. Munichandraiah, Electrochemical impedance studies of a decade-aged magnesium/manganese dioxide primary cell, J. Appl. Electrochem. 29 (1999) 463–471.
[62] N. Sato, Anodic breakdown of passive films on metals, J. Electrochem. Soc. 129 (1982) 255–260, https://doi.org/10.1149/1.2123808.

5.3 Clarifying the decisive factors for utilization efficiency of Mg anodes for primary aqueous batteries

Paper 3: Clarifying the decisive factors for utilization efficiency of Mg anodes for primary aqueous batteries (published in Journal of Power Sources)

The emphasis of the work presented in this paper is to clarify the individual effect of different factors, i.e. corrosion at OCP, self-corrosion under polarization and chunk effect, on anode utilization efficiency for purpose of gaining more information concerning the design of Mg alloy anodes for battery system with high energy density and long service life. Anodic efficiencies of several Mg anodes at different current densities were measured in 3.5 wt.% NaCl electrolyte. The contribution of self-corrosion at OCP and at constant applied current to efficiency of Mg anodes were compared. Additionally, the efficiency loss caused by chunk effect (CE) was determined with a proposed new approach. The effect of self-corrosion and CE on anodic efficiency were assessed accordingly. The results indicated that self-corrosion rates determined at OCP cannot be utilized to estimate the utilization efficiency of Mg anodes during discharge, because the real-time self-corrosion was dependent on the applied discharge current density. The occurrence of CE was derived from a large fraction of secondary phases and non-uniform dissolution of Mg anodes. It can also result in a large efficiency loss of Mg anodes, especially at low current densities, which, in some cases, could exceed the loss caused by self-corrosion of anode substrate. Hence, regarding the design of Mg alloy anodes for high energy density batteries, attention should be paid to both aspects, particularly for application in long-term low-power battery system. In this context, micro-alloyed Mg-Ca anodes with high corrosion resistance could be a feasible approach.

Journal of Power Sources 441 (2019) 227201

Contents lists available at ScienceDirect

Journal of Power Sources

journal homepage: www.elsevier.com/locate/jpowsour

Clarifying the decisive factors for utilization efficiency of Mg anodes for primary aqueous batteries

Min Deng [a,*], Linqian Wang [a], Daniel Höche [a,b], Sviatlana V. Lamaka [a], Darya Snihirova [a], Bahram Vaghefinazari [a], Mikhail L. Zheludkevich [a,c]

[a] MagIC – Magnesium Innovation Centre, Helmholtz-Zentrum Geesthacht (HZG), 21502, Geesthacht, Germany
[b] Computational Material Design, Faculty of Mechanical Engineering, Helmut-Schmidt-University University of the Federal Armed Forces, 22043, Hamburg, Germany
[c] Institute of Materials Science, Faculty of Engineering, Kiel University, 24143, Kiel, Germany

HIGHLIGHTS

- Real-time self-corrosion rate of Mg anodes during discharge was determined.
- Anodic efficiency loss of different Mg anodes due to "chunk effect" was calculated.
- Increasing rate of self-corrosion versus current density depends on alloy category.
- "Chunk effect" significantly reduces the anodic efficiency of Mg anodes.

GRAPHICAL ABSTRACT

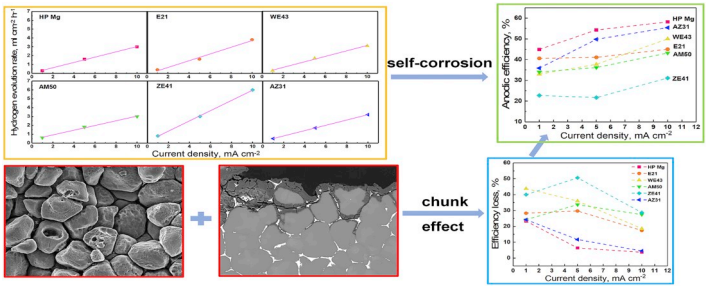

ARTICLE INFO

Keywords:
Mg batteries
Anodic efficiency
Self-corrosion
Chunk effect

ABSTRACT

Low anodic efficiency of metallic Mg, which results in low discharge capacity and specific energy density, hinders the wider application of aqueous primary Mg batteries. In this work, we clarify the decisive factors effecting the utilization efficiency of Mg anodes. Anodic efficiency of several Mg anodes at different current densities is measured in 3.5 wt% NaCl electrolyte. The contribution of self-corrosion at open circuit potential and at constant applied current to efficiency of Mg anodes is compared. Additionally, efficiency loss caused by detachment of undissolved metallic portions, namely "chunk effect", is determined with a proposed new approach. The effect of self-corrosion and "chunk effect" on anodic efficiency is assessed accordingly. The results indicate that "chunk effect" can also result in large efficiency loss of Mg anodes, especially at low current densities, which, in some cases, could exceed the loss caused by other mechanisms of self-corrosion of anode substrate. Hence, attention should be paid to both aspects when developing novel Mg anodes with high anodic efficiency, particularly for application in long-term low-power battery system.

1. Introduction

Nowadays, the wide application and commercialization of primary aqueous Mg batteries are still hindered in spite of the attractive theoretical properties of these promising energy storage devices. The issues could be partially originated from the cathode materials, such as the

* Corresponding author.
E-mail address: Min.Deng@hzg.de (M. Deng).

https://doi.org/10.1016/j.jpowsour.2019.227201
Received 2 July 2019; Received in revised form 22 August 2019; Accepted 22 September 2019
Available online 17 October 2019

sluggish kinetics of cathodic reactions or the limited diffusion of reactants, leading to large overvoltage. The problems concerning cathode materials have been widely discussed in the last decades [1–4] and some approaches have been proposed as effective solutions, like the adoption of selected advanced catalysts and porous substrate materials with nanostructures [5–10]. However, there are also major issues relevant to the Mg anode materials, including large overpotential caused by discharge products on anode surface and severe self-corrosion of Mg under polarization due to the well-known NDE [11–13]. These problems still exist despite recent progresses achieved through the development of novel Mg alloy anodes [14–17] and electrolyte additives [18–22]. Therefore, more effort needs to be made for modification and optimization of Mg anodes.

The anodic efficiency (or utilization efficiency) has great impact on the specific performance of aqueous Mg-based battery system, e.g., energy density and service life. The decreased anodic efficiency leads to low discharge capacity and specific energy density of Mg batteries, since a large portion of Mg anode is consumed via self-corrosion processes and, consequently, does not participate in the power supply. Unfortunately, the utilization efficiency of Mg anodes is normally below 60% at current density of 10 mA cm^{-2} and was found to be even less than 50% under smaller current densities [15,23–29]. As a consequence, the reported optimized specific energy density, like 1800 W h kg^{-1} in Mg-air system [14], is far below the theoretical level (6800 W h kg^{-1} based on anode only). Hence, the service life of primary Mg-based batteries are severely shortened, especially for those battery system designed for long-term and low power applications. Generally, the utilization efficiency of Mg anodes is inversely proportional to the weight loss caused by self-corrosion during discharge. In fact, the self-corrosion of Mg includes two different processes, namely the electrochemical dissolution of Mg substrate and the detachment of some metallic pieces from anode surface, which is known as “chunk effect” (CE). CE has been shown in some publications at the cross section morphology of Mg after corrosion tests. It is identified by the existence of some metallic pieces in corrosion products, including impurity particles, second phases or undissolved matrix [14,30–33].

Until now, nearly all the published work regarding improving the utilization efficiency of Mg anodes follows the direction of controlling the self-corrosion of anode substrate. Meanwhile, the corrosion resistance measured via electrochemical impedance spectroscopy (EIS) and corrosion rate determined with hydrogen evolution (HE) at open circuit potential (OCP) are normally utilized to conclude the effect of self-corrosion on Mg anode efficiency at different current densities. However, the feasibility of evaluating the real time self-corrosion rate of Mg during discharge based on determined corrosion behavior at OCP is doubtful. To the best of our knowledge, no published research has put emphasis on particularly clarifying this issue. Nonetheless, relevant information can be found from some publications. In the published paper of Samaniego et al. [34], Mg-33 at%Li alloy exhibits lower HE rate than pure Mg at OCP, but its HE rate becomes similar or even higher than pure Mg with applied anodic current densities. Similarly, according to the work of Chu et al. [35], HE rate of Mg–Zn–Ca–Mn alloy is similar to pure Mg in NaCl solution with applied current density of 1 mA cm^{-2} but tends to be higher when the current density increases to 10 mA cm^{-2}. Therefore, more systematic work is necessary to specify the relevance of self-corrosion to anodic efficiency of different Mg alloy anodes, especially under varying current densities. On the other hand, the impact of CE on anode utilization efficiency seems to be not fully taken into account in the selection procedure of Mg alloy anodes [15–17,20,23,27,29,36–41]. Only a few published works mention the possible influence of CE when evaluating the anodic efficiency of Mg anodes [14,28,42–44]. In fact, opposite results regarding utilization efficiency of same Mg anodes are found at different current densities in the work of Wang et al. [28]. Mg–Al–Pb–In anode has lower utilization efficiency than Mg–Al–Pb and pure Mg anode at current density of 10 mA cm^{-2}. However, adverse results are obtained when the current density increases to 180 and 300 mA cm^{-2}, as Mg–Al–Pb–In anode exhibits the highest efficiency comparing to the other two anode materials. The inconsistent utilization efficiency is supposed to be the consequence of different extent of CE at different current densities, concluded from the different surface morphologies after discharge. Despite the absence of more direct evidence in that work, it demonstrates that CE could have decisive effect on the utilization efficiency of Mg anodes.

Table 1
Chemical composition of as-cast HP Mg and Mg alloys [14,22]. The values are in ppm if other is not indicated.

Element	HP Mg	AZ31	AM50	E21	WE43	ZE41
Fe	50	11	2	12	38	18
Cu	<1	19	17	20	47	19
Ni	<2	7	5	52	46	7
Si	<1	309	637	4	0.9	2
Ca	<1	11	11	42	225	27
Zn	35	0.73%	418	0.29%	268	4.2%
Mn	8	0.36%	0.43%	38	60	79
Al	30	2.97%	4.85%	145	133	144
Zr	-	-	-	0.19%	0.17%	0.3%
Nd	-	-	-	3.2%	1.95%	0.24%
La	-	-	-	26	0.14%	0.42%
Pr	-	-	-	340	0.1%	647
Th	-	-	-	920	0.15%	0.29%
Y	-	-	-	72	4.49%	50
Ce	-	-	-	70	206	0.65%
Mg	99.98%	95.90%	94.61%	96.09%	92.85%	93.75%

In this present work, we examine the influence of the decisive factors for anodic efficiency of Mg anodes in aqueous electrolyte under relatively small load. Corrosion resistance and self-corrosion rate at OCP of high purity Mg (HP Mg) and several industrially relevant Mg alloys are determined through EIS and HE tests as well as the real time HE rate during discharge at different current densities. The possible occurrence of CE on these anode materials is observed from the cross section morphology after discharge tests. Meanwhile, the anodic efficiency of these selected Mg anodes after discharge are measured. The efficiency loss resulted from self-corrosion of anode substrate and CE is determined respectively by a proposed approach. Accordingly, the effect of both self-corrosion and CE on anodic efficiency of Mg anodes is evaluated.

2. Experimental procedures

Six magnesium alloys were used in this work. Of these, the discharge properties of HP Mg, AZ31 and AM50 alloys as anode for Mg-air batteries have been reported in our previous work [14]. Besides, we also investigated three more industrially relevant Mg alloys with different chemical compositions, i.e., Elektron 21 (E21 hereafter), WE43 and ZE41, which are the same materials studied in the published work of Lamaka et al., where new corrosion inhibitors for Mg were reported [22]. All six possess significantly different corrosion rates. All the samples were taken from as-cast ingots of corresponding materials. The chemical composition of all studied materials is presented in Table 1, showing the contents of all main elements and detrimental impurities like Fe, Cu and Ni. Fig. S1 in the supplementary materials shows the micrographs of all materials after polishing via a Tescan VEGA scanning electron microscope (SEM), indicating different microstructures, including diverse second phase fraction and distribution.

HE rate on different Mg anodes at open circuit potential was determined with an ordinary set-up, which includes a funnel inserted into a 100 ml inverted burette (0.2 ml graduations) and covering the sample. The specimens, with surface area of approximately 8 cm^2, were hung up with fishing line via an inserted plastic screw. The solution for all the measurements in this work was 3.5 wt% NaCl unbuffered solution prepared with deionized water, with pH of around 5.6. Before immersion, all the specimens were ground with SiC sand paper up to 1200 grit. The immersion test for each material was repeated three times to ensure the

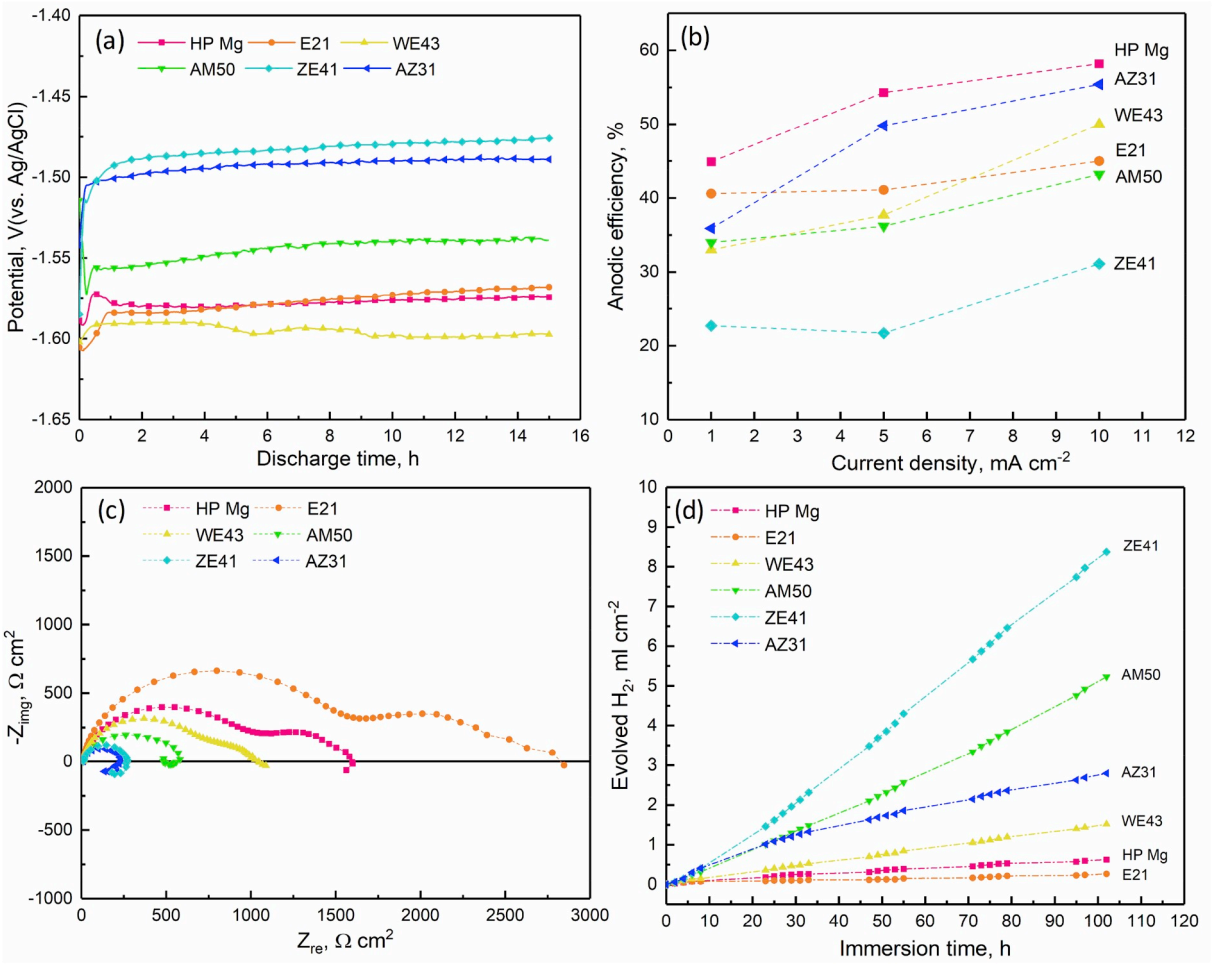

Fig. 1. (a) Discharge curves of high purity Mg and Mg alloys at 5 mA cm^{-2}; (b) Anodic efficiency after discharge at different current densities; (c) EIS (Nyquist plots) at OCP; (d) Hydrogen evolution curves of all selected materials. All the measurements are performed in unbuffered 3.5 wt% NaCl solution.

reproducibility. The duration time of each immersion measurement was 100 h.

Real-time HE rate during discharge was measured with a similar set-up used in the work of Frankel et al. [45] to collect the gas during galvanostatic polarization of Mg. The schematic corresponding to this experimental set-up is presented in Fig. S2. A Gamry Potentiostat was used to apply current to the Mg anodes in galvanostatic mode. A classical three-electrode system was adopted with Mg samples embedded into epoxy as a working electrode, exposing one rectangle surface with 1 cm^2. The counter electrode and reference was Pt wire and saturated Ag/AgCl electrode, respectively. Evolved hydrogen was collected via the 50 ml inverted burette with graduations of 0.1 ml. The volume of evolved hydrogen was determined under applied current densities of 1 mA cm^{-2}, 5 mA cm^{-2} and 10 mA cm^{-2}. The duration time for 1 mA cm^{-2} was 6 h, while for 5 and 10 mA cm^{-2} is 90 and 60 min respectively due to the rapid hydrogen evolution rate under severe polarization. Real-time HE rate was then calculated according to the recorded data. Note that only data in the later discharge period was used for calculation after a relatively constant HE rate was achieved. In detail, HE data after 3 h was used for 1 mA cm^{-2}, while data after 30 min was used for 5 and 10 mA cm^{-2}. Real-time HE measurement was carried out twice, showing a low deviation below 10%.

Electrochemical impedance was also measured to evaluate the corrosion resistance of different Mg anodes. Each sample was carefully treated with sand paper and then immersed into the solution with 1 cm^2 working surface. EIS measurements were performed after one-hour OCP test in order to obtain relatively stable surface condition. The scanned frequency ranged from 100 kHz to 0.01 Hz with sinusoidal excitation voltage of 10 mV rms referred to OCP.

Half-cell discharge test at different current densities was carried out in 3.5 wt% NaCl electrolyte. The discharge process under 1 mA cm^{-2} lasts 16 h, while 8 h in the case of 5 mA cm^{-2} and 10 mA cm^{-2}. After discharge, precipitated products were removed from the surface with chromic acid (200 g L^{-1} CrO_3) and the anode utilization efficiency of each material was calculated. . The details of the calculation procedure can be found elsewhere [14,46]. The surface morphology after discharge and cleaning the discharge products was observed with SEM. The morphology of corresponding cross section for each anode after discharge at 5 mA cm^{-2} for 16 h was also observed. Additionally, elemental mapping for selected zones in cross section was determined with the SEM coupled with energy dispersive X-ray spectroscopy (EDS) via backscattered-electrons (BSE) detector at 15 kV.

3. Results and discussion

3.1. Anodic efficiency during discharge

Fig. 1 presents the discharge curves and anodic efficiency of pure Mg and different Mg alloys. During the 15-h discharge measurement, all the materials maintain relatively stable discharge potential after the initial unstable periods for approximately one hour. This indicates that all the Mg anodes can keep a steady surface condition during the long-term discharge, attributed to the balance between actual surface area, changing pH, accumulation and self-peeling of discharge products. The

Table 2
Hydrogen evolution rate of high purity Mg and selected Mg alloys at OCP and under applied current in 3.5 wt% NaCl solution.

Self- corrosion P_H (ml cm^{-2} h^{-1})	HP Mg	E21	WE43	AM50	ZE41	AZ31
OCP	$(6 \pm 2)\cdot10^{-3}$	$(3 \pm 1)\cdot10^{-3}$	$(16 \pm 1)\cdot10^{-3}$	$(52 \pm 3)\cdot10^{-3}$	$(87 \pm 15)\cdot10^{-3}$	$(33 \pm 7)\cdot10^{-3}$
1 mA cm^{-2}	0.3	0.4	0.3	0.6	0.8	0.5
5 mA cm^{-2}	1.6	1.6	1.7	1.8	3.0	1.7
10 mA cm^{-2}	3.0	3.8	3.1	3.0	6.0	3.2

discharge potential is relevant to the Mg anode composition, which, however, is not the emphasis of this work. According to Fig. 1(b), these six Mg anodes show rather different anodic efficiency after discharge at various current densities. HP Mg exhibits highest anodic efficiency at all current densities, with that being above 50% at 5 and 10 mA cm^{-2}. Anodic efficiency of AZ31 alloy approaches that of HP Mg at 5 and 10 mA cm^{-2}. E21 alloy shows second highest anodic efficiency at 1 mA cm^{-2}, but with increasing current density its anodic efficiency becomes inferior comparing to HP Mg, AZ31 as well as WE43, which shows lower efficiency than E21 anode at 1 and 5 mA cm^{-2}. AM50 alloy has lower efficiency than E21 alloy at different current densities. However, the difference tends to be less with increasing current densities from 1 to 10 mA cm^{-2}. Among all the measured materials, ZE41 alloy possesses the lowest anodic efficiency at all current densities. It is worth noting that nearly all the anodes show enhanced anodic efficiency at higher discharge current density, except E21 and ZE41 at current density of 5 mA cm^{-2}. As mentioned in the introduction section, the anodic efficiency of Mg anodes depends on the self-corrosion performance, including substrate dissolution rate and the CE. The respective contribution of substrate dissolution rate and CE on efficiency loss may vary with different current densities, leading to the different anodic efficiency of Mg anodes at each current density. Therefore, we would like to investigate the effect from both aspects, respectively, in the following sections.

3.2. Self-corrosion rate

3.2.1. Self-corrosion at OCP

EIS and hydrogen evolution test are commonly used to evaluate the corrosion resistance and corrosion rate of magnesium [12]. Fig. 1(c) presents the results of EIS measurement for all selected materials at OCP after immersion for one hour in 3.5 wt% NaCl solution. Obviously, these materials have completely different impedance, indicating varying corrosion resistance following the order: E21 > HP Mg > WE43 > AM50 > ZE41 > AZ31. Nevertheless, these results can only reflect the initial corrosion resistance of these materials. Mg alloys with different chemical composition typically show different corrosion behavior after long immersion time due to the changing surface

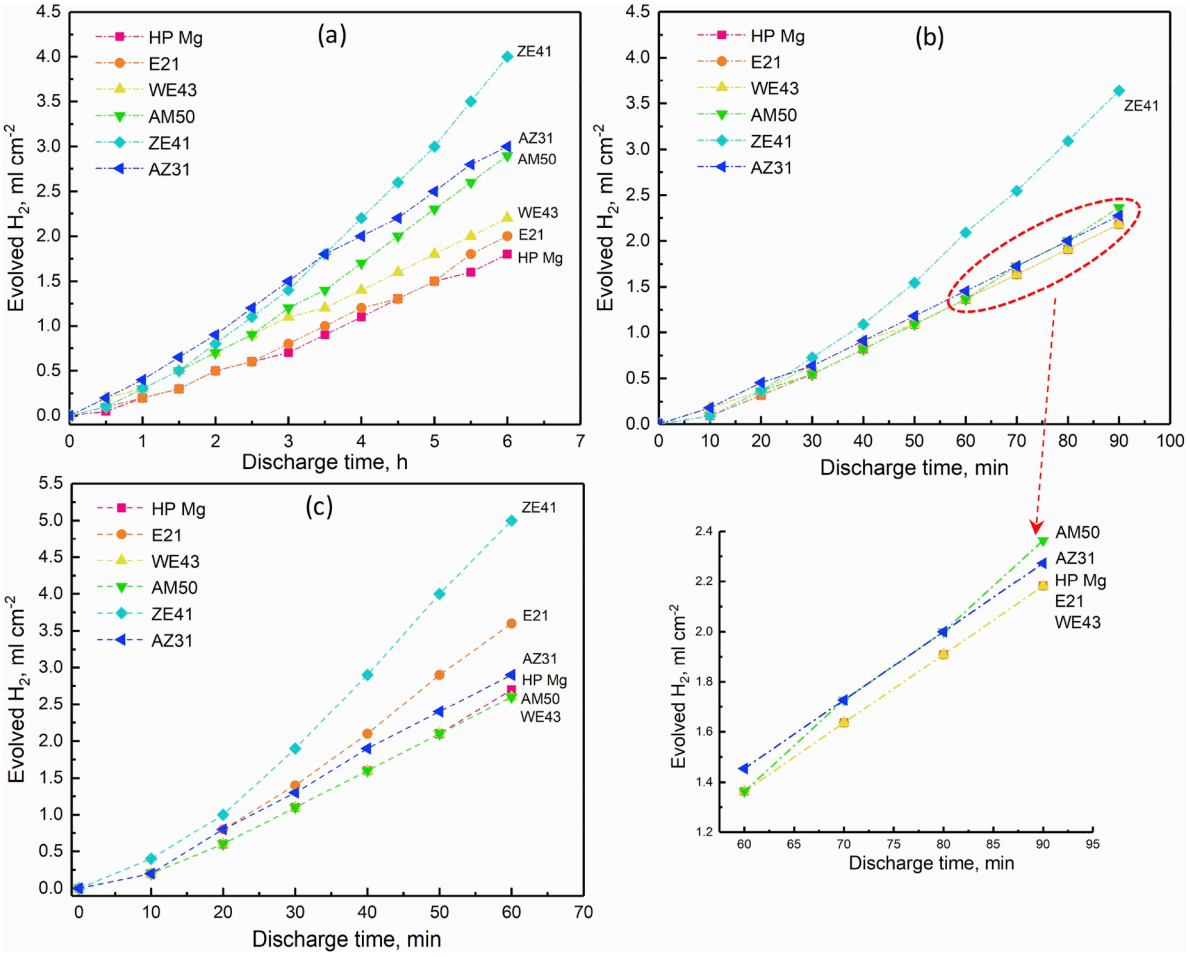

Fig. 2. Hydrogen evolution curves of different Mg anodes during discharge in 3.5 wt% NaCl solution applied with different current densities: (a) 1 mA cm^{-2}; (b) 5 mA cm^{-2}; (c) 10 mA cm^{-2}. Typical results from replicated experiments are presented.

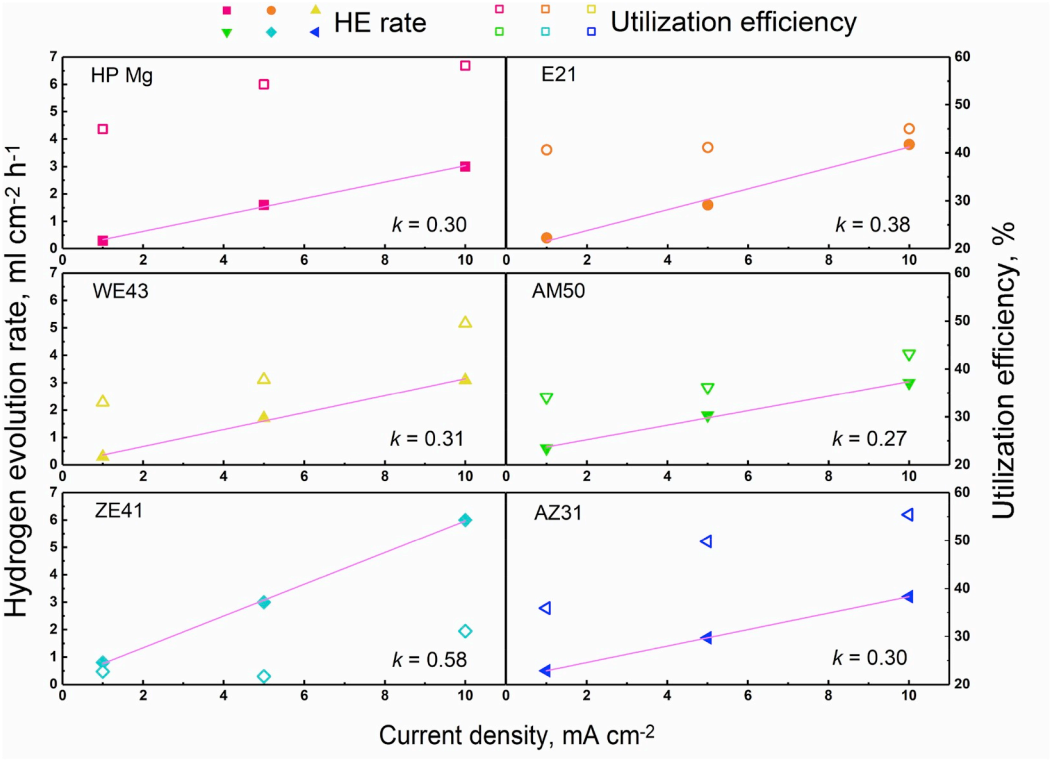

Fig. 3. Real-time hydrogen evolution rate as a function of applied current density. The solid symbols represent the measured real-time hydrogen evolution rate at different current densities. The straight lines are the linear fits with a slope of *k*. Utilization efficiency of all anodes is also presented for comparison as indicated by open symbols.

condition, such as the formation of protective oxide film [47–49]. The hydrogen evolution curves obtained from immersion test in 3.5 wt% NaCl solution for more than 100 h are indicated in Fig. 1(d) and utilized to evaluate the overall self-corrosion rate of these Mg anodes. The average self-corrosion rate calculated from hydrogen evolution test are presented in Table 2, following the order: E21 < HP Mg < WE43 < AZ31 < AM50 < ZE41. For all the materials, the results obtained from hydrogen evolution test are consistent with the EIS results except AZ31 alloy. It is not surprising because from the hydrogen evolution curves we can see that, during the initial stage of immersion (see Fig. S3), AZ31 alloy shows the fastest hydrogen evolution rate, indicating the highest self-corrosion rate, which is consistent with the EIS results. After immersion for nearly 30 h, the hydrogen evolution rate of AZ31 decreases and becomes slower than that of AM50 and ZE41 alloys. Interestingly, from the comparison of anodic efficiency and self-corrosion rate of these Mg anodes, something noteworthy is that the self-corrosion rate at OCP of Mg anodes should not be used as a direct indicator for the utilization efficiency. For instance, E21 shows the lowest self-corrosion rate obtained from both EIS and hydrogen evolution test, but it has lower anodic efficiency than HP Mg and AZ31 alloys, especially at high current densities. AZ31 alloy exhibits higher efficiency than E21 and WE43 alloys, even though its hydrogen evolution rate at OCP ($0.033\ ml\ cm^{-2}\ h^{-1}$) is greatly higher than E21 ($0.003\ ml\ cm^{-2}\ h^{-1}$) and WE43 ($0.016\ ml\ cm^{-2}\ h^{-1}$). The hydrogen evolution rate of AM50 is $0.052\ ml\ cm^{-2}\ h^{-1}$, which is nearly 20 times that of E21. However, their utilization efficiencies at 10 mA cm^{-2}, which are 43.2% and 45% respectively, indicate little difference.

3.2.2. *Self-corrosion during discharge*

In Fig. 2, the hydrogen evolution was recorded while applying different current densities so that the self-corrosion rate of Mg anodes during discharge can be compared. After an initial incubation period, all the materials maintained a relatively stable hydrogen evolution rate under different current densities. This incubation period lasts from several hours at low current density to less than 30 min at high current densities. Therefore, the real-time HE rate of these anode materials are calculated via the recorded HE data in the later discharge period with a relatively constant hydrogen evolution rate (more details in the section of experimental procedures). Table 2 shows the average value of hydrogen evolution rate obtained from two measurements that show deviation below 10%. No doubt that the hydrogen evolution rate of all the Mg anodes increases with increasing discharge current densities, which is a typical manifestation of the negative difference effect (NDE) of Mg in the unbuffered pH neutral NaCl solution. Interestingly, several alloys show similar hydrogen evolution rate measured with applied current, even though their self-corrosion rates at OCP appear to be of different magnitudes. At current density of 1 mA cm^{-2}, HP Mg and WE43 show the same hydrogen evolution rate, which is even lower than E21 despite that their self-corrosion rates at OCP are higher than that of E21. At 5 mA cm^{-2}, the hydrogen evolution rates of all Mg anodes, but ZE41, indicate no large difference. The situation changes at 10 mA cm^{-2}, as the difference between the hydrogen evolution rates of these Mg anodes tends to be more distinct. Surprisingly, E21 alloy exhibits the second highest hydrogen evolution rate among all the studied materials while HP Mg and AM50 shows the lowest, which is completely inconsistent with their self-corrosion rates determined at OCP, Fig. 1(d).

The plots of the hydrogen evolution rates of all selected Mg anodes as a function of applied current density are presented in Fig. 3. Within the current range in this work, from 1 mA cm^{-2} to 10 mA cm^{-2}, the hydrogen evolution rate of every material indicates a linearly increasing tendency with increasing current density. Previous reports show the examples of the linearly increasing hydrogen evolution rate for ultra-high purity Mg and AZ91 alloy in a wide range of current density [11, 45,50,51]. Fig. 3 also presents the linear fitting curves for all Mg anodes and lists the corresponding slope *k*, which represents the increase of hydrogen evolution rate as the function of current density. HP Mg, WE43, and AZ31 show similar slope, nearly 0.31, indicating a similar increasing tendency of hydrogen producing. By contrast, E21 and ZE41

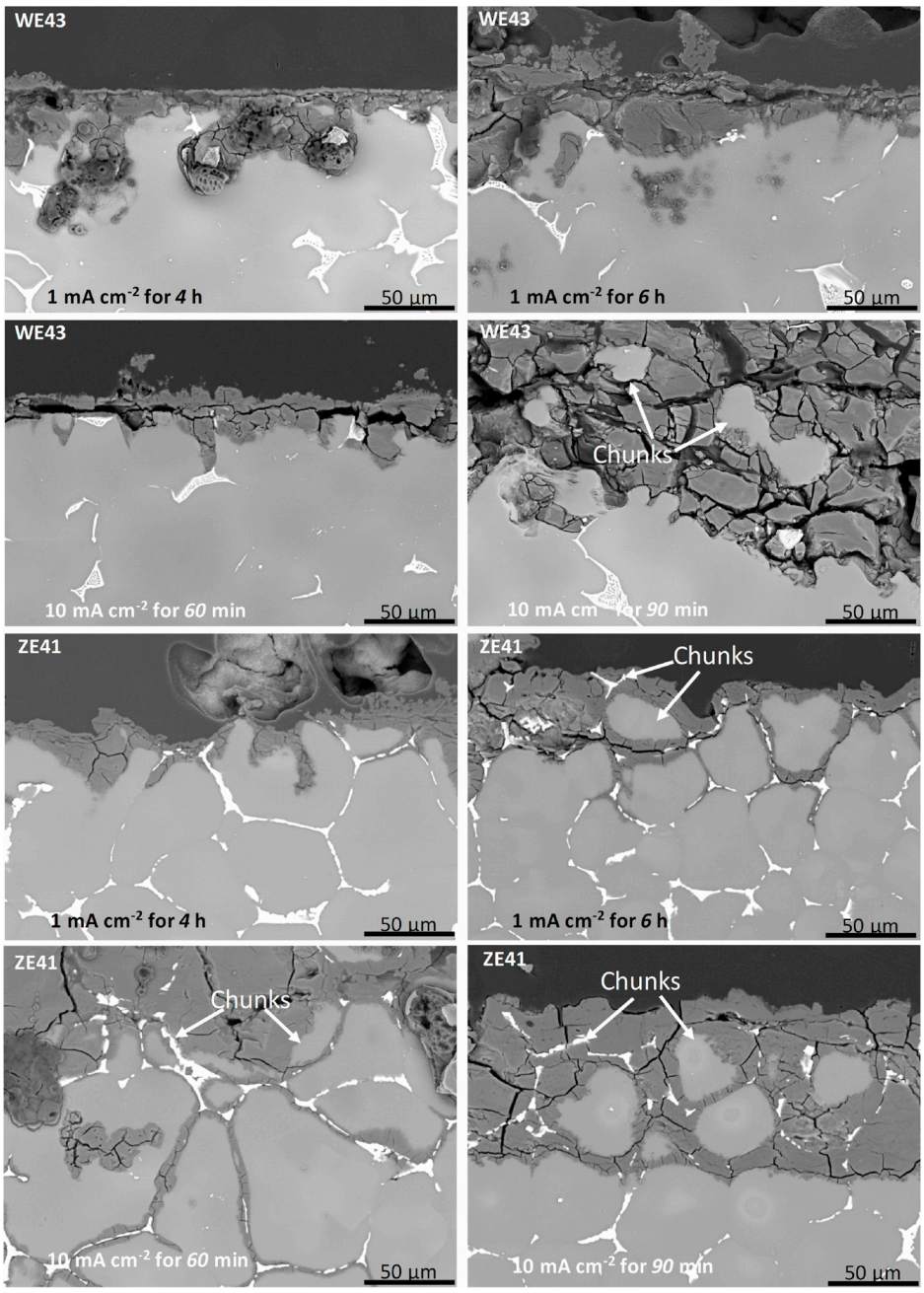

Fig. 4. Cross section morphologies of WE43 and ZE41 alloy after discharge for different duration time at 1 and 10 mA cm^{-2} in 3.5 wt% NaCl solution.

exhibit much higher slopes than most materials, i.e., 0.38 and 0.58 respectively. This could be a sensible reason for the higher hydrogen evolution rate of E21 and ZE41 compared with other materials at high current density. The coefficient *k* for different Mg anode is probably dependent on the chemical composition and microstructure, which is beyond the scope of this work. In conclusion, the self-corrosion rate of Mg anodes during discharge varies with different current density and the corresponding increasing rate highly depends on the properties of the alloy.

Severe self-corrosion of Mg anodes during discharge, appearing as fast hydrogen evolution, is the most well-known reason for the large efficiency loss of Mg anodes in aqueous battery. Taking consideration of the real-time self-corrosion rate during discharge, we find it reasonable that HP Mg has the highest anodic efficiency among tested alloys due to its lowest self-corrosion rate under different current densities. Similarly, the highest self-corrosion rate of ZE41 anode during discharge could be an important reason for its lowest anodic efficiency. However, the anodic utilization efficiency of WE43 alloy could not be explained from the aspect of self-corrosion as it shows similar hydrogen evolution rate with HP Mg but inferior efficiency, which is even worse than AZ31 and E21, especially at low current densities. Note that, comparing to E21, the efficiencies of WE43 and AM50 anodes are much lower at low current densities but in similar level at high current density. This could be attributed to their varied hydrogen evolution rates under different current densities. E21 shows much higher hydrogen evolution rate than WE43 and AM50 at 10 mA cm^{-2} while reverse situation happens with current density of 1 and 5 mA cm^{-2}. Regarding AZ31 alloy, its good anodic efficiency at all current densities seems to be contradictory with its relatively high self-corrosion rate during discharge. Therefore, it is sensible to pay more attention to the aforementioned "chunk effect" factor.

3.3. Influence of "chunk effect"

The efficiency loss resulting from CE cannot be directly determined by weight loss measurements since the undissolved anode parts will drop into the electrolyte and then degrade via independent self-corrosion processes. Other undissolved portions existing in the discharge products layer would fall out into the chromic acid solution in the chemical cleaning procedure. Therefore, we propose a novel method to calculate the efficiency loss caused by CE.

Generally, the specific weight loss (W) of Mg anode during discharge process can be expressed as following:

$$W = W_{discharge} + W_{self-corrosion} + W_{CE} \quad (1)$$

where $W_{discharge}$ represents the weight loss resulting from Faradaic process driven by the applied current, $W_{self\text{-}corrosion}$ means the weight loss caused by the self-corrosion of anode substrate and W_{CE} indicates the weight loss due to the mechanically detachment of undissolved anode portions. Therefore, similar to the equation for anode efficiency calculation [14,46], anodic efficiency (η) during discharge can also be defined as:

$$\eta = \frac{W_{discharge}}{W} \times 100\% \quad (2)$$

Meanwhile, the efficiency loss due to self-dissolution of anode substrate (η_{sc}) is defined as:

$$\eta_{sc} = \frac{W_{self-corrosion}}{W} \times 100\% \quad (3)$$

Hence, the efficiency loss caused by CE (η_{ce}) can be calculated via the following relationship:

$$\eta_{ce} = \frac{W_{Chunk\ effect}}{W} \times 100\% = 100\% - \eta - \eta_{sc} \quad (4)$$

The anodic efficiency η is determined after removing the discharge products from anode surface and presented in Fig. 1(d). In this context, η_{ce} can also be obtained supposing that the efficiency loss due to self-corrosion (η_{sc}) were known. Meanwhile, the weight loss due to self-corrosion of Mg is directly proportional to the volume of produced hydrogen gas (assuming that water reduction accompanied by hydrogen evolution is by far the main cathodic reaction during Mg corrosion at anodic polarizations and the contribution of oxygen reduction is negligible [52]). Hence, it could be possible to determine the weight loss caused by self-corrosion and corresponding η_{sc} via the measured hydrogen evolution data if the collected hydrogen were all produced by self-corrosion of Mg substrate. However, it should be noted that the detached undissolved anode parts (chunks) also produce hydrogen gas during corrosion, which definitely affects the determination. Therefore, to minimize the contribution of the chunk effect into the self-corrosion quantified by measuring H_2 evolution, the hydrogen evolution tests with applied current are only performed for relatively short time after a constant hydrogen evolution rate appears. The applied measurement durations are decided according to the time for the initial formation of CE, which is estimated from the cross section morphologies of WE43 and ZE41 alloys after discharge for different time (as shown in Fig. 4). After discharge at 1 mA cm^{-2} for 4 h, both WE43 and ZE41 do not show apparent "chunks" in the discharge products. When the discharge time increases to 6 h, the formation of "chunk" does not happen on WE43. In contrast, visible "chunks" are found from ZE41 alloy. At 10 mA cm^{-2}, CE is evident for both WE43 and ZE41 after discharge for 90 min. However, after discharge for 60 min, "chunks" are discovered only at cross section of ZE41 but not in the case of WE43. Note that, among all the studied Mg anodes, ZE41 offers the theoretically optimum condition for the formation of CE, attributed to the large fraction and continued distribution of second phases (see Fig. S1). Therefore, the selected time for real-time hydrogen evolution test at 1 mA cm^{-2} is 6 h, while for 5 and 10 mA cm^{-2} the measurement time is only 90 and 60 min, respectively, as stated in the section of experimental procedures. It is reasonable to assume that, in these initial discharge periods, the produced hydrogen is mostly resulted from the dissolution of bulk anode substrate. Besides, we can know directly from Table 2 that the dissolution of Mg anode without applied current is dozens of times lower than its NDE-increased self-corrosion during discharge, especially at high current densities. It could be another evidence for the negligible effect of possible hydrogen evolution by "chunks" in the determination of η_{sc}. Another considerable factor is the stability of Mg hydrogen evolution rate during long-time discharge, in view of the varying anode surface and solution properties, like the composition and pH. On one hand, as discussed in section 3.1, generally all Mg anodes maintain a relatively steady surface condition during the long-term discharge, after initial stabilization period of one to two hours. Therefore, the issue concerning possibly changing surface condition can be ignored after the surface stabilization. On the other hand, possible influence of changing solution composition was clarified experimentally. The hydrogen evolution results during discharge of AM50 in fresh 3.5 wt% NaCl solution and in similar solution remained in the electrochemical cell from previous experiment are presented in Fig. S4. The used solution is collected after a 15-h discharge measurement at 5 mA cm^{-2} with AM 50 anode (1 cm^2 working surface). Note that this used solution was saturated with dissolved hydrogen, its pH was 10.8 and concentration of dissolved Mg^{2+} was 2.35 mM as shown by atomic absorption spectroscopy measurements. The results indicate that AM50 anode showed identical hydrogen evolution rate, 1.8 ml cm^{-2} h^{-1}, in fresh and in used electrolyte. The difference between the total volumes of evolved hydrogen gas originates from the initial stage of several minutes, which could be attributed to the solubility of hydrogen in water, fast increase of local and bulk pH, saturation with Mg^{2+} and other aspects. The results demonstrate that the changing solution composition and bulk pH during the discharge process have no apparent influence on the constant hydrogen evolution rate of AM50 (and possibly all other studied Mg anodes in this paper) at our experimental condition. This is also in agreement with previous reports were the fast increase of local pH near Mg surface after exposure in different media has been shown [53–55]. The rapid dissolution of Mg induced by applied current certainly accelerates the alkalization in the vicinity of Mg anodes, minimizing the effect of increasing bulk pH on self-corrosion. Therefore, eliminating the possible influence of these factors, the determined hydrogen evolution rate in the present work can be used to evaluate the self-corrosion rate of anodes during long-term

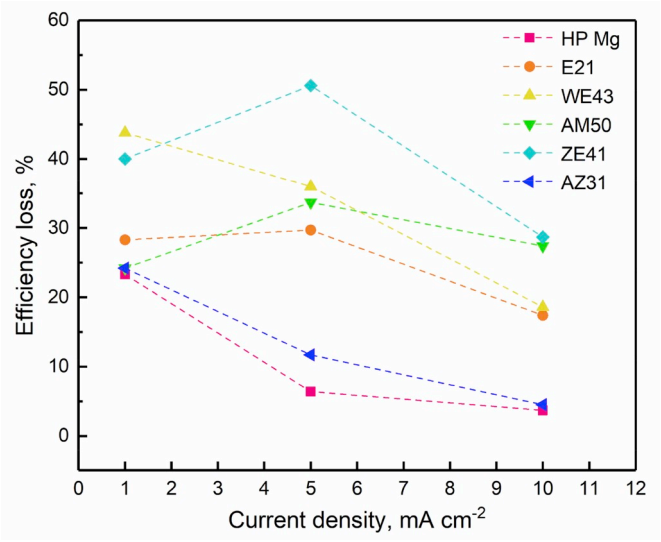

Fig. 5. Calculated efficiency loss caused by "chunk effect" for various Mg anodes at different current densities in 3.5 wt% NaCl solution (1 mA cm^{-2} for 16 h, 5 and 10 mA cm^{-2} for 8 h).

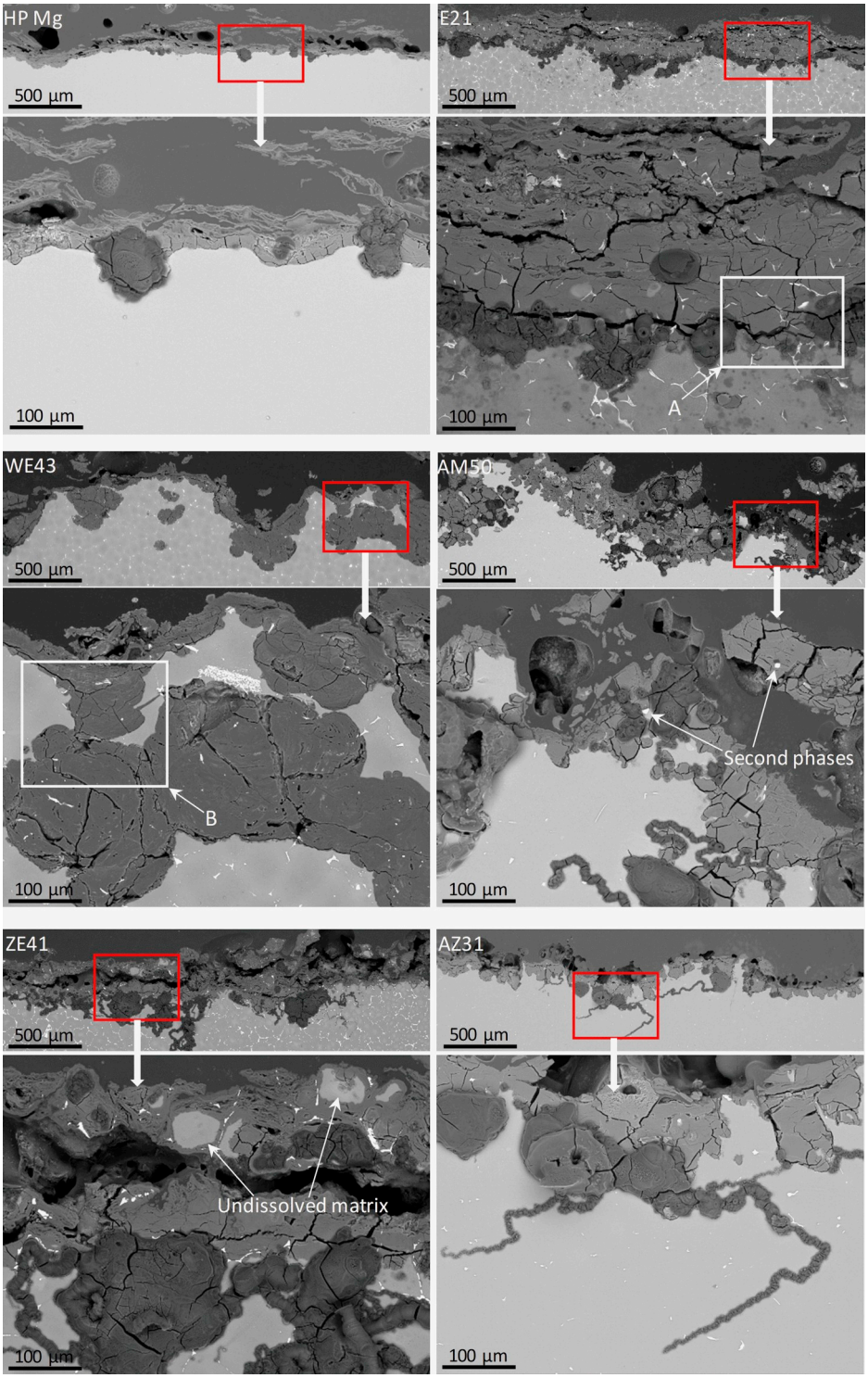

Fig. 6. Morphologies of the cross section of different Mg anodes after discharge at 5 mA cm^{-2} for 8 h in 3.5 wt% NaCl solution. The top layer in each cross section is an epoxy layer followed by a discharge products layer and Mg matrix.

discharge. Consequently, the proposed approach to determine the efficiency loss caused by self-corrosion is believed to have relatively high accuracy.

The measured hydrogen evolution rate (P_H) of different Mg anodes are listed in Table 2. The corresponding weight loss rate (P_w) can be calculated with the conversion: P_w (mg cm^{-2} h^{-1}) = 0.994 P_H (ml cm^{-2} h^{-1}), as the working condition is nearly 25 °C at a pressure of 1 atm [56]. Therefore, the efficiency loss due to self-corrosion can be calculated using the following formula:

$$\eta_{sc} = \frac{W_{self-corrosion}}{W} \times 100\% = \frac{P_W \times t}{W} \times 100\% = \frac{0.994 P_H \times t}{W} \times 100\% \quad (5)$$

where t (h) is the duration time of discharge. η_{ce} is then calculated using equation (4).

The determined efficiency loss caused by CE, η_{ce}, via this proposed approach is shown in Fig. 5. The results indicate that E21, WE43, AM50 and ZE41 anodes all exhibit high η_{ce}, especially at low current density.

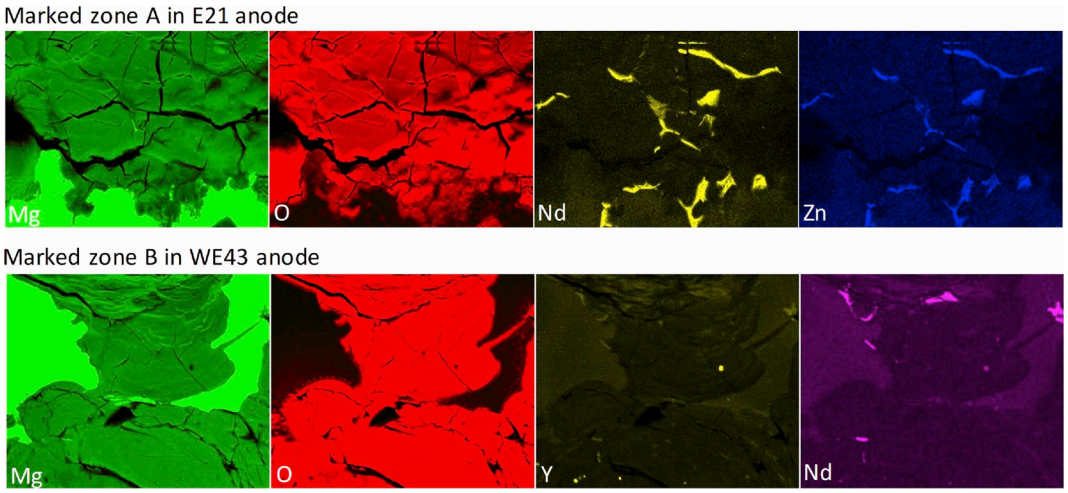

Fig. 7. Corresponding EDS mapping for the marked zone A and B respectively in the cross section of E21 and WE43 anodes after discharge as presented in Fig. 6.

HP Mg and AZ31 anodes show relatively low η_{ce} and the efficiency loss is below 10% at current density of 10 mA cm^{-2}. This offers a plausible explanation for the relatively high anodic efficiency of AZ31 in spite of its fast self-corrosion rate during discharge compared to other anodes, such as E21. It is remarkable that an apparent decreasing tendency of the efficiency loss from low current density to high current density is found for all the evaluated Mg anodes, except ZE41 and AM50 at 5 mA cm^{-2}. Nevertheless, E21, WE43, AM50 and ZE41 alloys still have efficiency loss around 20–30% originated from CE. Definitely, the high η_{ce} of E21 and WE43 alloys leads to their low anodic efficiency even though they show relatively low self-corrosion rate during discharge. For instance, efficiency loss of WE43 caused by CE is 43.8% at 1 mA cm^{-2}, much higher than that resulted from self-corrosion, 23.3%. ZE41 suffers the highest efficiency loss caused by CE as well as by self-corrosion, leading to the lowest anode utilization efficiency at all current densities. Generally, higher applied current density leads to more anode dissolution forced by faradaic process and increased total weight loss of anode. Therefore, the proportion of weight loss caused by chunk effect in total weight loss decreases, leading to lower efficiency loss by chunk effect. However, in some cases, with increased current density, the formation of chunk effect may also be promoted, resulting in more weight loss by chunk effect. The efficiency loss due to chunk effect in this case would possibly increase even under slightly enhanced current density, the same situation for ZE41 and AM50 at 5 mA cm^{-2}. The results presented here indicate that the formation of chunk effect closely relates to the applied current density and Mg alloy category, including the microstructure and alloying elements.

The morphologies of cross section after discharge at 5 mA cm^{-2} for 8 h are presented in Fig. 6, as a supportive evidence for the calculation results concerning efficiency loss by CE. For E21, WE43, AM50 and ZE41 alloys, the cross section indicates severe CE, appearing as large amounts of undissolved metallic portions in the discharge products layer. These separated portions are undissolved Mg matrix or second phases as demonstrated by the EDS element mapping presented in Fig. 7. Note that the elemental mapping is performed on selected areas in the cross section of E21 and WE43 anodes after discharge as shown in Fig. 6. Only the mapping results of main elements are presented here. By contrast, HP Mg and AZ31 anodes exhibit more homogeneous dissolution and corresponding discharge product layer with few separated parts, indicating only slight chunk effect. From Figs. 6 and 7, it is clear that CE appears in two forms, i.e., the separated second phases attributed to the preferential dissolution of Mg matrix around these phases (e.g., in E21) and the undermined Mg grains after the detachment of second phases surrounding this matrix (like in WE43, AM50 and ZE41). The formation of CE closely depends on the microstructure of Mg anodes, especially the constitution, quantity and distribution of the second phases. Additionally, 3D reconstruction of the surface topographies of these Mg anodes after discharge at 1 mA cm^{-2} for 16 h are also shown in Fig. 8. It should be noted that HP Mg suffers from relatively uniform dissolution for most working surface; however, some individual grains show severe localized dissolution (see Fig. S5(a)) possibly because of special crystal orientation [57–59]. Topography of this non-uniform area is displayed here. Apparently, HP Mg, WE43 and AM50 show some large cavities on the surface after discharge. These cavities, most probably left by detachment of chunks, are the manifestation of severe CE regarding WE43 and AM50 anodes. Meanwhile, this could also be the reason that HP Mg exhibits around 20% efficiency loss by CE when discharge at 1 mA cm^{-2}. By contrast, E21, ZE41 and AZ31 alloys show relatively flat surface morphologies macroscopically. Nevertheless, separate chunks of magnesium matrix are clearly separated by dissolved second phase in case of ZE 41 alloy as seen from the SEM image under high magnification (see Fig. S5 (b)). Consequently, it is noticeable that the possible occurrence of CE, especially as the form of matrix undermining, can be examined by surface morphology after discharge, but should be determined both macroscopically and microscopically.

All the experimental results mentioned here indicate that CE, namely the detachment of undissolved Mg matrix and second phases, has great influence on the efficiency of Mg anodes. In some cases, the effect of CE could exceed the impact of self-corrosion of Mg substrate, leading to low anode utilization efficiency for the Mg anodes characterized by low self-corrosion rate during the discharge. Since the presence of CE depends tightly on the chemical composition and microstructure of Mg anodes, the finding in this work demonstrates another decisive factor for the development of novel Mg anodes apart from the commonly considered self-corrosion resistance. No doubt, alloying is still an important approach to improve the self-corrosion and discharge properties of Mg anodes. However, the influence on anode utilization efficiency resulted from second-phase-relevant CE need to be elaborately considered. In order to minimize the efficiency loss caused by CE, Mg anodes with small fraction of second phase as well as discontinued distribution are requested.

4. Conclusions

Discharge tests in 3.5 wt% NaCl solution were performed on HP Mg and five Mg alloys at current densities of 1, 5 and 10 mA cm^{-2} to evaluate their utilization efficiency when served as anodes for primary aqueous batteries under relatively small load. Corrosion resistance and self-corrosion rate at OCP of these Mg anodes are measured as well as their real-time self-corrosion rate during discharge under different

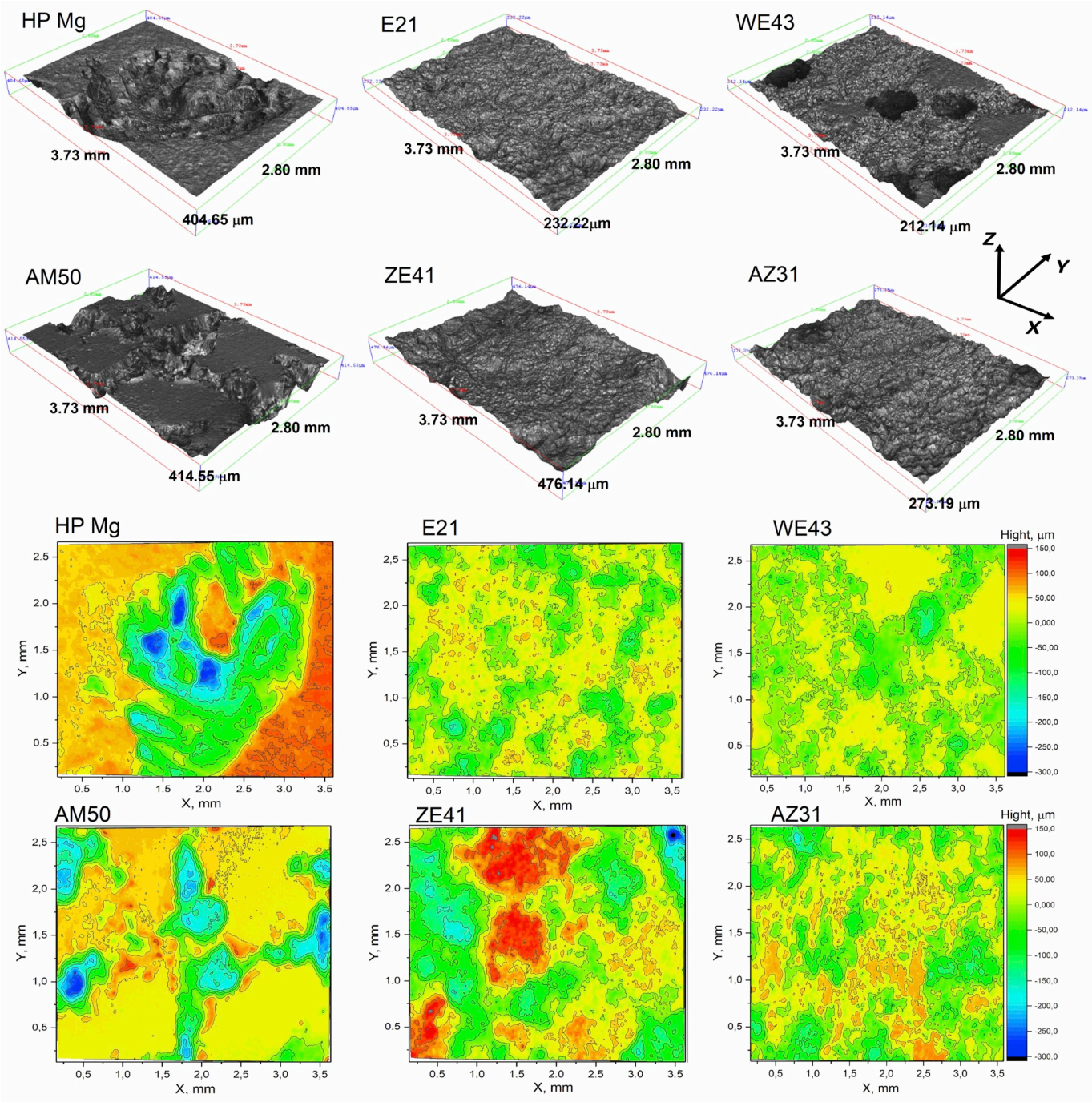

Fig. 8. 3D reconstruction indicating the topography of different Mg anodes after discharge at 1 mA cm^{-2} for 16 h in unbuffered 3.5 wt% NaCl solution and removal of discharge products. Corresponding depth profiles are also presented.

current densities. The efficiency loss caused by self-corrosion of anode substrate and by detachment of undissolved metallic pieces, namely "chunk effect", is determined via a newly proposed approach. The impact of self-corrosion, at OCP and under polarization, and "chunk effect" on anodic efficiency of Mg anodes is evaluated. The following can be concluded:

(1) Self-corrosion rate determined at OCP cannot be utilized to estimate the utilization efficiency of Mg anodes during discharge. This is because the real-time self-corrosion depends on the applied discharge current density.

(2) Real-time self-corrosion rate of Mg anodes increases linearly with increase of applied discharge current density. The alloy composition and microstructure pre-determines how steeply the rate of self-corrosion increases with increase of applied discharge current density.

(3) "Chunk effect" can also cause large efficiency loss to Mg anodes, up to 50% as was shown in this work. Generally, the efficiency loss resulted from "chunk effect" is reduced with increase of current density (by 10–25% when discharge current increases from 1 to 10 mA cm^{-2}).

(4) In some cases, anodic efficiency loss due to "chunk effect" exceeds that caused by self-corrosion of anode, especially at low

current density, being the decisive factor for the efficiency of Mg anodes.

Acknowledgement

The authors wish to acknowledge the technical support from Mr. Ulrich Burmester, Mr. Volker Heitmann and Mr. Gert Wiese regarding sample preparation and SEM operation. Additionally, M. Deng and L. Wang are grateful for the support from China Scholarship Council concerning the award of fellowship No. 201606370031 and No. 201706370183. D. Snihirova acknowledges Humboldt Foundation for Postdoctoral grant and Seamag Project for financial support (MarTera ERA-NET cofund).

Appendix A. Supplementary data

Supplementary data to this article can be found online at https://doi.org/10.1016/j.jpowsour.2019.227201.

References

[1] R. Renuka, AgCl and Ag2S as additives to CuI in Mg-CuI seawater activated batteries, J. Appl. Electrochem. 27 (1997) 1394–1397. https://doi.org/10.1023/A:1018481314511.
[2] F. Cheng, J. Chen, Metal-air batteries: from oxygen reduction electrochemistry to cathode catalysts, Chem. Soc. Rev. 41 (2012) 2172–2192. https://doi.org/10.1039/c1cs15228a.
[3] N.G. Wang, R.C. Wang, C.Q. Peng, C.W. Hu, Y. Feng, B. Peng, Research progress of magnesium anodes and their applications in chemical power sources, Trans. Nonferrous Metals Soc. China 24 (2014) 2427–2439. https://doi.org/10.1016/S1003-6326(14)63367-7.
[4] T. Zhang, Z. Tao, J. Chen, Magnesium–air batteries: from principle to application, Mater. Horiz. 1 (2014) 196–206. https://doi.org/10.1039/c3mh00059a.
[5] R.R. Bessette, M.G. Medeiros, C.J. Patrissi, C.M. Deschenes, C.N. LaFratta, Development and characterization of a novel carbon fiber based cathode for semi-fuel cell applications, J. Power Sources 96 (2001) 240–244. https://doi.org/10.1016/S0378-7753(01)00492-X.
[6] W. Yang, S. Yang, W. Sun, G. Sun, Q. Xin, Nanostructured palladium-silver coated nickel foam cathode for magnesium–hydrogen peroxide fuel cells, Electrochim. Acta 52 (2006) 9–14. https://doi.org/10.1016/j.electacta.2006.03.066.
[7] W. Yang, S. Yang, J. Guo, G. Sun, Q. Xin, Comparison of CNF and XC-72 carbon supported palladium electrocatalysts for magnesium air fuel cell, Carbon 45 (2007) 397–401. https://doi.org/10.1016/j.carbon.2006.09.003.
[8] C.J. Patrissi, R.R. Bessette, Y.K. Kin, C.R. Schumacher, Fabrication and rate performance of a microfiber cathode in a Mg-H_2O_2 flowing electrolyte semi-fuel cell, J. Electrochem. Soc. 155 (2008) B558–B562. https://doi.org/10.1149/1.2901043.
[9] Z. Li, J. Yang, G. Xu, S. Wang, Non-precious cathode electrocatalyst for magnesium air fuel cells: activity and durability of iron-polyphthalocyanine absorbed on carbon black, J. Power Sources 242 (2013) 157–165. https://doi.org/10.1016/j.jpowsour.2013.05.082.
[10] C. Shu, E. Wang, L. Jiang, G. Sun, High performance cathode based on carbon fiber felt for magnesium-air fuel cells, Int. J. Hydrogen Energy 38 (2013) 5885–5893. https://doi.org/10.1016/j.ijhydene.2013.02.093.
[11] T.R. Thomaz, C.R. Weber, T. Pelegrini, L.F.P. Dick, G. Knörnschild, The negative difference effect of magnesium and of the AZ91 alloy in chloride and stannate-containing solutions, Corros. Sci. 52 (2010) 2235–2243. https://doi.org/10.1016/j.corsci.2010.03.010.
[12] M. Esmaily, J.E. Svensson, S. Fajardo, N. Birbilis, G.S. Frankel, S. Virtanen, R. Arrabal, S. Thomas, L.G. Johansson, Fundamentals and advances in magnesium alloy corrosion, Prog. Mater. Sci. 89 (2017) 92–193. https://doi.org/10.1016/j.pmatsci.2017.04.011.
[13] G.L. Song, A. Atrens, Corrosion mechanisms of magnesium, Adv. Eng. Mater. 1 (1999) 11–33. https://doi.org/10.1002/(SICI)1527-2648(199909)1:1<11::AID-ADEM11>3.0.CO;2-N.
[14] M. Deng, D. Höche, S.V. Lamaka, D. Snihirova, M.L. Zheludkevich, Mg-Ca binary alloys as anodes for primary Mg-air batteries, J. Power Sources 396 (2018) 109–118. https://doi.org/10.1016/j.jpowsour.2018.05.090.
[15] X. Li, H. Lu, S. Yuan, J. Bai, J. Wang, Y. Cao, Q. Hong, Performance of Mg–9Al–1In alloy as anodes for Mg-air batteries in 3.5 wt% NaCl solutions, J. Electrochem. Soc. 164 (2017) A3131–A3137. https://doi.org/10.1149/2.0971713jes.
[16] X. Liu, S. Liu, J. Xue, Discharge performance of the magnesium anodes with different phase constitutions for Mg-air batteries, J. Power Sources 396 (2018) 667–674. https://doi.org/10.1016/j.jpowsour.2018.06.085.
[17] Y. Ma, N. Li, D. Li, M. Zhang, X. Huang, Performance of Mg–14Li–1Al–0.1Ce as anode for Mg-air battery, J. Power Sources 196 (2011) 2346–2350. https://doi.org/10.1016/j.jpowsour.2010.07.097.
[18] D. Hoche, S.V. Lamaka, B. Vaghefinazari, T. Braun, R.P. Petrauskas, M. Fichtner, M.L. Zheludkevich, Performance boost for primary magnesium cells using iron complexing agents as electrolyte additives, Sci. Rep. 8 (2018) 7578. https://doi.org/10.1038/s41598-018-25789-8.
[19] M.A. Deyab, Decyl glucoside as a corrosion inhibitor for magnesium–air battery, J. Power Sources 325 (2016) 98–103. https://doi.org/10.1016/j.jpowsour.2016.06.006.
[20] Y. Li, J. Ma, G. Wang, F. Ren, Y. Zhu, Y. Song, Investigation of sodium phosphate and sodium dodecylbenzenesulfunate as electrolyte additives for AZ91 magnesium-air battery, J. Electrochem. Soc. 165 (2018) A1713–A1717. https://doi.org/10.1149/2.0581809jes.
[21] M.M. Dinesh, K. Saminathan, M. Selvam, S.R. Srither, V. Rajendran, Water soluble graphene as electrolyte additive in magnesium-air battery system, J. Power Sources 276 (2015) 32–38. https://doi.org/10.1016/j.jpowsour.2014.11.079.
[22] S.V. Lamaka, B. Vaghefinazari, D. Mei, R.P. Petrauskas, D. Höche, M. L. Zheludkevich, Comprehensive screening of Mg corrosion inhibitors, Corros. Sci. 128 (2017) 224–240. https://doi.org/10.1016/j.corsci.2017.07.011.
[23] H. Xiong, K. Yu, X. Yin, Y. Dai, Y. Yan, H. Zhu, Effects of microstructure on the electrochemical discharge behavior of Mg-6wt%Al-1wt%Sn alloy as anode for Mg-air primary battery, J. Alloy. Comp. 708 (2017) 652–661. https://doi.org/10.1016/j.jallcom.2016.12.172.
[24] N. Wang, R. Wang, Y. Feng, W. Xiong, J. Zhang, M. Deng, Discharge and corrosion behaviour of Mg-Li-Al-Ce-Y-Zn alloy as the anode for Mg-air battery, Corros. Sci. 112 (2016) 13–24. https://doi.org/10.1016/j.corsci.2016.07.002.
[25] Y. Feng, W. Xiong, J. Zhang, R. Wang, N. Wang, Electrochemical discharge performance of the Mg–Al–Pb–Ce–Y alloy as the anode for Mg–air batteries, J. Mater. Chem. 4 (2016) 8658–8668. https://doi.org/10.1039/c6ta02574a.
[26] M. Yuasa, X. Huang, K. Suzuki, M. Mabuchi, Y. Chino, Discharge properties of Mg–Al–Mn–Ca and Mg–Al–Mn alloys as anode materials for primary magnesium–air batteries, J. Power Sources 297 (2015) 449–456. https://doi.org/10.1016/j.jpowsour.2015.08.042.
[27] S. Yuan, H. Lu, Z. Sun, L. Fan, X. Zhu, W. Zhang, Electrochemical performance of Mg-3Al modified with Ga, in and Sn as anodes for Mg-air battery, J. Electrochem. Soc. 163 (2016) A1181–A1187. https://doi.org/10.1149/2.0371607jes.
[28] N. Wang, R. Wang, C. Peng, B. Peng, Y. Feng, C. Hu, Discharge behaviour of Mg-Al-Pb and Mg-Al-Pb-In alloys as anodes for Mg-air battery, Electrochim. Acta 149 (2014) 193–205. https://doi.org/10.1016/j.electacta.2014.10.053.
[29] M. Yuasa, X. Huang, K. Suzuki, M. Mabuchi, Y. Chino, Effects of microstructure on discharge behavior of AZ91 alloy as anode for Mg-air battery, Mater. Trans. 55 (2014) 1202–1207. https://doi.org/10.2320/matertrans.MC201403.
[30] G.A. Marsh, E. Schaschl, The difference effect and the chunk effect, J. Electrochem. Soc. 107 (1960) 960–965. https://doi.org/10.1149/1.2427579.
[31] M.E. Straumanis, B.K. Bhatia, Disintegration of magnesium while dissolving anodically in neutral and acidic solutions, J. Electrochem. Soc. 110 (1963) 357–360. https://doi.org/10.1149/1.2425763.
[32] M. Andrei, F.d. Gabriele, P.L. Bonora, D. Scantlebury, Corrosion behaviour of magnesium sacrificial anodes in tap water, Mater. Corros. 54 (2003) 5–11. https://doi.org/10.1002/maco.200390010.
[33] P. Jiang, C. Blawert, R. Hou, N. Scharnagl, J. Bohlen, M.L. Zheludkevich, Microstructural influence on corrosion behavior of MgZnGe alloy in NaCl solution, J. Alloy. Comp. 783 (2019) 179–192. https://doi.org/10.1016/j.jallcom.2018.12.296.
[34] A. Samaniego, N. Birbilis, X. Xia, G.S. Frankel, Hydrogen evolution during anodic polarization of Mg alloyed with Li, Ca, or Fe, Corrosion 71 (2015) 224–233. https://doi.org/10.5006/1367.
[35] P.-W. Chu, E. Le Mire, E.A. Marquis, Microstructure of localized corrosion front on Mg alloys and the relationship with hydrogen evolution, Corros. Sci. 128 (2017) 253–264. https://doi.org/10.1016/j.corsci.2017.09.022.
[36] D. Cao, L. Wu, Y. Sun, G. Wang, Y. Lv, Electrochemical behavior of Mg–Li, Mg–Li–Al and Mg–Li–Al–Ce in sodium chloride solution, J. Power Sources 177 (2008) 624–630. https://doi.org/10.1016/j.jpowsour.2007.11.037.
[37] M.C. Lin, C.Y. Tsai, J.Y. Uan, Electrochemical behaviour and corrosion performance of Mg–Li–Al–Zn anodes with high Al composition, Corros. Sci. 51 (2009) 2463–2472. https://doi.org/10.1016/j.corsci.2009.06.036.
[38] R. Udhayan, N. Muniyandi, P.B. mathur, Studies on magnesium and its alloys in battery electrolytes, Br. Corros. J. 27 (1992) 68–71. https://doi.org/10.1179/000705992798268927.
[39] Y.-Z. Lv, Y.-Z. Jin, Z.-B. Wang, M. Liu, Y.-F. Li, L. Wang, D.-X. Cao, The electrochemical behaviors of the Mg-7.5Li-3.5Al and Mg-7.5Li-3.5Al-1Y electrodes in sodium chloride solution, Ionics 21 (2014) 429–435. https://doi.org/10.1007/s11581-014-1187-z.
[40] D. Cao, L. Wu, G. Wang, Y. Lv, Electrochemical oxidation behavior of Mg–Li–Al–Ce–Zn and Mg–Li–Al–Ce–Zn–Mn in sodium chloride solution, J. Power Sources 183 (2008) 799–804. https://doi.org/10.1016/j.jpowsour.2008.06.005.
[41] J. Li, B. Zhang, Q. Wei, N. Wang, B. Hou, Electrochemical behavior of Mg-Al-Zn-In alloy as anode materials in 3.5 wt.% NaCl solution, Electrochim. Acta 238 (2017) 156–167. https://doi.org/10.1016/j.electacta.2017.03.119.
[42] D. Cao, X. Cao, G. Wang, L. Wu, Z. Li, Electrochemical discharge performance of Mg-Li based alloys in NaCl solution, J. Solid State Electrochem. 14 (2009) 851–855. https://doi.org/10.1007/s10008-009-0865-7.
[43] Y. Shi, C. Peng, Y. Feng, R. Wang, N. Wang, Microstructure and electrochemical corrosion behavior of extruded Mg–Al–Pb–La alloy as anode for seawater-activated battery, Mater. Des. 124 (2017) 24–33. https://doi.org/10.1016/j.matdes.2017.03.058.
[44] N. Wang, R. Wang, C. Peng, Y. Feng, Enhancement of the discharge performance of AP65 magnesium alloy anodes by hot extrusion, Corros. Sci. 81 (2014) 85–95. https://doi.org/10.1016/j.corsci.2013.12.005.

[45] G.S. Frankel, A. Samaniego, N. Birbilis, Evolution of hydrogen at dissolving magnesium surfaces, Corros. Sci. 70 (2013) 104–111. https://doi.org/10.1016/j.corsci.2013.01.017.
[46] L.Q. Wang, R.C. Wang, Y. Feng, M. Deng, N.G. Wang, Effect of Al and Pb contents on the corrosion electrochemical properties and activation of Mg-Al-Pb alloy anode, J. Electrochem. Soc. 164 (2017) A438–A446. https://doi.org/10.1149/2.1211702jes.
[47] A. Pardo, M.C. Merino, A.E. Coy, F. Viejo, R. Arrabal, S. Feliú, Influence of microstructure and composition on the corrosion behaviour of Mg/Al alloys in chloride media, Electrochim. Acta 53 (2008) 7890–7902. https://doi.org/10.1016/j.electacta.2008.06.001.
[48] R. Arrabal, A. Pardo, M.C. Merino, M. Mohedano, P. Casajús, K. Paucar, G. Garcés, Effect of Nd on the corrosion behaviour of AM50 and AZ91D magnesium alloys in 3.5 wt.% NaCl solution, Corros. Sci. 55 (2012) 301–312. https://doi.org/10.1016/j.corsci.2011.10.033.
[49] W. Liu, F. Cao, L. Chang, Z. Zhang, J. Zhang, Effect of rare earth element Ce and La on corrosion behavior of AM60 magnesium alloy, Corros. Sci. 51 (2009) 1334–1343. https://doi.org/10.1016/j.corsci.2009.03.018.
[50] S. Fajardo, G.S. Frankel, Effect of impurities on the enhanced catalytic activity for hydrogen evolution in high purity magnesium, Electrochim. Acta 165 (2015) 255–267. https://doi.org/10.1016/j.electacta.2015.03.021.
[51] S. Fajardo, G.S. Frankel, Gravimetric method for hydrogen evolution measurements on dissolving magnesium, J. Electrochem. Soc. 162 (2015) C693–C701. https://doi.org/10.1149/2.0241514jes.
[52] E.L. Silva, S.V. Lamaka, D. Mei, M.L. Zheludkevich, The reduction of dissolved oxygen during magnesium corrosion, ChemistryOpen 7 (2018) 664–668. https://doi.org/10.1002/open.201800076.
[53] D. Mei, S.V. Lamaka, J. Gonzalez, F. Feyerabend, R.W. Römer, M.L. Zheludkevich, The role of individual components of simulated body fluid on the corrosion behavior of commercially pure Mg, Corros. Sci. 147 (2018) 81–93. https://doi.org/10.1016/j.corsci.2018.11.011.
[54] S.V. Lamaka, J. Gonzalez, D. Mei, F. Feyerabend, R. Willumeit-Römer, M. L. Zheludkevich, Local pH and its evolution near Mg alloy surfaces exposed to simulated body fluids, Adv. Mater. Interfaces 5 (2018) 1800169. https://doi.org/10.1002/admi.201800169.
[55] J. Izquierdo, B.M. Fernández-Pérez, D. Filotás, Z. Őri, A. Kiss, R.T. Martín-Gómez, L. Nagy, G. Nagy, R.M. Souto, Imaging of concentration distributions and hydrogen evolution on corroding magnesium exposed to aqueous environments using scanning electrochemical microscopy, Electroanalysis 28 (2016) 2354–2366. https://doi.org/10.1002/elan.201600265.
[56] Z. Qiao, Z. Shi, N. Hort, N.I. Zainal Abidin, A. Atrens, Corrosion behaviour of a nominally high purity Mg ingot produced by permanent mould direct chill casting, Corros. Sci. 61 (2012) 185–207. https://doi.org/10.1016/j.corsci.2012.04.030.
[57] G.-L. Song, Z. Xu, Crystal orientation and electrochemical corrosion of polycrystalline Mg, Corros. Sci. 63 (2012) 100–112. https://doi.org/10.1016/j.corsci.2012.05.019.
[58] M. Liu, D. Qiu, M.-C. Zhao, G. Song, A. Atrens, The effect of crystallographic orientation on the active corrosion of pure magnesium, Scr. Mater. 58 (2008) 421–424. https://doi.org/10.1016/j.scriptamat.2007.10.027.
[59] L.G. Bland, K. Gusieva, J.R. Scully, Effect of crystallographic orientation on the corrosion of magnesium: comparison of film forming and bare crystal facets using electrochemical impedance and Raman spectroscopy, Electrochim. Acta 227 (2017) 136–151. https://doi.org/10.1016/j.electacta.2016.12.107.

5.4 Ca/In micro-alloying as a novel strategy to simultaneously enhance power and energy density of primary Mg-air batteries from anode aspect

Paper 4: Ca/In micro-alloying as a novel strategy to simultaneously enhance power and energy density of primary Mg-air batteries from anode aspect (published in Journal of Power Sources)

In this paper, element indium (In), which has been widely studied as activator for Al anodes [25, 62, 63], as an additional minor alloying element for binary Mg-Ca anodes was evaluated in terms of influence on self-corrosion resistance and discharge properties. Two micro-alloyed Mg-Ca-In anodes, with composition of Mg-0.1%Ca-0.2%In and Mg-0.2%Ca-0.4%In (all wt.%), were prepared by casting with water-cooling along with Mg-0.1%Ca. Re-deposition of metallic In on Mg-Ca-In anode surface after discharge was found and supposed to contribute to the breakage of surface film. Discharge potential of Mg-Ca-In anodes were more negative than the binary Mg-Ca due to film breakage and anodic activation promoted by galvanic coupling between Mg substrate and the re-deposited In. Besides, self-discharge was suppressed by minor In addition to binary Mg-Ca, although the reason was still unclear but was speculated to be related to NDE of Mg. Thus, utilization efficiency of the two Mg-Ca-In anodes were enhanced comparing to the binary Mg-Ca anode. Consequently, the battery failure testing indicated that Mg-air batteries based on Mg-Ca-In anodes showed increased service life, enhanced cell voltage and higher specific energy density than the system with binary Mg-Ca.

Journal of Power Sources 472 (2020) 228528

Contents lists available at ScienceDirect

Journal of Power Sources

journal homepage: www.elsevier.com/locate/jpowsour

Ca/In micro alloying as a novel strategy to simultaneously enhance power and energy density of primary Mg-air batteries from anode aspect

Min Deng [a,*], Linqian Wang [a], Daniel Höche [a,b], Sviatlana V. Lamaka [a], Pingli Jiang [a], Darya Snihirova [a], Nico Scharnagl [a], Mikhail L. Zheludkevich [a,c]

[a] MagIC – Magnesium Innovation Centre, Helmholtz-Zentrum Geesthacht (HZG), 21502, Geesthacht, Germany
[b] Computational Material Design, Faculty of Mechanical Engineering, Helmut-Schmidt-University University of the Federal Armed Forces, 22043, Hamburg, Germany
[c] Institute of Materials Science, Faculty of Engineering, Kiel University, 24143, Kiel, Germany

HIGHLIGHTS

- Effect of Ca/In micro-alloying on discharge properties of Mg anode is studied.
- Wasteful anode discharge is suppressed synergistically by Ca/In micro-alloying.
- Anodic dissolution is activated by re-deposition of metallic In at anode surface.
- Mg–Ca–In anode renders enhanced power and energy density to aqueous Mg-air cell.

ARTICLE INFO

Keywords:
Mg-air batteries
Micro-alloying
Mg–Ca–In anodes
Discharge activity
Anodic efficiency

ABSTRACT

Herein we report micro-alloying with the combination of Ca/In as a novel strategy to improve the anode performance for Mg-air batteries. Two micro-alloyed Mg–Ca–In anodes, i.e. Mg−0.1%Ca−0.2%In and Mg−0.2%Ca−0.4%In (wt%), are fabricated and evaluated in both configurations: half-cell and Mg-air full cell. Re-deposition of metallic In on anode surface during discharge is demonstrated. Anodic activation is then promoted by galvanic coupling between Mg and the re-deposited In, and film breakdown induced by In re-precipitation at the substrate/oxide film interface. Thus, the voltage and power density of Mg-air system are enhanced via adopting Mg–Ca–In anodes. Besides, wasteful-discharge of the Ca/In micro-alloyed anodes, which is related to the negative difference effect (NDE), is significantly suppressed. Anodic efficiency is consequently improved, reaching 80.2% at 5 mA cm^{-2} initial current density, and so is the service life of the Mg-air battery. Due to the enhanced voltage and anodic efficiency, Mg–Ca–In anodes enable Mg-air battery to exhibit outstanding energy density, e.g. 2259 Wh kg^{-1} at 5 mA cm^{-2}. Mg−0.1%Ca−0.2%In anode possesses superior performance in terms of low wasteful-discharge, enhanced discharge activity and high anodic efficiency. Therefore, we recommend micro-alloyed Mg–Ca–In, like Mg−0.1%Ca−0.2%In, as excellent candidates for anode materials of primary aqueous Mg-air batteries.

1. Introduction

The power sources with high energy density, high capacity, good stability and low cost are highly required. The investigation and development of rechargeable batteries attract much social attention due to their ability of recharging for many times, which results in a much lower cost of ownership than primary batteries. However, it is worth noting that rechargeable batteries are not applicable in some cases, such as in some places where recharging is impossible or impractical, like in the ocean or remote mountains. Primary batteries, under such circumstances, are better choices instead of rechargeable batteries because of their long self-life and high energy density [1,2]. Besides, primary batteries are also important as backup power sources, for schools, hospitals, etc. Therefore, much effort should also be paid to search for economically feasible primary batteries with no hazard to the environment. Primary Mg-air batteries are promising power sources attributed to the good theoretical electrochemical properties of Mg metal, like the large volumetric capacity (3832 mA h cm^{-3} versus 2061 mA h cm^{-3} of Li) and

* Corresponding author. Helmholtz-Zentrum Geesthacht, Max-Planck-Str. 1, 21502, Geesthacht, Germany.
E-mail address: Min.Deng@hzg.de (M. Deng).

https://doi.org/10.1016/j.jpowsour.2020.228528
Received 1 April 2020; Received in revised form 15 May 2020; Accepted 17 June 2020
Available online 7 July 2020

relatively negative electrode potential (−2.37 V vs. SHE) [3–6]. Besides, the adoption of oxygen from air as cathodic reactant reduces total weight of the battery system and, thus, remarkably enhances the energy density. Generally, the electrolytes used in primary Mg-air batteries are simple saline solutions with additives or natural seawater directly from the ocean [7–10]. Therefore, all components in this battery system are nonhazardous to the nature, rendering it a kind of environmentally benign energy system meeting the social requirement for green energy. In addition, the produced hydrogen gas accompanying the discharge process of Mg anode can also be the fuel source for fuel cells [11]. However, wide commercialization of primary Mg-air batteries is not yet achieved because of the insufficient practical properties. The rapid self-corrosion (or wasteful anode discharge) of Mg anodes during discharge leads to a shortened service life and reduced energy density of Mg-based battery system, due to the well-known negative difference effect (NDE) on Mg [12–14]. Besides, the battery voltage is relatively low because of the high open circuit potential (OCP, typically 1 V more positive than the theoretical thermodynamic potential) of ordinary Mg anode and large overpotential caused by sluggish anodic reaction kinetics or dense discharge products on anode surface [15–19]. Therefore, searching for Mg anode with low wasteful-discharge rate, more negative OCP and low anodic overpotential is vital for the improvement of Mg-air batteries.

Alloying as a conventional approach is effective to improve various properties of Mg via controllable microstructure and chemical composition. Likewise, some alloying elements, like Al, Zn, Pb, Sn, In, Li and RE [17,20–25], have been evaluated in attempt to modify the corrosion and discharge performance of Mg-based anode materials. Improvement has been achieved by an alloy with composition of Mg−11 wt%Li−3 wt% Al−1 wt%Zn−0.2 wt%Y, as reported by Liu et al. [20]. The voltage of a Mg-air battery with this Mg alloy as anode at 10 mA cm^{-2} in 3.5 wt% NaCl electrolyte reaches around 1.32 V and the discharge capacity is approximately 1300 mA h g^{-1}. Apart from these, Mg–Hg alloys also attract interests as anode materials as they possess the most negative OCP among all Mg alloys as found [26–28]. As reported by Feng et al. [26], Mg-6 wt% Hg alloy exhibits extremely negative corrosion potential in 3.5 wt% NaCl solution (around – 2.2 V vs. SCE), which, in fact, is the most negative corrosion potential reported of any Mg alloy. Nevertheless, the usage of toxic elements, like Hg and Pb, is against the vital social requirement for green energy. It should also be noted that most research work focuses on Mg anode development via high content of alloying elements. The heavy alloying load results in high fraction of second phases and, therefore, leads to severe exfoliation of undissolved metallic pieces during discharge, which is normally termed as chunk effect (CE). As reported by Deng et al. [29], large loss of anodic efficiency (up to 50%) could be arisen from the occurrence of CE that is induced by preferential dissolution of Mg matrix surrounding the noble second phases. Consequently, the energy density of Mg-air system is reduced and the service life is decreased. In such cases, development of micro-alloyed Mg anodes is a feasible strategy to avoid this issue. Micro-alloyed Mg anodes with excellent discharge properties are highly required. Besides, it is noteworthy that Mg anodes should have low wasteful-discharge rate during discharge to obtain high anodic efficiency and, consequently, enhanced energy density and service life. Virtually, all recent research concerning Mg anodes paid more attention to the corrosion rate of Mg anodes at OCP, which is normally considered as the evaluation criterion of wasteful-discharge rate under varied applied current. However, recent work of Deng et al. [29] indicates that the wasteful anode discharge of Mg electrode is greatly dependent on the applied current density. To assess the wasteful anode discharge behavior of Mg in time of discharging by the corrosion rate measured at OCP is not advisable. Different Mg alloys show varied increasing rate of real-time wasteful-discharge rate with the rising applied current density, resulting from different extent of NDE. Therefore, advanced Mg anodes should have low wasteful-discharge rate during discharging at different current densities (inhibited NDE) rather than low corrosion rate simply at OCP condition.

Our previous research indicates that binary Mg–Ca alloys possess great potential as environmentally benign anode materials with superior discharge properties [30,31]. Micro-alloyed Mg−0.1 wt%Ca alloy shows higher discharge voltage and energy density than that of high purity Mg, AM50 and AZ31 alloys measured in a lab-made Mg-air full cell. Nevertheless, the voltage (e.g., 1.6 V at 0.5 mA cm^{-2}) and peak energy density (1800 Wh kg^{-1}) should be improved towards the theoretical value, which is 3.1 V and 6.8 kWh kg^{-1} respectively. Thus, further improvement on Mg–Ca based anodes is desirable via micro alloying with other elements. Indium (In) as an alloying element has been successfully used in Al anodes for primary Al batteries to improve relevant discharge performance [32–36]. The In-induced activation on Al anodes is proposed to be the result of film disruption by In re-deposition back to anode surface. Likewise, recently, some work has been done to investigate the effect of In addition on performance of some Mg anodes [22,26,37–39]. Improvement to different extent has been achieved. As reported, the discharge voltage at 10 mA cm^{-2} of a Mg-air cell increases from 1.16 V to 1.22 V after replacing the Mg−9 wt%Al anode with Mg−9 wt%Al−1 wt%In Ref. [39]. Interestingly, almost all the relevant work regarding In-alloyed Mg anodes is based on Mg–Al alloys with high Al contents, from 3 to 9 wt%. Mg–Al based anodes normally output low discharge voltage because of low open circuit voltage (OCV) and relatively protective surface oxidation film caused by accumulation of Al_2O_3 [40–42]. In such cases, all the studied Mg anodes retain a low cell voltage (around 1.2 V at 10 mA cm^{-2}) although an enhancement by In addition (popularly 1 wt%) is achieved. On the other side, the corrosion rate of Mg anodes in NaCl-based electrolytes at OCP is accelerated after In alloying. Nevertheless, no information regarding the wasteful-discharge of these Mg–In anodes during discharge can be found. The possible different dissolution behavior at OCP condition and with applied current is neglected. Of late, Gore et al. [43] investigated the effect of In^{3+} ions existing in the electrolyte on the dissolution kinetics of Mg at OCP as well as under polarization. The dissolution rate of a high purity Mg at OCP is increased after addition of 1 mM $InCl_3$ into 0.1 M NaCl solution, whilst the self-corrosion under applied current densities is inhibited in the solution with $InCl_3$. Although the inhibition mechanism of In remains unclear, the authors propose that $InCl_3$ as a electrolyte additive could be an effective approach for developing Mg primary batteries with high performance. However, it should be noted that free In^{3+} ions would be consumed via precipitation as oxide or hydroxide during long-term battery operation, which consequently negatively affects the battery properties. A better alternative could be alloying Mg anode with an appropriate In content. In such a case, In ions are constantly replenished along with the continuous dissolution of anode materials.

Considering all the aforementioned strategies concerning Mg anodes development, we suppose that Mg micro alloyed with Ca and In is a high quality anode of aqueous Mg-air batteries. In the present work, two micro-alloyed Mg–Ca–In alloys are fabricated and appraised as anodes in half-cell and a lab-made Mg-air full cell. Corrosion rates at OCP condition and wasteful-discharge rates under different current densities are measured and compared. The activation effect of In on Mg anodes is confirmed and the activation mechanism is investigated from different aspects.

2. Experimental section

2.1. Materials preparation

Conventional gravity casting method was utilized to prepare all the micro-alloyed Mg anodes with nominal composition of Mg−0.1%Ca, Mg−0.1%Ca−0.2%In and Mg−0.2%Ca−0.4%In (hereafter weight percent). The raw materials used for alloy preparation were pure Mg ingot (MAGONTEC Ltd., Australia), Ca chips (Alfa Aesar GmbH & Co. KG, Germany) and In bars (Grirem Advanced Materials Co., Ltd., China)

with purity of 99.96 wt%, 99.9 wt% and 99.95 wt% respectively. All the raw materials for each alloy were melted at 760 °C in a steel crucible coated with boron nitride under protection of Ar/SF_6 (5:1) mixed gas to prevent melt oxidation and burning. Afterwards, the melts were cast and then quenched in water with a cylindrical steel mold with diameter of 60 mm preheated to 300 °C. The actual chemical compositions of all processed materials were shown in Table 1 as analyzed by spark spectrometer (spark OES, Ametek-Spectro) and X-ray micro fluorescence (μXRF, Bruker). The impurities Fe, Ni and Cu [12,44–47] that have deleterious influence on Mg corrosion resistance were below the generally accepted tolerance limits.

2.2. Microstructure characterization

All specimens after embedding in resin were carefully ground and polished to obtain high-quality surface for microstructure observation. Grinding process was carried out on silicon carbide papers consecutively up to 4000 grit. Afterwards, samples were polished to remove scratches using a water-free oxide polishing suspension (OPS) containing SiO_2 followed by a cleaning process in ethanol by ultrasonication. Second phase morphology and distribution were observed with a scanning electron microscope (SEM, TESCAN VEGA3) combined with energy dispersive X-ray spectroscopy (EDS) to analyze the phase composition. Elemental mapping was also obtained with the SEM to investigate the distribution of each selected alloying element via backscattered-electrons (BSE) detector at 15 kV. Besides, atomic Force Microscopy (AFM, Nanowizard, JPK Instruments AG) combined with Scanning Kelvin Probe force microscopy (SKPFM) was utilized to measure the Volta potential difference between second phase particles and the Mg matrix. The adopted silicon probe supplied by Innovative Solutions Bulgaria Ltd. (Bulgaria) is coated with a Cr/Pt conductive coating and possesses a resonance frequency of 75 kHz and a force constant of 3 N m^{-1}. The measurements were conducted immediately after sample polishing via the aforementioned processes.

2.3. Corrosion and wasteful anode discharge rate determination

The corrosion rates of all prepared alloys at OCP and wasteful-discharge rates during discharge were determined by the commonly accepted hydrogen evolution (HE) method at 23 ± 2 °C. Hydrogen gas produced during immersion at OCP was collected simultaneously via a widely used set-up combining a funnel and an inverted burette [48,49]. The solution used throughout was 3.5 wt% NaCl solution based on deionized water. The volume of solution was 350 ml for each test. Two bulk specimens with a total surface area of approximately 14 cm^2 were used for each measurement applied with stirring by an electromagnetic stirrer at 350 rpm. HE rates during discharge were measured with the same set-up adopted in our recent work [29]. Each sample was embedded in epoxy exposing a working surface of 15× 15 mm. A potentiostat (Gamry interface 1000) was used to apply specific current densities with a classic three-electrode system consisting of a Pt wire counter electrode, a saturated-KCl filled Ag/AgCl reference electrode and an Mg electrode. HE rates of each Mg anode were determined when discharge at varied current densities, i.e. 1, 5, 10 and 20 mA cm^{-2} for 8 h, 2 h, 2 h and 1 h, respectively. Each measurement was conducted for three times to ensure data reproducibility.

2.4. Electrochemical measurements

The aforementioned three-electrode system was also applied to measure the potentiodynamic polarization curves and electrochemical impedance spectra (EIS) via a Gamry Interface-1000 potentiostat. Samples with 1 cm^2 working surface area were utilized. Anodic and cathodic polarization curves were measured separately with a scanning rate of 1 mV s^{-1} after a stabilization period of 1 h in the solution to obtain a relatively stable OCP. The scanning potential of anodic curves was – 10 mV versus OCP upwards to – 1.4 V versus the reference electrode, while for cathodic curves it was +10 mV versus OCP downwards to – 2.2 V versus the reference. Besides, polarization curves were also obtained after immersion in the solution for 48 h via direct scanning from – 250 mV to +400 mV versus OCP. For each alloy, the EIS was determined after immersion for different period, i.e., 0.5, 4, 8, 24, and 48 h, to evaluate the corrosion evolution. The scanned frequency range was 100 kHz to 0.01 Hz, and the sinusoidal AC voltage was 10 mV rms. The EIS results were fitted by Zview software according to a proposed equivalent circuit. All the electrochemical measurements were carried out for three times with diverse specimens to ensure data reproducibility.

Half-cell discharge curves were recorded via the Gamry potentiostat with the aforementioned three-electrode system at constant current densities. The surface area of each specimen as working electrode was 1 cm^2. EIS was also determined after discharge, such as at 1 mA cm^{-2} for 8 h and 20 mA cm^{-2} for 2 h, to evaluate the discharge activity of each Mg anode. The lowest scanning frequency was set as 0.1 Hz for the EIS measurement after discharge. Besides, the surface and cross-sectional morphologies after discharge were observed under SEM. X-ray photoelectron spectroscopic (XPS) measurements for investigating the anode surface after discharge were performed using a Kratos Axis Ultra DLD instrument (Kratos Analytical, Manchester UK) equipped with a monochromatic Al Kα anode working at 15 kV (225 W). The pass energy for recording of the survey spectra and region spectra was 160 eV and 20 eV, respectively. The investigated area of the sample was selected as 700 × 300 μm. In order to analyze the inside of the surface film, Ar etching was applied for 30 min by a rate of 10 nm min^{-1} with respect to Ta_2O_5. The acceleration voltage and extraction current for the Ar etching were 3.8 kV and 160 mA. The XPS data were validated and evaluated using CASA-XPS software (version 2.3.18). Background subtraction (U2 Tougaard) was conducted for calculation and deconvolution of the region spectrum. The C 1s signal was used for spectra calibration and adjusted to 284.5 eV.

2.5. Mg-air battery tests

Discharge properties of prepared Mg anodes were evaluated in a lab-made Mg-air full cell. The adopted cathode, with surface area of around 2.5 cm^2, was a commercial air cathode (Gaskatel GmbH, No. 82011) with C/MnO_2 catalysts, nickel mesh current-collector and PTFE gas diffusion layer, while the electrolyte was 3.5 wt% NaCl solution. The anode was an alloy specimen embedded in resin with exposing surface area of approximately 2.2 cm^2. An as-cast AZ31 Mg alloy, which is commercially accepted as anode materials for Mg batteries, was tested as well for comparison. Cell voltage was recorded simultaneously during discharge at different current densities for 1 h. Afterwards, the average voltage and power density at different current densities were calculated.

Battery discharge tests were performed in a constructed Mg-air full

Table 1
Chemical composition of as-cast Mg anodes (wt%).

Materials	Ca	In	Fe	Ni	Cu	Al	Mn	Si	Mg
Mg−0.1Ca	0.07	–	0.0018	0.0011	0.0012	<0.01	0.017	0.0036	Bal.
Mg−0.1Ca−0.2In	0.09	0.25	0.0016	0.0008	0.0009	<0.01	0.014	0.0052	Bal.
Mg−0.2Ca−0.4In	0.19	0.37	0.0043	0.0008	0.0009	<0.01	0.015	0.0052	Bal.

cell with the schematic shown in Fig. 1 to evaluate the service life of varied anodes. The anode was strip-shaped sample corresponding to each Mg alloy. The dimension of the anode working part immersed into the electrolyte is 30 × 5 × 2.5 mm. The Mg-air cell assembled with varied anode material was discharged at constant current of 23.75 and 47.5 mA, which respectively correspond to an initial current density of 5 and 10 mA cm^{-2}. A cut-off voltage of 0.5 V was set for each test. Afterwards, service life and average voltage of the Mg-air cell with different anode can be obtained from the voltage-time curves. Besides, anodic efficiency, discharge capacity and energy density can be calculated via the same equations used in other literatures [30,31], as the weight of consumed anode was known. This kind of battery discharge test for all anodes at different current densities were repeated twice. Good reproducibility was indicated as slight deviation (below 5%) between the two measurements was obtained.

3. Results and discussion

3.1. Microstructure

Fig. 2a-c presents the SEM images of all prepared Mg alloys, indicating increasing amount of intermetallic particles (IMPs) with the rising In content. The IMPs in Mg−0.1Ca alloy are mainly MgCaSi because of the existence of trace Si in the alloy. This is consistent with the solidification simulation results reported by Jin et al. [50], which indicates that MgCaSi phase solidifies prior to Mg_2Ca in the Mg−0.5 wt%Zn−0.2 wt%Ca system with 145 ppm Si. The chemical compositions of the IMPs are also analyzed by EDS (one representative result is indicated in Table 2), proving the preferential formation of MgCaSi. In the case of Mg–Ca–In alloys, two types of IMPs, i.e. Mg–Ca–Si and Mg–Ca–In–Si, are determined by EDS and elemental mapping as presented in Fig. 2d-g and Table 2. The stoichiometry of Mg–Ca–In–Si phases is not known since there is a paucity of phase diagram or relevant thermodynamic data available for predicting the equilibrium phases in Mg–Ca–In based alloys, e.g. using Pandat™ 2017. Some literatures reported Mg–Ca–In precipitates with a Ca/In content ratio of 2:1 after aging heat treatment [51,52], but Si was not included in these work. Apparently, no fixed ratio of Ca/In is detected in the present work from the EDX results and Si indicates a highly random content in the Mg–Ca–In–Si IMPs. Nevertheless, determination of the specific stoichiometry and crystal structure of Si-enriched Mg–Ca–In phases are beyond the scope of this work. Much attention is paid to the electrochemical potential of these IMPs relative to Mg matrix, which is more relevant to the self-corrosion and discharge performance of Mg anodes. Fig. 2h-j presents the Volta potential map and corresponding Volta potential along line *I* and *II* in Mg−0.1Ca−0.2In alloy obtained by SKPFM. The results indicate that all the IMPs have higher Volta potential than surrounding Mg matrix. Micro galvanic couples, in which the matrix acts as anode and IMP acts as cathode, are pronounced during corrosion and discharge process. Thus, preferential dissolution of Mg matrix is favored by the existence of different IMPs.

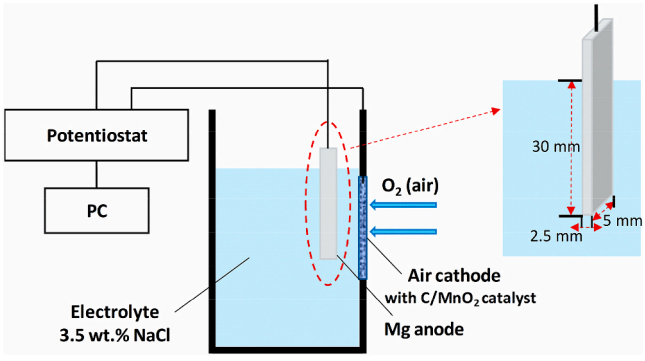

Fig. 1. Schematic of a lab-made Mg-air cell for battery discharge test.

3.2. Half-cell discharge properties

Discharge potential at different current densities was measured in half-cell and presented in Fig. 3(a–d). Obviously, more negative potential is achieved by In addition to Mg−0.1Ca anode, which would consequently contribute to higher output voltage of Mg-air full cell. It is noticeable that both Mg–Ca–In anodes exhibit a negatively shifting potential at the beginning stage before presenting a relatively stable potential afterwards. The time for reaching the steady discharge differs with varied current densities, such as approximately 3 h at 5 mA cm^{-2} while less than 1 h at 20 mA cm^{-2}. Besides, at all applied current densities, Mg−0.2Ca−0.4In anode requires less time for the stabilization than Mg−0.1Ca−0.2In. The activation of Mg anodes induced by In addition is probably related to the re-deposition of In onto the anode surface from In^{3+} produced by anode dissolution as proposed by Li et al. [22]. A displacement reaction contributing to the re-precipitation of In is described in Eq. (1) as assumed by Gore et al. [43].

$$3\,Mg\,(s) + 2In^{3+}\,(aq) = 3Mg^{2+}\,(aq) + 2In\,(s) \quad (1)$$

XPS measurements were applied in attempt to prove the existence of metallic In either for the surface of a Mg–Al–Zn–In anode after discharge in blank 3.5 wt% NaCl solution [22] or a pure Mg surface after immersion in 0.1 M NaCl + 1 mM $InCl_3$ solution [43]. However, from the exhibited results, the existence of $In_2O_3/In(OH)_3$ is more pronounced than pure In. Dissimilarly, in this work, apart from the surface outermost layer, the inside of the surface film on Mg−0.2Ca−0.4In anode after discharge is also analyzed by XPS after Ar etching for 30 min by a rate of 10 nm min^{-1}. The survey spectrum related to the inside film presented in Fig. 4a indicates the presence of Na, Cl and O, ensuring that the measurement is performed still on the products film rather than anode substrate. The In 3d XPS region spectrum indicated in Fig. 4b confirms the existence of metallic In. The In 3d 5/2 peak at 443.55 eV and In 3d 3/2 peak at 451.09 eV, with a specific distance of 7.54 eV, are related to indium in the form of elementary In Ref. [53,54]. It is noteworthy that no information of metallic Ca is found from the XPS spectra. Therefore, the possibility can be excluded that In signal in XPS results may be from the possible existence of IMPs in discharge products layer, since Ca shows a much higher content than In the mentioned IMPs as shown by EDS (Table 2). Note that, however, metallic In has not been detected by the XPS performed on the surface outermost layer without etching, implying that In re-deposition takes place at the vicinity of anode substrate. Since In has more positive electrochemical potential than Mg, the re-deposition of metallic In on Mg anode substrate would definitely promote the dissolution of Mg driven by micro galvanic couples and, consequently, increase the discharge activity. Meanwhile, the redeposited In would be detached from the anode substrate after dissolution of surrounding Mg matrix. It is convincible that the re-deposition and detachment of In could reach a dynamic equilibrium after a period, leading to relatively stable discharge voltage. Because of the low In contents in the anodes (0.2 and 0.4 wt%) studied in this work, several hours are needed before reaching the dynamic equilibrium as indicated from the discharge curves due to insufficient In^{3+} ions within initial discharge period. Reasonably, enhanced discharge current density and higher In content in anode, which both contribute to a higher concentration of generated In^{3+}, are able to decrease the time required for the stabilization process. Similar phenomenon is not found from other published work regarding Mg anodes with In Ref. [22,37,39,55], possibly because of the relatively higher applied In content (e.g., 1 wt%) and the synergetic effect of other elements in high contents.

Moreover, it is noteworthy that the discharge potential of Mg−0.2Ca−0.4In anode is more positive than Mg−0.1Ca−0.2In at 1 mA cm^{-2}, but shows a tendency of being comparable or more negative with the increased current density. EIS determined after discharge are presented in Fig. 3e and f, illustrating varying discharge activity under different current densities. Remarkably, In-based Mg–Ca anodes show

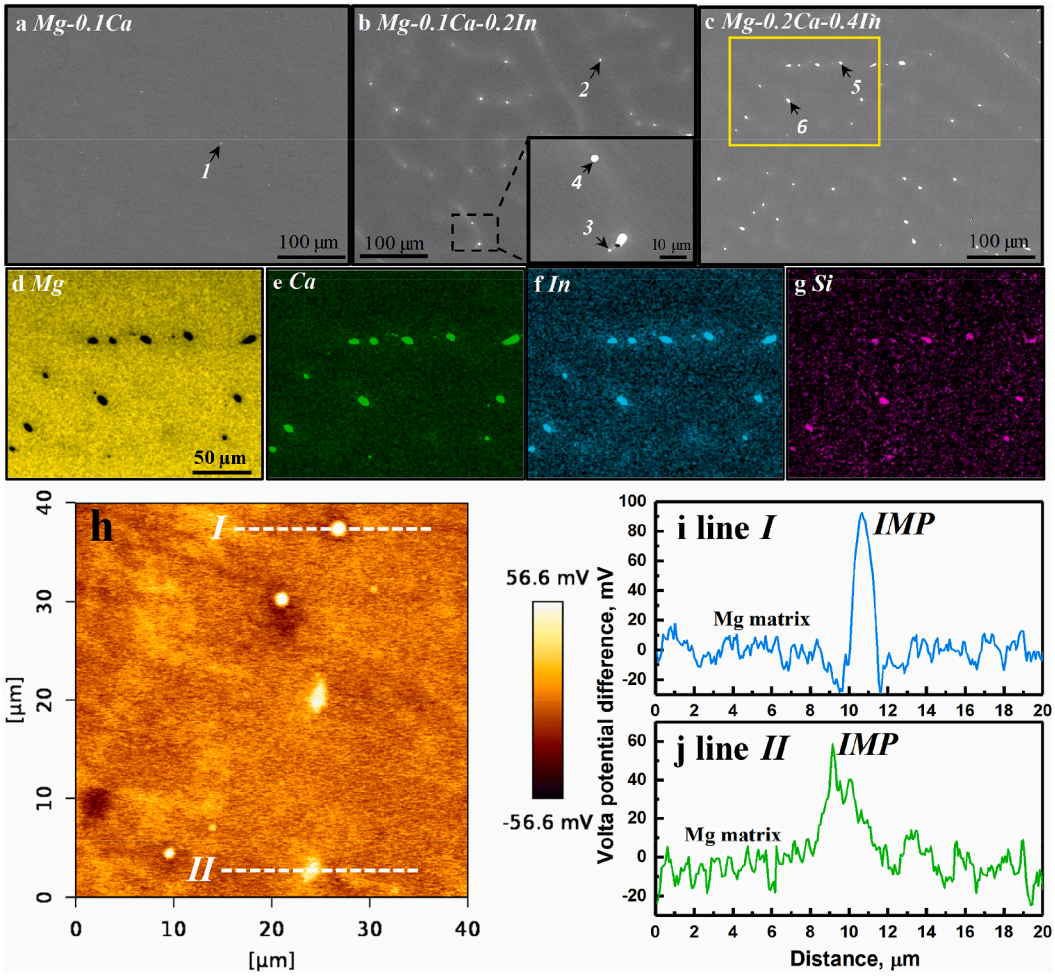

Fig. 2. (a–c) SEM images of three as-cast Mg alloys; (d–g) Corresponding elemental mappings for the marked region in (c) Mg−0.2Ca−0.4In alloy. (h) Volta potential map of Mg−0.1Ca−0.2In alloy obtained by SKPFM. (i, j) Corresponding Volta potential along line *I* and *II*, respectively.

Table 2
Chemical compositions of the particles marked in Fig. 2(a–c) by EDS analysis (wt %).

Particle	*1*	*2*	*3*	*4*	*5*	*6*
Mg	73.5	57.9	65.9	84.0	75.7	65.3
Ca	13.9	24.6	20.4	8.4	18.7	25.0
In	/	9.3	/	7.3	5.2	6.3
Si	12.6	8.2	13.7	0.3	0.4	3.4

significantly lower electrochemical impedance after discharge than binary Mg−0.1Ca, corresponding to enhanced discharge activity and decreased overpotential by In addition. Mg−0.2Ca−0.4In shows slightly higher electrochemical impedance than Mg−0.1Ca−0.2In measured after discharge at 1 mA cm^{-2}, while lower regarding 20 mA cm^{-2}. Therefore, it is speculated that different In content would lead to varying discharge activity of the Mg–Ca–In anodes with relevance to varied discharge current densities. Besides, the surface morphologies after discharge presented in Fig. 5(a–c) explicate altered diffusion overpotential during discharge process after In addition. Mg−0.1Ca anode surface is densely and integrally covered by discharge products (Fig. 5a), which causes large transport overpotential. In contrast, the discharge products film on the surface of Mg–Ca–In anodes is deformed (Fig. 5b and c). Dense discharge products are only found at specific spots. Most areas are covered by thin and porous products film. Besides, some cavities without discharge products are apparently visible from the Mg–Ca–In surface after discharge, indicating effortless breakage and peeling of the products. Consequently, the transport overpotential during discharge decreases, being conducive to achieve enhanced battery voltage. The exfoliation of products is promoted by In addition possibly because of the accumulation of redeposited In on the interface of anode substrate and products film, which certainly reduces the adherence between the substrate and products, similar to the proposed activation mechanism of In on Al anodes [33].

In addition, the cross-sectional morphologies after discharge are illustrated in Fig. 5(d–f) to evaluate the possible occurrence of "chunk effect", which has been proved to have significant influence on the anodic efficiency and capacity of Mg anodes during discharge. No detached metallic pieces can be found from the cross sections of Mg−0.1Ca and Mg−0.1Ca−0.2In anodes, implying that no large loss of anodic efficiency would be caused by chunk effect. On the contrary, large metallic pieces, which are undissolved Mg matrix as confirmed by EDS (not shown here), are detached from the substrate and exist in the discharge products layer. The loss of these portions would certainly result in large efficiency loss of Mg−0.2Ca−0.4In anode and, thus, reduce the energy density of Mg-air cell. The chunk effect is related to the non-uniform dissolution of Mg−0.2Ca−0.4In anode, which is possibly due to the higher amount of IMPs and inhomogeneous deposition of In.

3.3. Corrosion and wasteful anode discharge rate

Importantly, Mg anodes should have low corrosion rate during non-discharge interval (at OCP condition) to ensure relatively long battery life. The corrosion rate of the micro-alloyed anode are evaluated via HE

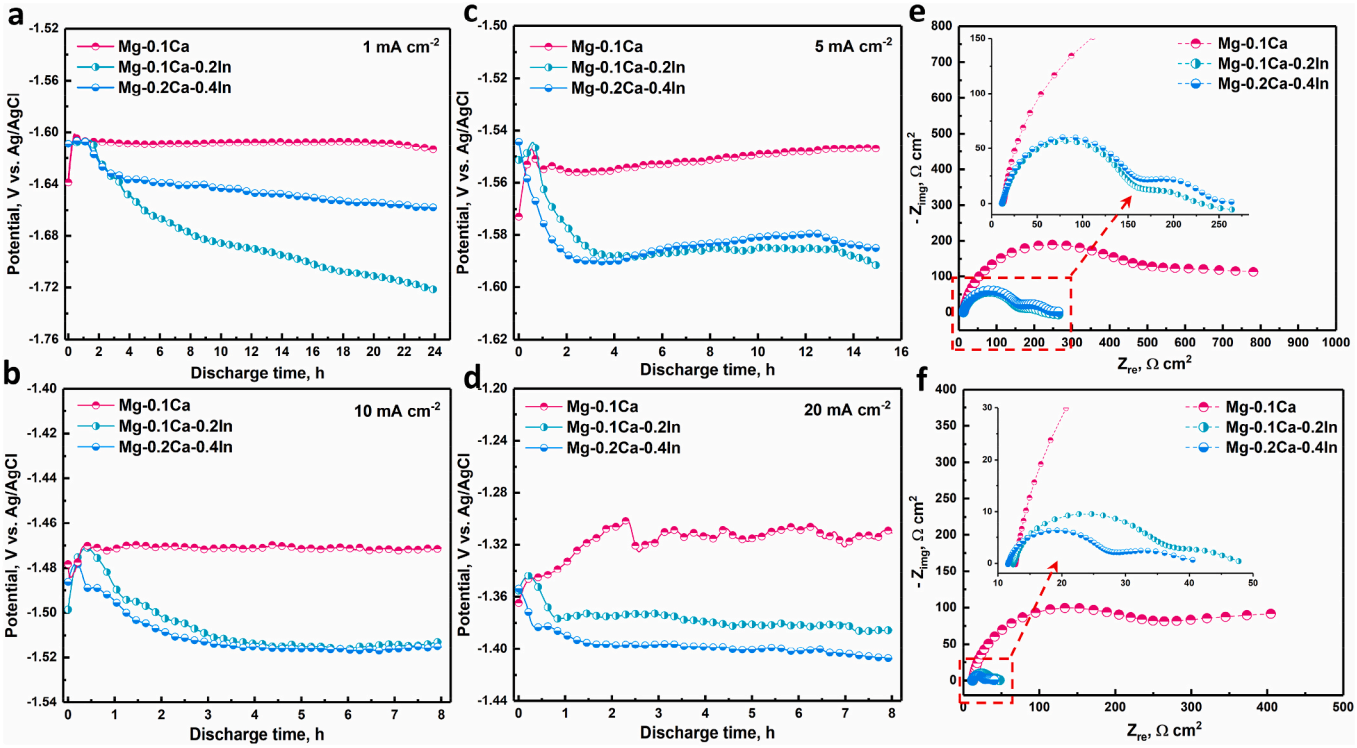

Fig. 3. (a–d) Half-cell discharge curves of as-cast Mg anodes at different current densities in 3.5 wt% NaCl solution. (e, f) Nyquist plots of EIS measured after discharge at 1 mA cm^{-2} for 8 h and 20 mA cm^{-2} for 2 h, respectively.

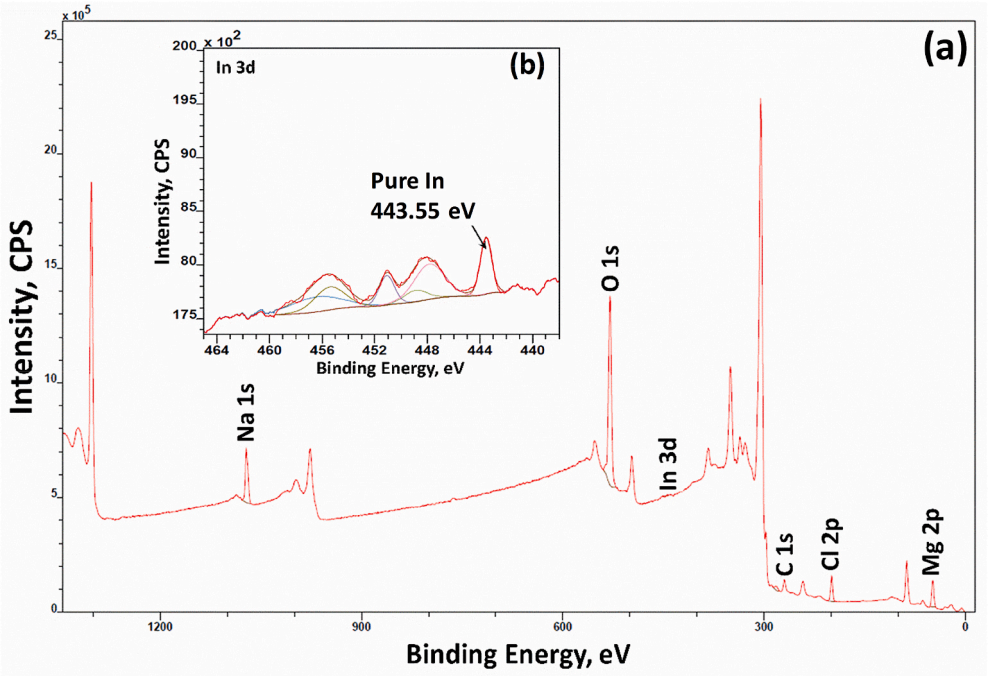

Fig. 4. (a) XPS survey spectrum and (b) High resolution In 3d region spectrum obtained on the Mg−0.2Ca−0.4In anode surface after discharge at 1 mA cm^{-2} for 1 h in 3.5 wt% NaCl solution (after Ar etching for 30 min by a rate of 10 nm min^{-1}).

tests as indicated in Fig. 6a. Generally, the HE rate (V_H) of Mg−0.1Ca anode is enhanced with addition of In, but the acceleration is slight at 0.2 wt% In load. The corrosion rate (P_H), which can be calculated via the formula $P_H = 2.088\ V_H$ [56], is 0.44 mm y^{-1} for Mg−0.1Ca and 0.48 mm y^{-1} for Mg−0.1Ca−0.2In, lower than that of majority of Mg alloys in NaCl solution with similar concentration as summed up in literatures [57,58]. Before reaching the stage with steady corrosion related to the formation of a protective film, all the studied alloys show a relatively fast corrosion rate at the initial stage indicated by the hydrogen evolution curves. Interestingly, Mg−0.1Ca shows slightly higher corrosion rate than Mg−0.1Ca−0.2In alloy during the first several hours, differing from the situation in the latter period. EIS results presented in Fig. 6(c–f)

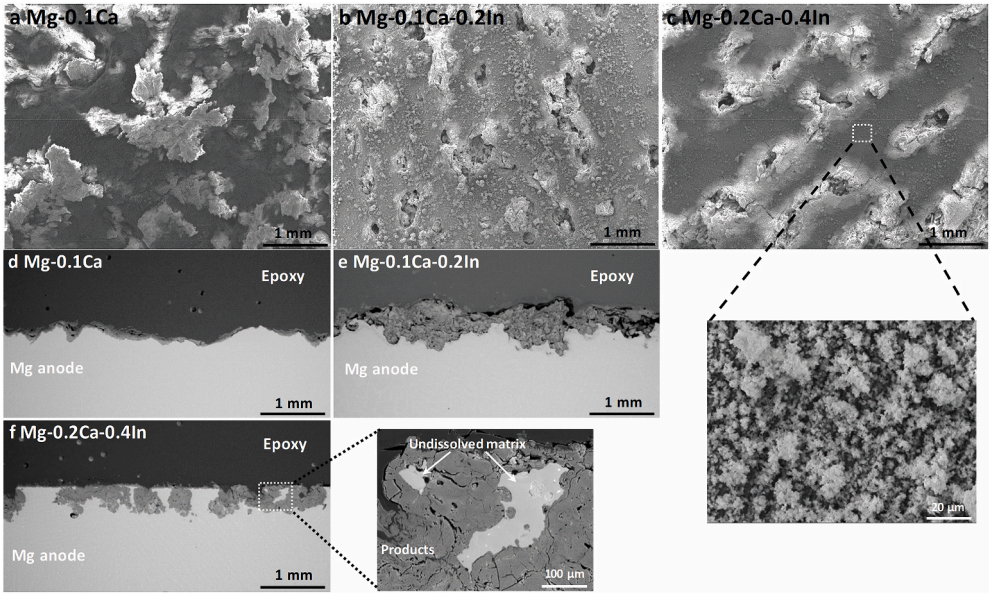

Fig. 5. Surface morphology after discharge at 5 mA cm^{-2} for 15 h in 3.5 wt% NaCl solution corresponds to (a) Mg−0.1Ca, (b) Mg−0.1Ca−0.2In and (c) Mg−0.2Ca−0.4In. Cross-sectional morphology of (e) Mg−0.1Ca, (d) Mg−0.1Ca−0.2In and (f) Mg−0.2Ca−0.4In after discharge at 5 mA cm^{-2} for 15 h.

reveal the same variation of the corrosion rate corresponding to all the studied Mg alloys during the whole immersion period. R_{sum}, which equals to the sum of charge transfer resistance (R_{ct}) and film resistance (R_f), is used to evaluate the corrosion resistance of Mg alloys. R_{ct} and R_f can be obtained via fitting the EIS results according to the proposed equivalent circuit as shown in Fig. S1 [59]. Apparently, from Fig. 6c, R_{sum} of Mg−0.1Ca is slightly lower than that of Mg−0.1Ca−0.2In during the initial immersion period of 8 h, indicating higher corrosion rate in this period. With prolonging immersion time, R_{sum} of Mg−0.1Ca increases and tends to be higher than Mg−0.1Ca−0.2In, corresponding to the lowering corrosion rate as shown by HE tests. According to the polarization curves after 1-h OCP measurement (Fig. 6h), the cathodic reaction kinetics is weakened after addition of 0.2 wt% In to Mg−0.1Ca, whilst no significant variation is indicated regarding anodic reaction kinetics. However, after immersion for 48 h, Mg−0.1Ca shows moderated kinetics for both anodic and cathodic reactions compared to Mg−0.1Ca−0.2In (Fig. 6i). A protective film forms on the surface of Mg−0.1Ca after long time immersion, speculated from the anodic polarization curve that shows dilatorily increasing current density within the scanning potential range. In contrast, a breakdown potential, after which the current density increases rapidly, can be found with respect to the Mg–Ca–In alloys. According to the EIS results presented in Fig. 6d-f, the film resistance of Mg−0.1Ca increases from 800 Ω cm^2 at the beginning to 4000 Ω cm^2 after 48 h. By contrast, the film resistance alteration of Mg−0.1Ca−0.2In is slight, from 1200 to 2000 Ω cm^2. The much higher film resistance also indicates a more protective film formed on Mg−0.1Ca surface after long time immersion. The absence of a film with sufficient protection, which is because of the accumulation of redeposited In close to Mg substrate as mentioned above, is one of the reason for the increased corrosion rate at OCP. Another reason should be the additional galvanic corrosion caused by the contact of Mg substrate and re-precipitated metallic In. Noticeably, Mg−0.2Ca−0.4In shows higher corrosion rate than other two alloys during the whole immersion period. The slightly faster corrosion at the beginning is due to the enhanced cathodic reaction kinetics caused by more cathodic IMPs as the result of higher alloying content. Afterwards, the much higher corrosion rate compared with other alloys is because of more re-deposition of In due to the higher In content, which favors a higher concentration of In^{3+} ion.

Service life and energy density of Mg-air batteries are tightly dependent on the wasteful-discharge rate of anodes in time of operating, which is the main issue hindering their application. It must be noted that corrosion rate measured under OCP condition is unable to exactly reflect the wasteful-discharge rate during discharge at different current densities as mentioned above [29]. Therefore, the wasteful-discharge behavior of the prepared Mg anodes were also determined via HE tests with varied applied current density as depicted in Fig. 7(a–d). Hydrogen evolution rate at varying current densities (Fig. 7e) are calculated according to the steady-state HE and then the wasteful-discharge rate (converted to current density) (Fig. 7f) are obtained accordingly using Faraday's law. Apparently known from the presented results, all the studied anodes exhibit a linearly increasing wasteful-discharge rate as a function of applied current density over the whole current density range, which is consistent with the well-known NDE on Mg metal. The data are linearly fitted into straight lines with different slopes, k, which reflects the increasing rate of wasteful-discharge rate with raising applied current density. The slope is 0.68, 0.29 and 0.39 for Mg−0.1Ca, Mg−0.1Ca−0.2In and Mg−0.2Ca−0.4In, respectively. Hence, the wasteful-discharge rate of Mg−0.1Ca−0.2In is similar to that of Mg−0.1Ca at 1 mA cm^{-2} current density, but shows a tendency of being much lower than Mg−0.1Ca with increasing current density. So is the Mg−0.2Ca−0.4In anode, although the slope is larger than Mg−0.1Ca−0.2In. The different slopes demonstrate varied extent of NDE happening on the three Mg anodes. In general, the addition of In suppresses the NDE and reduces the wasteful-discharge rate of Mg–Ca anode, which is definitely beneficial for achieving higher anodic efficiency. Additionally, the Mg–Ca–In alloys show significantly lower wasteful-discharge rate and k than high purity Mg, AZ31 and AM50 alloys (see Fig. S2), which are widely used as anode materials. No doubt, this issue is related with NDE. However, unfortunately, the mechanism of NDE is still a controversial puzzle despite several models has been proposed in last decades in attempt to explain it [12,13,60–63]. Therefore, the reason for the inhibited NDE by In addition deserves more effort, but is not within the scope of this work.

3.4. Mg-air battery tests

Fig. 8a illustrates the cell voltage and power density of a lab-made Mg-air battery adopting different Mg anodes. Note, it is not sensible to compare the voltage-involved battery properties between different

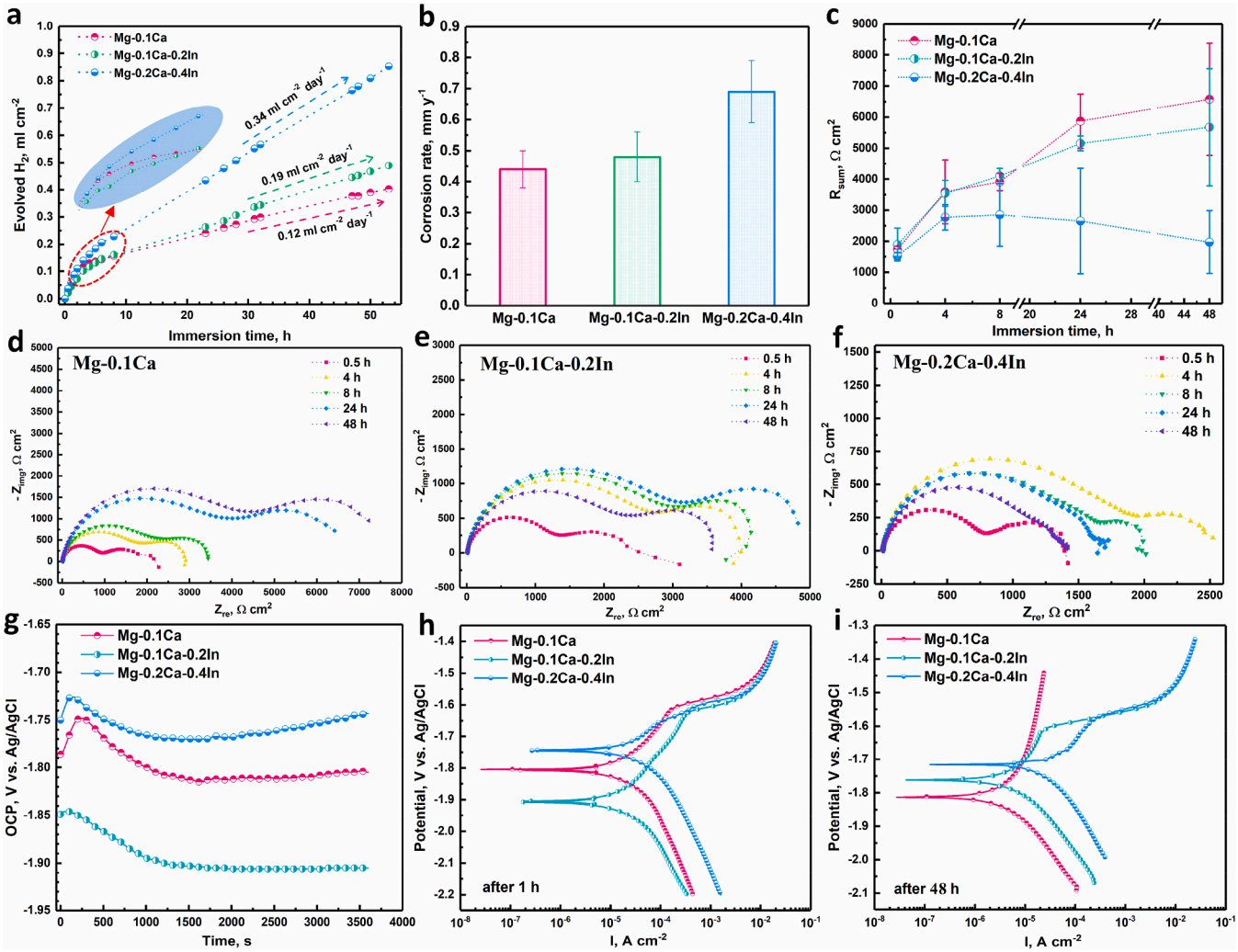

Fig. 6. (a) Hydrogen evolution of as-cast alloys during immersion. (b) Calculated average corrosion rate during immersion of 52 h based on hydrogen evolution. (c) Sum of charge transfer resistance and film resistance varies with immersion time obtained via EIS fitting results. (d–f) Nyquist plots from EIS of as-cast alloys after immersion for different time. (g) OCP of as-cast Mg anodes. (h, i) Polarization curves after immersion for 1 h and 48 h, respectively, without IR compensation. Note that all the measurements are carried out in 3.5 wt% NaCl solution.

literature sources as varied cathode materials are used, which is also one important limiting factor for battery voltage. Therefore, in this work, AZ31 is included for comparison, as it is a commercially acceptable anode material for aqueous Mg primary batteries. Obviously, the Mg-air system based on Mg−0.1Ca shows much higher cell voltage than that based on AZ31, which is consistent with the previously reported results [30]. Besides, the cell voltage is further enhanced by replacing the Mg−0.1Ca anode with Mg–Ca–In anodes, especially at high current densities. For instance, at 5 mA cm^{-2}, the voltage is 1.31, 1.40 and 1.46 V for the battery with AZ31, Mg−0.1Ca and Mg−0.1Ca−0.2In anode, separately, while 0.68, 0.78 and 0.92 V respectively at 40 mA cm^{-2}. In addition, the peak power density is enhanced as well by the adoption of In-based anodes. The battery with Mg−0.1Ca−0.2In anode possesses a peak power density of 39.8 mW cm^{-2} at 55 mA cm^{-2}, while the batteries with AZ31 and Mg−0.1Ca anode show peak power densities of 27.8 and 31.2 mW cm^{-2} individually. Fig. S3 presents the results of intermittent discharge testing to evaluate the re-operation property with regard to the battery with different anodes. Apparently, the battery with Mg–Ca anode shows low voltage at the very beginning of the re-operation session after a non-discharge interval due to large overpotential caused by surface film. By comparison, the battery with Mg–Ca–In anode is able to be reactivated immediately during re-operation attributed to the less compact film and In re-deposition.

The voltage profiles for battery discharge tests with the configuration presented in Fig. 1 are depicted in Fig. 8b and c, and the relevant battery properties obtained are listed in Table 3. Not surprisingly, the batteries based on Mg–Ca–In anodes exhibit higher voltage than those based on AZ31 and binary Mg−0.1Ca anode. Importantly, battery service life is significantly enhanced via utilizing Mg–Ca–In anodes. Under 23.75 mA constant current load, the service life is 39.2, 40.6, 49.1 and 44.4 h for the cell with AZ31, Mg−0.1Ca, Mg−0.1Ca−0.2In and Mg−0.2Ca−0.4In anodes, independently. The improvement of battery service life associated with In addition is mainly due to the increased anodic efficiency of the anode material as indicated in Table 3. With 0.2 wt% In addition, the anodic efficiency of Mg−0.1Ca anode is boosted from 66.4% to 80.2% at 23.75 mA and from 61.9% to 77.8% at 47.5 mA. The improvement on anodic efficiency is attributed to the inhibited wasteful-discharge rate by the addition of In and the absence of chunk effect as mentioned in above sections. Moreover, attributing to the improved cell voltage and anodic efficiency, the energy density of the tested Mg-air battery is enhanced consequently. The system with Mg−0.1Ca−0.2In anode shows an energy density of 2259 Wh kg^{-1} at 23.75 mA. For comparison, 1629 and 1835 Wh kg^{-1} for the cell with AZ31 and Mg−0.1Ca anodes are obtained, respectively. In other words, an enhancement of 39% can be achieved via replacing AZ31 by Mg−0.1Ca−0.2In as the anode.

In conclusion, micro alloying with indium can improve the

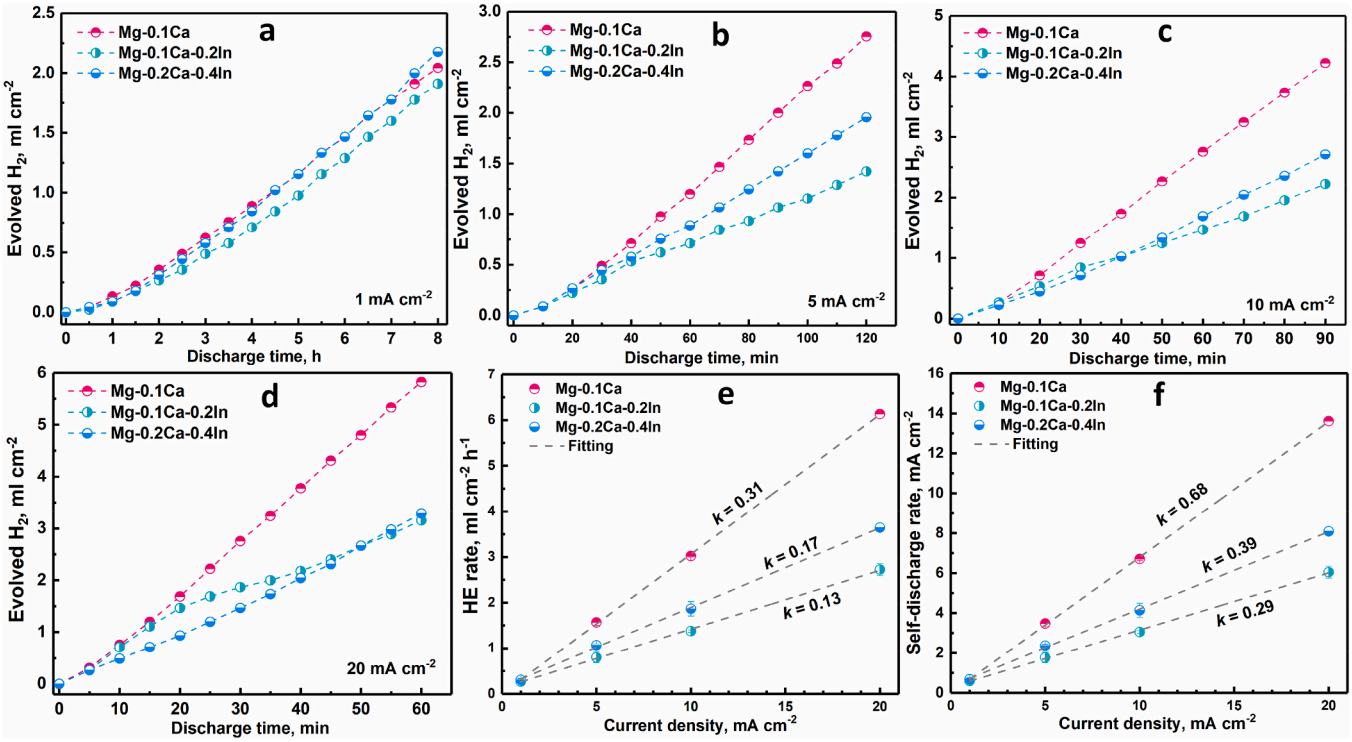

Fig. 7. (a–d) Hydrogen evolution of as-cast Mg anodes during discharge at different current densities in 3.5 wt% NaCl solution. Typical results of triplicate measurements are shown. (e) Hydrogen evolution rate as a function of discharge current density. (f) Wasteful-discharge rate associated with HE as a function of discharge current density. Linearly fitting results are presented in (e, f) with a slope *k*. Hydrogen evolution rate is determined based on the steady-state HE. Error bar is not visible when the standard deviation is less than the symbol.

properties of Mg–Ca anode and, thus, boost the cell voltage and energy density of Mg-air system. Mg−0.2Ca−0.4In anode renders similar discharge voltage to Mg−0.1Ca−0.2In but the anodic efficiency is slightly lower. Therefore, Mg−0.1Ca−0.2In is suggested herein as an excellent anode material enabling superior voltage and energy density for primary Mg-air batteries. The proposed strategy, i.e. micro alloying with Ca/In, is feasible for improving anode properties and, thus, achieving high performance Mg-air batteries.

4. Conclusions

Herein, we propose micro alloying Mg anode with the combination of Ca/In as a feasible strategy to improve the battery properties of primary Mg-air system. Two micro-alloyed Mg anodes, i.e., Mg−0.1%Ca−0.2%In and Mg−0.2%Ca−0.4%In (weight percent hereafter), are fabricated and evaluated in terms of corrosion performance, wasteful-discharge rate and discharge activity. The addition of trace In significantly improves the discharge activity and suppresses the wasteful-discharge rate of newly developed Mg−0.1%Ca anode [30]. Moreover, the Mg–Ca–In anodes exhibit significantly lower wasteful-discharge rate than commercially accepted Mg anodes, like high purity Mg, AZ31 and AM50.

The activation of Mg anodes induced by In is based on the re-deposition of metallic In on anode surface via continuous In^{3+} ions generation accompanying anode dissolution. The re-deposited In promotes the dissolution of anode substrate via galvanic coupling with Mg and ruptures the film structure as well, leading to lower transport overpotential. The suppressed wasteful-discharge after In addition is associated with the inhibited NDE, with further mechanism remaining unclear. Consequently, Mg-air battery tests indicate that the adoption of Mg−0.1%Ca−0.2%In enables the cell to exhibit enhanced voltage and power density, compared with the cell based on AZ31 and Mg−0.1%Ca. Additionally, the battery service life is increased by using Mg–Ca–In anodes because of the boosted anodic efficiency, such as from 40.6 to 49.1 h after replacing Mg−0.1%Ca with Mg−0.1%Ca−0.2%In at 23.75 mA current load.

Owing to the enhanced voltage and anodic efficiency, outstanding energy density is achieved via utilizing the Mg−0.1%Ca−0.2%In anode. Under 23.75 mA current load, the Mg−0.1%Ca−0.2%In-based Mg-air system exhibits an energy density of 2259 Wh kg^{-1}, which is much higher than that of a primary Zn-air (>700 Wh kg^{-1} as reported by Li et al. [64]). Therefore, with the results presented in this work, we recommend micro-alloyed Mg–Ca–In alloys, like Mg−0.1%Ca−0.2%In, as excellent candidates for anode materials of primary aqueous Mg-air batteries.

Declaration of competing interest

The authors declare that they have no known competing financial interests or personal relationships that could have appeared to influence the work reported in this paper.

CRediT authorship contribution statement

Min Deng: Methodology, Investigation, Validation, Resources, Writing - original draft, Writing - review & editing, Funding acquisition. **Linqian Wang:** Methodology, Investigation, Validation, Writing - review & editing, Funding acquisition. **Daniel Höche:** Conceptualization, Supervision, Writing - review & editing. **Sviatlana V. Lamaka:** Conceptualization, Supervision, Writing - review & editing. **Pingli Jiang:** Methodology, Investigation, Writing - review & editing, Funding acquisition. **Darya Snihirova:** Writing - review & editing, Funding acquisition. **Nico Scharnagl:** Methodology, Investigation, Writing - review & editing. **Mikhail L. Zheludkevich:** Conceptualization, Supervision, Writing - review & editing.

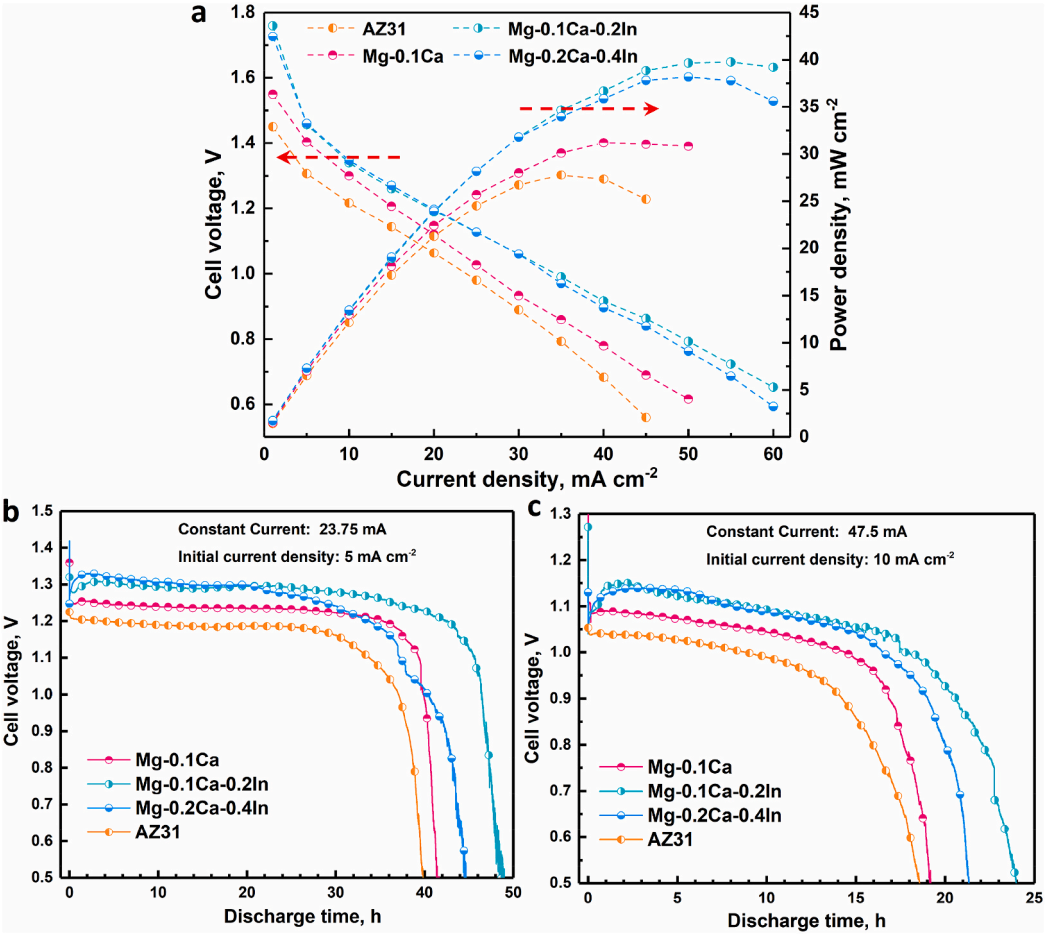

Fig. 8. (a) Cell voltage and power density of a lab-made Mg-air cell at different current densities adopting diverse Mg anodes. Average of three measurements is presented. (b, c) Voltage profiles of the Mg-air cell during the battery discharge tests applied with different current load. The adopted electrolyte is 3.5 wt% NaCl solution, while the cathode is a commercial air cathode with C/MnO_2 catalysts.

Table 3
Battery properties of Mg-air cells assembled with varied Mg anodes obtained from the battery failure tests. Note that the capacity and energy density are only based on the mass of Mg anode. Mean of data obtained from two independent measurements, which show a deviation below 5%, is presented.

Current drain parameters		Mg−0.1Ca	Mg−0.1Ca−0.2In	Mg−0.2Ca−0.4In	AZ31
23.75 mA	Service life, h	40.6	49.1	44.4	39.2
	Anodic efficiency, %	66.4	80.2	72.6	62.7
	Capacity, mA h g^{-1}	1482	1791	1621	1405
	Average voltage, V	1.21	1.26	1.24	1.14
	Energy density, Wh kg^{-1}	1835	2259	2011	1629
47.5 mA	Service life, h	19.2	24.0	21.3	18.6
	Anodic efficiency, %	61.9	77.8	68.3	60.6
	Capacity, mA h g^{-1}	1380	1736	1524	1354
	Average voltage, V	0.99	1.04	1.06	0.93
	Energy density, Wh kg^{-1}	1378	1808	1612	1282

Acknowledgement

Bahram Vaghefinazari is sincerely acknowledged for the discussion on experimental results. M. Deng, L. Wang and P. Jiang are grateful for the support from China Scholarship Council concerning the award of fellowship No. 201606370031, No. 201706370183 and No. 201606310043. D. Snihirova acknowledges Humboldt foundation for Postdoctoral grant and SeaMag project for financial support (MarTera ERA-NET cofund).

Appendix A. Supplementary data

Supplementary data to this article can be found online at https://doi.org/10.1016/j.jpowsour.2020.228528.

References

[1] David Linden, T.B. Reddy, Handbook of Batteries, McGraw-Hill, New York, 2002.
[2] C. Daniel, J. Besenhard, Handbook of Battery Materials, Wiley-VCH, Weinheim, 2012.
[3] F. Cheng, J. Chen, Chem. Soc. Rev. 41 (2012) 2172–2192.
[4] T. Zhang, Z. Tao, J. Chen, Mater. Horiz. 1 (2014) 196–206.
[5] Md Rahman, X. Wang, C. Wen, J. Electrochem. Soc. 160 (2013) A1759–A1771.

[6] M. Deng, D. Höche, D. Snihirova, L.Q. Wang, B. Vaghefinazari, S.V. Lamaka, M. L. Zheludkevich, Aqueous Mg batteries, in: M. Fichtner (Ed.), Magnesium Batteries: Research and Applications, Royal Society of Chemistry, United Kingdom, 2019, pp. 275–308.
[7] R. Udhayan, N. Muniyandi, P.B. mathur, Br. Corroison J. 27 (1992) 68–71.
[8] D. Höche, S.V. Lamaka, B. Vaghefinazari, T. Braun, R.P. Petrauskas, M. Fichtner, M. L. Zheludkevich, Sci. Rep. 8 (2018) 7578.
[9] Y. Li, J. Ma, G. Wang, F. Ren, Y. Zhu, Y. Song, J. Electrochem. Soc. 165 (2018) A1713–A1717.
[10] M. Shinohara, E. Araki, M. Mochizuki, T. Kanazawa, K. Suyehiro, J. Power Sources 187 (2009) 253–260.
[11] R. Hahn, J. Mainert, F. Glaw, K.D. Lang, J. Power Sources 288 (2015) 26–35.
[12] G.L. Song, A. Atrens, Adv. Eng. Mater. 1 (1999) 11–33.
[13] S. Thomas, N.V. Medhekar, G.S. Frankel, N. Birbilis, Curr. Opin. Solid State Mater. Sci. 19 (2015) 85–94.
[14] T.R. Thomaz, C.R. Weber, T. Pelegrini, L.F.P. Dick, G. Knörnschild, Corrosion Sci. 52 (2010) 2235–2243.
[15] B.V. Ratnakumar, J. Appl. Electrochem. 18 (1988) 268–279.
[16] M. Yuasa, X. Huang, K. Suzuki, M. Mabuchi, Y. Chino, J. Power Sources 297 (2015) 449–456.
[17] T. Zheng, Y. Hu, Y. Zhang, S. Yang, F. Pan, Mater. Des. 137 (2018) 245–255.
[18] L.Q. Wang, R.C. Wang, Y. Feng, M. Deng, N.G. Wang, J. Electrochem. Soc. 164 (2017) A438–A446.
[19] K. Gusieva, C.H.J. Davies, J.R. Scully, N. Birbilis, Int. Mater. Rev. 60 (2014) 169–194.
[20] X. Liu, S. Liu, J. Xue, J. Power Sources 396 (2018) 667–674.
[21] Y. Shi, C. Peng, Y. Feng, R. Wang, N. Wang, Mater. Des. 124 (2017) 24–33.
[22] J. Li, B. Zhang, Q. Wei, N. Wang, B. Hou, Electrochim. Acta 238 (2017) 156–167.
[23] G. Huang, Y. Zhao, Y. Wang, H. Zhang, F. Pan, Mater. Lett. 113 (2013) 46–49.
[24] Y. Feng, W. Xiong, J. Zhang, R. Wang, N. Wang, J. Mater. Chem. 4 (2016) 8658–8668.
[25] Y. Lv, Y. Xu, D. Cao, J. Power Sources 196 (2011) 8809–8814.
[26] Y. Feng, R.-c. Wang, K. Yu, C.-Q. Peng, W.-x. Li, Trans. Nonferrous Metals Soc. China 17 (2007) 1363–1366.
[27] Y. Feng, R. Wang, K. Yu, C. Peng, J. Zhang, C. Zhang, J. Alloys Compd. 473 (2009) 215–219.
[28] J. Zhao, K. Yu, Y. Hu, S. Li, X. Tan, F. Chen, Z. Yu, Electrochim. Acta 56 (2011) 8224–8231.
[29] M. Deng, L. Wang, D. Höche, S.V. Lamaka, D. Snihirova, B. Vaghefinazari, M. L. Zheludkevich, J. Power Sources 441 (2019) 227201.
[30] M. Deng, D. Höche, S.V. Lamaka, D. Snihirova, M.L. Zheludkevich, J. Power Sources 396 (2018) 109–118.
[31] M. Deng, D. Höche, S.V. Lamaka, L. Wang, M.L. Zheludkevich, Corrosion Sci. 153 (2019) 225–235.
[32] H.A.E. Shayeb, F.M.A.E. Wahab, S.Z.E. Abedin, J. Appl. Electrochem. 29 (1999) 601–609.
[33] M. Pourgharibshahi, P. Lambert, Mater. Corros. 67 (2016) 857–866.
[34] J.B. Bessone, D.O. Flamini, S.B. Saidman, Corrosion Sci. 47 (2005) 95–105.
[35] D.O. Flamini, S.B. Saidman, Mater. Chem. Phys. 136 (2012) 103–111.
[36] I.-J. Park, S.-R. Choi, J.-G. Kim, J. Power Sources 357 (2017) 47–55.
[37] N. Wang, R. Wang, C. Peng, B. Peng, Y. Feng, C. Hu, Electrochim. Acta 149 (2014) 193–205.
[38] S. Yuan, H. Lu, Z. Sun, L. Fan, X. Zhu, W. Zhang, J. Electrochem. Soc. 163 (2016) A1181–A1187.
[39] X. Li, H. Lu, S. Yuan, J. Bai, J. Wang, Y. Cao, Q. Hong, J. Electrochem. Soc. 164 (2017) A3131–A3137.
[40] A. Pardo, M.C. Merino, A.E. Coy, F. Viejo, R. Arrabal, S. Feliú, Electrochim. Acta 53 (2008) 7890–7902.
[41] K.A. Unocic, H.H. Elsentriecy, M.P. Brady, H.M. Meyer III, G.L. Song, M. Fayek, R. A. Meisner, B. Davis, J. Electrochem. Soc. 161 (2014) C302–C311.
[42] N.-g. Wang, R.-c. Wang, C.-q. Peng, Y. Feng, X.-y. Zhang, Trans. Nonferrous Metals Soc. China 20 (2010) 1403–1411.
[43] P. Gore, S. Fajardo, N. Birbilis, G.S. Frankel, V.S. Raja, Electrochim. Acta 293 (2019) 199–210.
[44] D. Hoche, C. Blawert, S.V. Lamaka, N. Scharnagl, C. Mendis, M.L. Zheludkevich, Phys. Chem. Chem. Phys. 18 (2016) 1279–1291.
[45] S.V. Lamaka, D. Höche, R.P. Petrauskas, C. Blawert, M.L. Zheludkevich, Electrochem. Commun. 62 (2016) 5–8.
[46] S.V. Lamaka, B. Vaghefinazari, D. Mei, R.P. Petrauskas, D. Höche, M. L. Zheludkevich, Corrosion Sci. 128 (2017) 224–240.
[47] S. Fajardo, G.S. Frankel, Electrochim. Acta 165 (2015) 255–267.
[48] G.L. Song, A. Atrens, D. StJohn, Magnesium Technology, 2001, pp. 255–262.
[49] M. Esmaily, J.E. Svensson, S. Fajardo, N. Birbilis, G.S. Frankel, S. Virtanen, R. Arrabal, S. Thomas, L.G. Johansson, Prog. Mater. Sci. 89 (2017) 92–193.
[50] Y. Jin, C. Blawert, F. Feyerabend, J. Bohlen, M. Silva Campos, S. Gavras, B. Wiese, D. Mei, M. Deng, H. Yang, R. Willumeit-Römer, Corrosion Sci. 158 (2019) 108096.
[51] C.L. Mendis, K. Oh-ishi, T. Ohkubo, K. Hono, Scripta Mater. 64 (2011) 137–140.
[52] H. Xie, H. Pan, Y. Ren, L. Wang, Y. He, X. Qi, G. Qin, Phys. Rev. Lett. 120 (2018), 085701.
[53] A.W.C. Lin, N.R. Armstrong, T. Kuwana, Anal. Chem. 49 (2002) 1228–1235.
[54] M. Faur, M. Faur, D.T. Jayne, M. Goradia, C. Goradia, Surf. Interface Anal. 15 (1990) 641–650.
[55] S. Yuan, H. Lu, Z. Sun, L. Fan, X. Zhu, W. Zhang, J. Electrochem. Soc. 163 (2016) A1181–A1187.
[56] Z. Qiao, Z. Shi, N. Hort, N.I. Zainal Abidin, A. Atrens, Corrosion Sci. 61 (2012) 185–207.
[57] F. Cao, Z. Shi, G.-L. Song, M. Liu, A. Atrens, Corrosion Sci. 76 (2013) 60–97.
[58] M. Liu, P.J. Uggowitzer, A.V. Nagasekhar, P. Schmutz, M. Easton, G.-L. Song, A. Atrens, Corrosion Sci. 51 (2009) 602–619.
[59] P. Jiang, C. Blawert, R. Hou, N. Scharnagl, J. Bohlen, M.L. Zheludkevich, J. Alloys Compd. 783 (2019) 179–192.
[60] S. Fajardo, C.F. Glover, G. Williams, G.S. Frankel, Electrochim. Acta 212 (2016) 510–521.
[61] G.S. Frankel, A. Samaniego, N. Birbilis, Corrosion Sci. 70 (2013) 104–111.
[62] G.G. Perrault, Electroanal. Chem. Magn. Elect. Sol. 27 (1970) 47–58.
[63] C.D. Taylor, J. Electrochem. Soc. 163 (2016) C602–C608.
[64] Y. Li, M. Gong, Y. Liang, J. Feng, J.E. Kim, H. Wang, G. Hong, B. Zhang, H. Dai, Nat. Commun. 4 (2013) 1805.

5.5 Corrosion and discharge properties of Ca/Ge micro-alloyed Mg anodes for primary aqueous Mg batteries

Paper 5: Corrosion and discharge properties of Ca/Ge micro-alloyed Mg anodes for primary aqueous Mg batteries (submitted to Corrosion Science)

Trace addition of germanium (Ge) has been found to be able to improve the corrosion resistance of Mg through suppressing the kinetics of the cathodic reaction [30, 31, 49]. The focus of this paper is to reveal the potential of Ge as an alloying element for Mg and Mg-Ca anodes. Mg-0.1%Ge and Mg-0.1%Ca-0.1%Ge alloys (all wt.%) were fabricated via casting followed by water-cooling. The corrosion and discharge performance were determined with comparison to recast pure Mg and Mg-0.1%Ca. The inhibition effect of Ge and Ca on cathodic kinetics were demonstrated, contributing to the remarkably lower corrosion rate of Mg-0.1%Ge and Mg-0.1%Ca than pure Mg and the slowest corrosion rate of Mg-0.1%Ca-0.1%Ge alloy. Meanwhile, the inhibited cathodic reaction also resulted in the more negative OCP of Mg-0.1%Ca-0.1%Ge alloy than Mg-0.1%Ge and Mg-0.1%Ca. However, the three micro-alloyed anodes showed similar discharge potential at different current densities due to different voltage drop partially induced by varied protectiveness of the surface film. Discharge tests indicated that the voltage drop could be eliminated by Mg^{2+} complexing agents, like salicylic acid (SAL), as electrolyte additives owning to the capability of hindering the formation of $Mg(OH)_2$. Therefore, the battery with Mg-0.1%Ca-0.1%Ge anode yielded much higher cell voltage than those based on Mg-0.1%Ge and Mg-0.1%Ca in 0.1 M SAL-based electrolyte. The self-discharge rates of all prepared anodes were also assessed. Interestingly, Mg-0.1%Ge, Mg-0.1%Ca and Mg-0.1%Ca-0.1%Ge showed alike self-discharge rates under 1 and 10 mA cm^{-2} current densities, which were significantly lower than the recast pure Mg. The utilization efficiency of the three alloy anodes were consequently similar but much higher than that of the pure Mg.

Corrosion and discharge properties of Ca/Ge micro-alloyed Mg anodes for primary aqueous Mg batteries

Min Deng[a,*], Linqian Wang[a, *], Daniel Höche[a], Sviatlana V. Lamaka[a], Darya Snihirova[a], Pingli Jiang[a], Mikhail L. Zheludkevich [a, b]

[a] *MagIC – Magnesium Innovation Centre, Helmholtz-Zentrum Geesthacht (HZG), 21502 Geesthacht, Germany*

[b] *Institute of Materials Science, Faculty of Engineering, Kiel University, 24143 Kiel, Germany*

Abstract: Ge is evaluated as a micro-alloying element for newly-developed Mg-Ca anodes. The combination of Ca/Ge is effective for suppressing cathodic HER kinetics, resulting in highly negative OCP and a low corrosion rate (0.2 mm y^{-1}). For air battery, Mg-0.1%Ca-0.1%Ge (wt%) anode exhibits similar voltage to Mg-0.1%Ca in NaCl solution, but the highly negative OCP enables it with enhanced voltage in salicylate-containing electrolyte (1.7 V at 1 mA cm^{-2} versus 1.63 V of Mg-0.1%Ca). Beside, all micro-alloyed Mg-Ca, Mg-Ge and Mg-Ca-Ge anodes show similar self-discharge rates and high utilization efficiency (~60% at 10 mA cm^{-2}).

Keywords: A. Magnesium; B. Galvanostatic; B. Polarization; B. Weight loss; C. Anodic dissolution.

1. Introduction

Primary batteries, which are non-rechargeable and designed to be used only once, are being utilized in numerous applications, like offshore equipment, implanted medical devices, and as standby power sources for schools, hospitals, etc., due to their long shelf-life, high energy density and instant readiness [1, 2]. Among all developed primary batteries, primary Mg system owns great promise attributed to the low cost of Mg raw materials and good theoretical electrochemical properties of Mg metal, e.g. the large volumetric capacity (3832 mA h g^{-1} versus 2061 mA h g^{-1} of Li) and highly negative electrode potential (− 2.37 V vs. SHE) [3-6]. Primary Mg batteries can be designed as several types, e.g., Mg-air battery, Mg-seawater battery and Mg dry cell, via adopting different oxidizing agents, like oxygen from air, AgCl and MnO_2 [1, 7, 8]. The electrolyte used in primary Mg system is manmade nontoxic saline solution (often with additives) or natural ocean water [9-12]. The utilization of all nonhazardous components renders the Mg primary system an environmentally benign power source meeting the social demand for green energy. However, their commercialization is not widely fulfilled, especially the Mg-air batteries, being hindered by several issues weakening the practical properties. Concern on Mg anode derives from two main aspects. Firstly, copious hydrogen evolution takes place on Mg anode surface under anodic polarization in aqueous solutions. The hydrogen evolution rate increases with elevating anodic current (or anodic potential), leading to severe wasteful dissolution of Mg anode. This unusual phenomenon, which is termed as negative difference effect (NDE), leads to a shortened shelf life and reduced energy density of Mg-based battery system. Secondly, the battery voltage is relatively low comparing to the theoretical value because of the high open circuit potential (OCP) of ordinary Mg anode and large voltage drop caused by sluggish anodic reaction kinetics or dense discharge products film on anode surface [13-17]. In this context, the performance boost of Mg-based primary batteries

requires more effort for development of Mg anodes with higher corrosion resistance, low self-discharge rate, low OCP (high cell voltage) and high discharge activity.

Increasing the purity grade of Mg could be an effective method to improve the properties of Mg anode. As reported, an Mg-air cell based on a high-purity Mg (99.99%) anode showed higher discharge voltage than the system with some commercial Mg alloy anodes, e.g. AM50 and AZ91 [18]. However, the corrosion and electrochemical performance of high purity Mg are dominated by the amount and composition of Fe-containing precipitates [19-22], which are uncontrollable during solidification process. It was proposed high purity Mg with minimal Fe-rich particles should have an intrinsic corrosion rate of ~ 0.3 mm y^{-1} in concentrated NaCl solution [23]. In contrast, with presence of Fe-rich precipitates, significantly higher corrosion rate and altered electrochemical properties are induced. The poor reproducibility of pure Mg properties, which is associated with metallurgic processing, results in its inadequacy as an anode material. Modification of pure Mg morphology also attracts some interests regarding anode developing. Further, Mg with varied nano/mesoscale structures has been evaluated as the anode material for Mg primary system, such as nanospheres, nanorods and porous thin film [24-28]. Enhancement on cell voltage was obtained due to increased contact with electrolyte and reduced charge transfer polarization. However, the usage of nanostructured Mg accelerated the anode self-corrosion, which reduced battery capacity and energy density and, therefore, lead to the request for electrolyte additives with capability of inhibiting self-corrosion. Another popular approach for Mg anode development is alloying by other metallic elements with consequent composition optimization. Many Mg alloys have been proposed as anode materials for primary Mg batteries during the past decades [15, 17, 29-33], among which most are based on Mg-Al system as Al is the most commonly used alloying element for Mg to improve its corrosion resistance and mechanical properties. The improved corrosion resistance by Al alloying is believed to be associated with the formation of a protective film attributed to Al enrichment [34, 35]. However, at the same time, the protective film certainly results in large voltage drop during discharge and then leads to reduced battery voltage [36]. Moreover, as summarized, Mg-Al based alloys normally possess more positive OCP [17]. Therefore, novel Al-free Mg anodes with excellent performance are preferred. Importantly, our previous work indicates that binary Mg-Ca alloys possess great potential as environmentally benign anode materials with superior discharge properties [37, 38]. Mg-0.1 wt% Ca alloy showed higher discharge voltage and energy density than high purity Mg, AM50 and AZ31 alloys measured in a custom-made Mg-air full cell. Nevertheless, there is still space for improvement in what concerns the Mg-Ca anodes because the voltage and peak energy density were insufficient comparing to the theoretical values. Thus, further enhancement on Mg-Ca based anodes is desirable.

Improvement is possible by introducing electrolyte additives. For instance, by using Mg^{2+} complexing agents, like salicylate (SAL), the formation of surface $Mg(OH)_2$ film was impeded and thus the pure Mg- and Mg-Ca-based battery voltage was enhanced, particularly under low current densities [10, 39, 40]. The working condition needs to be optimized to obtain sufficiently high utilization

efficiency along with enhanced voltage. Besides, alloying remains a worth-trying approach for the performance boosting of Mg-Ca anodes. However, the alloying elements should be carefully selected. Besides, the alloying content should be controlled within a relatively low level for purpose of reducing second phase fraction. Deng et al. [41] demonstrated that cathodic acting secondary phases with respect to Mg matrix will be detached from anode substrate during discharge process because of the preferential dissolution of surrounding Mg matrix. Besides, secondary phases and impurity particles may also lead to localized and non-uniform anodic dissolution, resulting in Mg matrix undermining and then peeling from substrate. The detachment of secondary phases and undermined matrix, which is named chunk effect (CE), leads to large anodic efficiency loss and consequently reduces battery service life and energy density. Therefore, low alloyed Mg anodes are required to moderate the performance loss related to CE [42, 43]. Recently, published work demonstrated that germanium (Ge) as a trace alloying element is able to enhance the corrosion resistance of pure Mg (99.95%, corrosion rate of 20 mm y^{-1} in 0.1 M NaCl solution) and Mg-Zn alloy via reducing the kinetics of cathodic reaction (hydrogen evolution reaction (HER)) [44-47]. The OCP of Mg became more negative with addition of Ge as a result of inhibited cathodic reaction. The findings provide a possibility of developing novel corrosion resistant Mg anode materials with satisfying operating potential by alloying with Ge and combination with other elements.

In the present work, we evaluated the possibility of binary Mg-Ge alloy as an anode material for primary aqueous Mg batteries. The influence of Ge addition on Mg-0.1wt% Ca anode has also been investigated from the aspects of corrosion performance and discharge properties. It should be noted that Ge has extremely low solubility in Mg matrix (approximately 0.003 at.% at 602 ℃ [48]), leading to large fraction of secondary phase when alloying with high Ge content. Thus, only micro-alloyed Mg-Ge and Mg-Ca-Ge alloy were investigated in this work to avoid severe micro-galvanic corrosion induced by coupling of Mg matrix and cathodic secondary phases and to allay the negative effect of CE on anode performance.

2. Experimental procedures

2.1 Materials manufacturing

All the micro-alloyed Mg anodes with nominal composition of Mg-0.1wt% Ca, Mg-0.1wt% Ge and Mg-0.1wt% Ca-0.1wt% Ge were fabricated via conventional gravity casting. Firstly, pure Mg was melted in a boron nitride coated steel crucible placed in a furnace at 760 °C with protection of Ar/SF_6 (5:1) mixed gas. Alloying elements were then added into the Mg melt, holding for 30 min followed by a manual stirring process of 5 min. Afterwards, the melt was poured into a boron nitride coated cylindrical steel mould (60 mm diameter) preheated to 300 °C. The mould filled with melt was then immersed into a water bath for cooling and solidification. The raw materials used were pure Mg ingot, Ca chips and Ge bulks with purity of 99.96 wt%, 99.9 wt% and 99.99 wt% respectively. Pure Mg was recast with the same casting procedure in this work as reference. The actual chemical composition of

all processed materials is shown in Table 1 as analyzed by spark spectrometer (spark OES, Ametek-Spectro) and X-ray micro fluorescence (μXRF, Bruker). The impurities Fe, Ni and Cu [19, 49-52] that have deleterious influence on Mg corrosion resistance indicate extremely low content below 20 ppm. The content of Si in different materials ranges from 36 to 97 ppm. Note that Si, which has not been widely accepted as a detrimental impurity to Mg, has been demonstrated recently to have significant effect on corrosion resistance of pure Mg even in trace amount in combination with Fe [22, 53].

Table 1 Chemical composition of recast pure Mg and Mg alloys (wt%).

Materials	Ca	Ge	Fe	Ni	Cu	Al	Mn	Si	Mg
Mg	0.0019	-	0.0015	0.0002	0.0003	0.0095	0.018	0.0086	balance
Mg-0.1Ca	0.07	-	0.0018	0.0011	0.0012	< 0.01	0.017	0.0036	balance
Mg-0.1Ge	-	0.09	0.0019	0.0012	0.0012	< 0.01	0.018	0.0048	balance
Mg-0.1Ca-0.1Ge	0.11	0.11	0.0018	0.0010	0.0010	< 0.01	0.015	0.0060	balance

2.2 Microstructure characterization

All specimens after embedding in resin were carefully ground and polished to obtain high-quality samples for microstructure observation. Grinding process was carried out on silicon carbide papers consecutively up to 4000 grit. Afterwards, samples were polished to remove scratches using a water-free oxide polishing suspension (OPS) containing SiO_2 followed by a cleaning process in ethanol by ultrasonication. After etching with an acetic-picric acid solution, second phase morphology and distribution were observed with a scanning electron microscope (SEM, TESCAN VEGA3) combined with energy dispersive X-ray spectroscopy (EDS) to analyze the element composition. Besides, atomic force microscopy (AFM, Nanowizard, JPK Instruments AG) combined with Scanning Kelvin Probe Force Microscopy (SKPFM) was utilized to measure the Volta potential difference between secondary phase particles and the Mg matrix. The adopted silicon probe supplied by Innovative Solutions Bulgaria Ltd. (Bulgaria) was coated with a Cr/Pt conductive coating and possesses a resonance frequency of 75 kHz and a force constant of 3 N m^{-1}. Electric connection was achieved using a conductive tape between the sample and the grounded AFM stage. The lift height between the probe and sample surface was set as 100 nm. The scanning was conducted on an area of 30 × 30 μm with a resolution of 512 × 512 pixels immediately after sample polishing via the aforementioned processes.

2.3 Immersion tests

Long-term immersion tests for 7 days were applied to evaluate the corrosion rates of all prepared materials. Note, the electrolyte used for all measurements in this work is unbuffered 3.5 wt% NaCl solution with pH of 5.6 ± 0.2 if other not specified. Hydrogen gas produced by corrosion of immersed samples was collected simultaneously via a widely used set-up combining a funnel and an inverted

burette [54]. Plug-in samples of 15 × 15× 5 mm were hung in the solution with fishing line fastened to a plastic screw inserted into the samples. The weight loss of each sample after testing was determined after removing corrosion products by a diluted chromic acid (200 g L^{-1}). Corrosion rate, P_w (mm y^{-1}), can be calculated based on weight loss via the following formula:

$$P_w = \frac{365*24*10*\Delta m}{\rho*A*t} \quad (1)$$

Where Δm is sample weight loss during immersion, g; ρ is density of Mg, g cm^{-3}; A is sample surface area, cm^2; t is immersion time, h. Then, the formula can be simplified as following [23]:

$$P_w = 2.10\ W \quad (2)$$

Where W is weight loss rate (mg cm^{-1} d^{-1}) determined based on immersion tests.

Afterwards, surface morphology of each material after immersion was characterized by the SEM. Immersion test for each material was conducted for three times to ensure data reproducibility. In order to evaluate the corrosion origination and the role of secondary phases in the corrosion behavior of the newly designed Mg-Ca-Ge alloy, a quasi - in situ approach was applied with the same procedures as reported previously by Jin et al.[55]. A specimen was polished and then observed under SEM to record the morphologies of uncorroded secondary phases in specific regions with a relatively low voltage of 10 kV. After that, a short-term immersion (10 min) in 3.5 wt% NaCl solution was carried out, following an extra polishing process for 1 min with OPS to eliminate the possible influence of SEM observation on the corrosion behavior of this alloy. Subsequently, the morphologies of the secondary phases from the previously recorded regions were collected. The specimen was then immersed in chromic acid for 30 s to remove corrosion products. The morphologies of the same regions without corrosion products were also recorded then. For easy access to the regions of interest, some minor tracks were made on the sample surface via an aluminum tweezer in advance.

2.4 Electrochemical measurements

Potentiodynamic polarization curves were obtained using a Gamry interface 1000 potentiostat in 3.5 wt% NaCl solution with a conventional three-electrode cell consisting of a Pt wire counter electrode, a Ag/AgCl reference electrode and a Mg electrode with 1 cm^2 working surface area. A stabilization period lasted for one hour before each measurement to obtain a relatively stable OCP. Afterwards, anodic polarization curves were collected by scanning from – 5 mV to + 600 mV (vs. OCP) with a scan rate of 1 mV s^{-1}. Besides, cathodic polarization curves following the immersion for 1 and 24 hours were measured separately via scanning from + 5 mV vs. OCP negatively forwards to – 400 mV vs. OCP with the same scan rate.

2.5 Discharge testing

Half-cell discharge tests were conducted in the aforementioned three-electrode set-up in 3.5 wt% NaCl solution with all prepared Mg anodes. Two current densities, i.e. 1 and 10 mA cm^{-2}, were applied. Afterwards, weight loss of each sample due to discharge was determined. Accordingly, utilization

efficiency and discharge capacity of each anode were calculated with the following equations [14, 56].

$$\text{Utilization efficiency (\%)} = \frac{W_{theo}}{\Delta W} \times 100\% \quad (3)$$

$$\text{Specific capacity (Ah g}^{-1}) = \frac{I \times t}{\Delta W} \quad (4)$$

Where I (A) is the discharge current, t (h) is discharge time, ΔW (g) is the actual mass loss of samples during discharge process and W_{theo} (g) is the theoretical mass loss due to faradaic process. ΔW was determined by measuring the mass of samples before discharge and after removal of discharge products. W_{theo} was calculated via the following equation:

$$W_{theo} = \frac{I \times t}{F \times \sum(\frac{x_i \times n_i}{m_i})} \quad (5)$$

Where F represents the Faraday constant (26.8 Ah mol^{-1}), x_i, n_i, m_i represent the mass fraction, number of exchanged electrons and atomic weight, respectively, of each element in the materials.

In addition, self-discharge rate during discharge at different current densities was measured via hydrogen evolution tests with the same configuration used in previous work [41]. The measurements were replicated for three times and indicated very good reproducibility. Electrochemical impedance spectroscopy (EIS) testing was carried out immediately after discharge to evaluate anode activity associated with the surface condition. The scanned frequency range was 100 kHz to 0.1 Hz, and the sinusoidal AC voltage was 10 mV rms. Discharge testes were also performed in a fully assembled custom-made Mg-air cell filled with 3.5 wt% NaCl solution. The cathode material, with a 2.5 cm^2 working area, was a commercial air cathode based on C/MnO_2 catalyst, while the anode material was the manufactured Mg alloys embedded in resin with an exposed area of approximately 2.3 cm^2. A commercially cast alloy AZ31, with impurities of 11 ppm Fe, 7 ppm Ni and 19 ppm Cu, was also tested for comparison reason under the same experimental condition. All the anodes were also evaluated in the electrolyte with the aforementioned Mg^{2+} complexing agent additive, i.e. salicylate (SAL). The electrolyte of 0.1 M SAL was prepared by dissolving sodium salicylate (Sigma-Aldrich S3007) in 3.5 wt. % NaCl as background solution. The specific concentration was selected according to the published work of Wang et al. [40]. The initial bulk pH of the solution was adjusted to 7 ± 0.2 by adding NaOH solution, controlled by Metrohm-691 pH meter equipped with a Mettler-Toledo LabExpert Pt-1000-pH glass electrode.

3. Results

3.1 Microstructure

The microstructure of all fabricated materials characterized via SEM is presented in Fig. 1. Further, chemical compositions analyzed by EDS for several randomly selected precipitates from each alloy are shown in Table 2. Obviously, precipitates with different morphologies and distributions are present in all micro-alloyed materials. For the Mg-0.1Ca alloy, the precipitates, appearing as small particles, are CaMgSi as detected by EDS, even though Si content is at a low level in the alloy (36 ppm). Similarly,

it has been reported that the existence of trace Si could promote the precipitation of CaMgSi phase in the Mg-Zn-Ca system during solidification [55]. Regarding the binary Mg-0.1Ge alloy, the precipitates are confidently recognized as Mg_2Ge intermetallics as known from the Ge-Mg phase diagram [57] and several published works [46, 58, 59]. The EDS results shown in Table 2 indicate much higher concentration of Mg in the intermetallic due to the tiny size of these precipitates, which leads to the inclusion of Mg matrix in the region assessed by EDS. For the Mg-0.1Ca-0.1Ge alloy, Mg, Ca and Ge elements are identified in all precipitates by point EDS analysis (Table 2) and elemental mapping (see Fig. 2), indicating the presence of a ternary intermetallic. Besides, it is distinct that the quantity of intermetallics in the Mg-Ca-Ge system is larger than that in binary Mg-Ca and Mg-Ge system, owing to the higher alloying load. Note that there is a lack of ternary phase diagram of Mg-Ca-Ge system and, therefore, the stoichiometry of the intermetallic in this alloy is not well known. Thus, we simply refer to it as $Mg_xCa_yGe_z$. Something noteworthy is that a small quantity of Si (less than 0.5 wt%) is detected in all the precipitates in Mg-0.1Ge and Mg-0.1Ca-0.1Ge alloys. Distinguished from the high quantity of Si in the MgCaSi intermetallic found in Mg-0.1Ca system, the traces of Si in the Mg-0.1Ge and Mg-0.1Ca-0.1Ge alloys is proposed to segregate around the Mg_2Ge and $Mg_xCa_yGe_z$ precipitates (possibly as Mg_2Si or CaMgSi) instead of forming new Si-containing intermetallics. As reported by Jung et al. [60], no ternary phase is predicted in Mg-Ge-Si alloy except for a combination of Mg_2Ge-Mg_2Si ($Mg_2Ge_xSi_{1-x}$) without fixed ratio.

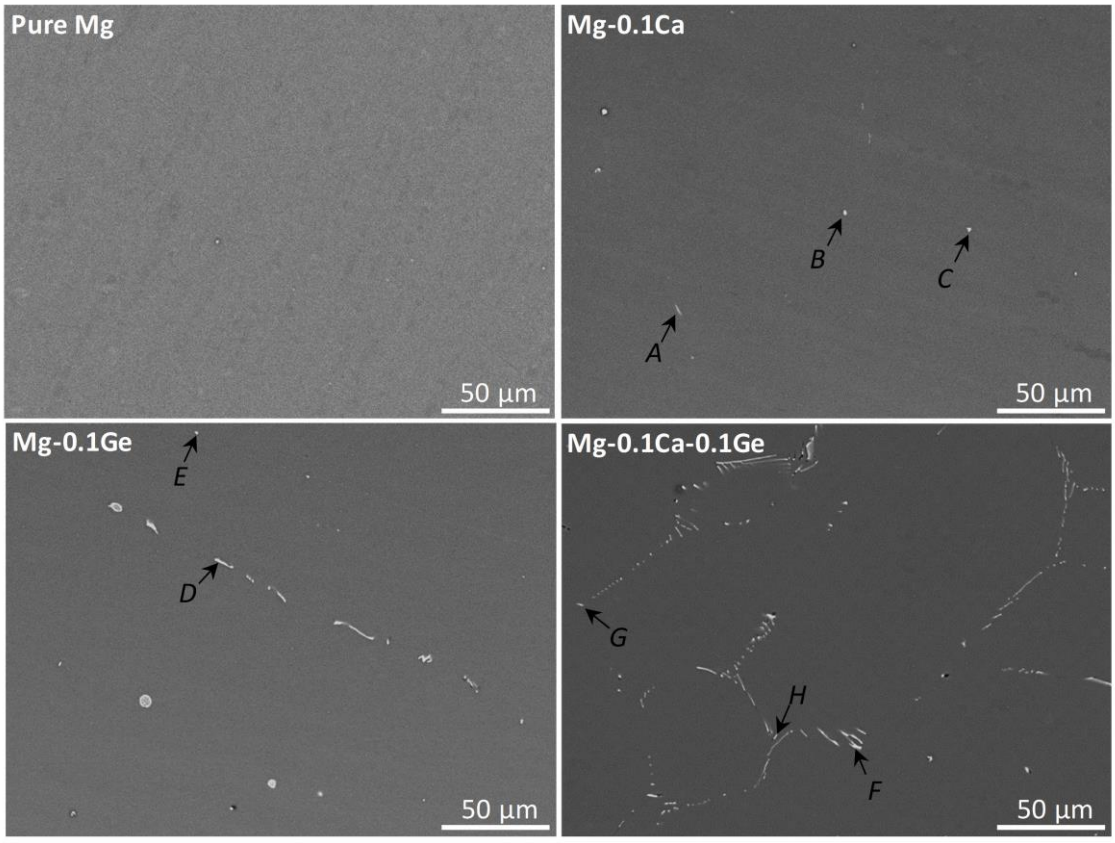

Fig. 1 SEM (BSE) images of as-cast pure Mg and Mg alloys.

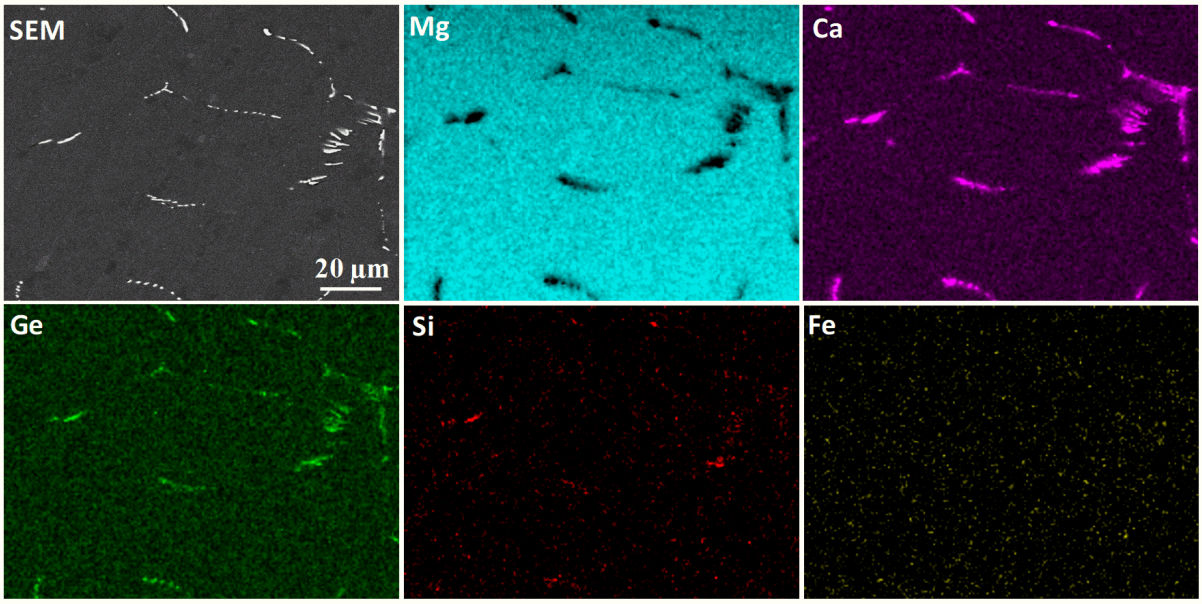

Fig. 2 Elemental mapping for a selected region in Mg-0.1Ca-0.1Ge alloy.

Table 2 Chemical compositions of some precipitates marked in Fig. 1 as analyzed by EDS (wt%).

Precipiates	*A*	*B*	*C*	*D*	*E*	*F*	*G*	*H*
Mg	91.6	79.6	80.2	94.9	97.0	82.3	87.5	94.8
Ca	4.9	10.5	10.7	/	/	5.4	4.1	1.9
Ge	/	/	/	4.8	2.6	11.8	8.2	3.0
Si	3.5	9.9	9.1	0.3	0.4	0.5	0.2	0.3

3.2 Electrochemical performance

Fig. 3a presents the results of one-hour OCP measurements corresponding to all as-cast materials. All micro-alloyed materials possess remarkably more negative OCP than that of the recast pure Mg. The average OCP values for Mg-0.1Ca, Mg-0.1Ge and Mg-0.1Ca-0.1Ge are –1.83 ± 0.02, –1.78 ± 0.04 and –1.91 ± 0.01 $V_{Ag/AgCl}$, respectively, comparing to –1.65 ± 0.02 $V_{Ag/AgCl}$ of the recast pure Mg. Apparently, ternary Mg-0.1Ca-0.1Ge shows a more negative OCP than the two binary alloys, demonstrating a good synergy effect of Ca and Ge micro-alloying. The highly negative OCP endows the micro-alloyed alloys with a great possibility to offer high discharge voltage as anode materials. Fig. 3b depicts the anodic polarization curves of all materials after immersion in 3.5 wt% NaCl for one hour. All alloyed Mg exhibits a pitting potential at around –1.60 $V_{Ag/AgCl}$, indicating the formation of a pseudo-protective film on the samples surface. All the curves associated with different alloys are generally overlapped within the potential range more positive than the pitting potential, elucidating similar anodic dissolution kinetics. Slight difference is only found within the potential range from the pitting potential to OCP but is most likely induced by varied OCP values of these alloys resulting from different cathodic HER kinetics as demonstrated in Fig. 3(c, d). Cathodic polarization curves were separately measured

after immersion for one hour (Fig. 3c) and 24 hours (Fig. 3d). Regarding one-hour immersion, varied cathodic kinetics corresponding to different materials are demonstrated, specifying that micro-alloying individually with Ca owns the ability of reducing the kinetics of cathodic reaction on pure Mg. Similar effect is found with minor Ge addition, in accordance with the results reported by Deng et al.[37] and Liu et al.[44, 45]. The updated finding here is that micro-alloying with Ca is better than Ge regarding suppressing cathodic HER amid the immersion period of 7 days and the combination of Ca and Ge is demonstrated to be more effective. The suppressed cathodic kinetics drives the cathodic polarization curve to move towards the direction of smaller current densities and, consequently, results in the more negative OCP. After 24-hour immersion, all the micro-alloyed materials maintain suppressed cathodic kinetics comparing to pure Mg. Interestingly, the polarization curves of Mg-0.1Ca and Mg-0.1Ca-0.1Ge partially overlap within the more negative potential range, elucidating that these two materials have similar kinetics of cathodic reaction after this immersion duration. Table 3 lists the current density of

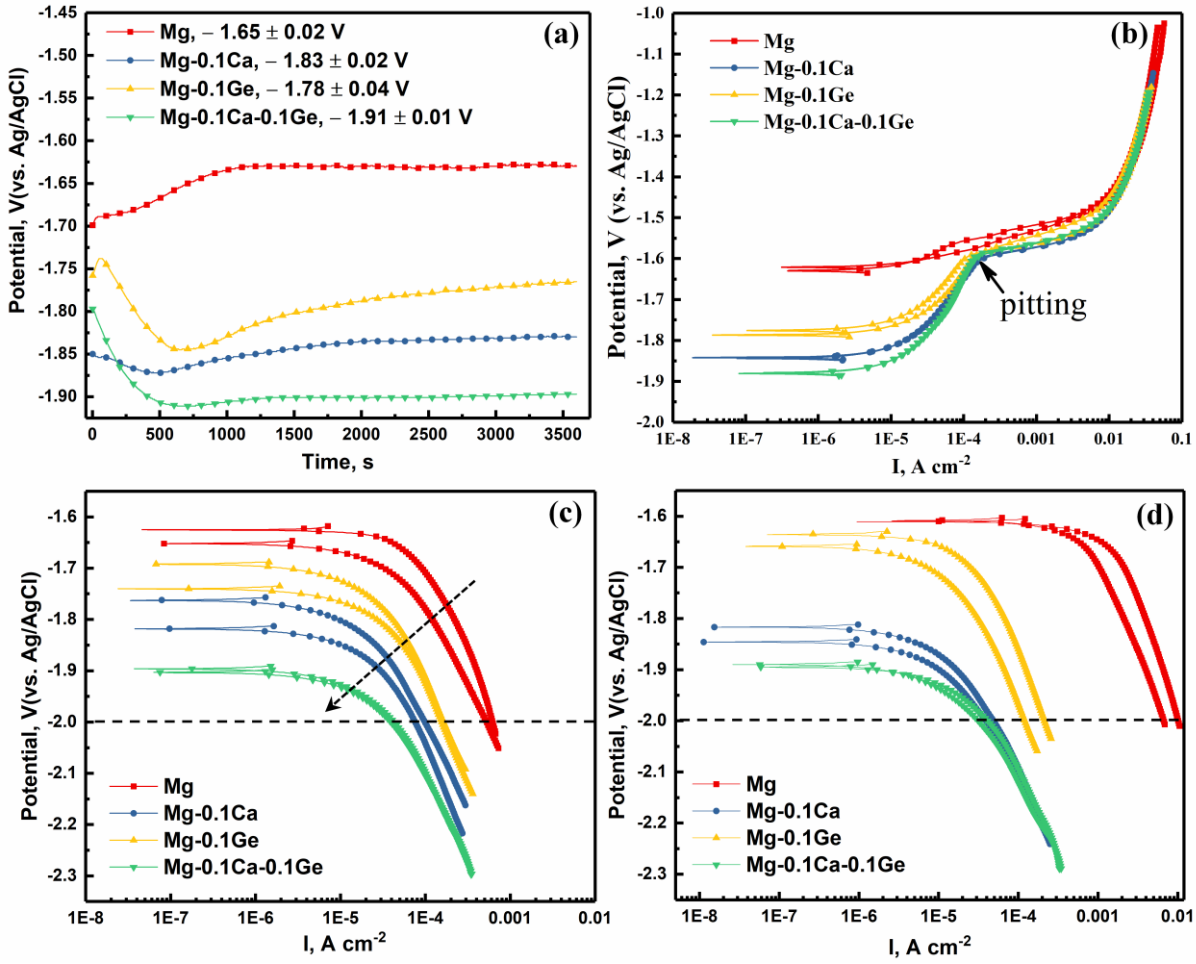

Fig. 3 (a) The evaluation of OCP curves during immersion and calculated average OCP values of three independent measurements. (b) Anodic polarization curves after one-hour OCP measurements. (c) Cathodic polarization curves after one-hour OCP measurements. (d) Cathodic polarization curves after 24-hour immersion. All measurements are performed in unbuffered 3.5 wt% NaCl solution with the initial pH 5.6 ± 0.2.

cathodic reaction at – 2.0 V (vs. Ag/AgCl) derived from these presented cathodic polarization curves measured after one-hour and 24-hour immersion, aiming to evaluate the variation of cathodic kinetics of each material after different immersion time. Obviously, a large increase of the defined current density, by a couple of orders of magnitude, is found regarding the pure Mg, which indicates a remarkable increase of its cathodic kinetics. The concerned current densities of Mg-0.1Ge and Mg-0.1Ca-0.1Ge both remain relatively constant, while a slight decrease is found from Mg-0.1Ca, showing that the cathodic kinetics of Mg-0.1Ca decreases with immersion, presumably related to fast detachment of fine CaMgSi precipitates. Generally, Mg-0.1Ca-0.1Ge possesses the lowest cathodic kinetics after immersion for 1 and 24 hours, being conducive to achieve a low corrosion rate.

Table 3 Current density of cathodic reaction at –2.0 V (vs. Ag/AgCl) derived from cathodic polarization curves shown in Fig. 3c and d. Results of two independent measurements are presented to demonstrate the reproducibility.

Current density	After 1 hour		After 24 hours	
µA cm^{-2}	Test #1	Test #2	Test #1	Test #2
Mg	527	620	10180	6690
Mg-0.1Ca	76	99	49	40
Mg-0.1Ge	159	164	120	214
Mg-0.1Ca-0.1Ge	43	39	42	31

3.3 Corrosion properties

Fig 4 illustrates the calculated corrosion rates of all materials based on the weight loss within 7-day immersion. The recast pure Mg exhibits a corrosion rate of nearly 0.6 mm y^{-1}, which is slightly higher than that of high-purity Mg (0.4 mm y^{-1}) reported by Shi et al. [21] and Qiao et al. [20] and intrinsic corrosion rate of ultra-high-purity Mg (0.3 mm y^{-1}) [23]. Likewise, large deviations between each measurement are also found in this work regarding the corrosion determination of pure Mg, resulting from the non-uniform Fe-rich precipitates. Remarkably, the corrosion rate of recast pure Mg is reduced after micro-alloying with 0.1 wt% Ca and Ge whereby corrosion rates of approximately 0.2 mm y^{-1} and 0.3 mm y^{-1} are achieved respectively. Further, combinative minor addition of Ca and Ge results in the lowest corrosion rate, which is similar to that of the binary Mg-0.1Ca and is even slightly below the intrinsic Mg corrosion rate of 0.3 mm y^{-1} [23]. Note that corrosion rates may be even lower if determined with fishing-line specimens instead of plug-in ones as demonstrated by Cao et al. [23]. Fig. 5 shows the surface morphologies of all materials after 7-day immersion tests and removal of corrosion products. Typical filiform-like corrosion is found on pure Mg, while generally uniform corrosion is characteristic for all micro-alloyed Mg. Some discrete corrosion cavities appear on the surface of Mg-0.1Ca alloy, whilst numerous but smaller pits are distinct on Mg-0.1Ge surface. Regarding Mg-0.1Ca-0.1Ge alloy,

the corrosion pits after immersion are rather shallow and inconspicuous, at least under the same magnification. Besides, grinding scratches are still visible from Mg-0.1Ca and Mg-0.1Ca-0.1Ge surface after 7-day immersion, manifesting the grossly high corrosion resistance of these two alloys.

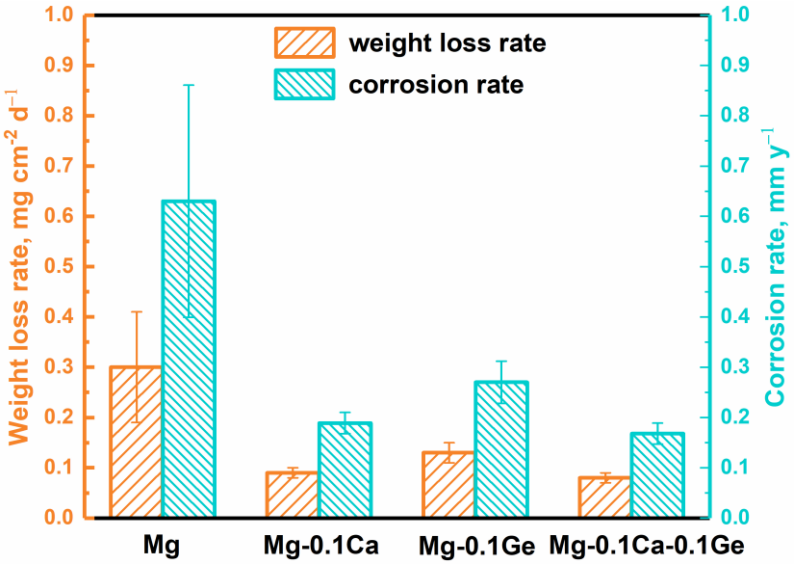

Fig. 4 Weight loss and associated corrosion rates of all studied materials within the 7-day immersion period in 3.5 wt% NaCl solution.

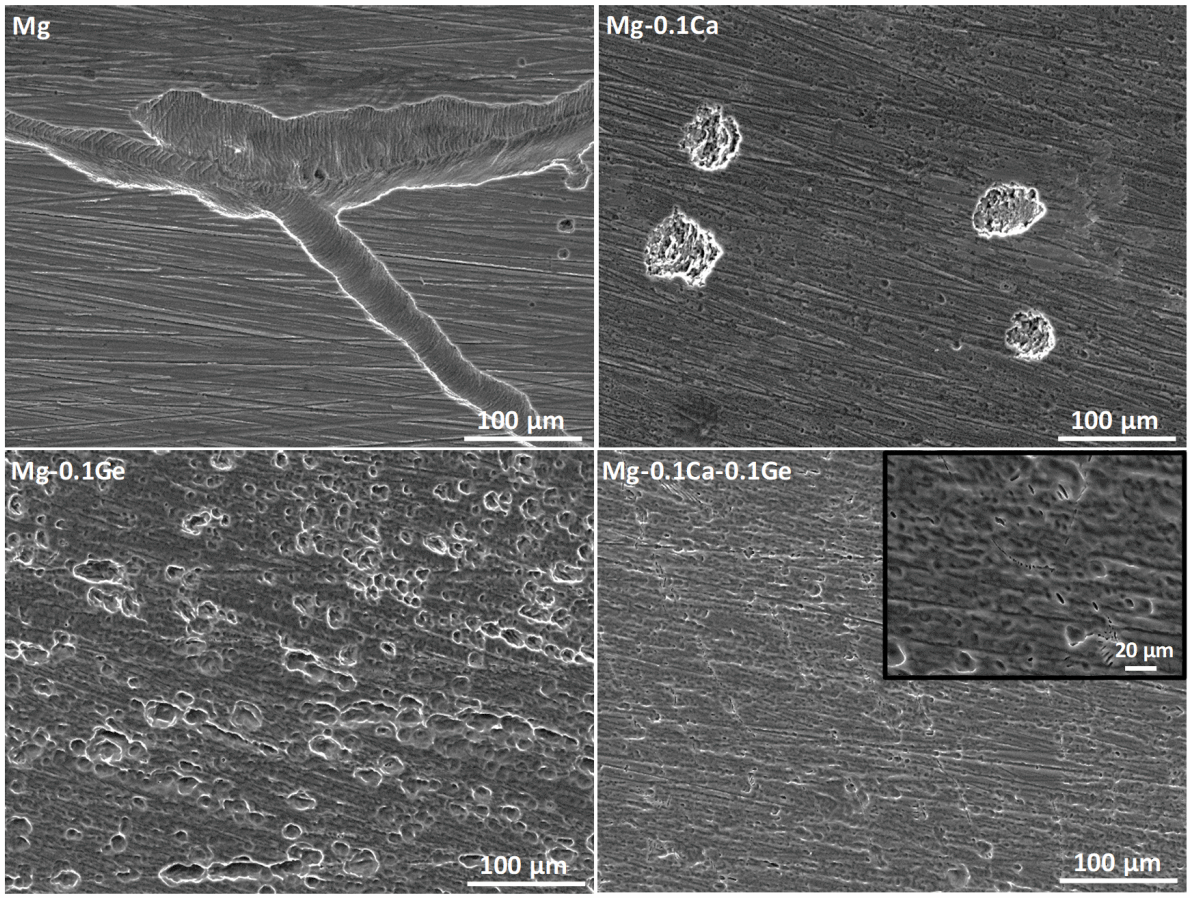

Fig. 5 Surface morphologies of all materials after 7-day immersion tests in 3.5 wt% NaCl solution and cleaning with chromic acid to remove corrosion products.

3.4 Electrochemical characteristic of MgxCayGez intermetallic

The electrochemical characteristic of the newfound $Mg_xCa_yGe_z$ intermetallic is first investigated in this work. The Volta potential difference of $Mg_xCa_yGe_z$ intermetallic with respect to Mg matrix is determined via SKPFM, as depicted in Fig. 6. Intriguingly, $Mg_xCa_yGe_z$ shows a negative potential difference to the matrix of ~ −100 mV, probably related to Ca enrichment. The results indicate that $Mg_xCa_yGe_z$ serves as local anode and suffers preferential dissolution during corrosion initiation after immersion, until complete degradation or detachment from alloy surface. To further unveil the anodic essence of the ternary phase with reference to Mg matrix, quasi-in situ corrosion measurements are applied. Relevant results are presented in Fig. 7, demonstrating the surface morphologies of same intermetallic-included regions prior to and after short-term immersion. The results indicate that $Mg_xCa_yGe_z$ intermetallic indeed suffers preferential corrosion prior to adjacent Mg matrix within the initial immersion stage, in accordance with the determined negative Volta potential with respect to the matrix. Besides, images presented in Fig. 7(a-3, b-3) exhibit the corrosion morphology with a striking characteristic, consisting of ambient shallow valleys surrounding deeper cavities in the center. The distinct corrosion morphology is similar to that reported upon a GW93 alloy (Mg-9.2wt%Gd-4.03wt%Y-0.52wt%Zr) [61], which contains Mg-Gd-Y anodic second phases. The central deeper cavities are proposed to be the result of preferential dissolution of anodic phases. Afterwards, corrosion propagates around the previous corrosion cavities and leads to the surrounding shallow corrosion areas. The difference between our work and the mentioned one is that corrosion is remarkably low for Mg-0.1Ca-0.1Ge alloy. Therefore, after long time immersion, severe pitting corrosion that is found regarding the reported GW93 alloy does not occur on the micro-alloyed Mg-Ca-Ge system in this work.

3.5 Discharge testing in half-cell

The discharge properties of all micro-alloyed Mg anodes are primarily evaluated via half-cell testing. Fig. 8 illustrates the potential variation with time for all anodes during discharge at 1 and 10 mA cm^{-2}. Obviously, minor addition of Ca and Ge both result in more negative discharge potential than the pure Mg at two studied current densities. Mg-0.1Ge anode shows similar potential to Mg-0.1Ca, and the addition of Ge to Mg-0.1Ca merely induces a slight improvement to the discharge potential. The slightly decreased potential at 1 mA cm^{-2} with time is possibly due to increased surface area. The potential difference among the three micro-alloyed anodes is around 10 mV, while comparing to pure Mg the difference is approximately 40 – 60 mV. Fig. 9 presents the utilization efficiency and discharge capacity of all studied anodes calculated after discharge at 1 and 10 mA cm^{-2}. Not surprisingly, micro-alloyed Mg-0.1Ca shows considerably enhanced utilization efficiency than the recast pure Mg as well as higher discharge capacity at both current densities, agreeing well with the results in our previous work [37]. The main finding here is that micro-alloyed Mg-0.1Ge and Mg-0.1Ca-0.1Ge also have much higher efficiency and capacity than pure Mg anode, although no improvement is found when compared with

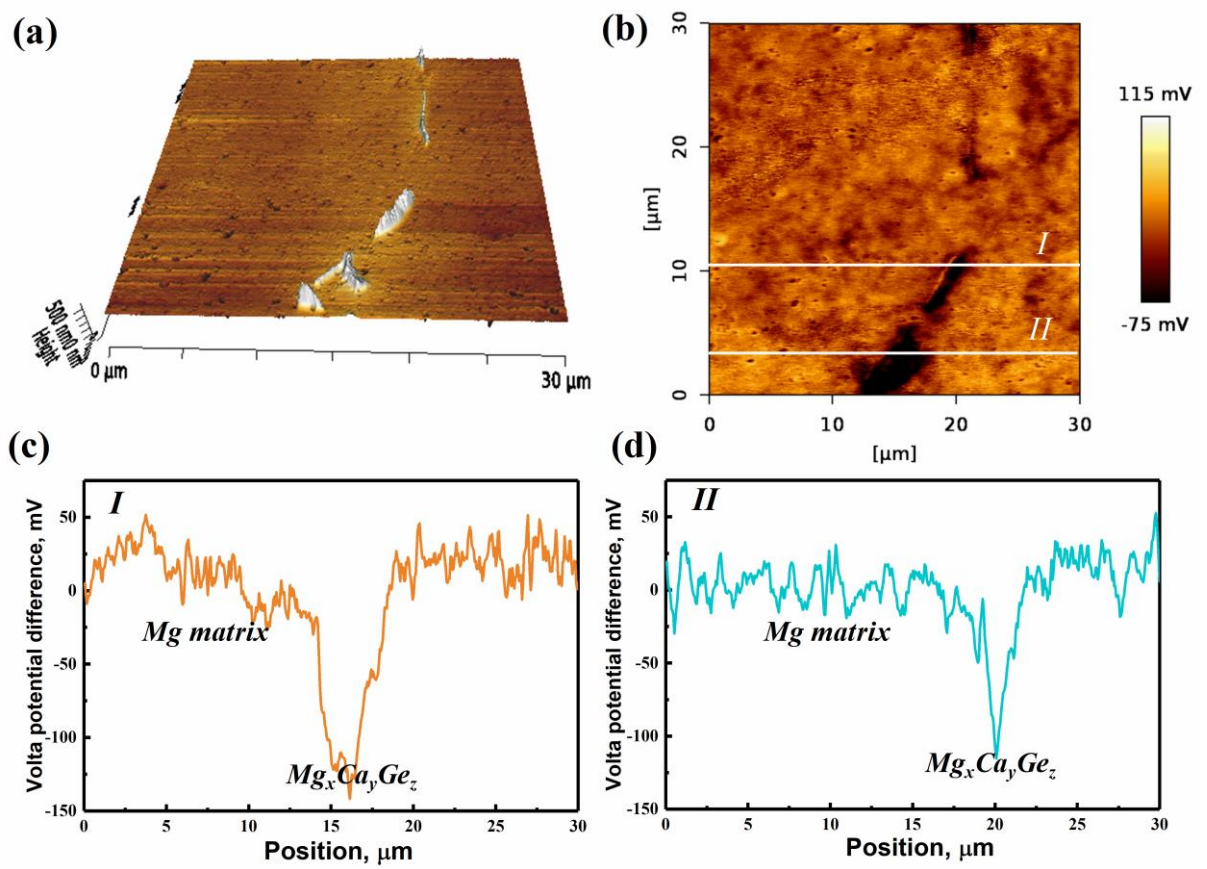

Fig. 6 SKPFM analysis of Mg-0.1Ca-0.1Ge alloy: (a) 3D height map; (b) corresponding Volta potential map; (c, d) corresponding line profile along line *I* and *II* marked in (b).

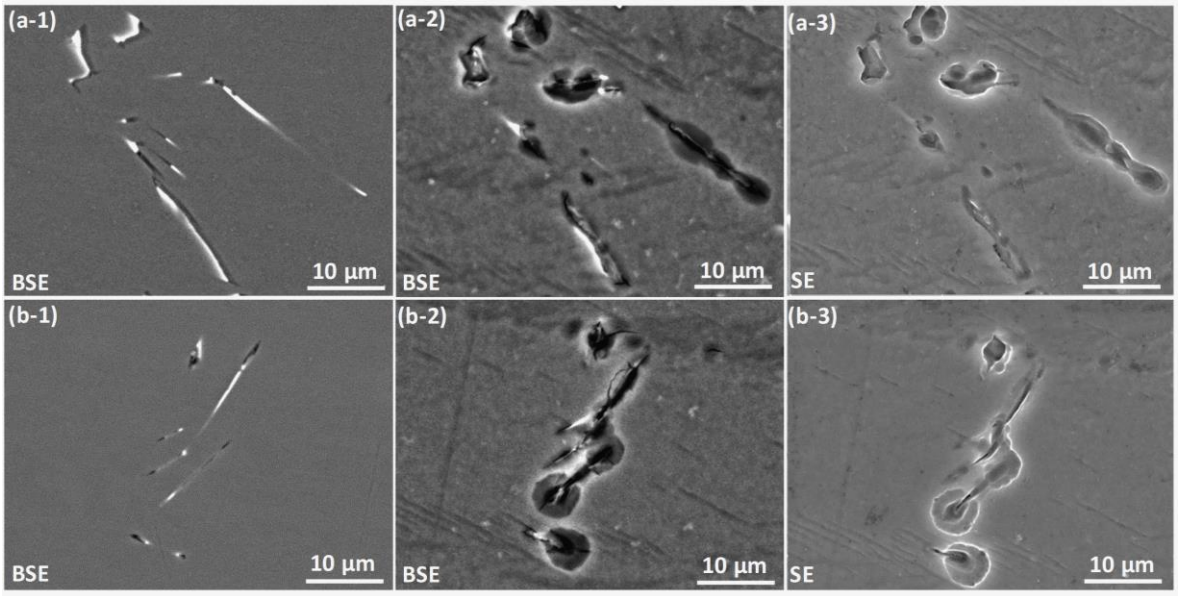

Fig. 7 (a-1, b-1) Morphologies of marked regions in Mg-0.1Ca-0.1Ge alloy before immersion. (a-2, b-2) Morphologies of the same regions after immersion for 10 min in 3.5 wt% NaCl solution. (a-3, b-3) Morphologies of the same regions after removing corrosion products with chromic acid.

Mg-0.1Ca anode. All the micro-alloyed anodes show utilization efficiency of nearly 50% at 1 mA cm^{-2} and 58% at 10 mA cm^{-2}, higher than that of most previously proposed Mg anodes, particularly under low current densities as summarized in Table 4. Fig. 10 illustrates the surface morphologies of all micro-alloyed anodes after discharge and removal of discharge products. A few localized cavities are visible, either macroscopically or microscopically, from the surface after discharge at 1 mA cm^{-2} for 15 h presented in Fig. 10(a-d), being the manifestation of detachment of chunks. Chunk effect is also apparently demonstrated by the cross-sectional morphology after discharge at 1 mA cm^{-2} presented in Fig. 10(i, j). Exfoliation of these chunks during discharge decreases the anode efficiency to some extent. In the case of 10 mA cm^{-2}, the surfaces of all micro-alloyed anodes after discharge are generally uniform with absence of visible deep cavities (Fig. 10(e-h)), elucidating more homogeneous anodic dissolution in comparison to that at low current density.

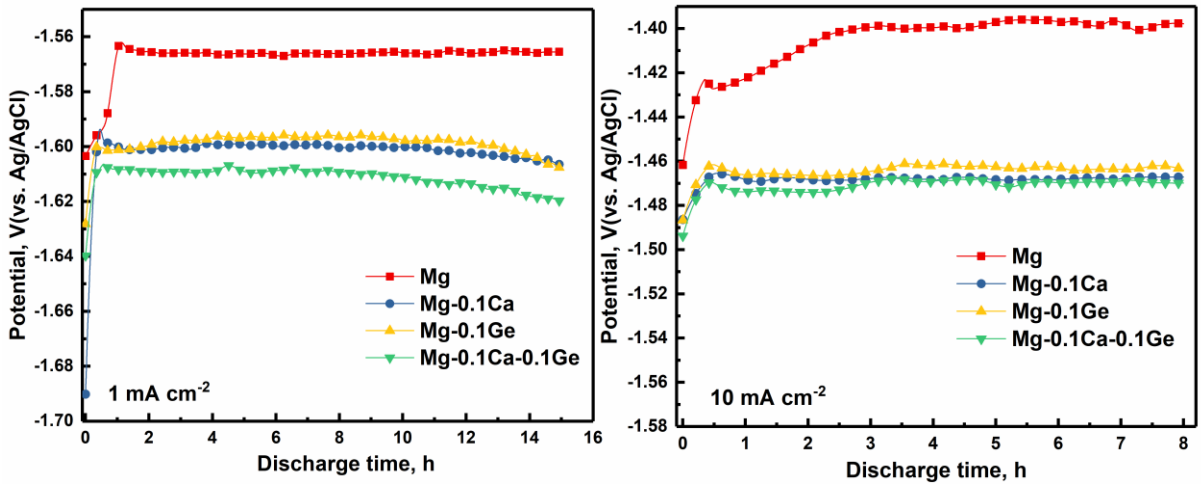

Fig. 8 Discharge curves of all cast Mg anodes at different current densities in 3.5 wt% NaCl solution. Typical results of replicated measurements are presented.

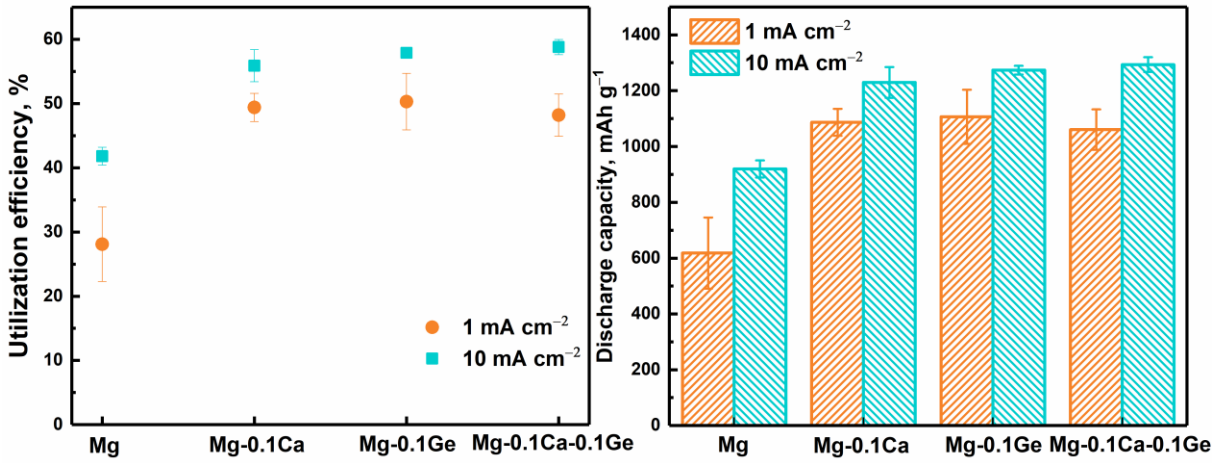

Fig. 9 Utilization efficiency and discharge capacity of Mg anodes under different discharge current densities in 3.5 wt% NaCl solution.

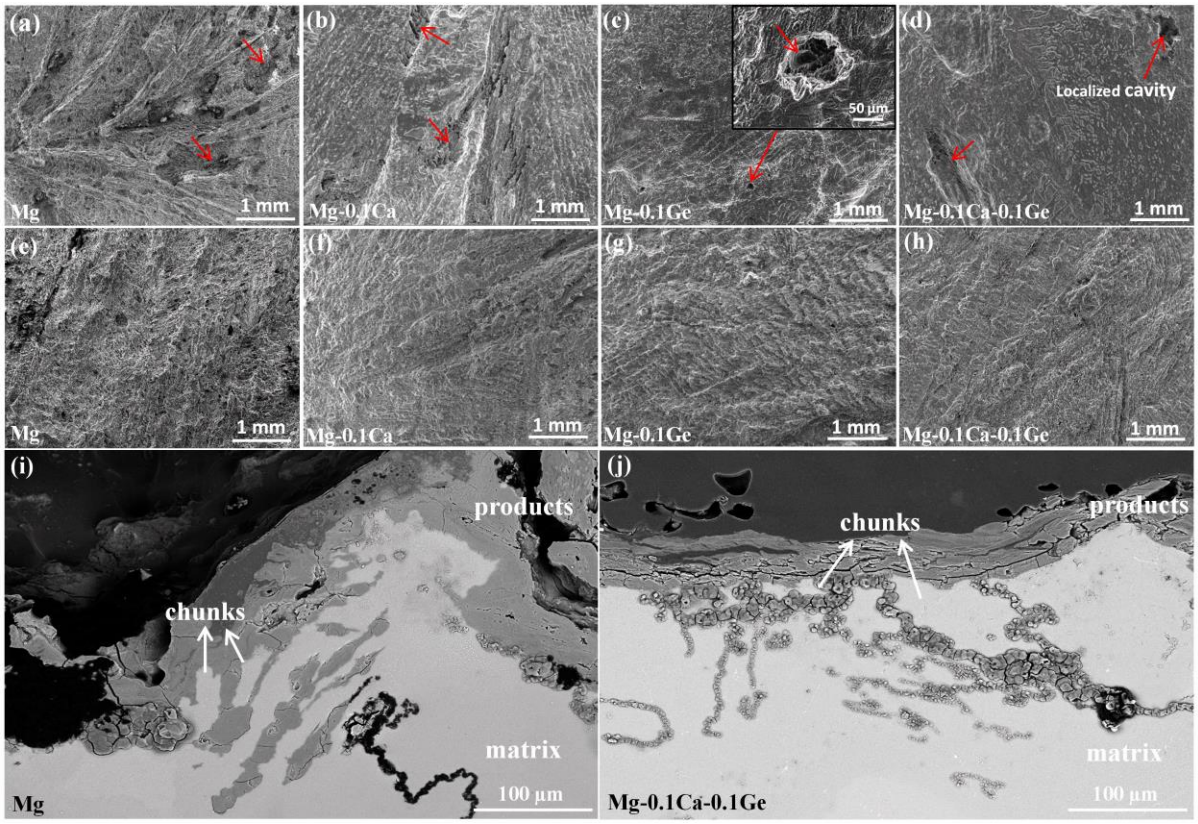

Fig. 10 Surface morphologies of different Mg anodes after discharge and removal of discharge products: (a-d) 1 mA cm^{-2} for 15 h, (e-h) 10 mA cm^{-2} for 8 h. The cross-sectional morphologies of recast pure Mg and Mg-0.1Ca-0.1Ge after discharge at 1 mA cm^{-2} are shown in (i) and (j), respectively.

Table 4 Utilization efficiency (UE) of diverse Mg anodes in 3.5 wt% NaCl solution under low current densities.

Mg anode	Alloying load	Condition	UE	Current density	Reference
Mg-0.1Ca	0.1 wt%	as-cast	49%	1 mA cm^{-2}	this work
Mg-0.1Ge	0.1 wt%		50%		
Mg-0.1Ca-0.1Ge	0.2 wt%		48%		
AZ91	10.1 wt%	extruded	25%	2.5 mA cm^{-2}	[62]
AZ91-Ca	11.5 wt%		32%		
AZ91-La	10.4 wt%		24%		
AZ91-Sm	10.5 wt%		18%		
AZ91-Ca-Sm-La	12.2 wt%		25%		
Mg-Zn-Y	7.1 wt%	as-cast	39%	2.5 mA cm^{-2}	[63]
	11 wt%		36%		
Mg-Zn-Zr	6.7 wt%		33%		
AZ80	9.1 wt%	as-cast	22%	1.5 mA cm^{-2}	[64]

		ultrasonic treated	32%		
		electromagnetic field treated	23%		
AZ61	7.1 wt%	as-cast	41%	2.5 mA cm^{-2}	[65]
		rolled	45%		
AZ61-LA	7.6 wt%	as-cast	44%		
		rolled	47%		
Mg	99.8 wt% Mg	plate	38%	1 mA cm^{-2}	[66]
EV31A	5.1 wt%		42%		
ZE10A	2 wt%		34%		
Mg-Al	9 wt%	as-cast and then	30%	2.5 mA cm^{-2}	[67]
Mg-Al-In	10 wt%	annealed	32%		
AZ91	10 wt%		30%		
Mg-Al	3 wt%	as-cast and then	38%	2.5 mA cm^{-2}	[68]
Mg-Al-Sn	4 wt%	annealed	52%		
Mg-Al-Ga	4 wt%		53%		
Mg-Al-In	4 wt%		42%		
AZ31	4 wt%		40%		

3.6 Mg-air battery tests

To evaluate the discharge properties of prepared Mg-0.1Ca, Mg-0.1Ge and Mg-0.1Ca-0.1Ge alloy as anode materials for primary Mg batteries, discharge testes are also performed in a custom-made Mg-air full cell. A commercially cast AZ31 alloy, which has been widely accepted as anode material for aqueous Mg batteries, is included for comparison. Fig. 11 presents the cell voltage profile of the Mg-air cell adopted with different anodes. Note that the adopted AZ31 anode in this work provides voltage of 1.16 V at 10 mA cm^{-1}, comparable to the existing value (1.2 V) for AZ31 from the work of Ma et al. [69]. Mg-0.1Ge and Mg-0.1Ca-0.1Ge both provide the Mg-air cell with significantly improved cell voltage comparing to the AZ31 anode, e.g. 1.26 V at 10 mA cm^{-1}. Besides, the utilization efficiency of AZ31 anode, around 36% at 1 mA cm^{-2} as reported in our previous work [41], is also inferior in comparison with M-0.1Ge and Mg-0.1Ca-0.1Ge, 50% as mentioned above. In addition, the two micro-alloyed alloys also exhibit similar discharge properties to the Mg-0.1Ca anode, which is a newly developed high quality anode material [37]. Thus, as good candidates, they provide additional options for anode materials concerning developing high performance primary Mg system. Interestingly, the minor addition of Ge to Mg-0.1Ca anode do not induce large enhancement regarding discharge potential or voltage measured in half-cell or Mg-air full cell.

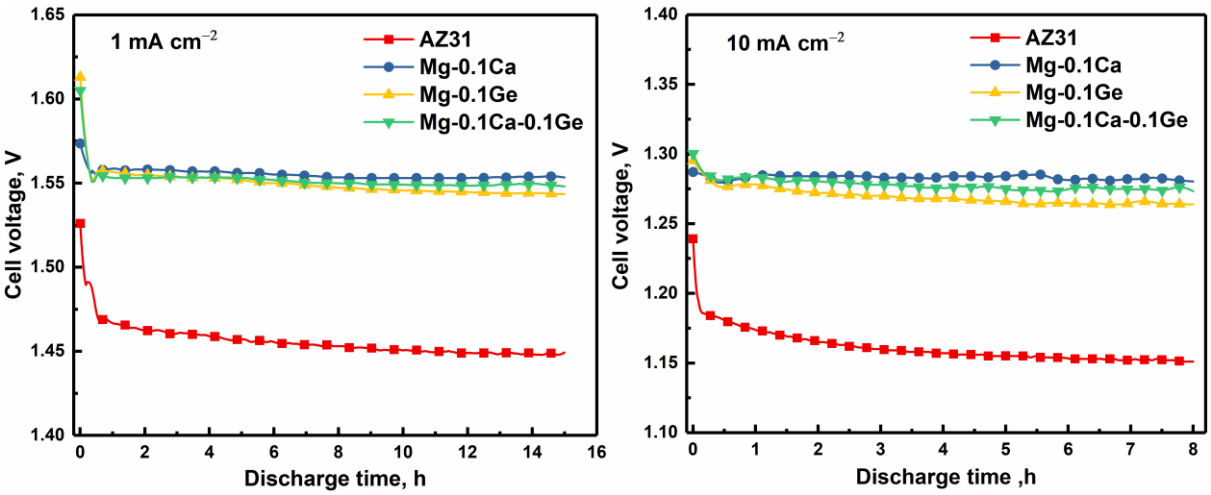

Fig. 11 Discharge curves of a custom-made Mg-air full cell adopting different anodes operated at two current densities. The electrolyte is 3.5 wt% NaCl solution (unbuffered, pH 5.6). The catalyst utilized in the commercially air cathode is C/MnO_2 mixture.

4. Discussion

4.1 Effect of Ca/Ge micro-alloying on corrosion performance

The present study indicates that low corrosion rates are achieved by Ca/Ge micro-alloying. The reduced corrosion rates are attributed to the inhibited cathodic kinetics and a pseudo-protective surface film. The lower cathodic reaction rates of Mg-0.1Ca and Mg-0.1Ca-0.1Ge result in slower corrosion rates than that of Mg-0.1Ge. Cathodic reaction kinetics of Mg-0.1Ca-0.1Ge is weaker than that of Mg-0.1Ca merely at the initial immersion stage and then tends to be similar, thus leading to the alike corrosion rate. Contemporarily, restricting kinetics of HER has been considered as a more logical approach for developing highly corrosion resistant Mg alloys with the inspiration of alloying element As [70, 71] and other Group 14 and Group 15 elements, like Ge [44-46]. The mechanism for kinetics restriction by these alloying elements remains unclear, but is most possibly related to restriction of impurity action and re-deposition. Cathodic poisons, such as As, is supposed to deposit and cover the surface of impurities-rich particles, which serve as primarily cathodic sites for HER, thus reducing the HER rate. Besides, the composition of surface oxide/hydroxide film is possibly altered by these elements and then leads to the suppressed cathodic kinetics, notwithstanding the possible influence has not been amply investigated. The results presented in this work (Fig. 3c and d) show that in the case of the recast pure Mg the HER increases with immersion time. This increment upon pure Mg is presumably related to impurity enrichment and build-up of a hydroxide film on Mg surface. The enrichment of noble impurities, like Fe at Mg surface as a result of re-deposition process [50], increases the cathodic HER kinetics to a certain extent, although some works have demonstrated the Fe enrichment efficiency is low [72, 73]. Besides, as reported, an ultra-high-purity Mg (0.1 ppm Fe) showed accelerated cathodic HER kinetics after anodic polarization comparing to the non-polarized state, elucidating possible influence of hydroxide film on cathodic reaction [52]. By contrast, there is no such an increase in other

systems with Ca and Ge. It seems the effect of noble impurities and hydroxide film on HER is restricted by the alloying elements, speculatively attributed to altered film composition and reduced impurities enrichment. Additionally, kinetics restriction is also accessible through alloying elements with capability of sequestering impurities via either reducing the impurities contents during solidification or alleviating the cathodic activity of impurity-rich particles by altering the particles chemistry. Regrettably, few elements with this function are found, with Mn [49, 74] and Y [75] as representatives. Herein, it is not fully clear which factors contribute to the restricted cathodic kinetics of Mg-0.1Ca, Mg-0.1Ge and Mg-0.1Ca-0.1Ge alloys. Nevertheless, it is apparent that addition of 0.1% Ca as well as the combination of minor Ca and Ge is more effective than Ge regarding kinetic control, as shown in Fig. 3.

The effect of induced intermetallics in fabricated lean alloys should also be considered, as the intermetallic normally possesses different electrochemical potential with respect to Mg matrix, being drivers for severe galvanic corrosion. Mg_2Ge phase exhibits a positive potential difference of ~ 400 mV with respect to the matrix of Mg-0.3 wt% Ge alloy as reported by Liu et al.[44], whilst merely ~50 mV in Mg-0.5Zn-0.2Ge system reported by Jiang et al.[46] Nevertheless, only superficial corrosion occurs around this cathodic phase as indicated by the mentioned work and Fig. 5 in this study. Therefore, it is reasonable to conclude that the low corrosion rate of micro-alloyed Mg-Ge alloy is attributed at least partially to the absence of severe galvanic corrosion related to Mg_2Ge phase. Alike, CaMgSi intermetallic in Mg-0.1Ca alloy also possesses higher electrochemical potential than the matrix, ~ 400 mV as determined by Ben-Hamu et al.[76] and ~200 mV by Mohedano et al.[77]. However, this kind of cathodic intermetallic also does not induce severe localized corrosion as proved by the surface morphology in Fig. 5. Only some shallow corrosion cavities are seen even after immersion for 7 days in the highly corrosive 3.5 wt% NaCl solution, possibly due to small size and low quantity of CaMgSi particles. Regarding Mg-0.1Ca-0.1Ge alloy, $Mg_xCa_yGe_z$ ternary phase acts as micro-anode with respect to Mg matrix, leading to its preferential dissolution and protection to matrix. Subsequently, this anodic phase is completely degraded or loss contact with the solution due to accumulation of corrosion products. In this case, corrosion starts upon the matrix, particularly around the dissolved secondary phases. Due to inhibited cathodic HER kinetics and absence of severe galvanic corrosion in this stage, the Mg-0.1Ca-0.1Ge matrix merely suffers superficial corrosion as shown in Fig. 5. Summarizing, the inhibited cathodic kinetics of HER and low amount of secondary phase particles contribute to the low corrosion rates of these alloys micro-alloyed with Ca/Ge, which are comparable to intrinsic Mg corrosion rate.

4.2 Effect of Ca/Ge micro-alloying on discharge properties

It is noteworthy that the difference of discharge potential for all studied anodes is much smaller comparing to the difference of OCP measured either before (up to 260 mV, Fig. 3a) or after discharge (up to 280 mV, Fig. 12a). In principle, apart from OCP, the discharge potential of Mg anodes is tightly dependent on the over potential under applied anodic current, which is determined by anodic dissolution

kinetics and surface film conditions. EIS measured immediately after discharge is performed to evaluate the electrode activity of all anodes as presented in Fig. 12b. The lowest scan frequency was set as 0.1 Hz, due to the non-stationarity of the active surface caused by discharge. Consequently, regarding all the alloys only one capacitive loop is distinct within the whole frequency range. By contrast, for the recast pure Mg, some scattered data points appear in the low frequency range. Although the interpretation for EIS of Mg is still controversial, the impedance of each anode can be roughly estimated and compared with each other to provide information concerning different electrode activity. Apparently, the recast pure Mg exhibits the highest activity, as forecasted by the lowest impedance value, indicating its fastest activity during discharge, which contributes to the mild difference between the discharge potential of Mg and other alloys. Mg-0.1Ge and Mg-0.1Ca are much alike in OCP as well as overall impedance value after discharge (at 10 mA cm^{-2} for 0.5 hour), implying similar activity and being the reason for the similar discharge potential. In comparison, Mg-0.1Ca-0.1Ge anode still maintains more negative OCP even after discharge, approximately –1.90 $V_{Ag/AgCl}$, comparing to – 1.75 $V_{Ag/AgCl}$ for binary Mg-0.1Ca and Mg-0.1Ge. However, this ternary alloy anode shows a remarkably higher impedance value measured after discharge, indicating more sluggish electrode activity in comparison to that of the two binary alloy anodes. Thus, its discharge potential has not been further improved even in the case of significantly negative OCP. The sluggish activity of Mg-0.1Ca-0.1Ge anode is possibly partially related to a more protective surface film of discharge products. In this case, electrolyte additives, like the aforementioned Mg^{2+} complexing agents, is favorable for achieving better discharge potential, with the benefit of highly negative OCP of micro-alloyed Mg-Ca-Ge anodes.

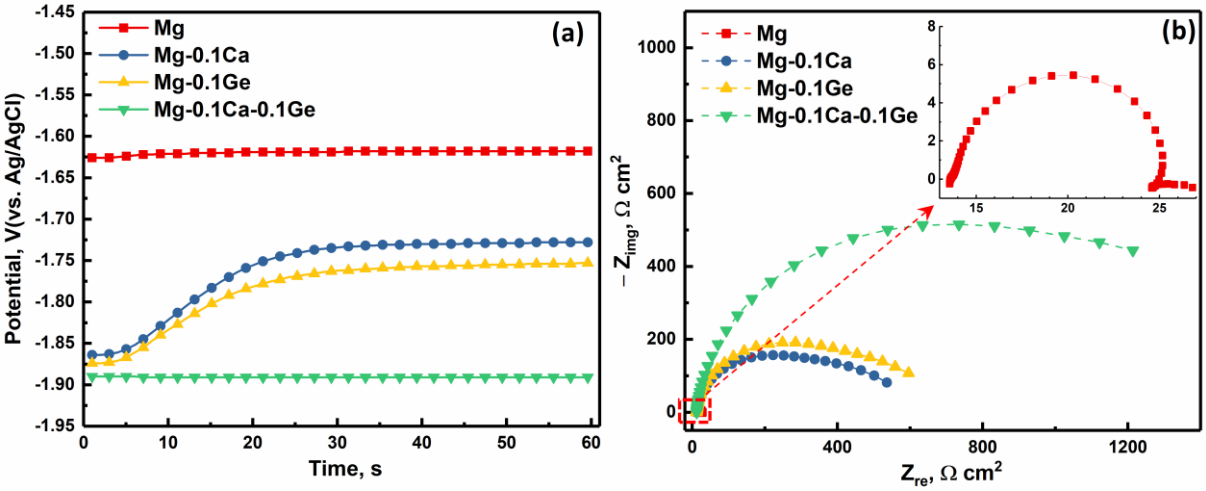

Fig. 12 (a) OCP- time curves and (b) EIS Nyquist plots of all materials measured after discharge at 10 mA cm^{-2} for 0.5 hour.

As mentioned in the Introduction section, utilization efficiency and capacity of Mg anodes are associated with chunk effect (CE) and real-time self-discharge rate with applied anodic current, rather than corrosion rate at OCP [41]. Hence, the self-discharge rate of all prepared anodes was determined by real-time hydrogen evolution and is presented in Fig. 13. Notably, al the micro-alloyed anodes

exhibit suppressed real-time hydrogen evolution rate, implying lower self-discharge rate, comparing to recast pure Mg anode during discharge at different current densities. However, no obvious difference is seen regarding the hydrogen evolution of the three micro-alloyed anodes, even though they show different corrosion rates measured at OCP condition as shown in Fig. 4. Interestingly, all the three alloy anodes show stable hydrogen evolution behavior after a short stabilization at initial stage. The rate of hydrogen generation is approximately 0.3 ml cm^{-2} h^{-1} at 1 mA cm^{-2} and 3.0 ml cm^{-2} h^{-1} at 10 mA cm^{-2}. Accordingly, the self-discharge current densities calculated via Faraday's law are 0.67 and 6.66 mA cm^{-2} at 1 and 10 mA cm^{-2}, respectively. Thereafter, the utilization efficiency without consideration of efficiency loss by CE ($\boldsymbol{\eta}$) can be estimated roughly via the following formula:

$$\eta = \frac{i_{applied}}{i_{applied} + i_{self-discharge}} \quad (6)$$

where $i_{applied}$ is the applied current density, and $i_{self-discharge}$ is the calculated self-discharge current density associated with hydrogen evolution. The estimated $\boldsymbol{\eta}$ is 60.0% when discharge at both 1 and 10 mA cm^{-2}, respectively. It is noticeable that the actual utilization efficiency at 10 mA cm^{-2}, around 58%, is similar to the estimated value (60.0%), indicating negligible efficiency loss caused by CE, which is attributed to the uniform anodic dissolution as shown in Fig. 10 (e-h). By contrast, the actual utilization efficiency at 1 mA cm^{-2}, nearly 50%, is lower than the estimated value (59.9%), implying an apparent efficiency loss of approximately 10% by CE (related to the localized cavities shown in Fig. 10 (b-d)). Nevertheless, this 10% efficiency loss by CE is much lower comparing to that of high purity Mg and some commercially alloy anodes, 20% - 45% at the same current density as reported in our previous work [41]. To conclude, micro-alloying of Ca and Ge enables Mg anodes to achieve higher utilization efficiency (50% and 60% at 1 and 10 mA cm^{-2} respectively) via reduced self-discharge rate and suppressed occurrence of chunk effect.

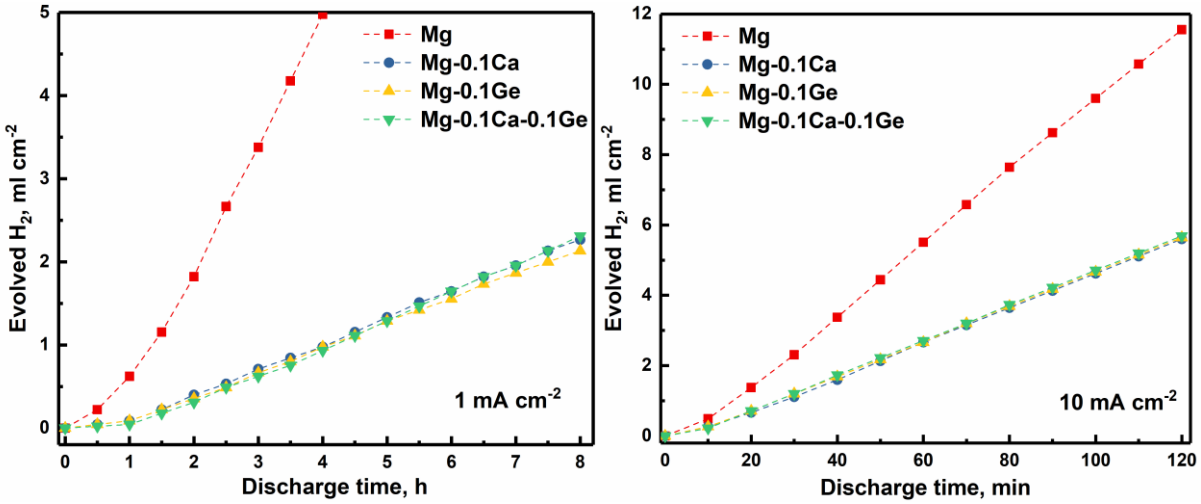

Fig. 13 Real-time hydrogen evolution determined during discharge at different current densities in 3.5 wt% NaCl solution. Representative results of triplicated measurements are presented.

4.3 Anode performance in additive-containing electrolyte

As mentioned above, the highly negative OCP of Mg-0.1Ca-0.1Ge alloy provides a possibility to achieve further enhanced battery voltage with adoption of electrolyte additives, like Mg^{2+} complexing agents. To prove this hypothesis, cell voltage of the custom-made Mg-air battery adopting varied anode materials was measured in 3.5 wt% NaCl with 0.1 M salicylate (SAL) and is shown in Fig. 14. The voltage profile measured in blank 3.5 wt% NaCl extracted from Fig. 11 is included for the sake of comparison. Predictably, the battery with the same anode material exhibits higher cell voltage when 0.1 M SAL is added into the electrolyte, since SAL is Mg^{2+} complexing agent with the capability of hindering the formation of $Mg(OH)_2$ film . The boosted voltage is attributed to the decreased voltage drop associated with absence of thick hydroxide film. Something noteworthy is that the battery with Mg-0.1Ca-0.1Ge anode shows remarkably improved voltage than that based on Mg-0.1Ca anode in SAL-containing electrolyte, in spite of the similar voltage in the electrolyte without SAL. The difference might be due to the varied protection ability of surface film formed in blank 3.5 wt% NaCl as indicated by EIS presented in Fig. 12b. Regarding Mg-0.1Ca-0.1Ge, more overvoltage related to surface film is released after adding SAL via impeding the formation of $Mg(OH)_2$, leading to the higher operating voltage. The results indicate that the micro-alloyed Mg-0.1Ca-0.1Ge alloy is capable of providing better battery properties than Mg-0.1Ca, particularly in additive-containing electrolytes. In such a case, more work is desirable for optimizing the electrolyte additives and elucidating their effect on the novel Mg-Ca-Ge anode.

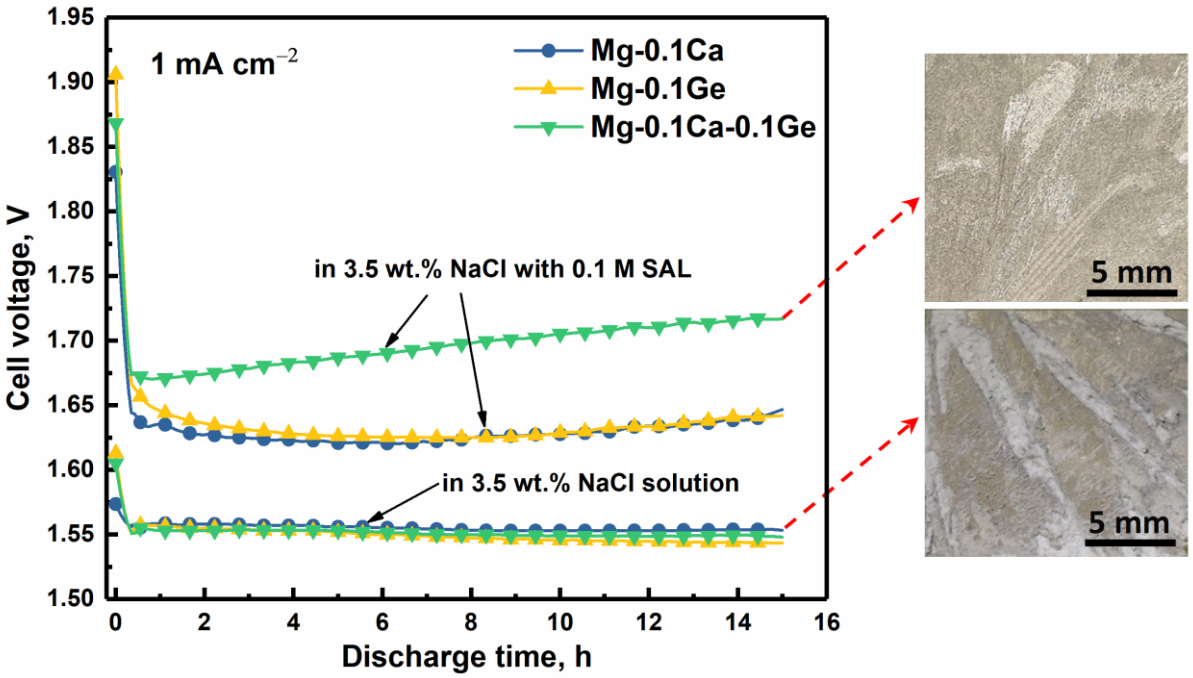

Fig. 14 Voltage profile of the custom-made Mg-air full cell adopting different anodes at 1 mA cm^{-2} in the electrolyte with an additive, i.e. 0.1 M salicylate (SAL, initial pH adjusted to 7). Data in blank NaCl solution extracted from Fig. 11 are included for comparison. Optical images of anode surface after discharge is also presented.

5. Conclusions

Herein, the corrosion and discharge properties of micro-alloyed Mg-0.1%Ge (hereafter weight percent) as an anode material for primary Mg battery are evaluated in comparison to newly developed high performance Mg-0.1%Ca anode. Besides, the synergetic effect of micro-alloying of Ge and Ca to Mg anode is investigated in terms of microstructure, corrosion behavior and discharge properties. The following conclusion can be drawn:

1) Restriction of cathodic HER kinetics via minor Ge alloying is inferior compared to that of Ca, leading to the faster corrosion rate of Mg-0.1%Ge alloy than Mg-0.1%Ca. Nevertheless, the self-discharge rate of Mg-0.1%Ge anode is similar to that of Mg-0.1%Ca, contributing to their alike high utilization efficiency (~60% at 10 mA cm^{-2}) and superior discharge capacity.

2) The addition of 0.1% Ge decreases the cathodic kinetics of Mg-0.1%Ca alloy, albeit only at initial immersion stage, implying a positive synergetic effect of Ge and Ca on cathodic HER kinetics restriction. Consequently, Mg-0.1%Ca-0.1%Ge alloy exhibits a low corrosion rate (0.2 mm y^{-1} in 3.5 wt% NaCl solution) within 7-day exposure in the solution.

3) Mg-0.1%Ca-0.1%Ge possesses highly negative OCP owing to the intensively restricted cathodic reaction, showing a great promise to offer higher voltage for Mg batteries. However, it exhibits similar voltage to micro-alloyed Mg-Ca and Mg-Ge anodes in 3.5% NaCl electrolyte, due to large voltage drop caused by a more protective film on the surface.

4) In electrolyte containing 0.1 M salicylate, Mg-0.1%Ca-0.1%Ge anode provides higher voltage (1.70 V at 1 mA cm^{-2}) in comparison to Mg-0.1%Ca anode (1.63 V) due to the absence of thick $Mg(OH)_2$ film.

5) Both Mg-0.1%Ge and Mg-0.1%Ca-0.1%Ge anodes show good discharge properties, which are better than those of AZ31 and comparable to Mg-0.1%Ca anode. Therefore, they are also good candidates for anode materials of primary batteries and, meanwhile, provide more options for the development of high performance Mg batteries considering the necessity of optimizing anode geometry and electrolyte composition.

Acknowledgement

Bahram Vaghefinazari is sincerely acknowledged for the discussion on experimental results. M. Deng, L. Wang and P. Jiang are grateful for the support from China Scholarship Council concerning the award of fellowship No. 201606370031, No. 201706370183 and No. 201606310043. D. Snihirova acknowledges SeaMag project for financial support (MarTera ERA-NET cofund).

Data availability

The raw/processed data required to reproduce these findings cannot be shared at this time as the data also forms part of an ongoing study.

Reference

[1] David Linden, T.B. Reddy, Handbook of Batteries, McGraw-Hill, New York, 2002.
[2] C Daniel, J. Besenhard, Handbook of Battery Materials, Wiley-VCH, Weinheim, 2012.
[3] F. Cheng, J. Chen, Metal-air batteries: from oxygen reduction electrochemistry to cathode catalysts, Chem. Soc. Rev. , 41 (2012) 2172-2192. https://doi.org/10.1039/c1cs15228a.
[4] T. Zhang, Z. Tao, J. Chen, Magnesium–air batteries: from principle to application, Mater. Horiz., 1 (2014) 196-206. https://doi.org/10.1039/c3mh00059a.
[5] Md. Rahman, X. Wang, C. Wen, High Energy Density Metal-Air Batteries: A Review, J. Electrochem. Soc. , 160 (2013) A1759-A1771. https://doi.org/10.1149/2.062310jes.
[6] M. Deng, D. Höche, D. Snihirova, L.Q. Wang, B. Vaghefinazari, S.V. Lamaka, M.L. Zheludkevich, Aqueous Mg batteries, in: M. Fichtner (Ed.) Magnesium Batteries: Research and Applications, Royal Society of Chemistry, United Kingdom, 2019, pp. 275-308. https://doi.org/10.1039/9781788016407-00275.
[7] N.G. Wang, R.C. WANG, C.Q. Peng, C.W. Hu, Y. Feng, B. Peng, Research progress of magnesium anodes and their applications in chemical power sources, Transactions of Nonferrous Metals Society of China, 24 (2014) 2427-2439. https://doi.org/10.1016/S1003-6326(14)63367-7.
[8] R. Mohtadi, F. Mizuno, Magnesium batteries: Current state of the art, issues and future perspectives, Beilstein J Nanotechnol, 5 (2014) 1291-1311. https://doi.org/10.3762/bjnano.5.143.
[9] R. Udhayan, N. Muniyandi, P.B. mathur, Studies on magnesium and its alloys in battery electrolytes, British Corroison Journal, 27 (1992) 68-71. https://doi.org/10.1179/000705992798268927.
[10] D. Höche, S.V. Lamaka, B. Vaghefinazari, T. Braun, R.P. Petrauskas, M. Fichtner, M.L. Zheludkevich, Performance boost for primary magnesium cells using iron complexing agents as electrolyte additives, Sci Rep, 8 (2018) 7578. https://doi.org/10.1038/s41598-018-25789-8.
[11] Y. Li, J. Ma, G. Wang, F. Ren, Y. Zhu, Y. Song, Investigation of Sodium Phosphate and Sodium Dodecylbenzenesulfunate as Electrolyte Additives for AZ91 Magnesium-Air Battery, J. Electrochem. Soc. , 165 (2018) A1713-A1717. https://doi.org/10.1149/2.0581809jes.
[12] M. Shinohara, E. Araki, M. Mochizuki, T. Kanazawa, K. Suyehiro, Practical application of a sea-water battery in deep-sea basin and its performance, J. Power Sources 187 (2009) 253-260. https://doi.org/10.1016/j.jpowsour.2008.10.105.
[13] B.V. Ratnakumar, Passive films on magnesium anodes in primary batteries, J. Appl. Electrochem. , 18 (1988) 268-279. https://doi.org/10.1007/BF01009274.
[14] M. Yuasa, X. Huang, K. Suzuki, M. Mabuchi, Y. Chino, Discharge properties of Mg–Al–Mn–Ca and Mg–Al–Mn alloys as anode materials for primary magnesium–air batteries, J. Power Sources 297 (2015) 449-456. https://doi.org/10.1016/j.jpowsour.2015.08.042.
[15] T. Zheng, Y. Hu, Y. Zhang, S. Yang, F. Pan, Composition optimization and electrochemical

properties of Mg-Al-Sn-Mn alloy anode for Mg-air batteries, Materials & Design, 137 (2018) 245-255. https://doi.org/10.1016/j.matdes.2017.10.031.
[16] L.Q. Wang, R.C. Wang, Y. Feng, M. Deng, N.G. Wang, Effect of Al and Pb Contents on the Corrosion Electrochemical Properties and Activation of Mg-Al-Pb Alloy Anode, J. Electrochem. Soc. , 164 (2017) A438-A446. https://doi.org/10.1149/2.1211702jes.
[17] K. Gusieva, C.H.J. Davies, J.R. Scully, N. Birbilis, Corrosion of magnesium alloys: the role of alloying, Int. Mater. Rev. , 60 (2014) 169-194. https://doi.org/10.1179/1743280414y.0000000046.
[18] Y.D. Milusheva, R.I. Boukoureshtlieva, S.M. Hristov, A.R. Kaisheva, Environmentally-clean Mg-air electrochemical power sources, Bulgarian Chemical Communications, 43 (2011) 42-47.
[19] S.V. Lamaka, B. Vaghefinazari, D. Mei, R.P. Petrauskas, D. Höche, M.L. Zheludkevich, Comprehensive screening of Mg corrosion inhibitors, Corros. Sci. , 128 (2017) 224-240. https://doi.org/10.1016/j.corsci.2017.07.011.
[20] Z. Qiao, Z. Shi, N. Hort, N.I. Zainal Abidin, A. Atrens, Corrosion behaviour of a nominally high purity Mg ingot produced by permanent mould direct chill casting, Corros. Sci. , 61 (2012) 185-207. https://doi.org/10.1016/j.corsci.2012.04.030.
[21] Z. Shi, A. Atrens, An innovative specimen configuration for the study of Mg corrosion, Corros. Sci. , 53 (2011) 226-246. https://doi.org/10.1016/j.corsci.2010.09.016.
[22] L. Yang, X. Zhou, S.-M. Liang, R. Schmid-Fetzer, Z. Fan, G. Scamans, J. Robson, G. Thompson, Effect of traces of silicon on the formation of Fe-rich particles in pure magnesium and the corrosion susceptibility of magnesium, J. Alloys Compd. , 619 (2015) 396-400. https://doi.org/10.1016/j.jallcom.2014.09.040.
[23] F. Cao, Z. Shi, J. Hofstetter, P.J. Uggowitzer, G. Song, M. Liu, A. Atrens, Corrosion of ultra-high-purity Mg in 3.5% NaCl solution saturated with Mg(OH)2, Corros. Sci. , 75 (2013) 78-99. https://doi.org/10.1016/j.corsci.2013.05.018.
[24] G. Xin, X. Wang, C. Wang, J. Zheng, X. Li, Porous Mg thin films for Mg-air batteries, Dalton Trans. , 42 (2013) 16693-16696. https://doi.org/10.1039/c3dt52482e.
[25] C. Li, F. Cheng, W. Ji, Z. Tao, J. Chen, Magnesium microspheres and nanospheres: Morphology-controlled synthesis and application in Mg/MnO2 batteries, Nano Research, 2 (2009) 713-721. https://doi.org/10.1007/s12274-009-9075-y.
[26] W. Li, C. Li, C. Zhou, H. Ma, J. Chen, Metallic Magnesium Nano/Mesoscale Structures: Their Shape-Controlled Preparation and Mg/Air Battery Applications, Angewandte Chemie, 118 (2006) 6155-6158. https://doi.org/10.1002/ange.200600099.
[27] J. Liu, H. Wang, Q. Yuan, X. Song, A novel material of nanoporous magnesium for hydrogen generation with salt water, J. Power Sources 395 (2018) 8-15. https://doi.org/10.1016/j.jpowsour.2018.05.062.
[28] I.V. Okulov, S.V. Lamaka, T. Wada, K. Yubuta, M.L. Zheludkevich, J. Weissmüller, J. Markmann, H. Kato, Nanoporous magnesium, Nano Research, 11 (2018) 6428-6435.

https://doi.org/10.1007/s12274-018-2167-9.
[29] A. Pardo, M.C. Merino, A.E. Coy, F. Viejo, R. Arrabal, S. Feliú, Influence of microstructure and composition on the corrosion behaviour of Mg/Al alloys in chloride media, Electrochim. Acta 53 (2008) 7890-7902. https://doi.org/10.1016/j.electacta.2008.06.001.
[30] N. Wang, Y. Mu, W. Xiong, J. Zhang, Q. Li, Z. Shi, Effect of crystallographic orientation on the discharge and corrosion behaviour of AP65 magnesium alloy anodes, Corroison Science, 144 (2018) 107-126. https://doi.org/10.1016/j.corsci.2018.08.003.
[31] X. Liu, S. Liu, J. Xue, Discharge performance of the magnesium anodes with different phase constitutions for Mg-air batteries, J. Power Sources 396 (2018) 667-674. https://doi.org/10.1016/j.jpowsour.2018.06.085.
[32] Y. Shi, C. Peng, Y. Feng, R. Wang, N. Wang, Microstructure and electrochemical corrosion behavior of extruded Mg–Al–Pb–La alloy as anode for seawater-activated battery, Materials & Design, 124 (2017) 24-33. https://doi.org/10.1016/j.matdes.2017.03.058.
[33] J. Li, B. Zhang, Q. Wei, N. Wang, B. Hou, Electrochemical behavior of Mg-Al-Zn-In alloy as anode materials in 3.5 wt.% NaCl solution, Electrochim. Acta 238 (2017) 156-167. https://doi.org/10.1016/j.electacta.2017.03.119.
[34] K.A. Unocic, H.H. Elsentriecy, M.P. Brady, H.M.M. III, G.L. Song, M. Fayek, R.A. Meisner, B. Davis, Transmission Electron Microscopy Study of Aqueous Film Formation and Evolution on Magnesium Alloys, J. Electrochem. Soc. , 161 (2014) C302-C311. https://doi.org/10.1149/2.024406jes.
[35] J.H. Nordlien, K. Nisancioglu, Morphology and Structure of Oxide Films Formed on MgAl Alloys by Exposure to Air and Water, J. Electrochem. Soc. , 143 (1996) 2564-2572. https://doi.org/10.1149/1.1837048.
[36] N. Wang, R. Wang, C. Peng, Y. Feng, X. Zhang, Influence of aluminium and lead on activation of magnesium as anode, Transactions of Nonferrous Metals Society of China, 20 (2010) 1403-1411. https://doi.org/10.1016/s1003-6326(09)60312-5.
[37] M. Deng, D. Höche, S.V. Lamaka, D. Snihirova, M.L. Zheludkevich, Mg-Ca binary alloys as anodes for primary Mg-air batteries, J. Power Sources 396 (2018) 109-118. https://doi.org/10.1016/j.jpowsour.2018.05.090.
[38] M. Deng, D. Höche, S.V. Lamaka, L. Wang, M.L. Zheludkevich, Revealing the impact of second phase morphology on discharge properties of binary Mg-Ca anodes for primary Mg-air batteries, Corros. Sci. , 153 (2019) 225-235. https://doi.org/10.1016/j.corsci.2019.03.050.
[39] B. Vaghefinazari, D. Höche, S.V. Lamaka, D. Snihirova, M.L. Zheludkevich, Tailoring the Mg-air primary battery performance using strong complexing agents as electrolyte additives, J. Power Sources 453 (2020). https://doi.org/10.1016/j.jpowsour.2020.227880.
[40] L. Wang, D. Snihirova, M. Deng, B. Vaghefinazari, S.V. Lamaka, D. Höche, M.L. Zheludkevich, Tailoring electrolyte additives for controlled Mg-Ca anode activity in aqueous Mg-air batteries, J.

Power Sources 460 (2020) 228106. https://doi.org/10.1016/j.jpowsour.2020.228106.
[41] M. Deng, L. Wang, D. Höche, S.V. Lamaka, D. Snihirova, B. Vaghefinazari, M.L. Zheludkevich, Clarifying the decisive factors for utilization efficiency of Mg anodes for primary aqueous batteries, J. Power Sources 441 (2019) 227201. https://doi.org/10.1016/j.jpowsour.2019.227201.
[42] G.A. Marsh, E. Schaschl, The Difference Effect and the Chunk Effect, J. Electrochem. Soc. , 107 (1960) 960-965. https://doi.org/10.1149/1.2427579
[43] M.E. Straumanis, B.K. Bhatia, Disintegration of Magnesium While Dissolving Anodically in Neutral and Acidic solutions, J. Electrochem. Soc. , 110 (1963) 357-360. https://doi.org/10.1149/1.2425763.
[44] R.L. Liu, M.F. Hurley, A. Kvryan, G. Williams, J.R. Scully, N. Birbilis, Controlling the corrosion and cathodic activation of magnesium via microalloying additions of Ge, Sci Rep, 6 (2016) 28747. https://doi.org/10.1038/srep28747.
[45] R.L. Liu, J.R. Scully, G. Williams, N. Birbilis, Reducing the corrosion rate of magnesium via microalloying additions of group 14 and 15 elements, Electrochim. Acta 260 (2018) 184-195. https://doi.org/10.1016/j.electacta.2017.11.062.
[46] P. Jiang, C. Blawert, R. Hou, N. Scharnagl, J. Bohlen, M.L. Zheludkevich, Microstructural influence on corrosion behavior of MgZnGe alloy in NaCl solution, J. Alloys Compd. , 783 (2019) 179-192. https://doi.org/10.1016/j.jallcom.2018.12.296.
[47] R.L. Liu, Z.R. Zeng, J.R. Scully, G. Williams, B. Birbilis, Simultaneously improving the corrosion resistance and strength of magnesium via low levels of Zn and Ge additions, Corros. Sci. , 140 (2018) 18-29. https://doi.org/10.1016/j.corsci.2018.06.027.
[48] A.A. Nayeb-Hashemi, J.B. Clark, R.W. Olesinski, G.J. Abbaschian, The Ge-Mg (Germanium-Magnesium) System.pdf, Bulletin of Alloy Phase Diagrams, 5 (1984) 359-365. https://doi.org/10.1007/BF02872950.
[49] G.L. Song, A. Atrens, Corrosion Mechanisms of magnesium, Advanced Enginnering Materials, 1 (1999) 11-33. https://doi.org/10.1002/(SICI)1527-2648(199909)1:1<11::AID-ADEM11>3.0.CO;2-N.
[50] D. Höche, C. Blawert, S.V. Lamaka, N. Scharnagl, C. Mendis, M.L. Zheludkevich, The effect of iron re-deposition on the corrosion of impurity-containing magnesium, Phys. Chem. Chem. Phys. , 18 (2016) 1279-1291. https://doi.org/10.1039/c5cp05577f.
[51] S.V. Lamaka, D. Höche, R.P. Petrauskas, C. Blawert, M.L. Zheludkevich, A new concept for corrosion inhibition of magnesium: Suppression of iron re-deposition, Electrochem. Commun. , 62 (2016) 5-8. https://doi.org/10.1016/j.elecom.2015.10.023.
[52] S. Fajardo, G.S. Frankel, Effect of impurities on the enhanced catalytic activity for hydrogen evolution in high purity magnesium, Electrochim. Acta 165 (2015) 255-267. https://doi.org/10.1016/j.electacta.2015.03.021.
[53] L. Yang, X. Zhou, M. Curioni, S. Pawar, H. Liu, Z. Fan, G. Scamans, G. Thompson, Corrosion Behavior of Pure Magnesium with Low Iron Content in 3.5 wt% NaCl solution, J. Electrochem. Soc. ,

162 (2015) C362-C368. https://doi.org/10.1149/2.1041507jes].
[54] G.L. Song, A. Atrens, D. StJohn, An Hydrogen Evolution Method for the Estimation of the Corrosion Rate of Magnesium Alloys, Magnesium Technology, (2001) 255-262. https://doi.org/10.1002/9781118805497.ch44.
[55] Y. Jin, C. Blawert, F. Feyerabend, J. Bohlen, M. Silva Campos, S. Gavras, B. Wiese, D. Mei, M. Deng, H. Yang, R. Willumeit-Römer, Time-sequential corrosion behaviour observation of micro-alloyed Mg-0.5Zn-0.2Ca alloy via a quasi-in situ approach, Corros. Sci. , 158 (2019) 108096. https://doi.org/10.1016/j.corsci.2019.108096.
[56] N. Wang, R. Wang, C. Peng, B. Peng, Y. Feng, C. Hu, Discharge behaviour of Mg-Al-Pb and Mg-Al-Pb-In alloys as anodes for Mg-air battery, Electrochim. Acta 149 (2014) 193-205. https://doi.org/10.1016/j.electacta.2014.10.053.
[57] A.A. Nayeb-Hasheml, J.B. Clark, R.W. Olesinskl, G.J. Abbaschian, The Ge-Mg (Germanium-Magnesium) System, Bulletin of Alloy Phase Diagrams, 5 (1984). https://doi.org/10.1007/BF02872950.
[58] B. Kim, K. Park, H. Kimura, Y. Park, I. Park, Influence of Addition of Ge on the Microstructure and Corrosion Properties of Magnesium, Mater. Trans. , 53 (2012) 240-243. https://doi.org/10.2320/matertrans.M2011240.
[59] D. Bian, W. Zhou, J. Deng, Y. Liu, W. Li, X. Chu, P. Xiu, H. Cai, Y. Kou, B. Jiang, Y. Zheng, Development of magnesium-based biodegradable metals with dietary trace element germanium as orthopaedic implant applications, Acta Biomater. , 64 (2017) 421-436. https://doi.org/10.1016/j.actbio.2017.10.004.
[60] I.-H. Jung, J. Kim, Thermodynamic modeling of the Mg–Ge–Si, Mg–Ge–Sn, Mg–Pb–Si and Mg–Pb–Sn systems, J. Alloys Compd. , 494 (2010) 137-147. https://doi.org/10.1016/j.jallcom.2010.01.045.
[61] Y. Song, D. Shan, E.-H. Han, Pitting corrosion of a Rare Earth Mg alloy GW93, Journal of Materials Science & Technology, 33 (2017) 954-960. https://doi.org/10.1016/j.jmst.2017.01.014.
[62] X. Liu, J. Xue, P. Zhang, Z. Wang, Effects of the combinative Ca, Sm and La additions on the electrochemical behaviors and discharge performance of the as-extruded AZ91 anodes for Mg-air batteries, J. Power Sources 414 (2019) 174-182. https://doi.org/10.1016/j.jpowsour.2018.12.092.
[63] X. Chen, Q. Zou, Q. Le, J. Hou, R. Guo, H. Wang, C. Hu, L. Bao, T. Wang, D. Zhao, F. Yu, A. Atrens, The quasicrystal of Mg–Zn–Y on discharge and electrochemical behaviors as the anode for Mg-air battery, J. Power Sources 451 (2020) 227807. https://doi.org/10.1016/j.jpowsour.2020.227807.
[64] X. Chen, S. Ning, Q. Le, H. Wang, Q. Zou, R. Guo, J. Hou, Y. Jia, A. Atrens, F. Yu, Effects of external field treatment on the electrochemical behaviors and discharge performance of AZ80 anodes for Mg-air batteries, Journal of Materials Science & Technology, 38 (2020) 47-55. https://doi.org/10.1016/j.jmst.2019.07.043.
[65] Y. Wu, Z. Wang, Y. Liu, G. Li, S. Xie, H. Yu, H. Xiong, AZ61 and AZ61-La Alloys as Anodes

for Mg-Air Battery, J. Mater. Eng. Perform. , 28 (2019) 2006-2016. https://doi.org/10.1007/s11665-019-03985-5.
[66] N. Shrestha, K.S. Raja, V. Utgikar, Mg-RE Alloy Anode Materials for Mg-Air Battery Application, J. Electrochem. Soc. , 166 (2019) A3139-A3153. https://doi.org/10.1149/2.0131914jes.
[67] X. Li, H. Lu, S. Yuan, J. Bai, J. Wang, Y. Cao, Q. Hong, Performance of Mg–9Al–1In Alloy as Anodes for Mg-Air Batteries in 3.5 wt% NaCl Solutions, J. Electrochem. Soc. , 164 (2017) A3131-A3137. https://doi.org/10.1149/2.0971713jes.
[68] S. Yuan, H. Lu, Z. Sun, L. Fan, X. Zhu, W. Zhang, Electrochemical Performance of Mg-3Al Modified with Ga, In and Sn as Anodes for Mg-Air Battery, J. Electrochem. Soc. , 163 (2016) A1181-A1187. https://doi.org/10.1149/2.0371607jes.
[69] J. Ma, G. Wang, Y. Li, F. Ren, A.A. Volinsky, Electrochemical performance of Mg-air batteries based on AZ series magnesium alloys, Ionics, 25 (2018) 2201-2209. https://doi.org/10.1007/s11581-018-2705-1.
[70] N. Birbilis, G. Williams, K. Gusieva, A. Samaniego, M.A. Gibson, H.N. McMurray, Poisoning the corrosion of magnesium, Electrochem. Commun. , 34 (2013) 295-298. https://doi.org/10.1016/j.elecom.2013.07.021.
[71] G. Williams, H.A.-L. Dafydd, H.N. McMurray, N. Birbilis, The influence of arsenic alloying on the localised corrosion behaviour of magnesium, Electrochim. Acta 219 (2016) 401-411. https://doi.org/10.1016/j.electacta.2016.10.006.
[72] N. Birbilis, T. Cain, J.S. Laird, X. Xia, J.R. Scully, A.E. Hughes, Nuclear Microprobe Analysis for Determination of Element EnrichmentFollowing Magnesium Dissolution, ECS Electrochemistry Letters, 4 (2015) C34-C37. https://doi.org/10.1149/2.0081510eel.
[73] T. Cain, S.B. Madden, N. Birbilis, J.R. Scully, Evidence of the Enrichment of Transition Metal Elements on Corroding Mg Surface Using Rutherford Backscattering Spectrometry, J. Electrochem. Soc. , 162 (2015) C228-C238. https://doi.org/10.1149/2.0541506jes].
[74] M. Liu, G.-L. Song, Impurity control and corrosion resistance of magnesium–aluminum alloy, Corros. Sci. , 77 (2013) 143-150. https://doi.org/10.1016/j.corsci.2013.07.037.
[75] J.I. Kim, H.N. Nguyen, B.S. You, Y.M. Kim, Effect of Y addition on removal of Fe impurity from magnesium alloys, Scr. Mater. , 162 (2019) 355-360. https://doi.org/10.1016/j.scriptamat.2018.11.046.
[76] G. Ben-Hamu, D. Eliezer, K.S. Shin, The role of Si and Ca on new wrought Mg–Zn–Mn based alloy, Materials Science and Engineering: A, 447 (2007) 35-43. https://doi.org/10.1016/j.msea.2006.10.059.
[77] M. Mohedano, B.J.C. Luthringer, B. Mingo, F. Feyerabend, R. Arrabal, P.J. Sanchez-Egido, C. Blawert, R. Willumeit-Römer, M.L. Zheludkevich, E. Matykina, Bioactive plasma electrolytic oxidation coatings on Mg-Ca alloy to control degradation behaviour, Surf. Coat. Technol. , 315 (2017) 454-467. https://doi.org/10.1016/j.surfcoat.2017.02.050.

5.6 Key outcomes

The aforementioned papers present main results of this study. Some high-performance anode materials are proposed. The decisive factors affecting the utilization efficiency of Mg anodes are clarified. Key outcomes of these papers are highlighted as following:

1) 0.1 wt.% Ca is the optimal composition for binary Mg-Ca alloy anodes due to inhibited cathodic HER reaction and a low secondary phases fraction.

2) Semi-continuous Mg_2Ca phase along grain boundaries results in lower corrosion rate and lower anode efficiency loss caused by chunk effect in comparison to dispersed fine Mg_2Ca particles.

3) Mg-air battery with binary Mg-Ca alloy anode owns the capability of supplying stable voltage during long-term intermittent discharge process, 1.5 V at 2 mA cm^{-2} for more than 60 h.

4) Concerning Mg anodes, the corrosion rate measured under OCP condition is not an indicator for the self-discharge rate under various applied current densities.

5) Chunk effect may cause a large anode efficiency loss (up to 50%), especially for the materials with high fractions of secondary phases and those suffering from non-uniform dissolution.

6) Indium micro-alloying effectively activates Mg-Ca anode via In re-deposition on anode surface.

7) Micro-alloying with 0.1 wt.% Ca and 0.2 wt.% In remarkably reduces the self-discharge rate of Mg anode, leading to high anode efficiency and enhanced battery energy density (80% and 2259 Wh kg^{-1} at 23.75 mA constant current).

8) Ca/Ge micro-alloying efficiently suppresses cathodic HER reaction of Mg, leading to a low corrosion rate (0.2 mm y^{-1}) and highly negative OCP (–1.91 $V_{Ag/AgCl}$) in 3.5 wt.% NaCl solution.

9) Mg-0.1wt.%Ca-0.1wt.%Ge anode supplies increased voltage than Mg-0.1wt.%Ca anode in 0.1 M salicylate-containing electrolyte, 1.7 V versus 1.63 V.

6 Discussion (Anode alloying elements selection guide)

6.1 Highly negative discharge potential of Mg-Ca based anodes

6.1.1 Binary Mg-Ca alloy anodes

In principle, the voltage E of one cell under an operating current i can be expressed as follow [1, 2]:

$$E = E_0 - (\eta_{ct} + \eta_c)_a - (\eta_{ct} + \eta_c)_c - iR \quad (6\text{-}1)$$

Where E_0 equals to the electromotive force, namely the open circuit voltage (OCV) of the cell. $(\eta_{ct})_a$ and $(\eta_c)_a$ represent the activation overvoltage due to charge transfer polarization and diffusion (or transportation) overvoltage caused by concentration polarization, respectively, related to the anode. Meanwhile, $(\eta_{ct})_c$ and $(\eta_c)_c$ are the overvoltage resulted from charge transfer and concentration polarization, separately, with relevance to the cathode. iR is the ohmic drop caused by internal resistance R of the cell, which is tightly affected by the electrolyte conductivity. Obviously, to obtain high battery voltage, the activation and diffusion overvoltage need to be controlled as low and the OCV is required approaching the theoretical value. Meanwhile, low cell internal resistance should be fulfilled via battery design for example with appreciate separator and highly conductive electrolytes. Specifically, from anode side, the activation and diffusion overvoltage are possible to be tailored via composition optimization as well as the OCV. Generally, an Mg anode material with a highly negative OCP in half-cell measurement is conducive to yield higher voltage for primary Mg batteries. Besides, low activation and diffusion overvoltage are favorable, which drive the anticipation for anode materials with fast dissolution kinetics and a non-protective surface oxide/hydroxide layer.

The development of high performance Mg-Ca alloy anodes follows the above-mentioned design principle. Results of half-cell discharge measurements presented in subsection 5.1 (***paper 1)*** and Fig. 6-1 demonstrate that Mg-0.1Ca and Mg-0.5Ca alloys show more negative discharge potential than the recast Mg at varied current densities. The reason should be the more negative OCP of these two Mg-Ca alloys than the recast Mg both before and after discharge as indicated in Fig. 6-2(a, b). However, interestingly, Mg-0.1Ca alloy has much more negative OCP than other studied materials but only slightly more negative discharge potential. Specifically, the OCP difference between Mg-0.1Ca and others is 80-160 mV, whilst the difference between discharge potential at various current densities is just 4-40 mV. The results indicate that Mg-Ca alloys with higher Ca content suffers from smaller voltage drop related to the anodic activation and film resistance than the micro-alloyed Mg-Ca. Given the time needed for film recovery, EIS measurements performed immediately after discharge is possibly able to evaluate the film resistance of Mg anodes. Fig. 6-3 shows the EIS results of air-cooled Mg-0.1Ca and Mg-2Ca measured after discharge at 1 mA cm^{-2} for 2 h. Mg-0.1Ca shows significantly larger impedance in a wide frequency range than Mg-2Ca, indicating a more sluggish discharge activity and larger voltage drop, which is consistent with the former conclusion obtained from the OCP and discharge results. The

morphologies of surface films presented in Fig. 6-3 illustrate that the products film of Mg-2Ca is more porous with cracks, while the surface film of Mg-0.1Ca is much denser. The difference between the surface film morphologies partly contributes to the different discharge activity and voltage drop with respect to varied Mg-Ca anodes. Besides, another reason should be the different microstructure related to varying Ca contents. Anode dissolution is absolutely accelerated by a large amount of Mg_2Ca phase, which is more electrochemically active with respect to the Mg Matrix [64], in the heavy-alloyed Mg-Ca anodes.

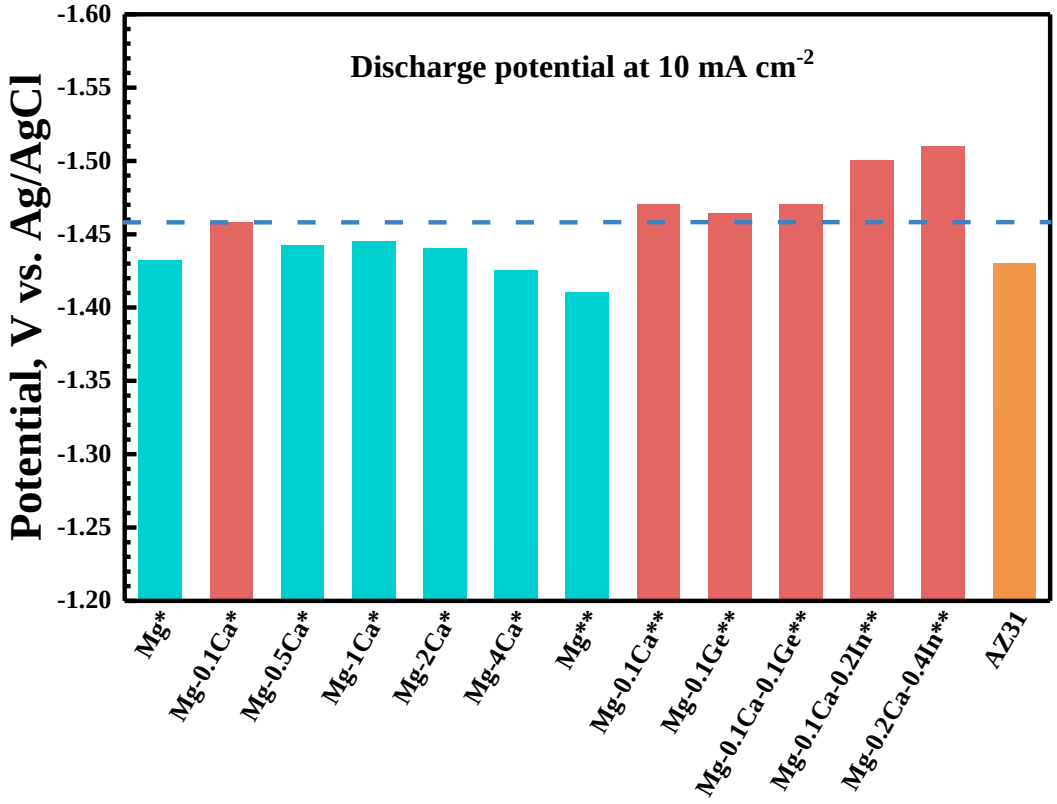

Fig. 6-1 Summary of the half-cell discharge potential of all prepared Mg anodes in this study at 10 mA cm^{-2} in 3.5 wt.% NaCl solution. Cast materials * via air-cooling, ** via water-cooling.

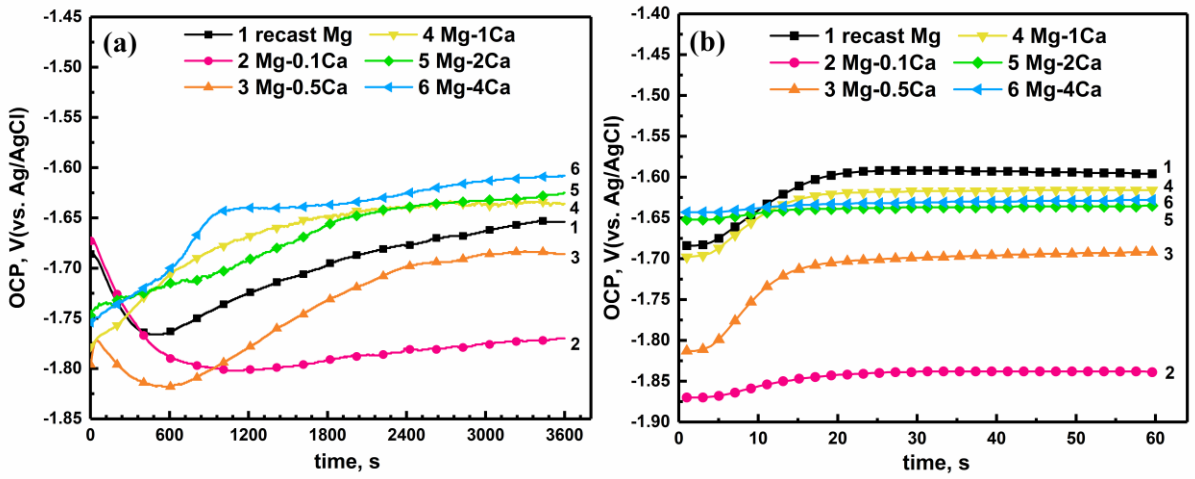

Fig. 6-2 OCP of as-cast pure Mg and Mg-Ca binary alloys via air-cooling. (a) prior to and (b) after discharge at 1 mA cm^{-2} for 2 h in 3.5 wt.% NaCl solution.

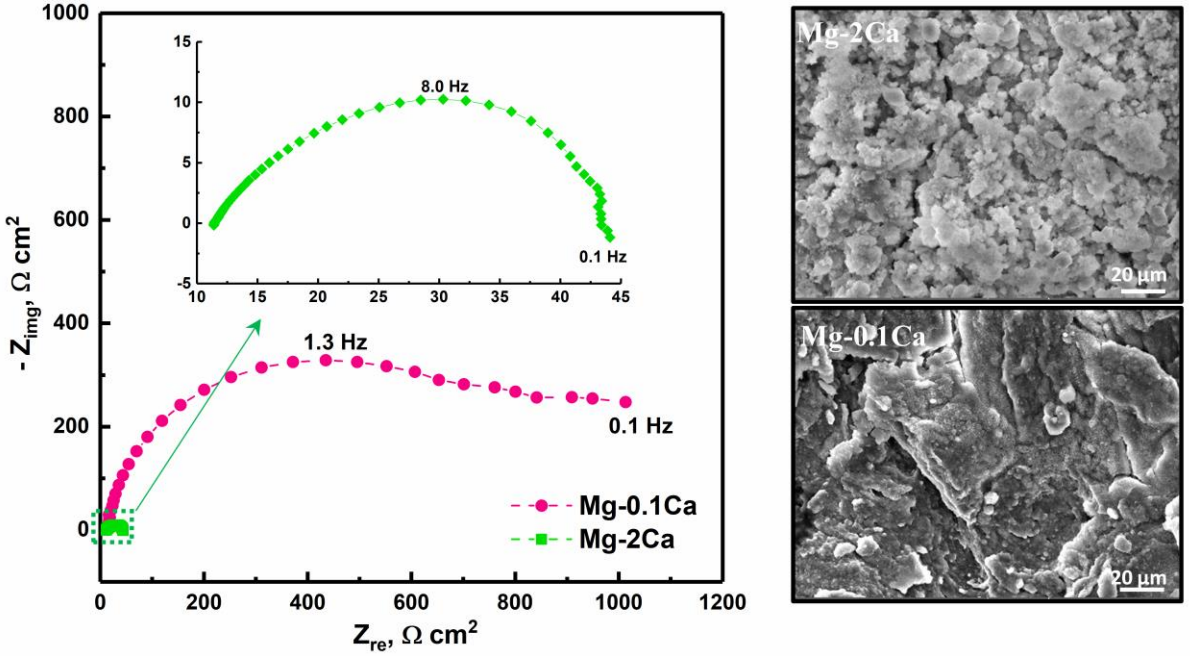

Fig. 6-3 EIS results and surface morphologies of Mg-Ca cast with air-cooling after discharge in 3.5 wt.% NaCl solution at 1 mA cm^{-2} for 2 h.

6.1.2 Micro-alloyed Mg-Ca-X (In, Ge) alloy anodes

In order to further boost the discharge properties of the binary micro-alloyed Mg-0.1Ca anode, two alloying elements, i.e. In and Ge, have been evaluated in this work. Low alloying contents are adopted in order to maintain a low secondary phase fraction to minimize possible utilization efficiency decrement caused by anode mass loss due to chunk effect.

Minor addition of In is found to be able to improve the discharge potential of Mg-Ca anode in 3.5 wt.% NaCl solution (Fig. 6-1), being consistent with the first glance that Mg-0.1Ca-0.2In possesses more negative OCP (–1.9 $V_{Ag/AgCl}$) than Mg-0.1Ca both prior to and after discharge (see Fig. 6-4(a, b)). The improved discharge potential of Mg-Ca-In anodes is also attributed to re-deposition of metallic In on anode surface, accelerating Mg dissolution through galvanic coupling between In and Mg as revealed in subsection 5.4 (***paper 4)***. Besides, In alloying contributes to the formation of a porous products layer (Fig. 6-5(b, c)) that can readily breakdown, reducing the voltage drop associated with film resistance. The high discharge activity with regard to micro-alloyed Mg-Ca-In anodes can be deduced from the EIS results presented in Fig. 6-5a. Two Mg-Ca-In alloy anodes both show much lower impedance than other materials.

Mg-0.1Ge alloy shows similar OCP after discharge and alike discharge activity to Mg-0.1Ca. Hence, the two binary alloys exhibit slight difference between their discharge potential at varied current densities. By contrast, Mg-0.1Ca-0.1Ge alloy exhibits more sluggish discharge activity than the binary Mg-0.1Ca (as indicated by the larger impedance from EIS results in Fig. 6-5a), leading to the similar discharge potential in spite of the more negative OCP. The relatively noble activity of Mg-0.1Ca-0.1Ge is supposed to be partly related to higher film resistance indicated by the EIS results. This is also

demonstrated by the discharge tests conducted in an additive-based electrolyte that includes 0.1 M salicylate, which is a Mg^{2+} complexing agent with the ability of preventing the formation of $Mg(OH)_2$ film [65]. Mg-0.1Ca-0.1Ge anode yields higher voltage to Mg-air battery in the additive-containing electrolyte than Mg-0.1Ca and Mg-0.1Ge anodes in the case that no visible thick $Mg(OH)_2$ film is formed on the anode surface (as shown in Fig. 14 in subsection 5.5 (***paper 5***)). Clearly, the advantage of Mg-Ca-Ge anode in OCP is showed up in the additive-containing electrolyte.

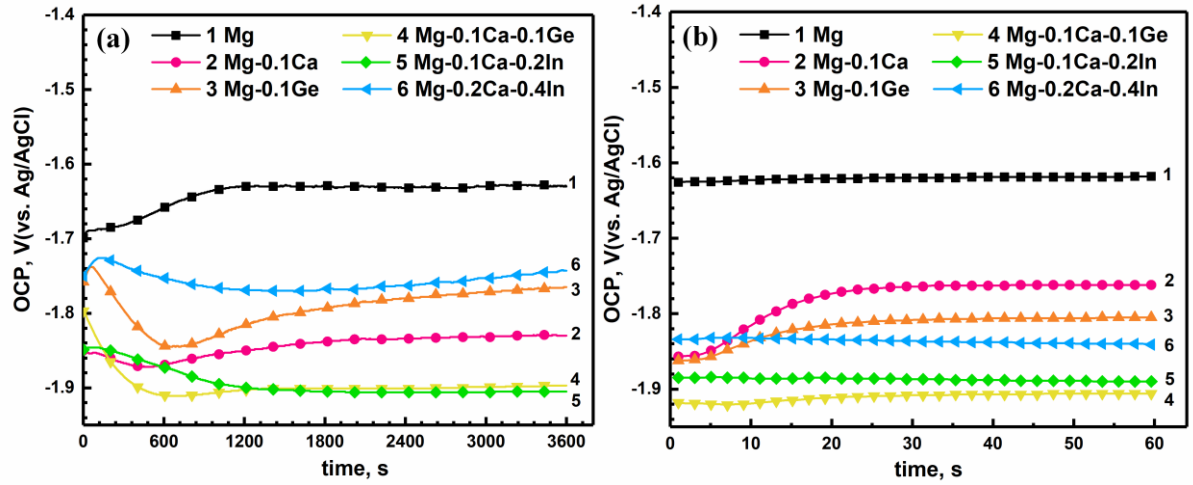

Fig. 6-4 OCP (a) before and (b) after discharge in 3.5 wt.% NaCl solution at 1 mA cm^{-2} for 2 h corresponding to recast pure Mg and micro-alloyed Mg alloys via casting with water-cooling.

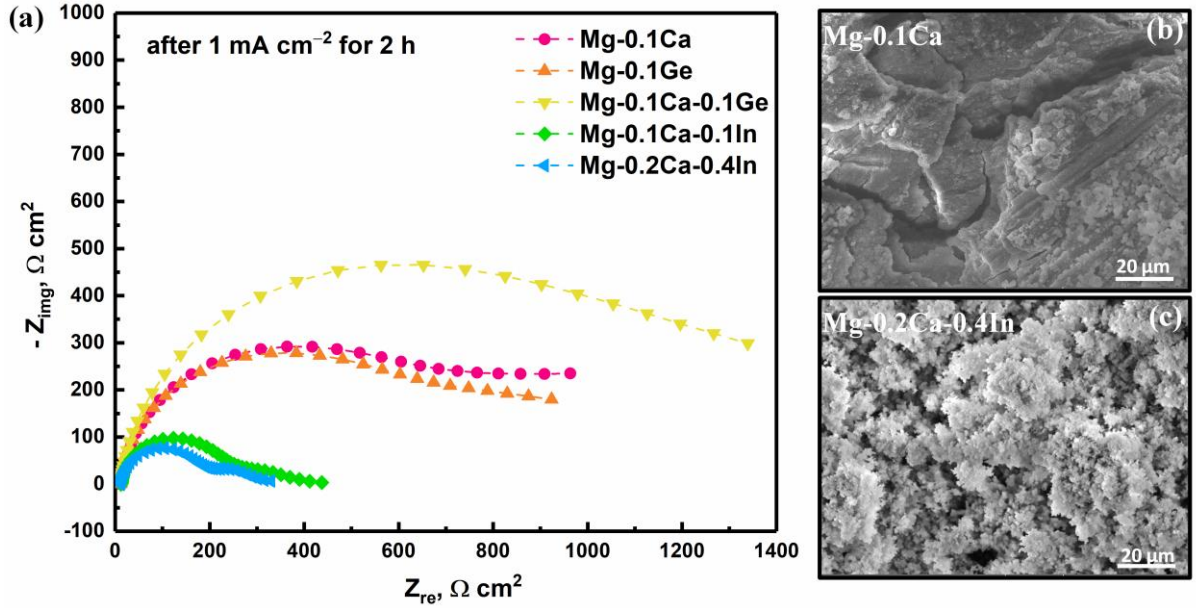

Fig. 6-5 (a) EIS results of water-cooled Mg anodes measured after discharge at 1 mA cm^{-2} for 2 h. The scanned frequency ranges from 10 kHz to 0.1 Hz. (b, c) Surface morphologies of Mg-Ca anodes cast via water-cooling after discharge in 3.5 wt.% NaCl solution at 5 mA cm^{-2} for 15 h.

6.2 Distinction between corrosion rate at OCP and during discharge

In subsection 5.3 (***paper 3)***, the hydrogen evolution rates of a HP Mg and some commercially Mg alloys

were measured at OCP condition and during discharge at different current densities. The results are reorganized and presented in Fig. 6-6, apparently revealing that the corrosion rates of all the studied materials (by hydrogen evolution in 3.5 wt.% NaCl solution at OCP) vary as the following ranking: E21<HP Mg<WE43<AZ31<AM50<ZE41. Interestingly, the situation is altered regarding the self-corrosion rates measured with applied current densities. For instance, E21 shows higher HE rate than HP Mg when discharge at 1 mA cm^{-2}, differing from its lower corrosion rate at OCP as mentioned above. By contrast, the self-corrosion rate of WE43 is similar to that of HP Mg as determined at 1 mA cm^{-2} in spite of its significantly higher corrosion rate at OCP. Similarly, AM50 alloy possesses secondly highest corrosion rate measured at OCP and with applied 1 and 5 mA cm^{-2} current densities. However, it shows the slowest real-time HE rate when the applied current density reaches 10 mA cm^{-2}, indicating slower self-corrosion that other Mg materials. The same distinction between corrosion rate at OCP and self-corrosion rate during discharge is also found upon the micro-alloyed Mg-Ca based anodes. As indicated in subsection 5.5 (***paper 5)***, all the prepared Mg-0.1Ca, Mg-0.1Ge and Mg-0.1Ca-0.1Ge alloy exhibit diverse corrosion rates as measured at OCP condition in 3.5 wt.% NaCl solution. However, they show similar real-time HE rates at both current densities of 1 and 10 mA cm^{-2} (shown in Fig. 6-7), which reflects alike self-corrosion rates and, thus, contributes to the same utilization efficiency. The results presented in subsection 5.4 (***paper 4)*** reveal that both Mg-0.1Ca-0.2In and Mg-0.2Ca-0.4In have faster corrosion rates than binary Mg-0.1Ca under OCP condition as determined by HE tests and EIS. Nevertheless, the applied current densities induce great impact and lead to opposite results. Both micro-alloyed Mg-Ca-In anodes show slower self-corrosion rates than the binary Mg-0.1Ca, especially under relatively high current densities owning to smaller increasing rates with rising current densities (Fig. 6-7). The lower real-time self-corrosion of Mg-Ca-In anodes contributes to their higher anodic utilization efficiency and, consequently, enhances the specific energy density and service life of the battery system. The *k* value in **Fig. 6-5** represents how steep the self-corrosion increases with increment of applied current densities. It is dependent on alloy purity, composition and microstructure. Mg anodes with low *k* value are desired.

All the results remind us there is a significant distinction between the corrosion behavior at OCP condition and self-corrosion (or self-discharge) during discharge process with varied current densities. Therefore, it is not accurate to evaluate and judge the self-discharge rate of different Mg anodes with the corrosion-concerned results obtained at OCP condition, as done unfortunately in most published papers regarding Mg anodes development. The reason for the different corrosion behavior of Mg at OCP and under polarization is still unclear, but it is surely related to the NDE. However, the mechanism of NDE is still a controversial issue albeit it has been subjected of intense research in last decades and some models were proposed in attempt to explain it [34, 36, 66-69]. No doubt, the material chemistry and microstructure have significant influence on the corrosion properties of Mg and Mg alloys at OCP condition and, definitely, as well as the self-corrosion performance under polarization. However, not much information regarding the effect of different alloying elements and microstructure on self-

corrosion can be gained from literatures, since the real-time self-corrosion properties have always been omitted. Thus, much effort is highly required concerning searching for alloying elements that can inhibit the real-time self-corrosion rates of Mg anodes as well as other approaches with respect to impurity control and microstructure adjustment.

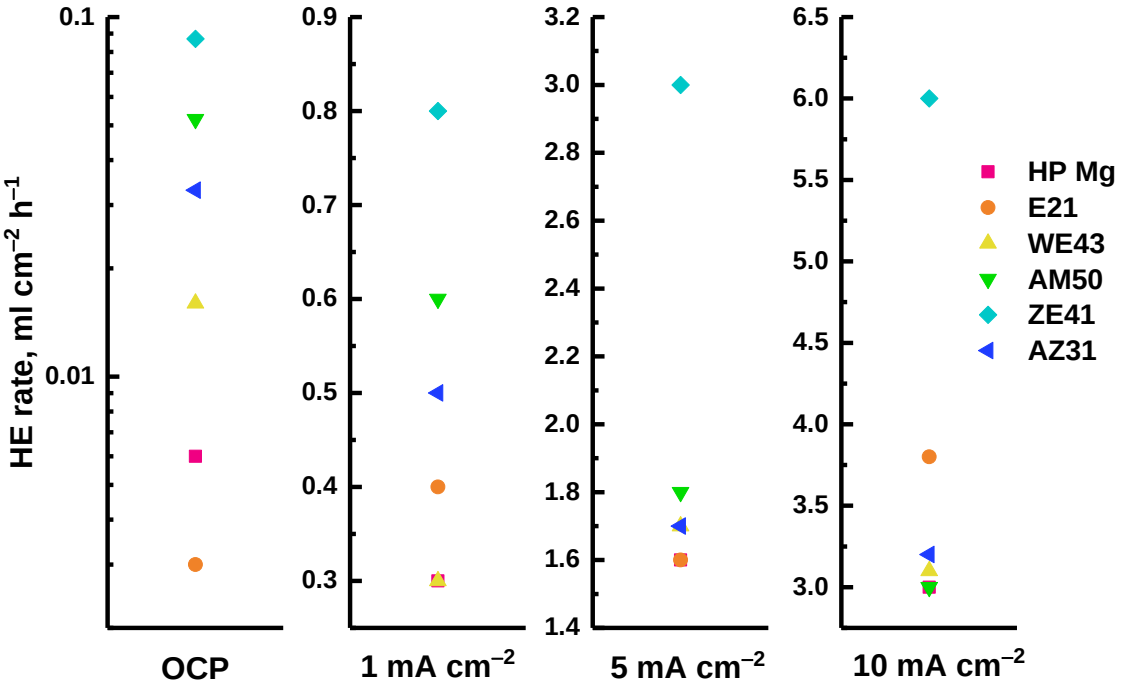

Fig. 6-6 Hydrogen evolution rates of as-cast HP Mg and commercially Mg alloys at OCP condition and during discharge at different current densities in 3.5 wt.% NaCl solution.

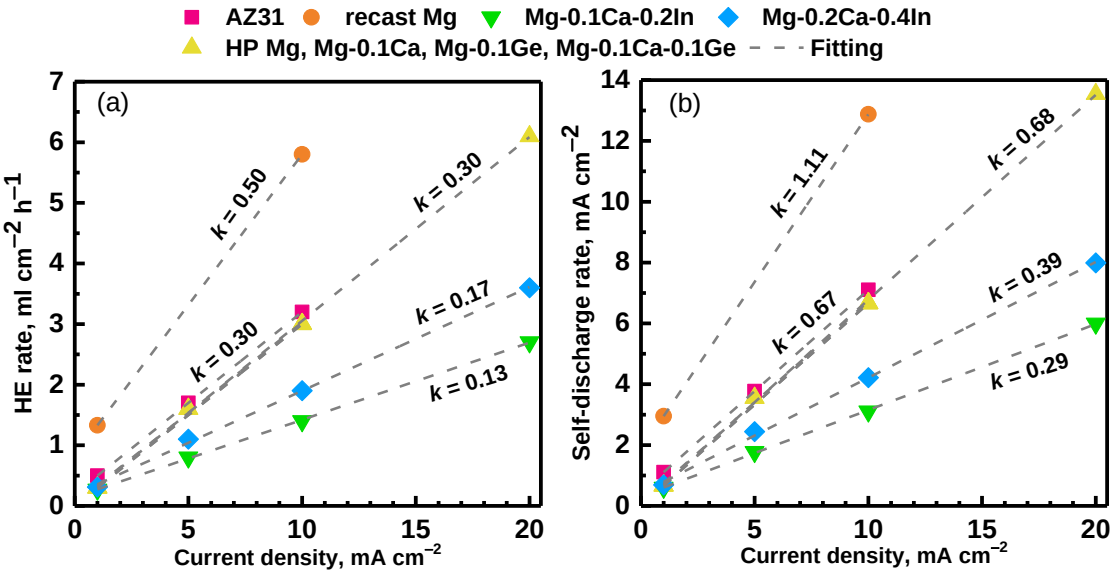

Fig. 6-7 (a) Real-time hydrogen evolution rates at varied current densities and (b) self-discharge rates converted from hydrogen evolution with respect to water-cooled pure Mg and micro-alloyed Mg anodes. Commercially AZ31 and HP Mg are included for comparison. Linear fitting results are also presented appearing as straight lines with slope *k*.

6.3 Enhanced utilization efficiency of micro-alloyed Mg-Ca based anodes

Utilization efficiency during discharge process is one of the most vital properties of Mg anode materials as it plays the critical role for the specific energy density, capacity and service life of Mg-based batteries. Searching for Mg anodes with high utilization efficiency is always the emphasis of research work concerning anode development of primary Mg batteries. The conclusions drawn from subsection 5.3 (***paper 3***) indicate that both self-corrosion of anode substrate and chunk effect have significant effect on the utilization efficiency of Mg anodes. Obviously, a large fraction of secondary phases caused by heavy alloying results in a large efficiency loss due to anode mass loss by detachment of undissolved chunks, such as Mg-4 wt.% Ca and ZE41 alloys (shown in Fig. 6-8). At low current density, i.e. 1 mA cm^{-2}, the efficiency loss caused by CE reaches up to 23% for HP Mg and 45% for WE43 alloy. Based on this conclusion, micro-alloying is adopted as a new strategy for developing high performance Mg-Ca based anodes. In and Ge with minor contents have been evaluated as additional alloying elements for the binary Mg-0.1Ca anode. Mg-0.1Ca, Mg-0.1Ge and Mg-0.1Ca-0.1Ge all show uniform dissolution during discharge, particularly at high current density, leading to approximately only 10% efficiency loss by CE at 1 mA cm^{-2} and negligible CE-associated loss at 10 mA cm^{-2}. Consequently, as shown in Fig. 6-9, Mg-0.1Ca anode exhibits utilization efficiency of 56% at 10 mA cm^{-2}, higher than other Mg-Ca anodes with high Ca contents and commercial anodes like AZ31 (55.4%) and AM50 (43.2%). Similarly high utilization efficiency is found upon Mg-0.1Ge (58%) and Mg-0.1Ca-0.1Ge (59%) alloy anodes. The high utilization efficiency of binary Mg-0.1Ca anodes is further improved by micro-alloying with In. The anode efficiency of Mg-0.1Ca-0.2In determined in full cell tests with a constant load of 47.5 mA is 78% comparing to 62% of the binary Mg-0.1Ca. The service life of the lab-made Mg-air battery increases from 19.2 h to 24 h after replacing the Mg-0.1Ca anode material with Mg-0.1Ca-0.2In. The great enhancement is attributed to the inhibited real-time self-discharge rate (as shown in Fig. 6-7) and a limited efficiency loss by CE due to low secondary phase fraction and uniform dissolution (as indicated in Fig. 6-8). Table 6-1 lists the utilization efficiency of micro-alloyed Mg-Ca-based anodes and other proposed Mg anodes (Pb and Hg free) from literatures. The comparison of data from different publications is rational because the experimental conditions are similar. Measured utilization efficiency is only dependent on anode mass loss during discharge measurements. Note that most alloy anodes from literatures included herein were treated after casting by heat treatment or mechanical processing. Enhancement to some extent was possibly achieved comparing to the as-cast materials. Nevertheless, obviously, the as-cast micro-alloyed Mg-Ca-based anodes in this study, especially Mg-Ca-In, show higher utilization efficiency than most other alloy anodes, exhibiting a good promise as candidates for anodes of aqueous Mg batteries.

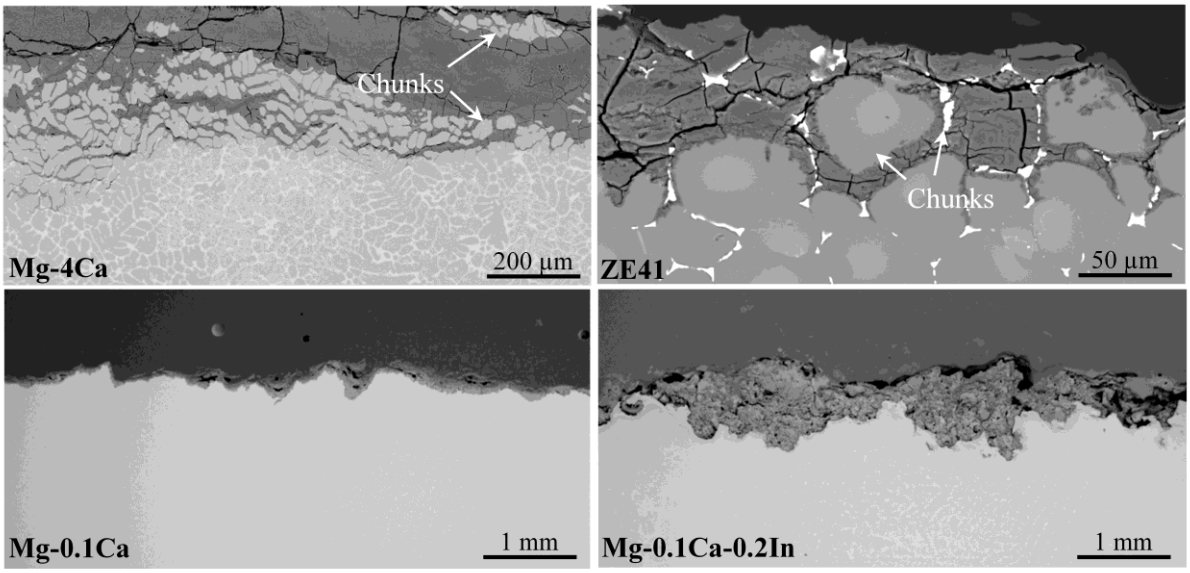

Fig. 6-8 Cross-sectional morphologies of Mg anodes after discharge in 3.5 wt.% NaCl solution. Mg-4Ca after 10 mA cm^{-2} for 8 h, reproduced with permission from Elsevier; commercially ZE41 alloy after 10 mA cm^{-2} for 1.5 h; Mg-0.1Ca after 5 mA cm^{-2} for 15 h; Mg-0.1Ca-0.2In after 5 mA cm^{-2} for 15 h.

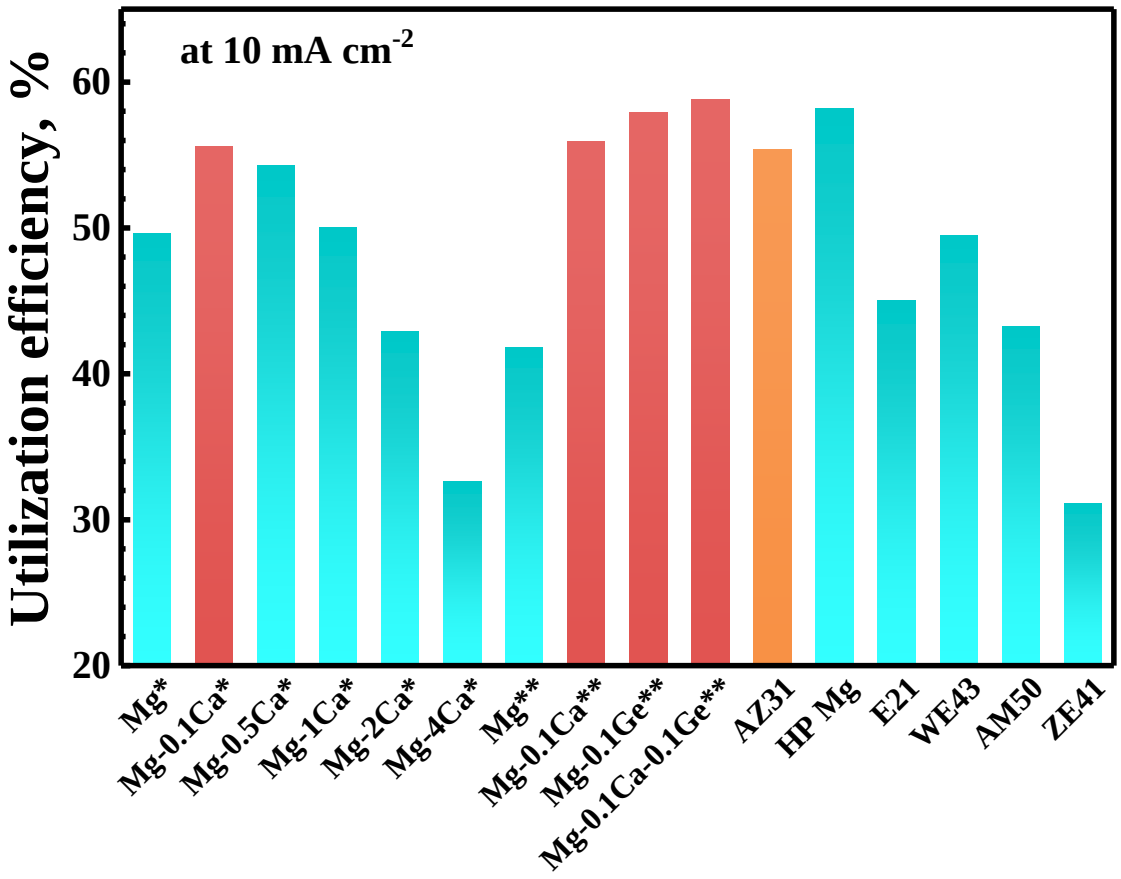

Fig. 6-9 Summary of the utilization efficiency of prepared Mg anodes in this study at 10 mA cm^{-2} in 3.5 wt.% NaCl solution in comparison to other commercially available Mg alloys. Cast materials * via air-cooling, ** via water-cooling.

Table 6-1 Utilization efficiency (UE) of micro-alloyed Mg-Ca-based anodes in comparison to other proposed Pb/Hg-free Mg anodes from literatures (in 3.5 wt.% NaCl solution at current density of 10 mA cm^{-2}). *Measured at a constant current of 47.5 mA cm^{-1} that corresponds to an initial current density of 10 mA cm^{-2} for a sample with 4.75 cm^2 surface area. **Tested in 5 wt.% NaCl solution.

Mg anode	Alloying load	Condition	UE	Reference
Mg-Ca	0.1 wt.%	as-cast	56%	this work
Mg-Ca-Ge	0.2 wt.%		59%	
Mg-Ca-In	0.3 wt.%		77.8%*	
	0.6 wt.%		68.3%*	
Mg-Sn-Zn-Ag	4 wt.%	extruded	51.8%	[70]
	6 wt.%		45.3%	
	10 wt.%		32.3%	
Mg-Bi	1 wt.%	extruded	40.1%	[71]
Mg-Bi-Ca	1.5 wt.%		52.1%	
Mg-Zn-Zr	6.7 wt.%	as-cast	41%	[72]
Mg-Zn-Y	7.1 wt.%		50%	
	11 wt.%		44%	
Mg-Al-Zn	7 wt.%	as-cast	56%	[11]
		rolled	59.3%	
Mg-Al-Zn-La	7.5 wt.%	as-cast	58.8%	
		rolled	61.9%	
Mg-Zn-RE	2 wt.%	plate	38.2%	[73]
	5.1 wt.%		47.5%	
Mg-Al-Zn	10 wt.%	extruded	50%	[12]
Mg-Al-Zn-Ca	11.5 wt.%		52%	
Mg-Al-Zn-Sm	10.5 wt.%		51%	
Mg-Al-Zn-La	10.5 wt.%		49%	
Mg-Al-Zn-(Ca, Sm, La)	12.3 wt.%		51%	
Mg-Al-Sn	7 wt.%	as-cast	32.2%	[7]
		Homogenized	33.2%	
		Extruded	45.2%	
		post-annealed	48.3%	
Mg-Al	9 wt.%	as-cast then	53.6%	[26]
Mg-Al-Zn	10 wt.%	annealed	52.6%	
Mg-Al-In	10 wt.%		54.8%	
Mg-Al-Zn	8.4 wt.%	as-cast	67.4%	[16]
Mg-Al-Zn-In	8.6 wt.%	as-cast	67.1%	
		homogenized	70.8%	
Mg-Al	3 wt.%	as-cast then	46.8%	[27]
Mg-Al-Sn	4 wt.%	annealed	60.4%	
Mg-Al-Ga	4 wt.%		61.6%	
Mg-Al-In	4 wt.%		61.9%	
Mg-Al-Zn	4 wt.%		61%	
Mg-Li-Al-Ce-Y	13 wt.%	as-cast	36.1%	[8]
Mg-Li-Al-Ce-Y-Zn	14 wt.%		60.6%	

Mg-Al-Mn Mg-Al-Mn-Ca	6.1 wt.% 7.8 wt.%	rolled	49.8% 60.4%	[23]
Mg-Li-Al-Ce Mg-Al-Zn	15.1 wt.% 4 wt.%	-	66.8% 44%	[74]
Mg-Al-Zn Mg-Al-Zn-Ca Mg-Al-Zn-Sm Mg-Al-Zn-La Mg-Al-Zn-(Ca, Sm, La)	4.6 wt.% 6.2 wt.% 5.4 wt.% 4.8 wt.% 7.2 wt.%	extruded	44.2% 52.5% 49.8% 49.3% 52%	[75]
Mg-Al Mg-Al-In	9 wt.% 9.5 wt.% 10 wt.%	extruded	35.2% 49.2% 40.1%	[76]
Mg-Al-Zn	4 wt.% 7 wt.% 10 wt.%	as-cast	32% 41% 36%	[77]
Mg-Al-Zn**	9.5 wt.%	rolled and then solution treated 10-h aging 16-h aging 19-h aging 24-h aging	 54.6% 56.4% 55.2% 52.9% 55.7%	[41]
Mg-Li-Al-Zn-Y	12.3 wt.% 15.2 wt.%	rolled	55% 58%	[9]

7 Conclusions and outlook

The launch of this work is due to the unsatisfactory practical performance of commercially used Mg anodes for primary aqueous Mg batteries. Ca alloying has been evaluated as a potential method to develop high-performance anode materials. The composition of Mg-Ca is optimized in terms of high corrosion resistance and enhanced discharge properties. Afterwards, the effect of microstructure, particularly secondary phase morphology, on the corrosion and discharge performance of optimized binary Mg-Ca anode is investigated. Meanwhile, the decisive factors for utilization efficiency of Mg anode materials during discharge process are clarified. Thereafter, indium and germanium with minor contents are assessed as additional alloying elements for improving the concerned properties of binary Mg-Ca system. Accordingly, some high-performance anode materials are proposed and the following conclusions are drawn:

1) The addition of minor amount of Ca into Mg reduces the grain size and suppresses the kinetics of cathodic reaction, leading to enhanced corrosion resistance and highly negative OCP (–1.83 $V_{Ag/AgCl}$). Thus, Mg-0.1%Ca (weight percent hereafter) exhibits improved discharge potential and higher utilization efficiency than pure Mg recast with the same procedure. The efficiency is 56% regarding Mg-0.1%Ca at 10 mA cm^{-2}, comparing to 50% of pure Mg.

2) Full cell tests indicate that the battery with Mg-0.1%Ca anode shows higher cell voltage and specific energy density than those based on as-cast HP Mg, AZ31 and AM50 alloy anodes. For instance, the peak energy density is 1800 Wh kg^{-1} regarding Mg-0.1Ca anode in comparison to 1400 Wh kg^{-1} of AZ31 anode. Therefore, micro-alloyed binary Mg-Ca is a good candidate for the anode material of primary aqueous Mg-based batteries.

3) Binary Mg-Ca anode owns the capability of providing stable voltage for Mg-air battery amid long-term intermittent operation.

4) Secondary phase morphology has significant influence on the corrosion and discharge performance of binary Mg-0.5% Ca anodes. Large amount of disperse Mg_2Ca phase and impurity rich particles in air-cooled Mg-0.5% Ca alloy result in non-uniform corrosion and discharge behavior, leading to a higher efficiency loss caused by detachment of undissolved chunks in comparison to the water-cooled one with relatively continuous Mg_2Ca phase along grain boundaries.

5) The addition of minor amount of In is able to simultaneously improve the discharge potential and utilization efficiency of micro-alloyed Mg-Ca anode. The boosted discharge potential is attributed to accelerated anodic activation and film breakage caused by In re-deposition on anode surface. The real-time self-discharge rate of Mg-0.1%Ca anode is reduced by 0.2%In addition and, thus, leads to higher

anodic utilization efficiency (80% at 5 mA cm^{-2} initial current density) and elevated energy density of Mg battery (e.g. 2259 Wh kg^{-1}).

6) The addition of minor Ge suppresses the cathodic kinetics of micro-alloyed Mg-Ca. Mg-0.1%Ca-0.1%Ge shows much more negative OCP (–1.91 $V_{Ag/AgCl}$) and slightly lower corrosion rate that binary Mg-0.1%Ca. Mg-0.1%Ge and Mg-0.1%Ca-0.1%Ge both exhibit low self-discharge rates and, thus, high utilization efficiency (around 60% at 10 mA cm^{-2}).

7) The Mg-air battery with Mg-0.1%Ca-0.1%Ge anode yields similar cell voltage to that based on Mg-0.1%Ca (1.55 V at 1 mA cm^{-2}), which is remarkably higher than AZ31-based system (1.45 V). However, in electrolyte containing additive (0.1 M salicylate), Mg-0.1%Ca-0.1%Ge anode provides higher voltage (1.70 V at 1 mA cm^{-2}) in comparison to Mg-0.1%Ca anode (1.63 V).

8) There is a significant distinction between corrosion performance at OCP and under polarization. Corrosion rate determined at OCP cannot be utilized to estimate the utilization efficiency of Mg anodes during discharge. The real-time self-corrosion depends on the applied discharge current density. The alloy composition and microstructure pre-determines how steeply the rate of self-corrosion increases with increase of applied discharge current density

9) The detachment of undissolved secondary phases and matrix, namely "chunk effect", can also cause a large efficiency loss to Mg anodes, up to 50% as shown in this work. In some cases, anodic efficiency loss due to "chunk effect" exceeds that caused by self-corrosion of anode substrate, especially at low current density, being the decisive factor for the efficiency of Mg anodes.

The results obtained in this work indicate that In and Ge are suitable alloying elements for Mg-Ca anodes regarding boosting discharge performance. The proposal of micro-alloyed Mg-Ca-Ge anode provides a possibility to develop primary Mg batteries with more desirable properties in cooperation with additive-containing electrolytes. The additive category needs to be tailored in terms of overall battery performance, including discharge voltage, utilization efficiency and specific energy density. Additionally, the composition of Mg-Ca-In and Mg-Ca-Ge anodes have not yet been optimized. The effect of element contents and varied microstructure induced by different alloying loads on discharge properties need to be investigated. Meanwhile, it must be noted that the composition optimization should base on the principle of micro-alloying to avoid large fraction of secondary phases, which will cause a significant efficiency loss as clarified in this work. Searching for other effective alloying elements is also desirable, such as some elements that can act as inhibitor of cathodic kinetics, like Sn, Bi and Sb as reported [30, 78]. Mechanical and heat treatment are capable of modifying the microstructure of Mg and sequentially affecting the corrosion and discharge properties [6, 13, 16, 41, 79-81]. However, the treatment parameters should be cautiously selected regarding micro-alloyed Mg. It has been reported that heat treatment at relatively high temperature deteriorated the corrosion property of pure Mg [82] and some Mg alloys, like Mg-0.3wt.%Ca and Mg-0.3wt.%Si [55]. The effect of pre-

heat treatment prior to mechanical treatment on the anode properties achieved after post processes needs to be revealed. Considering the necessity of geometry adjustment and performance boost for anode materials by mechanical processing, the information given in the present work is helpful as it indicates several optional Mg alloy anodes with superior performance. Generally, much effort is still required for developing high performance and satisfactory Mg anodes that can be utilized in practical Mg batteries. Notably, the recommended Mg-Ca-based anodes in this study yield discharge potential close to or even higher than the theoretical limit of Mg anode in aqueous electrolytes as proposed by Chen and co-workers (–1.4 V vs SHE) [83]. To further go beyond this limit, electrolyte modification is feasible, such as using ionic liquid electrolytes or adoption of electrolyte additives (big successes were achieved by our group via using Mg complexing agents [65, 84, 85]).

Bibliography

[1] David Linden, T.B. Reddy, Handbook of Batteries, McGraw-Hill, New York, 2002.
[2] C Daniel, J. Besenhard, Handbook of Battery Materials, Wiley-VCH, Weinheim, 2012.
[3] M. Deng, D. Höche, D. Snihirova, L.Q. Wang, B. Vaghefinazari, S.V. Lamaka, M.L. Zheludkevich, Aqueous Mg batteries, in: M. Fichtner (Ed.) Magnesium Batteries: Research and Applications, Royal Society of Chemistry, United Kingdom, 2019, pp. 275-308. https://doi.org/10.1039/9781788016407-00275.
[4] Y. Sun, X. Liu, Y. Jiang, J. Li, J. Ding, W. Hu, C. Zhong, Recent advances and challenges in divalent and multivalent metal electrodes for metal–air batteries, Journal of Materials Chemistry A, 7 (2019) 18183-18208. https://doi.org/10.1039/c9ta05094a.
[5] T. Zheng, Y. Hu, Y. Zhang, S. Yang, F. Pan, Composition optimization and electrochemical properties of Mg-Al-Sn-Mn alloy anode for Mg-air batteries, Materials & Design, 137 (2018) 245-255. https://doi.org/10.1016/j.matdes.2017.10.031.
[6] N. Wang, Y. Mu, W. Xiong, J. Zhang, Q. Li, Z. Shi, Effect of crystallographic orientation on the discharge and corrosion behaviour of AP65 magnesium alloy anodes, Corroison Science, 144 (2018) 107-126. https://doi.org/10.1016/j.corsci.2018.08.003.
[7] H. Xiong, K. Yu, X. Yin, Y. Dai, Y. Yan, H. Zhu, Effects of microstructure on the electrochemical discharge behavior of Mg-6wt%Al-1wt%Sn alloy as anode for Mg-air primary battery, J. Alloys Compd. , 708 (2017) 652-661. https://doi.org/10.1016/j.jallcom.2016.12.172.
[8] N. Wang, R. Wang, Y. Feng, W. Xiong, J. Zhang, M. Deng, Discharge and corrosion behaviour of Mg-Li-Al-Ce-Y-Zn alloy as the anode for Mg-air battery, Corros. Sci. , 112 (2016) 13-24. https://doi.org/10.1016/j.corsci.2016.07.002.
[9] X. Liu, S. Liu, J. Xue, Discharge performance of the magnesium anodes with different phase constitutions for Mg-air batteries, J. Power Sources 396 (2018) 667-674. https://doi.org/10.1016/j.jpowsour.2018.06.085.
[10] X. Liu, J. Xue, The role of Al2Gd cuboids in the discharge performance and electrochemical behaviors of AZ31-Gd anode for Mg-air batteries, Energy, 189 (2019) 116314. https://doi.org/10.1016/j.energy.2019.116314.
[11] Y. Wu, Z. Wang, Y. Liu, G. Li, S. Xie, H. Yu, H. Xiong, AZ61 and AZ61-La Alloys as Anodes for Mg-Air Battery, J. Mater. Eng. Perform. , 28 (2019) 2006-2016. https://doi.org/10.1007/s11665-019-03985-5.
[12] X. Liu, J. Xue, P. Zhang, Z. Wang, Effects of the combinative Ca, Sm and La additions on the electrochemical behaviors and discharge performance of the as-extruded AZ91 anodes for Mg-air batteries, J. Power Sources 414 (2019) 174-182. https://doi.org/10.1016/j.jpowsour.2018.12.092.
[13] X. Chen, S. Ning, Q. Le, H. Wang, Q. Zou, R. Guo, J. Hou, Y. Jia, A. Atrens, F. Yu, Effects of external field treatment on the electrochemical behaviors and discharge performance of AZ80 anodes for Mg-air batteries, Journal of Materials Science & Technology, 38 (2020) 47-55. https://doi.org/10.1016/j.jmst.2019.07.043.
[14] J. Li, Z. Chen, J. Jing, J. Hou, Electrochemical behavior of Mg-Al-Zn-Ga-In alloy as the anode for seawater-activated battery, Journal of Materials Science & Technology, 41 (2020) 33-42. https://doi.org/10.1016/j.jmst.2019.08.052.
[15] Y. Shi, C. Peng, Y. Feng, R. Wang, N. Wang, Enhancement of discharge properties of an extruded Mg-Al-Pb anode for seawater-activated battery by lanthanum addition, J. Alloys Compd. , 721 (2017) 392-404. https://doi.org/10.1016/j.jallcom.2017.05.267.
[16] J. Li, B. Zhang, Q. Wei, N. Wang, B. Hou, Electrochemical behavior of Mg-Al-Zn-In alloy as anode materials in 3.5 wt.% NaCl solution, Electrochim. Acta 238 (2017) 156-167. https://doi.org/10.1016/j.electacta.2017.03.119.
[17] K.A. Unocic, H.H. Elsentriecy, M.P. Brady, H.M.M. III, G.L. Song, M. Fayek, R.A. Meisner, B. Davis, Transmission Electron Microscopy Study of Aqueous Film Formation and Evolution on Magnesium Alloys, J. Electrochem. Soc. , 161 (2014) C302-C311. https://doi.org/10.1149/2.024406jes.
[18] J.H. Nordlien, K. Nisancioglu, Morphology and Structure of Oxide Films Formed on MgAl Alloys by Exposure to Air and Water, J. Electrochem. Soc. , 143 (1996) 2564-2572.

https://doi.org/10.1149/1.1837048.
[19] N. Wang, R. Wang, C. Peng, Y. Feng, X. Zhang, Influence of aluminium and lead on activation of magnesium as anode, Transactions of Nonferrous Metals Society of China, 20 (2010) 1403-1411. https://doi.org/10.1016/s1003-6326(09)60312-5.
[20] Y. Wan, G. Xiong, H. Luo, F. He, Y. Huang, X. Zhou, Preparation and characterization of a new biomedical magnesium–calcium alloy, Materials & Design, 29 (2008) 2034-2037. https://doi.org/10.1016/j.matdes.2008.04.017.
[21] Y.S. Jeong, W.J. Kim, Enhancement of mechanical properties and corrosion resistance of Mg–Ca alloys through microstructural refinement by indirect extrusion, Corros. Sci. , 82 (2014) 392-403. https://doi.org/10.1016/j.corsci.2014.01.041.
[22] J.W. Seong, W.J. Kim, Mg-Ca binary alloy sheets with Ca contents of ≤1 wt.% with high corrosion resistance and high toughness, Corros. Sci. , 98 (2015) 372-381. https://doi.org/10.1016/j.corsci.2015.05.068.
[23] M. Yuasa, X. Huang, K. Suzuki, M. Mabuchi, Y. Chino, Discharge properties of Mg–Al–Mn–Ca and Mg–Al–Mn alloys as anode materials for primary magnesium–air batteries, J. Power Sources 297 (2015) 449-456. https://doi.org/10.1016/j.jpowsour.2015.08.042.
[24] I.-J. Park, S.-R. Choi, J.-G. Kim, Aluminum anode for aluminum-air battery – Part II: Influence of In addition on the electrochemical characteristics of Al-Zn alloy in alkaline solution, J. Power Sources 357 (2017) 47-55. https://doi.org/10.1016/j.jpowsour.2017.04.097.
[25] M. Pourgharibshahi, P. Lambert, The role of indium in the activation of aluminum alloy galvanic anodes, Mater. Corros. , 67 (2016) 857-866. https://doi.org/10.1002/maco.201508685.
[26] X. Li, H. Lu, S. Yuan, J. Bai, J. Wang, Y. Cao, Q. Hong, Performance of Mg–9Al–1In Alloy as Anodes for Mg-Air Batteries in 3.5 wt% NaCl Solutions, J. Electrochem. Soc. , 164 (2017) A3131-A3137. https://doi.org/10.1149/2.0971713jes.
[27] S. Yuan, H. Lu, Z. Sun, L. Fan, X. Zhu, W. Zhang, Electrochemical Performance of Mg-3Al Modified with Ga, In and Sn as Anodes for Mg-Air Battery, J. Electrochem. Soc. , 163 (2016) A1181-A1187. https://doi.org/10.1149/2.0371607jes.
[28] N. Wang, R. Wang, C. Peng, B. Peng, Y. Feng, C. Hu, Discharge behaviour of Mg-Al-Pb and Mg-Al-Pb-In alloys as anodes for Mg-air battery, Electrochim. Acta 149 (2014) 193-205. https://doi.org/10.1016/j.electacta.2014.10.053.
[29] P. Gore, S. Fajardo, N. Birbilis, G.S. Frankel, V.S. Raja, Anodic activation of Mg in the presence of In3+ ions in dilute sodium chloride solution, Electrochim. Acta 293 (2019) 199-210. https://doi.org/10.1016/j.electacta.2018.09.155.
[30] R.L. Liu, J.R. Scully, G. Williams, N. Birbilis, Reducing the corrosion rate of magnesium via microalloying additions of group 14 and 15 elements, Electrochim. Acta 260 (2018) 184-195. https://doi.org/10.1016/j.electacta.2017.11.062.
[31] R.L. Liu, M.F. Hurley, A. Kvryan, G. Williams, J.R. Scully, N. Birbilis, Controlling the corrosion and cathodic activation of magnesium via microalloying additions of Ge, Sci Rep, 6 (2016) 28747. https://doi.org/10.1038/srep28747.
[32] P. Jiang, C. Blawert, R. Hou, N. Scharnagl, J. Bohlen, M.L. Zheludkevich, Microstructural influence on corrosion behavior of MgZnGe alloy in NaCl solution, J. Alloys Compd. , 783 (2019) 179-192. https://doi.org/10.1016/j.jallcom.2018.12.296.
[33] R.L. Liu, Z.R. Zeng, J.R. Scully, G. Williams, B. Birbilis, Simultaneously improving the corrosion resistance and strength of magnesium via low levels of Zn and Ge additions, Corros. Sci. , 140 (2018) 18-29. https://doi.org/10.1016/j.corsci.2018.06.027.
[34] G.L. Song, A. Atrens, Corrosion Mechanisms of magnesium, Advanced Enginnering Materials, 1 (1999) 11-33. https://doi.org/10.1002/(SICI)1527-2648(199909)1:1<11::AID-ADEM11>3.0.CO;2-N.
[35] T.R. Thomaz, C.R. Weber, T. Pelegrini, L.F.P. Dick, G. Knörnschild, The negative difference effect of magnesium and of the AZ91 alloy in chloride and stannate-containing solutions, Corros. Sci. , 52 (2010) 2235-2243. https://doi.org/10.1016/j.corsci.2010.03.010.
[36] S. Thomas, N.V. Medhekar, G.S. Frankel, N. Birbilis, Corrosion mechanism and hydrogen evolution on Mg, Curr. Opin. Solid State Mater. Sci. , 19 (2015) 85-94. https://doi.org/10.1016/j.cossms.2014.09.005.
[37] J.L. Robinson, P.F. King, Electrochemical Behavior of the Magnesium Anode, J. Electrochem. Soc. , 108 (1961) 36-41. https://doi.org/10.1149/1.2428007.

[38] A. Sivashanmugam, T.P. Kumar, N.G. Renganathan, S. Gopukumar, Performance of a magnesium–lithium alloy as an anode for magnesium batteries., J. Appl. Electrochem. , 34 (2004) 1135-1139. https://doi.org/10.1007/s10800-004-2728-3.
[39] D. Cao, L. Wu, Y. Sun, G. Wang, Y. Lv, Electrochemical behavior of Mg–Li, Mg–Li–Al and Mg–Li–Al–Ce in sodium chloride solution, J. Power Sources 177 (2008) 624-630. https://doi.org/10.1016/j.jpowsour.2007.11.037.
[40] N. Wang, R. Wang, C. Peng, Y. Feng, B. Chen, Effect of hot rolling and subsequent annealing on electrochemical discharge behavior of AP65 magnesium alloy as anode for seawater activated battery, Corros. Sci. , 64 (2012) 17-27. https://doi.org/10.1016/j.corsci.2012.06.024.
[41] M. Yuasa, X. Huang, K. Suzuki, M. Mabuchi, Y. Chino, Effects of Microstructure on Discharge Behavior of AZ91 Alloy as Anode for Mg-Air Battery, Materials Transaction, 55 (2014) 1202-1207. https://doi.org/10.2320/matertrans.MC201403.
[42] S. Yuan, H. Lu, Z. Sun, L. Fan, X. Zhu, W. Zhang, Electrochemical Performance of Mg-3Al Modified with Ga, In and Sn as Anodes for Mg-Air Battery, J. Electrochem. Soc. , 163 (2016) A1181-A1187. https://doi.org/10.1149/2.0371607jes.
[43] A. Samaniego, N. Birbilis, X. Xia, G.S. Frankel, Hydrogen Evolution During Anodic Polarization of Mg Alloyed with Li, Ca, or Fe, Corrosion, 71 (2015) 224-233. https://doi.org/10.5006/1367.
[44] P.-W. Chu, E. Le Mire, E.A. Marquis, Microstructure of localized corrosion front on Mg alloys and the relationship with hydrogen evolution, Corros. Sci. , 128 (2017) 253-264. https://doi.org/10.1016/j.corsci.2017.09.022.
[45] G.A. Marsh, E. Schaschl, The Difference Effect and the Chunk Effect, J. Electrochem. Soc. , 107 (1960) 960-965. https://doi.org/10.1149/1.2427579
[46] M. Andrei, F.d. Gabriele, P.L. Bonora, D. Scantlebury, Corrosion behaviour of magnesium sacrificial anodes in tap water, Mater. Corros. , 54 (2003) 5-11. https://doi.org/10.1002/maco.200390010.
[47] B. Campillo, C. Rodriguez, J. Genesca, J. Juarez-Islas, O. Flores, L. Martinez, Effect of heat treatment on the efficiency of Mg anodes, Journal of Material Engineering and Performance, 6 (1997) 449-453. https://doi.org/10.1007/s11665-997-0115-z.
[48] G.-L. Song, K.A. Unocic, The anodic surface film and hydrogen evolution on Mg, Corros. Sci. , 98 (2015) 758-765. https://doi.org/10.1016/j.corsci.2015.05.047.
[49] P. Jiang, C. Blawert, N. Scharnagl, M.L. Zheludkevich, Influence of water purity on the corrosion behavior of Mg0.5ZnX (X=Ca, Ge) alloys, Corros. Sci. , 153 (2019) 62-73. https://doi.org/10.1016/j.corsci.2019.03.044.
[50] V. Shkirskiy, A.D. King, O. Gharbi, P. Volovitch, J.R. Scully, K. Ogle, N. Birbilis, Revisiting the electrochemical impedance spectroscopy of magnesium with online inductively coupled plasma atomic emission spectroscopy, Chemphyschem, 16 (2015) 536-539. https://doi.org/10.1002/cphc.201402666.
[51] E.L. Silva, S.V. Lamaka, D. Mei, M.L. Zheludkevich, The Reduction of Dissolved Oxygen During Magnesium Corrosion, ChemistryOpen, 7 (2018) 664-668. https://doi.org/10.1002/open.201800076.
[52] T.E. Crozier, S. Yamamoto, Solubility of Hydrogen in Water, Seawater, and NaCI Solutions, J. Chem. Eng. Data 19 (1974) 242-244. https://doi.org/10.1021/je60062a007.
[53] G.L. Song, A. Atrens, D. StJohn, An Hydrogen Evolution Method for the Estimation of the Corrosion Rate of Magnesium Alloys, Magnesium Technology, (2001) 255-262. https://doi.org/10.1002/9781118805497.ch44.
[54] N.T. Kirkland, N. Birbilis, M.P. Staiger, Assessing the corrosion of biodegradable magnesium implants: a critical review of current methodologies and their limitations, Acta Biomater. , 8 (2012) 925-936. https://doi.org/10.1016/j.actbio.2011.11.014.
[55] F. Cao, Z. Shi, G.-L. Song, M. Liu, A. Atrens, Corrosion behaviour in salt spray and in 3.5% NaCl solution saturated with Mg(OH)2 of as-cast and solution heat-treated binary Mg–X alloys: X=Mn, Sn, Ca, Zn, Al, Zr, Si, Sr, Corros. Sci. , 76 (2013) 60-97. https://doi.org/10.1016/j.corsci.2013.06.030.
[56] Z. Qiao, Z. Shi, N. Hort, N.I. Zainal Abidin, A. Atrens, Corrosion behaviour of a nominally high purity Mg ingot produced by permanent mould direct chill casting, Corros. Sci. , 61 (2012) 185-207. https://doi.org/10.1016/j.corsci.2012.04.030.
[57] F. Cao, Z. Shi, J. Hofstetter, P.J. Uggowitzer, G. Song, M. Liu, A. Atrens, Corrosion of ultra-high-purity Mg in 3.5% NaCl solution saturated with Mg(OH)2, Corros. Sci. , 75 (2013) 78-99. https://doi.org/10.1016/j.corsci.2013.05.018.

[58] M.C. Lin, C.Y. Tsai, J.Y. Uan, Electrochemical behaviour and corrosion performance of Mg–Li–Al–Zn anodes with high Al composition, Corros. Sci. , 51 (2009) 2463-2472. https://doi.org/10.1016/j.corsci.2009.06.036.
[59] Y.Y. Chen, T. Duval, U.D. Hung, J.W. Yeh, H.C. Shih, Microstructure and electrochemical properties of high entropy alloys—a comparison with type-304 stainless steel, Corros. Sci. , 47 (2005) 2257-2279. https://doi.org/10.1016/j.corsci.2004.11.008.
[60] D. Höche, C. Blawert, S.V. Lamaka, N. Scharnagl, C. Mendis, M.L. Zheludkevich, The effect of iron re-deposition on the corrosion of impurity-containing magnesium, Phys. Chem. Chem. Phys. , 18 (2016) 1279-1291. https://doi.org/10.1039/c5cp05577f.
[61] S.V. Lamaka, B. Vaghefinazari, D. Mei, R.P. Petrauskas, D. Höche, M.L. Zheludkevich, Comprehensive screening of Mg corrosion inhibitors, Corros. Sci. , 128 (2017) 224-240. https://doi.org/10.1016/j.corsci.2017.07.011.
[62] J.B. Bessone, D.O. Flamini, S.B. Saidman, Comprehensive model for the activation mechanism of Al–Zn alloys produced by indium, Corros. Sci. , 47 (2005) 95-105. https://doi.org/10.1016/j.corsci.2004.05.002.
[63] D.R. Egan, C. Ponce de León, R.J.K. Wood, R.L. Jones, K.R. Stokes, F.C. Walsh, Developments in electrode materials and electrolytes for aluminium–air batteries, J. Power Sources 236 (2013) 293-310. https://doi.org/10.1016/j.jpowsour.2013.01.141.
[64] Y. Liu, X. Liu, Z. Zhang, N. Farrell, D. Chen, Y. Zheng, Comparative, real-time in situ monitoring of galvanic corrosion in Mg-Mg2Ca and Mg-MgZn2 couples in Hank's solution, Corros. Sci. , 161 (2019) 108185. https://doi.org/10.1016/j.corsci.2019.108185.
[65] L. Wang, D. Snihirova, M. Deng, B. Vaghefinazari, S.V. Lamaka, D. Höche, M.L. Zheludkevich, Tailoring electrolyte additives for controlled Mg-Ca anode activity in aqueous Mg-air batteries, J. Power Sources 460 (2020) 228106. https://doi.org/10.1016/j.jpowsour.2020.228106.
[66] S. Fajardo, C.F. Glover, G. Williams, G.S. Frankel, The Source of Anodic Hydrogen Evolution on Ultra High Purity Magnesium, Electrochim. Acta 212 (2016) 510-521. https://doi.org/10.1016/j.electacta.2016.07.018.
[67] G.S. Frankel, A. Samaniego, N. Birbilis, Evolution of hydrogen at dissolving magnesium surfaces, Corros. Sci. , 70 (2013) 104-111. https://doi.org/10.1016/j.corsci.2013.01.017.
[68] G.G. Perrault, Potentiostatic study of the magnesium electrode in aqueous solution, Electroanlytical Chemistry of The Magnesium Electrode In Aqueous Solution, 27 (1970) 47-58. https://doi.org/10.1016/S0022-0728(70)80201-7.
[69] C.D. Taylor, A First-Principles Surface Reaction Kinetic Model for Hydrogen Evolution under Cathodic and Anodic Conditions on Magnesium, J. Electrochem. Soc. , 163 (2016) C602-C608. https://doi.org/10.1149/2.1171609jes.
[70] X.-J. Gu, W.-L. Cheng, S.-M. Cheng, H. Yu, Z.-F. Wang, H.-X. Wang, L.-F. Wang, Discharge Behavior of Mg–Sn–Zn–Ag Alloys with Different Sn Contents as Anodes for Mg-air Batteries, J. Electrochem. Soc. , 167 (2020) 020501. https://doi.org/10.1149/1945-7111/ab6284.
[71] S.-m. Cheng, W.-l. Cheng, X.-j. Gu, H. Yu, Z.-F. Wang, H.-x. Wang, L.-f. Wang, Discharge properties of low-alloyed Mg–Bi–Ca alloys as anode materials for Mg–air batteries: Influence of Ca alloying, J. Alloys Compd. , 823 (2020) 153779. https://doi.org/10.1016/j.jallcom.2020.153779.
[72] X. Chen, Q. Zou, Q. Le, J. Hou, R. Guo, H. Wang, C. Hu, L. Bao, T. Wang, D. Zhao, F. Yu, A. Atrens, The quasicrystal of Mg–Zn–Y on discharge and electrochemical behaviors as the anode for Mg-air battery, J. Power Sources 451 (2020) 227807. https://doi.org/10.1016/j.jpowsour.2020.227807.
[73] N. Shrestha, K.S. Raja, V. Utgikar, Mg-RE Alloy Anode Materials for Mg-Air Battery Application, J. Electrochem. Soc. , 166 (2019) A3139-A3153. https://doi.org/10.1149/2.0131914jes.
[74] Y. Ma, N. Li, D. Li, M. Zhang, X. Huang, Performance of Mg–14Li–1Al–0.1Ce as anode for Mg-air battery, J. Power Sources 196 (2011) 2346-2350. https://doi.org/10.1016/j.jpowsour.2010.07.097.
[75] X. Liu, Z. Guo, J. Xue, P. Zhang, The role of Al2Ca and Al2(Sm,Ca,La) particles in the microstructures and electrochemical discharge performance of as-extruded Mg-3wt.%Al-1wt.%Zn-based alloys for primary Mg-air batteries, Int. J. Energy Res. , 43 (2019) 4569-4579. https://doi.org/10.1002/er.4586.
[76] Z. Li, H. Wang, J. Li, Y. Zhuang, J. Gao, H. Li, W. Cheng, Synergistic Effect of Second Phase and Grain Size on Electrochemical Discharge Performance of Extruded Mg–9Al–xIn Alloys as Anodes for Mg–Air Battery, Adv. Eng. Mater. , 22 (2020) 1901332. https://doi.org/10.1002/adem.201901332.

[77] J. Ma, G. Wang, Y. Li, F. Ren, A.A. Volinsky, Electrochemical performance of Mg-air batteries based on AZ series magnesium alloys, Ionics, 25 (2018) 2201-2209. https://doi.org/10.1007/s11581-018-2705-1.
[78] H.Y. Tok, E. Hamzah, H.R. Bakhsheshi-Rad, The role of bismuth on the microstructure and corrosion behavior of ternary Mg–1.2Ca–xBi alloys for biomedical applications, J. Alloys Compd. , 640 (2015) 335-346. https://doi.org/10.1016/j.jallcom.2015.03.217.
[79] J.L. Wu, R.C. Wang, Y. Feng, C.Q. Peng, Effect of hot rolling on the microstructure and discharge properties of Mg-1.6wt%Hg-2wt%Ga alloy anodes, J. Alloys Compd. , 765 (2018) 736-746. https://doi.org/10.1016/j.jallcom.2018.05.070.
[80] G. Huang, Y. Zhao, Y. Wang, H. Zhang, F. Pan, Performance of Mg–air battery based on AZ31 alloy sheet with twins, Mater. Lett. , 113 (2013) 46-49. https://doi.org/10.1016/j.matlet.2013.09.041.
[81] N. Wang, W. Li, Y. Huang, G. Wu, M. Hu, G. Li, Z. Shi, Wrought Mg-Al-Pb-RE alloy strips as the anodes for Mg-air batteries, J. Power Sources 436 (2019).
[82] M. Liu, P.J. Uggowitzer, A.V. Nagasekhar, P. Schmutz, M. Easton, G.-L. Song, A. Atrens, Calculated phase diagrams and the corrosion of die-cast Mg–Al alloys, Corros. Sci. , 51 (2009) 602-619. https://doi.org/10.1016/j.corsci.2008.12.015.
[83] L.D. Chen, J.K. Nørskov, A.C. Luntz, Theoretical Limits to the Anode Potential in Aqueous Mg–Air Batteries, The Journal of Physical Chemistry C, 119 (2015) 19660-19667. https://doi.org/10.1021/acs.jpcc.5b05677.
[84] D. Höche, S.V. Lamaka, B. Vaghefinazari, T. Braun, R.P. Petrauskas, M. Fichtner, M.L. Zheludkevich, Performance boost for primary magnesium cells using iron complexing agents as electrolyte additives, Sci Rep, 8 (2018) 7578. https://doi.org/10.1038/s41598-018-25789-8.
[85] B. Vaghefinazari, D. Höche, S.V. Lamaka, D. Snihirova, M.L. Zheludkevich, Tailoring the Mg-air primary battery performance using strong complexing agents as electrolyte additives, J. Power Sources 453 (2020). https://doi.org/10.1016/j.jpowsour.2020.227880.

Appendix

1. Glossary

AFM	atomic force microscope
AGI	average grain intercept
BSE	backscattered-electron
CE	chunk effect
CFF	carbon fiber felts
CMA	carbon microfiber array
CNF	carbon nanofibers
CPE_{dl}	electric double layer capacitance
CPE_f	film capacitance
CP Mg	commercial purity magnesium
EC	equivalent circuit
EDS	energy-dispersive X-ray spectroscopy
EIS	electrochemical impedance spectra
F	Faraday constant
GDL	gas diffusion layer
HE	hydrogen evolution
HER	hydrogen evolution reaction
HP Mg	high purity magnesium
I	constant current
IMP	intermetallic particle
LMPE	low melting point element
I_{self}	self-discharge of Mg anodes
M	molar mass of Mg metal
m_i	atomic weight of each element
MWCNT	multi- walled carbon nanotube
NDE	negative difference effect
n_i	number of exchanged electrons of each element
NUWC	Naval Undersea Warfare Center
OCP	open circuit potential
OCV	open circuit voltage
OM	optical microscopy
OPS	oxide polishing suspension
ORR	oxygen reduction reaction

PANI	polyaniline
PDP	Potentiodynamic polarization
P_H	corrosion rate related to hydrogen evolution
PPcFe	planar iron–polyphthalocyanine
PTFE	polytetrafluoroethylene
P_W	corrosion rate related to mass loss
R_{ct}	charge transfer resistance
R_f	film resistance
R_s	solution resistance
R_{sum}	sum of film resistance and charge transfer resistance
SCE	saturated calomel electrode
SE	secondary electron
SEM	scanning electron microscope
SHE	standard hydrogen electrode
SKPFM	scanning Kelvin probe force microscope
SiC	silicon carbide
S_6	cyclohexasulphur
S_8	cyclooctasulphur
S_{12}	cyclododecasulphur
t	time
UUV	unmanned undersea vehicles
V_H	volume of produced H_2 gas
V_{RH}	real-time hydrogen evolution rate
W_H	mass loss of Mg
W_{theo}	theoretical mass loss
x_i	mass fraction of each element
XPS	X-ray photoelectron spectroscopy
XRD	X-ray diffraction
z	number of electrons transferred per ion
ΔW	practical mass loss
μXRF	X-ray micro fluorescence

2. Publications during candidature

Peer-reviewed papers

1) **M. Deng**, D. Höche, S.V. Lamaka, D. Snihirova, M.L. Zheludkevich, Mg-Ca binary alloys as anodes for primary Mg-air batteries, Journal of Power Sources, 396 (2018) 109-118.

2) **M. Deng**, D. Höche, S.V. Lamaka, L. Wang, M.L. Zheludkevich, Revealing the impact of second phase morphology on discharge properties of binary Mg-Ca anodes for primary Mg-air batteries, Corrosion Science, 153 (2019) 225-235.

3) **M. Deng**, L. Wang, D. Höche, S.V. Lamaka, D. Snihirova, B. Vaghefinazari, M.L. Zheludkevich, Clarifying the decisive factors for utilization efficiency of Mg anodes for primary aqueous batteries, Journal of Power Sources, 441 (2019) 227201.

4) Y. Jin, C. Blawert, F. Feyerabend, J. Bohlen, M. Silva Campos, S. Gavras, B. Wiese, D. Mei, **M. Deng**, H. Yang, R. Willumeit-Römer, Time-sequential corrosion behaviour observation of micro-alloyed Mg-0.5Zn-0.2Ca alloy via a quasi-in situ approach, Corrosion Science, 158 (2019) 108096.

5) L. Wang, D. Snihirova, **M. Deng**, B. Vaghefinazari, S.V. Lamaka, D. Höche, M.L. Zheludkevich, Tailoring electrolyte additives for controlled Mg-Ca anode activity in aqueous Mg-air batteries, Journal of Power Sources, 460 (2020) 228106.

6) **M. Deng**, L. Wang, D. Höche, S.V. Lamaka, P. Jiang, D. Snihirova, N. Scharnagl, M.L. Zheludkevich, Ca/In micro-alloying as a novel strategy to simultaneously enhance power and energy density of primary Mg-air batteries from anode aspect, Journal of Power Sources, 472 (2020) 228528.

7) Y. Jin, C. Blawert, H. Yang, B. Wiese, F. Feyerabend, J. Bohlen, D. Mei, **M. Deng**, M. Silva Campos, N. Scharnagl, K. Strecker, J. Bode, C. Vogt, R. Willumeit-Römer, Microstructure-corrosion behavior relationship of micro-alloyed Mg-0.5Zn alloy with the addition of Ca, Sr, Ag, In and Cu, Materials & Design, (2020). https://doi.org/10.1016/j.matdes.2020.108980

8) **M. Deng**, L. Wang, D. Höche, S.V. Lamaka, P. Jiang, D. Snihirova, M.L. Zheludkevich, Corrosion and discharge properties of Ca/Ge micro-alloyed Mg anodes for primary aqueous Mg batteries. (submitted)

Chapter in a published book

1) **M. Deng**, D. Höche, D. Snihirova, L.Q. Wang, B. Vaghefinazari, S.V. Lamaka, M.L. Zheludkevich, Aqueous Mg batteries, in: M. Fichtner (Ed.) Magnesium Batteries: Research and Applications, Royal Society of Chemistry, United Kingdom, 2019, pp. 275-308.

3. Own contribution to publications and manuscripts included in this dissertation

1) **M. Deng**, D. Höche, D. Snihirova, L.Q. Wang, B. Vaghefinazari, S.V. Lamaka, M.L. Zheludkevich, Aqueous Mg batteries, in: M. Fichtner (Ed.) Magnesium Batteries: Research and Applications, Royal Society of Chemistry, United Kingdom, 2019, pp. 275-308. (incorporated in **Section 2**)
M. Deng designed the outline and structure of this book chapter in discussion with D. Höche and D. Snihirova. The writing and modification of this chapter was implemented by M. Deng according to the comments and corrections made by D. Höche, D. Snihirova, L.Q. Wang, B. Vaghefinazari, S.V. Lamaka and M.L. Zheludkevich.

2) **M. Deng**, D. Höche, S.V. Lamaka, D. Snihirova, M.L. Zheludkevich, Mg-Ca binary alloys as anodes for primary Mg-air batteries, Journal of Power Sources, 396 (2018) 109-118. (incorporated in **Section 5.1**)
M. Deng conceived and planed this work in discussion with D. Höche, S.V. Lamaka and M.L. Zheludkevich. Experiments included in this work were carried out by M. Deng. M.L. Zheludkevich gave guidance and advices on the data analysis and results interpretation. M. Deng conducted the paper writing and modification according to all comments and corrections made by all authors.

3) **M. Deng**, D. Höche, S.V. Lamaka, L. Wang, M.L. Zheludkevich, Revealing the impact of second phase morphology on discharge properties of binary Mg-Ca anodes for primary Mg-air batteries, Corrosion Science, 153 (2019) 225-235. (incorporated in **Section 5.2**)
M. Deng conceived and planed this work in discussion with D. Höche and S.V. Lamaka. Experiments included in this work were carried out by M. Deng. All authors contributed to the data analysis and results interpretation. M. Deng conducted the paper writing and modification according to all comments and corrections made by all authors.

4) **M. Deng**, L. Wang, D. Höche, S.V. Lamaka, D. Snihirova, B. Vaghefinazari, M.L. Zheludkevich, Clarifying the decisive factors for utilization efficiency of Mg anodes for primary aqueous batteries, Journal of Power Sources, 441 (2019) 227201. (incorporated in **Section 5.3**)
M. Deng conceived the conceptual design of this work. L. Wang, D. Snihirova and B. Vaghefinazari gave valuable advices on the experimental design. Experiments included in this work were carried out by M. Deng. D. Höche, S.V. Lamaka and M.L. Zheludkevich gave constructive suggestions on the data analysis and results interpretation. M. Deng conducted the paper writing and modification according to all comments and corrections made by all authors.

5) **M. Deng**, L. Wang, D. Höche, S.V. Lamaka, P. Jiang, D. Snihirova, N. Scharnagl, M.L. Zheludkevich, Ca/In micro-alloying as a novel strategy to simultaneously enhance power and energy density of primary Mg-air batteries from anode aspect. (incorporated in **Section 5.4**)

M. Deng conceived and designed this work in discussion with D. Höche, S.V. Lamaka and M.L. Zheludkevich. M. Deng carried out most experiments included in this work. N. Scharnagl gave constructive suggestions on the data analysis. M. Deng conducted the paper writing and modification according to all comments and corrections made by all authors.

6) **M. Deng**, L. Wang, D. Höche, S.V. Lamaka, P. Jiang, D. Snihirova, M.L. Zheludkevich, Corrosion and discharge properties of Ca/Ge micro-alloyed Mg anodes for primary aqueous Mg batteries. (incorporated in **Section 5.5**)

M. Deng conceived and designed this work in discussion with D. Höche, S.V. Lamaka and M.L. Zheludkevich. Experiments included in this work were carried out by M. Deng and L. Wang. P. Jiang and D. Snihirova gave helpful suggestions on the data analysis and results interpretation. M. Deng conducted the paper writing and modification according to all comments and corrections made by all authors.

Acknowledgement

Here I would like to voice my heartfelt gratitude to all the people who have anyhow contributed to the implementation of this dissertation by their kind support, assistance and encouragement to me. The dissertation would not be accomplished successfully and timely without their contributions.

Firstly, I am particularly grateful to Prof. Mikhail Zheludkevich for offering me this great opportunity of conducting my PhD work in his research group. He is always willing to share his views and knowledge to all group members as far as possible. All of my ideas got support from him accompanying with his constructive advices. I would also like to thank Prof. Karl Ulrich Kainer, the director of Magnesium Innovation Centre (MagIC) during my candidature. Thanks to his great efforts of decades and outstanding achievement on magnesium research, MagIC has become a world-renowned organization regarding Mg investigation, being a good platform for conducting my PhD work concerning Mg anodes development.

Many thanks to my daily supervisors, Dr. Daniel Höche and Dr. Sviatlana Lamaka, two senior scientists on Mg corrosion research. Based on their expertise and experience, they are always ready to share valuable opinions and suggestions on my work, which is significant for me to address the problems I meet. I have truly learnt much about Mg corrosion from them in the daily discussions and regular battery meetings. Special thanks are given to Dr. Darya Snihirova and Mr. Bahram Vaghefinazari in our battery team. Discussion in our battery team is always important for me to modify the experimental design and to better understand my experimental results.

I also want to show my acknowledgement to Mr. Volker Heitman, Mr. Ulrich Burmester, Mr. Gert Wiese, Ms. Petra Fischer, Mr. Günter Meister, Mr. Daniel Strerath, Ms. Sabine Schubert and Dr. Jan Bohlen' team regarding all the assistance on materials preparation, characterization and chemical analysis. Besides, I would like to thank all the colleagues from WZK, especially the senior scientists Dr. Nico Scharnagl and Dr. Carsten Blawert. My research work would not go well without their kind collaboration and support. Many thanks to all my Chinese friends in Geesthacht enabling me to have cheerful leisure time after exhausted work, particularly our poker game team (Mr. Di Mei, Mr. Xun Zeng, Mr. Yiming Jin, Miss Hong Yang, Mrs Pingli Jiang, etc.). I really enjoy all the time travelling and hanging out with them.

Sincerely I appreciate the fellowship from China Scholarship Council (CSC) for supporting the whole work described in this thesis.

Most importantly, I would like to express my deepest gratitude to my family, particularly my parents and my girlfriend Miss Linqian Wang. I am grateful to my parents for supporting every of my career plans, including studying aboard to achieve higher educational degree. The lovely harmonious family atmosphere built by them is certainly the cornerstone of the completion of my PhD and my growing in good health. They set a good example for me to learn how to build a long-term and stable relationship

with Miss. Linqian Wang who has been accompanying me for five years. Many special thanks are given to Miss Wang for always encouraging me when I am depressed, trying best to take care of me when I am sick and, particularly, keeping company with me no matter what happens in the cruel real life. Thanks for keeping up the effort to make me a better person, and a good cook.